AN ABSTRACT OF THE DISSERTATION OF

Kunal H. Kate for the degree of Doctor of Philosophy in Materials Science
presented on June 15, 2015.

Title: Material Properties in Ceramic Injection Molding Design.

Abstract approved:

_____

Sundar V. Atre

Ceramic injection molding (CIM) is a high volume, near net shaping process used to manufacture ceramic parts with complex features and shapes. In CIM design it is important to understand the molding behavior as a function of powder-polymer (feedstock) composition in order to achieve desired part dimensions and properties, at high production rates. Standard practices in CIM product design typically involve performing multiple trial-and-error molding experiments for various feedstock compositions. Alternatively, CIM design simulations can be performed to reduce the iterations. However, they require the measurement of physical, thermal and rheological feedstock properties and the availability of such data is limited. Currently there is no reliable design approach available to perform mold-filling simulations for compositions that differ from those with measured feedstock properties. The present work develops and evaluates a new method to estimate feedstock properties critical to performing CIM simulations. The method utilizes the material properties of ceramic fillers from literature along with experimental measurements of an unfilled wax-polymer binder system.

The current work is divided into three parts. In the first part, nine different ceramic feedstocks and a wax-polymer binder, whose material properties were measured by our research group, formed the basis for this study. Experimental and estimated feedstock properties of these nine systems were compared to quantitatively evaluate the quality of correspondence. The second part uses the measured and estimated physical, thermal, and rheological properties for an aluminum nitride feedstock to perform mold-filling simulations to compare the differences in the output of CIM simulations based on the input feedstock property data from experiments and estimates. The third part examines the merits of CIM simulations to predict mold-filling behavior by conducting injection-molding experiments for an aluminum nitride feedstock. The findings from the current study can be used to improve CIM design practices and serve as a guide for estimating ceramic feedstock properties to conduct mold-filling simulations.

Material Properties in Ceramic Injection Molding Design

by.

Kunal H. Kate

A DISSERTATION

submitted to

Oregon State University

in partial fulfillment of
the requirements for the
degree of

Doctor of Philosophy

Presented June 15, 2015
Commencement June 2016

Doctor of Philosophy dissertation of Kunal H. Kate presented on June 15, 2015.

APPROVED:

Major Professor, representing Materials Science

Director of the Materials Science Program

Dean of the Graduate School

I understand that my dissertation will become part of the permanent collection of Oregon State University libraries. My signature below authorizes release of my dissertation to any reader upon request.

Kunal H. Kate, Author

ACKNOWLEDGEMENTS

I express my deepest gratitude and appreciation to Dr. Sundar Atre. As an advisor, your continued interest in my professional development has been significant. Through your mentoring I have developed research skills, learned how to mentor students, and strengthened skills to lead projects and begin collaborations. As a professional, I am confident that your guidance through graduate school will lead me through a successful and enjoyable career. As friends you have been no less perfect. Across four year in graduate school, I have enjoyed countless fun events and lunch beers from you.

I would also like to specifically thank Dr. John Simonsen. Your knowledge and friendship has improved my research and time at Oregon State University. I have thoroughly enjoyed doing research with you and thank you for providing financial support on the BEST-funded project on the product development of a bio-compostable polymer composite. This work would have not been possible without the research collaboration and inputs from Dr. Ravi K. Enneti. I look forward to see what we can solve in the future. I would like to thank Dr. Skip Rochefort for allowing me to work in his laboratory and teaching me everything about the rheology of polymers that was crucial in the analysis of my research.

Additionally, I would like to thank Dr. Seong Jin Park, Dr. Burak Ozdoganlar and Dr. Randall German who provided invaluable guidance throughout my research. I would like to thanks Dean Elliot, Linda Campbell and Matt Ramsdell from Entek Manufacturing (Albany, OR) for providing their technical expertise and helping me compound the aluminum nitride feedstock. Thank you Tim McCabe from Kinetics, a Dynacast Company (McMinnville, OR) for providing your technical expertise and help me injection mold the aluminum nitride feedstock. Thank you Don Whychell from CM Furnaces (Bloomfield, NJ) for helping me with the sintering studies. I would like to thank Teresa Sawyer from the electron microscopy facility at Oregon State University for helping me with scanning electron microscopy analysis.

I would also like to thank all of the members of the Materials Innovation Guild for providing a great environment to conduct research. Your feedback during weekly meetings had a tremendous impact on keeping this research moving forward. A special thanks to Mark Winseck, Zack McClure, and Brenton Barmore for providing your critical input for this dissertation.

Thank you to my wonderful parents Hemant and Netra Kate; your patience and understanding of my long days and nights is deeply appreciated. You have supported me and allowed me to follow something I am passionate about and I will never forget your support. Through your 27 years of support, your contribution to this work is certainly no less than mine.

Thank you National Science Foundation (Grant # CMMI 1200144) for funding this work. Thank you to the previous graduate students, Valmikanathan Onbattuvelli, Sachin Laddha, Roshan Urval, Jürgen Lenz, and Renee Martin from our group for your work on various ceramic feedstocks. This work would not have been possible without your feedstock property measurement studies.

CONTRIBUTION BY AUTHORS

I was involved in design, data collection, writing and interpretation of data for Chapters 2 Chapter 3 and Chapter 4. Dr. Sundar V. Atre and Dr. Ravi K. Enneti were also involved in design, interpretation and writing of Chapter 2, Chapter 3 and Chapter 4. Tim McCabe assisted in performing injection molding experiments for the aluminum nitride feedstock. Mark Winseck, and Dr. Valmikanathan Onbattuvelli assisted in data collection, writing and interpretation of Chapter 2. Dr. Seong Jin Park, Dr. Burak Ozdoganlar and Dr. Randall M. German assisted in the interpretation of the data in Chapter 2.

TABLE OF CONTENTS

Page

TABLE OF CONTENTS (Continued)

Page

TABLE OF CONTENTS (Continued)

Page

TABLE OF CONTENTS (Continued)

Page

LIST OF FIGURES

Figure Page

LIST OF FIGURES (Continued)

Figure Page

LIST OF FIGURES (Continued)

Figure Page

LIST OF FIGURES (Continued)

Figure Page

LIST OF FIGURES (Continued)

Figure Page

LIST OF TABLES

Table Page

LIST OF TABLES (Continued)

Table Page

LIST OF APPENDICES

Appendix Page

LIST OF APPENDICES TABLES

Table Page

LIST OF APPENDICES TABLES (Continued)

Table Page

LIST OF APPENDICES TABLES (Continued)

Table Page

LIST OF APPENDICES TABLES (Continued)

Table Page

LIST OF APPENDICES FIGURES

Figures Page

LIST OF APPENDICES FIGURES (Continued)

Figures Page

LIST OF APPENDICES FIGURES (Continued)

Figures Page

I dedicate this dissertation *to*

my parents Hemant and Netra Kate who have supported and guided me all throughout my life.

Chapter 1: Material Properties in Ceramic Injection Molding

1.1 Introduction

Ceramic injection molding (CIM) is a net-shaping process used to manufacture ceramic parts with diverse size, shape, complexity, material composition, and microstructures. The CIM process is economical to manufacture parts at high production volumes. Complex shapes manufactured using CIM have applications in a wide variety of sectors, for instance the medical, electronics, and consumer industries as shown in **Figure 1.1**

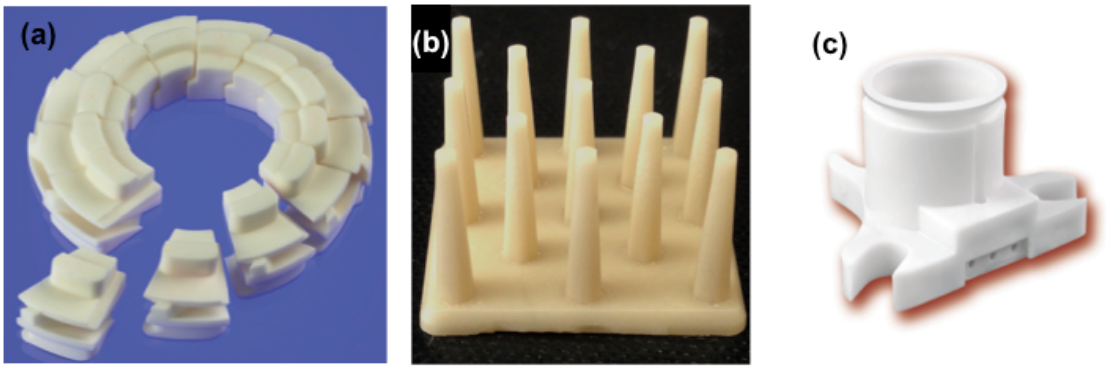

Figure 1.1. Complex shapes manufactured by CIM: (a) orthodontic bracket made from alumina (©Morgan Advanced Materials, used with permission), (b) aluminum nitride heat sink substrates, and (c) zirconia mounting bracket (©Ceramco, used with permission)

The CIM process can be divided into four basic steps. In the first process step, ceramic powder is compounded with a polymer (binder) to make a ceramic feedstock. In the second step, the ceramic feedstock is injection molded into a part of desired shape. Subsequently, the polymer phase is removed from the molded part (debound) and finally sintered under controlled time, temperature and atmospheric conditions to get a final part with desired dimensions, density, microstructure and properties.

In CIM design, it is important to identify an appropriate powder-binder ratio for the feedstock so that a part can be easily injection molded a part with desired final part properties. Standard practices in CIM product design often involve

multiple trial-and-error experiments to identify an optimum feedstock composition. Alternatively, CIM simulations can be utilized to reduce the expensive iterations early in the design and manufacturing cycle. In order to perform CIM simulations, measurements for feedstock properties are required. Feedstock properties crucial for performing CIM simulations include physical, thermal and rheological characteristics. However, the data for such properties is not widely available and are expensive to compile. There is currently no reliable method available to estimate these feedstock properties.

During the course of research, a first journal paper published as a part of my master's research involved an in-depth literature search to evaluate models for each thermal, physical and rheological property [1]. The selected models were curve fitted to experimental data on filled polymers and a coefficient of determination was calculated for data from each material system. The results of the analysis helped select models that had general applicability for a wide range of highly filled powder-polymer mixtures.

The selected models were used to predict the effect of powder content on the feedstock property data for two aluminum nitride-polymer mixtures and published in two additional journal papers [2, 3]. The predicted properties over a range of powder volume fractions helped to quantitatively understand the influence of material composition on mold-filling behavior using computer simulations performed with Autodesk Moldflow software [2-4].

The present work develops a new protocol to estimate feedstock properties and use them to perform CIM simulations with the help of ceramic filler material properties found in literature along with experimental measurements on an unfilled wax-polymer binder system. It is expected that the findings from this dissertation will be useful in revamping CIM design and manufacturing practices and serve as a guide for determining feedstock properties to routinely conduct mold-filling simulations.

Chapter 2 of this thesis evaluates nine different ceramic feedstocks and a wax-based polymer binder system and formed the basis for this study. Experimental and estimated feedstock properties of these nine systems were compared to look at the nature of the scatter in estimations. Regression analysis indicated the suitability of models for estimating material properties such as density, specific heat, specific volume, and viscosity. However, additional experimentation and model development would be required for properties such as thermal conductivity. The study presented in the **Chapter 2** has been prepared for submission to the journal, *Materials and Design*.

Chapter 3 evaluates the use of the feedstock property estimation approach identified in **Chapter 2** to estimate physical, thermal, and rheological feedstock properties for an aluminum nitride (AlN) feedstock. The AlN feedstock property estimates were compared to experimental measurements. Mold-filling simulations were performed for a set of process input parameters and heat-sink substrate geometries to compare the differences in the output of PIM simulations using the feedstock property data from experiments and estimates. **Chapter 3** has been prepared for submission to the journal, *Powder Technology*.

Chapter 4 evaluates the merits of CIM simulations in predicting mold filling behavior by conducting injection-molding experiments. Aluminum nitride feedstock of 80.5 wt.% was compounded using a twin-screw extruder and injection molded into a tensile bar geometry. Injection molding experiments were performed using the AlN feedstock at various melt temperatures and injection pressures to obtain complete and partially filled tensile bar parts. Mold-filling simulations were performed using experimentally measured and estimated AlN feedstock properties for the tensile bar geometry used during the injection molding experiments. The AlN feedstock properties were estimated using the method presented in **Chapters 2** and **3**. A comparison between injection molding experiments and simulations was made to understand the

effectiveness of PIM simulations in predicting molding behavior. **Chapter 4** has been prepared for submission to the journal, *Materials and Manufacturing Processes*.

Appendix A contains the raw experimental data for the feedstock and binder properties that were used in conjunction with semi-empirical models to obtain the results in **Chapters 2, 3** and **4**. **Appendix B** contains the ceramic filler data collected from literature that were used in conjunction with semi-empirical models to obtain the results in **Chapters 2, 3** and **4**. **Appendices C,** and **D** summarize the detailed procedures for the extraction of curve-fitting parameters. **Appendix E** presents the scanning electron micrographs (SEM) for sintered green micromachined AlN samples.

1.2 References

[1] K. H. Kate, R. K. Enneti, S.-J. Park, R. M. German, and S. V. Atre, “Predicting Powder-Polymer Mixture Properties for PIM Design,” *Crit. Rev. Solid State Mater. Sci.*, vol. 39, no. 3, pp. 197–214, Mar. 2014.

[2] K. H. Kate, V. P. Onbattuvelli, R. K. Enneti, S. W. Lee, S.-J. Park, and S. V. Atre, “Measurements of Powder–Polymer Mixture Properties and Their Use in Powder Injection Molding Simulations for Aluminum Nitride,” *JOM*, vol. 64, no. 9, pp. 1048–1058, Sep. 2012.

[3] K. H. Kate, R. K. Enneti, V. P. Onbattuvelli, and S. V. Atre, “Feedstock properties and injection molding simulations of bimodal mixtures of nanoscale and microscale aluminum nitride,” *Ceram. Int.*, vol. 39, no. 6, pp. 6887–6897, Aug. 2013.

[4] J. Lenz, R. K. Enneti, V. Onbattuvelli, K. Kate, R. Martin, and S. Atre, “Powder Injection Molding of Ceramic Engine Components for Transportation,” *JOM*, vol. 64, no. 3, pp. 388–392, Mar. 2012.

Chapter 2: Material Property Design in Ceramic Injection Molding

Abstract

Ceramic injection molding (CIM) is a near-net shaping process used to manufacture ceramic parts with complex shapes and features at high production volumes. Standard practices in CIM product design involve multiple trial and error experimentations for each process step. Process steps in CIM include feedstock formulation, mold design, injection molding, debinding and sintering. The current design approach to facilitate injection molding experiments involves mold filling computer simulations. However, the mold filling design simulations require material property data and feedstock composition as inputs. Even with carefully designed experiments and simulations, poor structural properties and molding defects are found in CIM parts. A probable cause for this can be related to incorrect feedstock composition. Currently there is no reliable design approach to perform mold filling simulations for compositions that differ from the measured feedstock properties. In the present work, semi-empirical models are used to estimate feedstock properties with the help of material properties of ceramic fillers from literature along with limited experimental measurements. In the current work, nine different ceramic feedstocks and a wax-based polymer binder whose material properties were reported in literature by our research group formed the basis for this study. Experimental and estimated feedstock properties of these nine systems were compared to look at the nature of the scatter in estimation. As a case study, experimental and estimated feedstock properties of AlN were used to perform mold filling simulations for predicting mold filling behavior. The findings from the current study can be used to improve CIM design practices and serve as a guide for using literature ceramic filler properties to conduct mold filling simulations.

List Of Symbols

1) ϕ_p volume fraction of powder
2) ϕ_b volume fraction of binder
3) ϕ_{max} maximum volume fraction
4) X_c mass fraction of composite
5) X_b mass fraction of binder
6) X_p mass fraction of powder
7) ρ_b density of binder
8) ρ_p density of powder
9) ρ_c density of composite
10) C_{p_c} specific heat of composite
11) C_{p_p} specific heat of powder
12) C_{p_b} specific heat of binder
13) A 0.2 (shape factor for spherical particles)
14) λ_c thermal conductivity of composite
15) λ_p thermal conductivity of powder
16) λ_b thermal conductivity of binder
17) η_b viscosity of binder
18) η_c viscosity of composite
19) υ_c specific volume of composite
20) υ_p specific volume of powder
21) υ_b specific volume of binder

2.1. Introduction

Ceramic injection molding (CIM) is a net shaping process that manufactures commercial products with diverse size, shape, complexity, material composition, and structure. Figure 2.1a shows alumina bobbin fabricated from a CIM process, Figure 2.1b shows a detector component made from alumina, Figure 2.1c shows an auger bit made from alumina, and Figure 2.1d shows a circuit coverlid made from alumina (©Ceramco images used with permission). Figure 2.1e shows a PIM heat sink geometry made from aluminum nitride that has 10 mm long and 2 mm hexagonal fins. Figure 2.1f shows a mounting bracket made from zirconia, Figure 2.1g shows an octahedron made mullite, Figure 2.1h shows a sensor caps made from zirconia, and Figure 2.1i shows a swirl baffle made from alumina (©Ceramco images used with permission).

Ceramic injection molding (CIM) is a net shaping process that manufactures commercial products with diverse size, shape, complexity, material composition, and structure. **Figure 2.1a** shows alumina bobbin fabricated from a CIM process, **Figure 2.1b** shows a detector component made from alumina, **Figure 2.1c** shows an auger bit made from alumina, and **Figure 2.1d** shows a circuit coverlid made from alumina (©Ceramco images used with permission). **Figure 2.1e** shows a PIM heat sink geometry made from aluminum nitride that has 10 mm long and 2 mm hexagonal fins. **Figure 2.1f** shows a mounting bracket made from zirconia, **Figure 2.1g** shows an octahedron made mullite, **Figure 2.1h** shows a sensor caps made from zirconia, and **Figure 2.1i** shows a swirl baffle made from alumina (©Ceramco images used with permission).

Ceramic injection molding is a multi-step complex process. To successfully fabricate a part it is important to optimize variables for each process step. In the first step, ceramic powder and polymer binder are mixed uniformly to form a ceramic feedstock. This is typically done with a twin-screw extruder. In the feedstock-compounding step it is crucial to identify the precise powder to binder ratio. This will correlate to how well a feedstock can be injection molded. The

extruded feedstock is pelletized and transported to a molding machine where a desired shape can be acquired. Variables such as the part geometry, mold design, material properties, process parameters, and feedstock homogeneity will determine the success of mold filling. Once the part is successfully molded, the polymer binder is removed by thermal or solvent extraction methods (debinding). In this step, retention of shape and surface texture are important. Debinding parameters will depend on process variables such as debinding rate, temperature, solvent, and the type of polymer/binder system. When most of the polymer is removed the part is then sintered to near-full density. Sintering process variables include time-temperature-rate conditions, sintering aid, material properties, and structural integrity [1].

2.1.1 Sintered material properties of ceramics

Properties of sintered ceramic materials are used to select the optimum ceramic material for a particular application. **Table 2.1** presents physical, thermal, and mechanical properties for sintered ceramics. The included compounds are alumina (Al_2O_3), silicon carbide (SiC), zirconia (ZrO_2), silicon nitride (Si_3N_4), barium titanate ($BaTiO_3$), titanium nitride (TiN), mullite ($3Al_2O_3.2SiO_2$), and aluminum nitride (AlN). Ceramics typically have low densities (Table 2.1) between 2200 and 6030 kg/m^3, a high hardness (Knoop) from 750 to 2530 kg/mm^2, high compressive strength between 970 and 4600 MPa, and moderate flexural strength from 90 to 1150 MPa. The relatively low density and favourable mechanical properties make ceramics the material of choice for a variety of applications. Ceramics (**Table 2.1**) also have lower dielectric constant values (3.8 to 10) making them excellent insulators. An exception to this is $BaTiO_3$, an excellent dielectric material, which has a dielectric constant of 3000. In short, ceramic materials can perform under extreme conditions such as high temperature, corrosive or abrasive environments, and high loads [1–5].

2.1.2 Applications of ceramic injection molded products

As stated previously, CIM product applications are diverse since ceramics offer a wide range of material properties. The majority of CIM applications can be found in industrial, transportation, electrical, medical, communications, lighting, textile, and consumer industries (**Table 2.2**). Typically, CIM products are made from alumina, silicon carbide, aluminum nitride, silica, and zirconia (**Table 2.2**). CIM industrial applications [6–10] such as stator, turbine blades, bearings, and aerofoil casting cores are generally manufactured from SiC, Si_3N_4, Al_2O_3, ZrO_2 and $3Al_2O_3.2SiO_2$. This is due to their high mechanical and thermal properties (**Table 2.1**), low cost, and chemical stability [6–10].

CIM medical and dental applications [8,11–16] such as implants, endoscopic cutters, catheter tips, prosthetic replacements, orthodontic brackets, and dental abutments are generally fabricated from Si_3N_4, Al_2O_3, and ZrO_2 (**Table 2.2**) due to their excellent mechanical properties (**Table 2.1**) and chemical stability [8,11–16]. Most CIM communication applications [17–19] such as connectors for telecom, ferrules, and optical sleeves are manufactured from ZrO_2 (**Table 2.2**) due to its excellent mechanical properties (**Table 2.1**) and chemical stability [17–19]. CIM electrical applications [8, 11–16] such as RF insulators [8] are typically made from Al_2O_3 due to its ideal insulation properties (**Table 2.1**). AlN is preferred for heat sinks and electronic packages[20, 21] (**Table 2.2**) due to its high thermal conductivity and low values of coefficient of thermal expansion (CTE). The CTE of AIN is also close to silicon's CTE (**Table 2.1**) making it an ideal choice of material for electronic packaging.

General applications of CIM in transportation include glow plugs, gear wheels, valve seats, breaking pads, and turbocharger rotors [22–26]. These products are usually manufactured from SiC, Si_3N_4, Al_2O_3, and ZrO_2 due to their good mechanical, thermal, and electrical insulation properties (**Table 2.1**) in addition to low cost and chemical stability[22–26]. In consumer industry, CIM products are manufactured for making cups, injection printheads, luxury pen bodies,

control switches, watch components and battery covers for mobile phones (**Table 2.2**) [8,27–29]. Due to the complex nature of the CIM process and its wide range of application the technology for fabricating parts from various material systems must be precise, cost effective, and produce defect free products.

2.1.3 Design requirements for CIM

Manufacturing defect free parts of high quality often poses a challenge to design and process engineers. Defects can occur at any part of the CIM process and are often resolved by trial and error experimentation which can be time consuming and expensive. The appearance of defects and sub-standard part quality are typically due to poor setup of the injection molding process parameters, feedstock composition and properties, inhomogeneous feedstock formulation, and improper mold design. A more efficient way to reduce molding defects and improve part quality is to conduct simulations with the help of computer aided engineering (CAE) design tools [30–42].

2.1.4 Mold filling simulations

The mold filling simulations are performed using CAE design software like Autodesk Moldflow, Sigmasoft, PIMsolver, and Modelx3D. These computer simulations need reliable feedstock property data and process parameters as input variables to simulate injection molding behavior. With the help of these simulations, design engineers can analyse mold filling dynamics, identify defect evolution, and optimize process parameters. **Figure 2.2** shows the use of mold filling simulations to study a variety of design geometries with part dimensions ranging between 5 mm and 200 mm along with various material systems such as AlN, $3Al_2O_3.2SiO_2$, Si_3N_4, Al_2O_3, SiC, and ZrO_2 composites. Mold filling simulations can be used to study the filling behavior in design geometries with an array of feature sizes. Complex geometries of a few millimetres can be modeled (**Figure 2.2A, 2D, 2F**) and simple design geometries (**Figure 2.2B, 2C**, and **2E**) with feature sizes of 10 mm or above can also be simulated.

In literature there is a limited database of feedstock properties that can be used in CAE design simulations. Sometimes, even after experimentally measuring feedstock properties and conducting simulations the expected mold filling results will not become apparent due to improper feedstock composition (powder/polymer ratio). Therefore, a technique to estimate ceramic feedstock properties and further use them to conduct mold filling simulations will be presented in this work.

In order to estimate ceramic feedstock properties pre-selected semi-empirical models were used along with ceramic filler properties gathered from literature. Further comparisons of experimentally measured feedstock properties with estimated feedstock properties were conducted to look at the nature of scatter in estimates. Comparative mold filling simulations using estimated and experimental feedstock properties as inputs were used to look at the influence of scatter in estimates on predicting mold filling behavior and output parameters. It is anticipated that the current material property design method will serve as step towards reducing the high level of trial and experimentation prevalent in CIM industry.

2.2 Feedstock properties

Feedstock properties required to simulate mold filling behavior include physical, thermal, rheological, and pressure-volume-temperature (PVT) parameters. A limited database of ceramic feedstock properties is available to perform mold-filling simulations. Experimental feedstock properties of various ceramic material systems were obtained from our research groups' previous work. Feedstock properties were estimated using pre-selected semi-empirical models and ceramic filler properties. By comparing estimated and experimental ceramic feedstock properties the scatter in estimates was studied.

2.2.1 Ceramic feedstocks

The experimental feedstock properties of various ceramic material systems were obtained from our research groups' previous work [30,35,36,43–49]. The ceramic material systems considered for this study included silicon carbide, aluminum nitride, silicon nitride, mullite composite, zirconia composite, alumina, and barium titanate (**Table 2.3**). All ceramic feedstocks contain a common wax polymer binder (**Table 2.3**). The considered ceramic systems for the current study comprise a large majority of ceramic systems used in CIM (**Figure 2.3**) [50].

2.2.2 Powder composition and particle attributes

The ceramic powder content in the feedstock ranged between 0.79 and 0.90 weight percent (**Table 2.3**). A co-rotating twin-screw extruder (Entek Manufacturing) was used to extrude all ceramic feedstocks. The ceramic feedstocks compositions are shown in **Table 2.3.** There are two types of ceramic powder considered for this study: 1) monomodal (microscale powders) and 2) bimodal (mixture of microscale and nanoscale powders). The average particle size of the microscale ceramic powders ranged between 0.7 and 1.1 μm and average particle size of nanoscale ceramic powders ranged between 20 and 50 nm. The amount of nanoscale ceramic powder in a system ranged between 14 and 19 weight percent of the powder.

2.3 Ceramic feedstock property measurements and estimates

The experimentally measured solid density, melt density, specific heat, and thermal conductivity reported in our previous work [41,42,44,46,51,52] for various ceramic feedstocks and binder at 300K are represented in **Table 2.4**. Measurements were made at Datapoints Labs (Ithaca, NY). The ceramic feedstock properties are measured for silicon carbide, aluminum nitride, silicon nitride, mullite composite, zirconia composite, alumina, and barium titanate systems (**Table 2.4**) with each feedstock made from a common wax polymer binder.

Viscosity measurements were made for shear rates between 10-1000 s^{-1} in conjunction with temperatures of 415 and 425 K for silicon carbide, aluminum nitride, silicon nitride, mullite composite, zirconia composite, alumina, and barium titanate (**Table 2.5**) ceramic feedstocks. The viscosity-shear rate-temperature dependence for all ceramic feedstocks is presented in **Table 2.5**.

Specific volume measurements were made for temperature ranges between 330 and 290 K with pressures from 0 to 200 MPa for silicon carbide, aluminum nitride, silicon nitride, mullite composite, zirconia composite, alumina, and barium titanate (Table 2.6) ceramic feedstocks. Temperature- specific volume-pressure dependence for all ceramic feedstocks is presented in Table 2.6.

The included feedstock property measurements serve as a basis for comparison with the estimated feedstock properties. To estimate ceramic feedstock properties semi-empirical equations, binder properties, and filler property data are required as inputs.

2.3.1 Semi-empirical models

Feedstock properties can be estimated using semi-empirical models [41,42,45,53]. **Table 2.7** shows the semi-empirical models used in this study to estimate various feedstock property and are selected based on our previous work [40]. The selection criteria for using these models is based on an in-depth analysis of various published models fitted to data on feedstock properties experimentally measured by our group [40]. The semi-empirical models use filler and binder properties to estimate feedstock properties.

2.3.2 Filler properties of ceramics

A literature survey was conducted to find typical values of filler material properties at 300 K and the findings are summarized in **Table 2.8**. More than 50 peer reviewed journal papers and several books published in the past 60 years were reviewed to find the filler properties for ceramic material systems represented in **Table 2.3**. The filler property values that were reported for 300 K

were selected to maintain the consistency in comparison between experimental and estimated feedstock properties.

A total of 78 filler solid density values were gathered for the seven ceramic systems in **Table 2.8**, with 5-20 data points per ceramic system. The solid density for the fillers ranged between 2980 and 6910 kg/cm^3. A total of 52 filler specific heat values were gathered for the seven ceramic systems in **Table 2.8**, with 5-16 data points per ceramic system. The specific heat capacity values for the fillers were reported between 390 and 830 J/kg-K. A total of 68 filler thermal conductivity values were gathered for the seven ceramic systems in **Table 2.8**, with 5-18 data points per ceramic system. The thermal conductivity for the fillers ranged from 3-300 W/m-K. In order to estimate specific volume over a range of temperatures during injection molding simulations an assumption was made that the solid density of the filler does not change with temperature. Another reason for this assumption is the lack of data reported in the literature for specific volume of ceramic fillers over a range of temperatures.

2.3.3 Density

Density measurements and estimations were conducted for silicon carbide, aluminum nitride, silicon nitride, mullite composite, zirconia composite, alumina, and barium titanate feedstocks with a wax polymer binder.

Density measurements

The feedstock solid density measurement was performed using Archimedes principle in accordance with ASTM D792. Measurements for density data are reported in **Table 2.4** [43,44,46–48]. The solid density values for ceramic feedstocks ranged between 2020 and 3590 kg/m^3 and binder density was 870 kg/m^3. The feedstock melt density was measured using a capillary rheometer in accordance with ASTM D3835 [43,44,46–48] The melt density values for ceramic feedstocks ranged between 1850 and 3370 kg/m^3 and binder melt density was 700 kg/m^3.

Density estimates

An inverse rule of mixture (**Equation 1**) was used to estimate solid density of AlN feedstock. This equation is suitable for predicting powder-polymer density at higher weight fractions of fillers [40]. **Equation 1** provides a coefficient of determination (R^2) of 0.97 when fitted to literature data on measured powder-polymer densities (50-70 wt%) [40]. The solid density for various feedstocks was estimated using the filler mass fractions from **Table 2.3**, the binder density from **Table 2.4**, the filler solid density from **Table 2.8**, and using the inverse rule-of-mixtures model represented by **Equation 1** (**Table 2.7**). In manufacturing feedstock formulation is represented by weight. However, volumetric comparisons are often useful when examining powders of differing densities. The volumetric fractions for powder and binder were calculated from the mass fraction using **Equation 2** and **3** (**Table 2.7**). The solid densities estimated for different feedstocks were plotted against the experimental feedstock solid density (**Table 2.4**) as shown in **Figure 2.4**. A coefficient of determination (R^2) value exceeding 0.97 was obtained for **Figure 2.4**, which indicates a good fit and applicability of Equation 1 to predict PIM feedstocks densities from literature filler density values.

2.3.4 Specific heat

Specific heat measurements and estimations were conducted for silicon carbide, aluminum nitride, silicon nitride, mullite composite, zirconia composite, alumina, and barium titanate feedstocks with a wax polymer binder.

Specific heat measurements

Specific heat measurements of all feedstocks were made using differential scanning calorimetry (DSC)[43,44,46–48]. The specific heat values for ceramic feedstocks ranged between 940 and 3300 J/kg-K and specific heat value for the polymer binder was 1240 J/kg-K.

Specific heat estimates

Several mathematical models published in literature that can estimate specific heat of a powder-polymer mixture include: rule of mixture model, modified rule of mixture model, and the Christensen model [40]. In the present study a modified rule of mixture model (**Equation 4**) was used to estimate specific heat. **Equation 4** provides R^2 values ranging from 0.92-0.97 when fitted to literature data on measured powder-polymer specific heats of five 47-75 wt.% filled material systems [40]. The specific heats for various feedstocks were estimated using the filler mass fractions from **Table 2.3**, the filler and binder specific heats from **Table 2.4** and then by using **Equation 4**. The specific heats estimated for different feedstocks were plotted against experimental feedstock specific heat (**Table 2.4**) as shown in **Figure 2.5**. A coefficient of determination (R^2) value exceeding 0.64 indicates a reasonable fit and applicability of the model to predict specific heat in PIM feedstocks. A probable cause for reasonable values of R^2 can be attributed to a large standard deviation of ±2-12% observed in the filler specific heats values presented in **Table 2.8**.

2.3.5 Thermal conductivity

Thermal conductivity measurements and estimations were conducted for silicon carbide, aluminum nitride, silicon nitride, mullite composite, zirconia composite, alumina, and barium titanate feedstocks with a wax polymer binder.

Thermal conductivity measurements

A transient line-source technique was used to make the thermal conductivity measurements (ASTM D5930) for all ceramic feedstocks. Measurements were performed on a K-system II thermal conductivity from 190°C to 30°C [43,44,46–48]. The thermal conductivity values for all ceramic feedstocks ranged between 1.0 and 3.8 W/m-K.

Thermal conductivity estimates

The Maxwell model, Bruggeman model, and Modified Lichtenecker model can be used to estimate thermal conductivity.[40] In the present study a Bruggeman model (**Equation 5**) was used to estimate thermal conductivity of AlN feedstock [40]. The thermal conductivity for various feedstocks were estimated using the filler volume fractions from **Table 2.3**, the binder thermal conductivity from **Table 2.4**, the filler thermal conductivity from **Table 2.8**, and semi-empirical model represented by Equation 5. The thermal conductivity estimated for different feedstocks were plotted against the experimental feedstock thermal conductivity (**Table 2.4**) as shown in **Figure 2.6**. A coefficient of determination (R^2) value of 0.23 indicates only a poor predictive ability of the model used. One source of error can be attributed to the large standard deviation of 4-33% observed in the filler thermal conductivity values obtained from the literature. These may be substantially different from the actual values of thermal conductivity for the fillers in the feedstock. Other models may provide a better prediction of the thermal conductivity of PIM feedstocks compared to Equation 5, or additional experimentations may be needed.

2.3.6 Viscosity

Viscosity measurements and estimations were conducted for silicon carbide, aluminum nitride, silicon nitride, mullite composite, zirconia composite, alumina, and barium titanate feedstocks with a wax polymer binder for various shear rates and temperatures.

Viscosity measurements

A capillary rheometer was used to measure viscosity of all ceramic feedstocks. ASTM D3835 standard was used for conducting the measurements [43,44,46–48]. Tests were run for temperatures between 415 K and 430 K at shear rates between $10s^{-1}$ and 10^4s^{-1}. The viscosities for various ceramic feedstocks for a range of shear rates and temperature are shown in **Table 2.5** [43,44,46–48]. A typical representation of viscosity shear rate dependence for 415 K and 425 K

is shown in **Figure 2.7**. It can be observed that viscosity decreases with increase in shear rate for all material systems representing shear thinning behavior. The inset image in **Figure 2.7** represents the common binder viscosity plotted as a function of shear rate for temperatures of 415 and 425 K and shows a similar shear thinning behavior.

Viscosity estimates

The Chong model, Eiler model, Mooney model, and Simplified Krieger Dougherty model can be used to estimate viscosity [40]. In the present study, the Simplified Krieger Dougherty model (**Equation 6**) was used to estimate viscosity. **Equation 6** provides R^2 values ranging from 0.94-0.99 when fitted to literature data on measured powder-polymer viscosity of three 10-60 vol.% filled material systems [40]. The viscosity for various ceramic feedstocks was estimated using a simplified Krieger Dougherty model (**Equation 6**). The feedstock viscosity was estimated by taking maximum filler content as 0.64 while using the feedstock and binder viscosity values at different shear rates from **Table 2.5** in tandem with **Equation 6**. The experimental feedstock viscosity is plotted as a function of estimated feedstock viscosity for different material systems as shown in **Figure 2.8**. Viscosity decreases with increase in shear rate for both experimental and estimated viscosity. The lowest values of viscosity for each material system correspond to $10^4 s^{-1}$ shear rate while the highest viscosity values correspond to $10 s^{-1}$ shear rate. The coefficient of determination (R^2) value of 0.6 supports the general applicability of the approach to predict the viscosity of PIM feedstocks. To improve viscosity estimations across all shear rate and temperature ranges is a part of our future research article.

2.3.7 Specific volume

Specific volume measurements and estimations were conducted for silicon carbide, aluminum nitride, silicon nitride, mullite composite, zirconia composite,

alumina, and barium titanate feedstocks with a wax polymer binder for various pressures and temperatures.

Specific volume measurements

Measurements for specific volume as a function of temperature and pressure were made using a high-pressure dilatometry. Tests were performed at temperature ranges between 298K and 543K and pressure ranges between 0MPa and 200MPa. Typical representation of specific volume for different ceramic feedstocks at various temperatures and pressures are shown in **Table 2.6** [43,44,46–48]. The specific volume for all feedstocks typically increased with an increase in temperature and decreased with an increase in pressure (**Figure 2.9**). Three distinct zones are observed in Figure 2.9 that represent solid, transition, and melt regions. The solid region occurs at low temperatures (300-320K) for all material systems while melt region occurs at high temperatures (360-450K) for all material systems. The transition region lies around 350 K for all material systems.

Specific volume estimates

A simple rule of mixture (**Equation 7**) was used to estimate specific volume of AlN feedstock. It is suitable for predicting powder-polymer specific volume at higher weight fractions of fillers [40]. It is suitable for predicting powder-polymer specific volume at higher weight fractions of fillers [42]. **Equation 7** provides an R^2 value of 0.99 when fitted to literature data on measured powder-polymer densities of two 20-80 wt.% filled material systems [40]. The specific volume for various feedstocks was estimated using the filler mass fractions from **Table 2.4**, binder specific volume at different temperature and pressures from **Table 2.7**, filler specific volume (as the reciprocal of density) from **Table 2.8**, and a rule-of-mixtures equation represented by **Equation 7**. The specific volume estimated for different feedstocks were plotted against the experimental feedstock specific volume (**Table 2.6**) as shown in **Figure 2.10**. It can be observed that there is an increase in estimated specific volume with an increase

in temperature. A decrease in estimated specific volume is observed with an increase in pressure for all material systems. This trend is similar to that observed for experimental specific volume (**Figure 2.9**). A coefficient of determination (R^2) value exceeding 0.98-0.99 indicates a good fit and the applicability of **Equation 7** to predict specific volume for PIM feedstocks.

2.4 Mold-filling simulations for AlN

As a case study, mold filling simulations for estimated and experimental feedstock properties of AlN were performed to understand the influence of scatter in feedstock property estimates on mold filling behavior. Mold filling simulations were performed using Autodesk Moldflow Insight software. The input parameters for mold filling simulations require properties like specific heat, thermal conductivity, viscosity, and specific volume over a range of temperatures. The feedstock properties were estimated at 300 K since all filler property data was gathered for 300 K. An assumption was made that a filler's property does not change with temperature in order to estimate feedstock properties for a range of temperatures. A reason for this assumption is that there is not much data available in literature for filler properties over a range of temperatures. Mold filling simulations require viscosity and specific volume to be entered as curve fitted constants.

2.4.1 Injection Molding Simulations

A typical heat sink geometry was chosen to conduct mold-filling simulations. Solidworks was used to design the heat sink geometry. Heat sink geometry was imported into Autodesk Moldflow to conduct mold filling simulations. Processing parameters were set at a mold temperature of 35°C, polymer melting temperature of 150°C, velocity to pressure switchover point at 99% volume filled, and a fill time of 0.1 seconds. The part was meshed with an automated solid three-dimensional meshing which makes use of finite element analysis. Simulations were conducted for fill-and-pack type conditions using estimated and experimental μ-AlN feedstock properties in order to understand the

injection molding behavior and its packing characteristics. The progressive mold fill for the heat sink geometry can be seen in **Figure 2.11**. Part filling takes place at the center of the cavity where the injection location is located. The flow front progresses away from the injection location symmetrically, and eventually fills the entire geometry. The blue contour indicates the first filled region in the part and the red contour represents the last filled region in the part.

The process output parameters were obtained by performing mold filling simulations using estimated and experimental μ-AlN feedstock properties. A comparison of simulation output parameters was made to understand the influence of scatter in feedstock property estimates on mold filling. **Figure 2.12** compares selected injection molding simulation output parameters. There is little difference between estimated and experimental values of part mass and volumetric shrinkage due to their dependence on density and specific volume respectively. Both density and specific volume yielded low scatter of values (**Figure 2.3** and **Figure 2.10**). The differences between estimated and experimental values of pressure related output parameters such as injection pressure and clamp force are large because both output parameters are dependent on viscosity. This can be attributed to a moderate fit of 0.64 obtained during viscosity estimation.

2.5 Design outlook

Ceramics considered for the current study included silicon carbide, aluminum nitride, silicon nitride, mullite composite, zirconia composite, alumina, and barium titanate. These ceramics account for majority of material compositions (**Figure 2.3**) that are CIM and form the basis for this study. The ceramic feedstock composition for the considered systems ranged between 0.51 and 0.61 volume fractions. Silicon carbide, aluminum nitride, silicon nitride, and barium titanate systems had bimodal particle size distribution. The variation in feedstock compositions and particle attributes allowed us to examine the

suitability of the selected semi-empirical models to estimate feedstock properties.

Ceramic filler properties gathered for considered ceramics from literature have some variation associated with them (**Table 2.8**). The variation was observed between each material system and material property. For instance, thermal conductivity showed maximum variation in filler property with aluminum nitride having ±33% change. Similarly, specific heat showed a maximum of ±12% change for silicon nitride. Density estimates showed least amount of percent change in filler property in comparison to thermal conductivity and specific heat. The maximum reported percent change in density filler property was ±1.5% for silicon carbide.

Consequently, as a result of this variation in filler properties the ceramic feedstock property estimates were affected. **Table 2.9** summarizes the nature of estimates for each feedstock property estimate in terms of coefficient of determination (R^2) values. It can be observed from **Table 2.9** that density and specific volume tend to have excellent values for estimates with R^2 of 0.96 and 0.97 respectively. Specific heat and viscosity have moderately good values of estimates with R^2 of 0.64 and 0.61 respectively. While, estimates for thermal conductivity tend to be poor with an R^2 of 0.23.

To understand the effect of scatter in material property estimates on predicting mold filling simulations experimental and estimated feedstock properties of μ-AlN were taken as inputs. The output parameters obtained from injection molding simulations indicate that part weight and percent volumetric shrinkage, which are functions of density and specific volume respectively, show little difference between experiments and estimates. Clamp force and injection pressure, which are functions of viscosity, show comparatively large differences between experiments and estimates. This large difference indicates that viscosity estimation needs to be improved and an R^2 of 0.64 gives poor values of pressure related mold filling predictions.

The findings from the current study can be used to improve CIM design practices and serve as a guide to utilize ceramic filler properties from literature to conduct mold filling simulations. The models discussed in this review do not specifically address variations in material properties with particle characteristics (e.g. shape, size, agglomeration) but can serve as a first step towards eliminating the trial-and-error procedures currently prevalent in the design of PIM parts.

2.6 Conclusions

A literature review of the physical, thermal, and rheological properties of powder-polymer mixtures was conducted. The experimental data for each material property as a function of filler volume, or mass fraction, was compared to estimated data from mixture models incorporating literature values of the corresponding filler properties. Regression analysis indicated the suitability of models for estimating material properties such as density, specific heat capacity, specific volume, and viscosity. However, additional experimentation and model development will be required for properties such as thermal conductivity. In addition, the variation between literature reports for filler properties and the actual fillers used in the PIM feedstocks that were selected in this study is unknown. It is expected that the approach presented in this paper will avoid expensive and time-consuming trial-and-error iterations currently prevalent in PIM.

Acknowledgment

The authors thank the financial support obtained from the National Science Foundation (CMMI 1200144).

2.7 References

[1] R. M. German and A. Bose, *Injection Molding of Metals and Ceramics*. Metal Powder Industries Federation, 1997.

[2] Jahanmir, *Machining of Ceramics and Composites*. CRC Press, 1999.

[3] F. Cardarelli, *Materials Handbook: A Concise Desktop Reference*. Springer Science & Business Media, 2008.

[4] R., William Davidge, *Mechanical behaviour of ceramics*. Cambridge ; New York : Cambridge University Press, 1979.

[5] A. Koller and M. Štulíková, *Structure and properties of ceramics*. Amsterdam; London [etc.]: Elsevier, 1994.

[6] D. Whittaker, “Powder injection moulding looks to automotive applications for growth and stability,” *PIM Int.*, vol. 1, no. 2, pp. 14–22, 2007.

[7] J. Neil, G. Bandopadhyay, D. Sordelet, and M. Mahoney, “Development in injection molding silicon nitride turbine components,” in *Proceeding of Gas Turbine and Aeroengine Congress and Exposition*, Brussels, Belgium, vol. 2, p. 186.

[8] T. Ayers and J. M. Hoffman, “Micromini ceramics sport SUPERSIZED PROPERTIES,” *Mach. Des.*, vol. 75, no. 9, p. 59, May 2003.

[9] H.-J. Sterzel, “Spritzgießen keramischer Bauteile,” *Mater. Werkst.*, vol. 28, no. 11, pp. 534–542.

[10] H. Ş. Soykan and Y. Karakaş, “Injection moulding of thin walled zirconia tubes for oxygen sensors,” *Adv. Appl. Ceram.*, vol. 104, no. 6, pp. 285–290, Dec. 2005.

[11] R. M. German, “Powder injection moulding in the aerospace industry: opportunities and challenges,” *PIM International*.

[12] Anonym, “MIM and CIM parts used in Cochlear hearing implant devices,” *PIM International*, Apr-2011.

[13] J. Yang, K. Wang, G. Liu, and D. Wang, “Fracture resistance of inter-joined zirconia abutment of dental implant system with injection molding technique,” *Clin. Oral Implants Res.*, vol. 24, no. 11, pp. 1247–1250, Nov. 2013.

[14] J. L. Johnson and D. F. Heaney, “Processing of biocompatible materials via metal and ceramic injection molding,” *Med. Device Mater. II*, pp. 325–330, 2005.

[15] Anonym, “Amedica signs agreement with Kyocera for silicon nitride medical devices,” *PIM Int.*, vol. 8, no. 1, p. 11, 2014.

[16] Anonym, “BioBone Research Network looks to CIM for promising candidate components for osseointegration,” *PIM Int.*, vol. 7, no. 4, p. 25, 2013.

[17] Anonym, “Formatec reports growth in demand for MicroCIM components,” *PIM International*, Feb-2012.

[18] B. Lin, M. Zhang, C. Wu, and F. Liu, “Optimization and Simulation for Ceramic Injection Mould of ZrO2 Fiber Ferrule,” in *Some Critical Issues for Injection Molding*, Dr. Jian Wang (Ed.)., 2012.

[19] S. I.-E. Lin, “Near-net-shape forming of zirconia optical sleeves by ceramics injection molding,” *Ceram. Int.*, vol. 27, no. 2, pp. 205–214, 2001.

[20] “HB-LED grade aluminum nitride meets thermal needs of today’s LEDs | Solid State Technology.” .

[21] F. Miyashiro, N. Iwase, A. Tsuge, F. Ueno, M. Nakahashi, and T. Takahashi, “High thermal conductivity aluminum nitride ceramic substrates and packages,” *IEEE Trans. Compon. Hybrids Manuf. Technol.*, vol. 13, no. 2, pp. 313–319, 1990.

[22] T. Moritz, “Two-component CIM parts for the automotive and railway sectors’,” *PIM Int.*, vol. 2, no. 4, pp. 38–39, 2008.

[23] M. Pidria, E. Merlone, F. Parussa, J. Handelsman, and A. Gorodnev, “Near Net Shape, Low Cost Ceramic Valves for Advanced Engine Applications,” *Mater. Sci. Forum*, vol. 426–432, pp. 2321–2326, 2003.

[24] J. W. Macbeth, “Ceramic engine components reduce wear, friction,” *Ceram. Ind.*, vol. 7, pp. 33–45, 1984.

[25] S. Kamiya, M. Murachi, H. Kawamoto, S. Kato, S. Kawakami, and Y. Suzuki, “Silicon Nitride Swirl Lower-Chamber for High Power Turbocharged Diesel Engines,” SAE International, Warrendale, PA, SAE Technical Paper 850523, Feb. 1985.

[26] Anonym, “Morgan Technical Ceramics highlights potential for CIM in energy efficient motors,” *PIM International*, 2012.

[27] I. Santacruz, “Aqueous injection moulding of porcelains,” *J. Eur. Ceram. Soc.*, vol. 23, no. 12, pp. 2053–2060.

[28] J. Ter-Maat, M. Blömacher, A. Kern, and A. Thom, “Ceramic injection moulded zirconia products enjoy success in high-value luxury applications,” *PIM Int.*, vol. 4, no. 4, pp. 33–37, 2010.

[29] B. Williams, “Oeschler AF proves its competence in ceramic injection moulding with new BMW applications,” *PIM Int.*, vol. 3, no. 2, pp. 31–35, 2009.

[30] R. Urval, S. Lee, S. V. Atre, S.-J. Park, and R. M. German, “Optimisation of process conditions in powder injection moulding of microsystem components using robust design method Part 2 – Secondary design parameters,” *Powder Metall.*, vol. 53, no. 1, pp. 71–81, Mar. 2010.

[31] S. J. Park, S. Y. Ahn, T. G. Kang, S. T. Chung, Y. S. Kwon, S. Chung, S. G. Kim, S. Kim, S. V. Atre, S. Lee, and R. M. German, “Computer Simulations in Powder Injection Molding,” *Int. J. Powder Metall.*, vol. 46, no. 3, pp. 37–46, 2010.

[32] R. K. Enneti, S. J. Park, J. Palagi de Souza, and S. V. Atre, “Critical Issues In Manufacturing Dental Brackets By Powder Injection Molding,” *Int. J. Powder Metall.*, vol. 48, no. 2, pp. 23–39, 2012.

[33] J. Kim, S. Ahn, S. V. Atre, S. J. Park, T. G. Kang, and R. M. German, “Imbalance filling of multi-cavity tooling during powder injection molding,” *Powder Technol.*, vol. 257, pp. 124–131, May 2014.

[34] R. Urval, C. Wu, S. V. Atre, S. J. Park, and R. M. German, “CAE-Based Process Design for Microfluidic Components,” Powder Injection Molding Internationa,” *PIM International*, no. I, pp. 48–54, 2007.

[35] S. Laddha, C. Wu, G. K. lingam, K. Simmons, S. vallury, S. Lee, S. J. Park, R. M. German, P. Vilma, A. Varez, and S. V. Atre, “Characterization of Alumina Feedstock with Polyacetal and Wax-Polymer Binder Systems for Micro Powder Injection Moulding,” *PIM International*, vol. 3, no. 3, pp. 64–70, 2009.

[36] S. Laddha, C. Wu, S. J. Park, S. Lee, S. Ahn, R. M. German, and S. V. Atre, “Analysis of Macroscale Mold Filling Defects in Micro Powder Injection Molding,” *Int. J. Powder Metall.*, vol. 46, no. 3, pp. 49–59, 2010.

[37] S. V. Atre, S.-J. Park, R. Zauner, and R. M. German, “Process simulation of powder injection moulding: identification of significant parameters during mould filling phase,” *Powder Metall.*, vol. 50, no. 1, pp. 76–85, Mar. 2007.

[38] S. Ahn, S. T. Chung, S. V. Atre, S. J. Park, and R. M. German, “Integrated filling, packing and cooling CAE analysis of powder injection moulding parts,” *Powder Metall.*, vol. 51, no. 4, pp. 318–326, Dec. 2008.

[39] S. W. Lee, S. Ahn, C. J. Whang, S. J. Park, S. V. Atre, J. Kim, and R. M. German, “Effects of process parameters in plastic, metal, and ceramic injection molding processes,” *Korea-Aust. Rheol. J.*, vol. 23, no. 3, pp. 127–138, Sep. 2011.

[40] K. H. Kate, R. K. Enneti, S.-J. Park, R. M. German, and S. V. Atre, “Predicting Powder-Polymer Mixture Properties for PIM Design,” *Crit. Rev. Solid State Mater. Sci.*, vol. 39, no. 3, pp. 197–214, Mar. 2014.

[41] K. H. Kate, R. K. Enneti, V. P. Onbattuvelli, and S. V. Atre, “Feedstock properties and injection molding simulations of bimodal mixtures of nanoscale and microscale aluminum nitride,” *Ceram. Int.*, vol. 39, no. 6, pp. 6887–6897, Aug. 2013.

[42] K. H. Kate, V. P. Onbattuvelli, R. K. Enneti, S. W. Lee, S.-J. Park, and S. V. Atre, “Measurements of Powder–Polymer Mixture Properties and Their Use in Powder Injection Molding Simulations for Aluminum Nitride,” *JOM*, vol. 64, no. 9, pp. 1048–1058, Sep. 2012.

[43] V. P. Onbattuvelli, “The effects of nanoparticle addition on the processing, structure and properties of SiC and AlN,” 2010.

[44] R. A. Martin, “Development of mullite-zirconia composite feedstocks for powder injection molding,” oregon state university, Corvallis Oregon, 2013.

[45] K. H. Kate, “Models for predicting powder-polymer properties and their use in injection molding simulations of aluminum nitride,” 2012.

[46] S. Laddha, “The effect of feedstock composition on defect evolution in powder injection molded ceramic microarrays using simulations and experiments,” Thesis, oregon state university, Corvallis Oregon, 2008.

[47] V. Onbattuvelli, R. K. Enneti, S. B. Sohn, T. McCabe, S. J. Park, and S. V. Atre, “Micro-powder injection molding of barium titanate,” *PIM Int.*, vol. 5, no. 1, pp. 59–65, 2011.

[48] J. H. (Juergen H. Lenz, “Materials and process design for powder injection molding of silicon nitride for the fabrication of engine components,” Mar. 2012.

[49] R. A. Martin, “Development of mullite-zirconia composite feedstocks for powder injection molding,” Jun. 2013.

[50] R. M. German and S. V. Atre, “PIM 2013 Market Study,” New York, SciPiVision, 2013.

[51] J. Lenz, R. K. Enneti, V. Onbattuvelli, K. Kate, R. Martin, and S. Atre, “Powder Injection Molding of Ceramic Engine Components for Transportation,” *JOM*, vol. 64, no. 3, pp. 388–392, Mar. 2012.

[52] V. P. Onbattuvelli, R. K. Enneti, S.-J. Park, and S. V. Atre, “The Effect of Nanoparticle Addition on SiC and AlN Powder-Polymer Mixtures: Part I. Packing & Flow Behavior,” *The effects of nanoparticle addition on SiC and AlN powder–polymer mixtures: Packing and flow behavior*, Jan. 2013.

[53] K. H. Kate, “Models for predicting powder-polymer properties and their use in injection molding simulations of aluminum nitride,” Dec. 2012.

[54] R. K. Enneti, S.-J. Park, J. Palagi de Souza, and S. V. Atre, “Critical issues in manufacturing dental brackets by powder injection molding,” *Int. J. Powder Metall.*, vol. 48, no. 2, pp. 23–29, 2012.

[55] M. Bauccio, *ASM engineered materials reference book*. ASM International, 1994.

[56] Y. S. Touloukian, *Thermophysical Properties of Matter: Thermal conductivity : nonmetallic solids*. IFI/Plenum, 1970.

[57] J. F. Shackelford and W. Alexander, *CRC Materials Science and Engineering Handbook, Third Edition*. CRC Press, 2000.

[58] A. J. Pigram and R. Freer, “The production of Mn-Zn ferrite ceramics by injection moulding,” *J. Mater. Sci.*, vol. 29, no. 24, pp. 6420–6426, Jan. 1994.

[59] S. Liu, V. A. Merrick, and N. Newman, “Structural, chemical and dielectric properties of ceramic injection moulded Ba(Zn1/3Ta2/3)O3 microwave dielectric ceramics,” *J. Eur. Ceram. Soc.*, vol. 26, no. 15, pp. 3273–3278, 2006.

[60] G. Schlieper, “Philips Lighting: The evolution of PIM HID lighting components and the potential for transparent alumina products,” *PIM Int.*, vol. 6, no. 4.

[61] Ç. Toy, Y. Palaci, and T. Baykara, “A new ceramic thread-guide composition via low-pressure injection molding,” *J. Mater. Process. Technol.*, vol. 51, no. 1–4, pp. 211–222, Apr. 1995.

[62] Anonym, “Ceramic inkjet printhead,” *PIM International*, vol. 2, no. 4, p. 26, 2008.

[63] J. B. Wachtman and D. G. Lam, “Young’s Modulus of Various Refractory Materials as a Function of Temperature,” *J. Am. Ceram. Soc.*, vol. 42, no. 5, pp. 254–260, 1959.

[64] “Granta’s CES EduPack and teaching resources: supporting Materials Education.” [Online]. Available: http://www.grantadesign.com/education/. [Accessed: 27-Sep-2013].

[65] R. G. Munro, “Material Properties of a Sintered α-SiC,” *J. Phys. Chem. Ref. Data*, vol. 26, no. 5, p. 1195, Sep. 1997.

[66] R. A. Alliegro, L. B. Coffin, and J. R. Tinklepaugh, “Pressure-Sintered Silicon Carbide,” *J. Am. Ceram. Soc.*, vol. 39, no. 11, pp. 386–389, 1956.

[67] S. Zhu, W. G. Fahrenholtz, and G. E. Hilmas, “Influence of silicon carbide particle size on the microstructure and mechanical properties of zirconium diboride–silicon carbide ceramics,” *J. Eur. Ceram. Soc.*, vol. 27, no. 4, pp. 2077–2083, 2007.

[68] M. Hotta and J. Hojo, “Inhibition of grain growth in liquid-phase sintered SiC ceramics by AlN additive and spark plasma sintering,” *J. Eur. Ceram. Soc.*, vol. 30, no. 10, pp. 2117–2122, Aug. 2010.

[69] J. Hu, H. Xiao, W. Guo, Q. Li, W. Xie, and B. Zhu, “Effect of AlN–Y2O3 addition on the properties and microstructure of in-situ strengthened SiC–TiB2 composites prepared by hot pressing,” *Ceram. Int.*, vol. 40, no. 1, Part A, pp. 1065–1071, Jan. 2014.

[70] V. A. Izhevskyi, L. A. Genova, A. H. A. Bressiani, and J. C. Bressiani, “Microstructure and properties tailoring of liquid-phase sintered SiC,” *Int. J. Refract. Met. Hard Mater.*, vol. 19, no. 4–6, pp. 409–417, Jul. 2001.

[71] L. S. Sigl, “Thermal conductivity of liquid phase sintered silicon carbide,” *J. Eur. Ceram. Soc.*, vol. 23, no. 7, pp. 1115–1122, Jun. 2003.

[72] W. M. Haynes, *CRC Handbook of Chemistry and Physics, 95th Edition*. CRC Press, 2014.

[73] P. U. T. P. R. Center, *Thermophysical Properties of Matter: Specific heat: metallic elements and alloys, by Y. S. Touloukian and E. H. Buyco*. IFI/Plenum, 1970.

[74] H. Nakano, K. Watari, Y. Kinemuchi, K. Ishizaki, and K. Urabe, “Microstructural characterization of high-thermal-conductivity SiC ceramics,” *J. Eur. Ceram. Soc.*, vol. 24, no. 14, pp. 3685–3690, Nov. 2004.

[75] K. Watari, H. Nakano, K. Sato, K. Urabe, K. Ishizaki, S. Cao, and K. Mori, “Effect of Grain Boundaries on Thermal Conductivity of Silicon Carbide Ceramic at 5 to 1300 K,” *J. Am. Ceram. Soc.*, vol. 86, no. 10, pp. 1812–1814, Oct. 2003.

[76] G.-D. Zhan, M. Mitomo, R.-J. Xie, and A. K. Mukherjee, “Thermal and Electrical Properties in Plasma-Activation-Sintered Silicon Carbide with Rare-Earth-Oxide Additives,” *J. Am. Ceram. Soc.*, vol. 84, no. 10, pp. 2448–2450, Oct. 2001.

[77] J. R. Groza and A. Zavaliangos, “Sintering activation by external electrical field,” *Mater. Sci. Eng. A*, vol. 287, no. 2, pp. 171–177, Aug. 2000.

[78] T. B. Jackson, A. V. Virkar, K. L. More, R. B. Dinwiddie, and R. A. Cutler, “High-Thermal-Conductivity Aluminum Nitride Ceramics: The Effect of Thermodynamic, Kinetic, and Microstructural Factors,” *J. Am. Ceram. Soc.*, vol. 80, no. 6, pp. 1421–1435, 1997.

[79] G. A. Slack, “Thermal Conductivity of Pure and Impure Silicon, Silicon Carbide, and Diamond,” *J. Appl. Phys.*, vol. 35, no. 12, p. 3460, Dec. 1964.

[80] W. M. Yim and R. J. Paff, “Thermal expansion of AlN, sapphire, and silicon,” *J. Appl. Phys.*, vol. 45, no. 3, p. 1456, Mar. 1974.

[81] K. Biswas, J. Schneider, G. Rixecker, and F. Aldinger, “Comparative bending creep behaviour of silicon carbide sintered with oxynitride additives,” *Scr. Mater.*, vol. 53, no. 5, pp. 591–596, Sep. 2005.

[82] J. Gu, Q. Zhang, J. Dang, J. Zhang, and Z. Yang, “Thermal conductivity and mechanical properties of aluminum nitride filled linear low-density polyethylene composites,” *Polym. Eng. Sci.*, vol. 49, no. 5, pp. 1030–1034, May 2009.

[83] W. Zhou, “Thermal and dielectric properties of the AlN particles reinforced linear low-density polyethylene composites,” *Thermochim. Acta*, vol. 512, no. 1–2, pp. 183–188, Jan. 2011.

[84] R. Kochetov, T. Andritsch, U. Lafont, P. H. F. Morshuis, S. J. Picken, and J. J. Smit, “Preparation and dielectric properties of epoxy - BN and epoxy - AlN nanocomposites,” in *IEEE Electrical Insulation Conference, 2009. EIC 2009*, 2009, pp. 397–400.

[85] B. L. Zhu, J. Ma, J. Wu, K. C. Yung, and C. S. Xie, “Study on the properties of the epoxy-matrix composites filled with thermally conductive AlN and BN ceramic particles,” *J. Appl. Polym. Sci.*, vol. 118, no. 5, pp. 2754–2764, Dec. 2010.

[86] S. H. Risbud, J. R. Groza, and M. J. Kim, “Clean grain boundaries in aluminium nitride ceramics densified without additives by a plasma-activated sintering process,” *Philos. Mag. Part B*, vol. 69, no. 3, pp. 525–533, 1994.

[87] K. A. Khor, K. H. Cheng, L. G. Yu, and F. Boey, “Thermal conductivity and dielectric constant of spark plasma sintered aluminum nitride,” *Mater. Sci. Eng. A*, vol. 347, no. 1–2, pp. 300–305, Apr. 2003.

[88] M. Medraj, “Understanding AlN sintering through computational thermodynamics combined with experimental investigation,” *J. Mater. Process. Tech*, vol. 161, no. 3, pp. 415–422.

[89] L. Qiao, H. Zhou, and R. Fu, “Thermal conductivity of AlN ceramics sintered with CaF2 and YF3,” *Ceram. Int.*, vol. 29, no. 8, pp. 893–896, 2003.

[90] L. Qiao, H. Zhou, H. Xue, and S. Wang, “Effect of Y2O3 on low temperature sintering and thermal conductivity of AlN ceramics,” *J. Eur. Ceram. Soc.*, vol. 23, no. 1, pp. 61–67, Jan. 2003.

[91] L. Qiao, H. Zhou, K. Chen, and R. Fu, “Effects of Li2O on the low temperature sintering and thermal conductivity of AlN ceramics,” *J. Eur. Ceram. Soc.*, vol. 23, no. 9, pp. 1517–1524, Aug. 2003.

[92] J.-W. Bae, W. Kim, S.-H. Cho, and S.-H. Lee, “The properties of AlN-filled epoxy molding compounds by the effects of filler size distribution,” *J. Mater. Sci.*, vol. 35, no. 23, pp. 5907–5913, Dec. 2000.

[93] G. Ziegler, J. Heinrich, and G. Wötting, “Relationships between processing, microstructure and properties of dense and reaction-bonded silicon nitride,” *J. Mater. Sci.*, vol. 22, no. 9, pp. 3041–3086, Sep. 1987.

[94] M. Fukuhara, K. Fukazawa, and A. Fukawa, “Physical properties and cutting performance of silicon nitride ceramic,” *Wear*, vol. 102, no. 3, pp. 195–210, Apr. 1985.

[95] X. Zhu, “Effects of processing method and additive composition on microstructure and thermal conductivity of Si3N4 ceramics,” *J. Eur. Ceram. Soc.*, vol. 26, no. 4–5, pp. 711–718.

[96] X. Zhu, Y. Zhou, and K. Hirao, “Effect of Sintering Additive Composition on the Processing and Thermal Conductivity of Sintered Reaction-Bonded Si3N4,” *J. Am. Ceram. Soc.*, vol. 87, no. 7, pp. 1398–1400, Jul. 2004.

[97] B. R. Golla, “Effect of particle size and oxygen content of Si on processing, microstructure and thermal conductivity of sintered reaction bonded Si3N4,” vol. 595, no. Complete, pp. 60–66.

[98] K. G. Budinski and M. K. Budinski, *Engineering Materials: Properties and Selection*. Prentice Hall, 2010.

[99] M. A. Camerucci, G. Urretavizcaya, M. S. Castro, and A. L. Cavalieri, “Electrical properties and thermal expansion of cordierite and cordierite-mullite materials,” *J. Eur. Ceram. Soc.*, vol. 21, no. 16, pp. 2917–2923, Dec. 2001.

[100] K. S. Mazdiyasni and L. M. Brown, “Synthesis and Mechanical Properties of Stoichiometric Aluminum Silicate (Mullite),” *J. Am. Ceram. Soc.*, vol. 55, no. 11, pp. 548–552, 1972.

[101] M. I. Osendi and C. Baudín, “Mechanical properties of mullite materials,” *J. Eur. Ceram. Soc.*, vol. 16, no. 2, pp. 217–224, 1996.

[102] H. Schneider, J. Schreuer, and B. Hildmann, “Structure and properties of mullite—A review,” *J. Eur. Ceram. Soc.*, vol. 28, no. 2, pp. 329–344, 2008.

[103] T. M. Kyaw, Y. Okamoto, and K. Hayashi, “Thermal Conductivity of Mullite-Zirconia Composites,” *J. Ceram. Soc. Jpn.*, vol. 103, no. 1204, pp. 1289–1292, 1995.

[104] J.-M. Wu and C.-M. Lin, “Effect of CeO2 on reaction-sintered mullite-ZrO2 ceramics,” *J. Mater. Sci.*, vol. 26, no. 17, pp. 4631–4636, Sep. 1991.

[105] B. Hildmann and H. Schneider, “Heat Capacity of Mullite - New Data and Evidence for a High-Temperature Phase Transformation,” *J. Am. Ceram. Soc.*, vol. 87, no. 2, pp. 227–234, 2004.

[106] J. B. Wachtman, T. G. Scuderi, and G. W. Cleek, “Linear Thermal Expansion of Aluminum Oxide and Thorium Oxide from 100° to 1100°K,” *J. Am. Ceram. Soc.*, vol. 45, no. 7, pp. 319–323, 1962.

[107] S. A. Hassanzadeh-Tabrizi and E. Taheri-Nassaj, “Compressibility and sinterability of Al2O3–YAG nanocomposite powder synthesized by an aqueous sol–gel method,” *J. Alloys Compd.*, vol. 506, no. 2, pp. 640–644, Sep. 2010.

[108] J. G. Li and X. Sun, “Synthesis and sintering behavior of a nanocrystalline α-alumina powder,” *Acta Mater.*, vol. 48, no. 12, pp. 3103–3112, Jul. 2000.

[109] N. Shinohara, M. Okumiya, T. Hotta, K. Nakahira, M. Naito, and K. Uematsu, “Seasonal Variation of Microstructure and Sintered Strength of Dry-Pressed Alumina,” *J. Am. Ceram. Soc.*, vol. 82, no. 12, pp. 3441–3446, Dec. 1999.

[110] M. Munro, “Evaluated Material Properties for a Sintered alpha-Alumina,” *J. Am. Ceram. Soc.*, vol. 80, no. 8, pp. 1919–1928, Aug. 1997.

[111] R. Barea, M. Belmonte, M. I. Osendi, and P. Miranzo, “Thermal conductivity of Al2O3/SiC platelet composites,” *J. Eur. Ceram. Soc.*, vol. 23, no. 11, pp. 1773–1778, Oct. 2003.

[112] T. Nemoto, “Thermal conductivity of alumina and silicon carbide ceramics at low temperatures,” *Cryogenics*, vol. 25, no. 9, pp. 531–532.

[113] C. Y. Ho and R. E. Taylor, *Thermal Expansion of Solids*. ASM International, 1998.

[114] A. Polotai, K. Breece, E. Dickey, C. Randall, and A. Ragulya, “A Novel Approach to Sintering Nanocrystalline Barium Titanate Ceramics,” *J. Am. Ceram. Soc.*, vol. 88, no. 11, pp. 3008–3012, 2005.

[115] X. Wang, X. Deng, H. Wen, and L. Li, “Phase transition and high dielectric constant of bulk dense nanograin barium titanate ceramics,” *Appl. Phys. Lett.*, vol. 89, no. 16, p. 162902, 2006.

[116] Y. He, “Heat capacity, thermal conductivity, and thermal expansion of barium titanate-based ceramics,” *Thermochim. Acta*, vol. 419, no. 1–2, pp. 135–141, Sep. 2004.

[117] J.-F. Chen, Z.-G. Shen, F.-T. Liu, X.-L. Liu, and J. Yun, “Preparation and properties of barium titanate nanopowder by conventional and high-gravity reactive precipitation methods,” *Scr. Mater.*, vol. 49, no. 6, pp. 509–514, Sep. 2003.

[118] K. S. Mazdiyasni, R. T. Dolloff, and J. S. Smith, “Preparation of High-Purity Submicron Barium Titanate Powders,” *J. Am. Ceram. Soc.*, vol. 52, no. 10, pp. 523–526, Oct. 1969.

2.8 List of Figures

2.9 List of Tables

Table 2.1. Representation of sintered properties for selected ceramics

Material	Al_2O_3	SiC	Si_3N_4	$BaTiO_3$	SiO_2	TiN	$3Al_2O_3.SiO_2$	AlN	ZrO_2
Density [kg/m^3][55]	3960	3100	3200	5900	2200	5220	3200	3260	6030
Thermal Conductivity [W/m.K][55]	40	130	20	3.3	1.7	30	3.5	200	2.65
CTE [10-6* K-1][55]	7.4	4.02	3.2	-	0.4	9.4	5.3	4.3	9.6
Heat Capacity [J/kg.K][55], [56]	780	670	740	440	690	600	760	710	480
Compressive Strength [MPa][55]	3790	4600	1730	-	1040	970	1000	2070	2900
Flexural Strength [MPa][55]	550	460	700	90	100	-	170	300	1150
Poissons Ratio[55], [57]	0.22	0.14	0.25	-	0.17	0.25	0.32	0.25	0.31
Hardness (Knoop kg/mm^2) [55], [57]	2030	2530	1380	-	750	2160	750	1230	1070
Band Gap [eV][55]	-	2.86	-	-	-	3.40	-	6.02	-
Dielectric Constant[55]	10	40	6.50	3000	3.80	-	6.50	8.8	-

Table 2.2. Current applications of CIM technology

type of component	ceramic material	reference #
industrial		
water pump seals	SiC	[6]
stators	Si_3N_4	[7]
turbine blades	Si_3N_4	[7]
precision dispension nozzles	Si_3N_4	[8]
sensor covers	Al_2O_3	[8]
cutting blades	ZrO_2-Al_2O_3	[8]
sensor tubes	Al_2O_3	[10]
bearings	MgO-ZrO_2, Al_2O_3	[8], [9]
jet engine turbine blades and aerofoil casting cores	Al_2O_3 SiO_2	[11]
medical and dental		
cochlear implant feedthrough	Al_2O_3	[12]
dental abutments	ZrO_2	[13]
orthodontic brackets	Al_2O_3	[8]
dental implants	Al_2O_3	[8]
endoscopic cutters	ZrO_2	[8]
catheter tips	ZrO_2	[8]
prosthetic replacements	Al_2O_3	[14]
tweezers	ZrO_2	[8]
spinal interbody devices	Si_3N_4	[15]
bone implants	ZrO_2	[16]
communication		
connector for telecom	ZrO_2	[17]
ferrules	ZrO_2	[18]
optical sleeves	ZrO_2	[19]
soft magnetic components	$(Mn,Zn)Fe_2O_4$	[58]

Table 2.2 Continued. Current applications of CIM technology

type of component	ceramic material	reference #
electrical		
electrical components for automotive exhaust RF and electrical insulators	Al_2O_3	[8]
hard disc drive assembly	ZrO_2-Al_2O_3	[8]
electrical microheater	$Ba(Zn_{1/3}Ta_{2/3})O_3$	[59]
heat sinks, electronic packages	AlN	[25]
transportation		
glow plug	Si_3N_4	[22]
gear wheel	Al_2O_3, ZrO_2	[22]
valve seat	SiAlON, Si_3N_4	[22]
braking pads	Al_2O_3, ZrO_2	[22]
valve components	Si_3N_4	[23]
turbocharger rotors	SiC	[24]
swirl chambers for high powered turbocharged diesel engines	Si_3N_4	[25]
oxygen sensor components	ZrO_2	[6]
shafts and bearings in motor pumps	Al_2O_3, ZrO_2, SiC	[26]
lighting		
industrial lighting	Al_2O_3	[60]
textiles		
wire guides	Al_2O_3	[8]
textile thread guides	Al_2O_3, SiC	[61]
consumer		
cups	porcelains	[27]
inkjet printheads	Al_2O_3	[62]
luxury pen bodies	ZrO_2-Al_2O_3	[28]
BMW controls and switches	ZrO_2	[29]
watch gears	ZrO_2-Al_2O_3	[8]
watch cases	ZrO_2-Al_2O_3	[28]
battery cover for mobile phones	ZrO_2	[28]

Table 2.3. Experimental feedstock compositions

feedstock	feedstock nomenclature	median particle size, $X10^{-6}$ m	filler mass fraction, X_f	filler volume fraction, ϕ_f	reference #
microscale silicon carbide	μ SiC	0.70	0.79	0.52	[43]
microscale-nanoscale silicon carbide	μ-n SiC	0.09	0.85	0.61	[43]
microscale aluminum nitride	μ AlN	1.10	0.81	0.53	[43], [45]
microscale-nanoscale aluminum nitride	μ-n AlN	0.10	0.85	0.61	[43], [45]
silicon nitride	μ-n Si_3N_4	0.13	0.80	0.52	[48]
mullite composite	20%ZrO_2-80%$Al_2O_3.2SiO_2$	0.72	0.85	0.57	[44]
zirconia composite	57%ZrO_2-43%$Al_2O_3.2SiO_2$	0.71	0.84	0.49	[44]
alumina	Al_2O_3	0.40	0.84	0.54	[46]
microscale-nanoscale barium titanate	μ-n $BaTiO_3$	0.20	0.9	0.58	[47]
wax polymer binder	binder	-	0	0	[43]

Table 2.4. Experimental feedstock properties

feedstock	solid density, kg/m^3	melt density, kg/m^3	specific heat, J/kg.K	thermal conductivity, W/m.K	reference #
μ SiC	2020	1850	1240	3.80	[43]
μ-n SiC	2180	1990	1190	2.90	[43]
μ AlN	2150	1940	1200	2.80	[43], [45]
μ-n AlN	2310	2140	1390	3.10	[43], [45]
μ-n Si_3N_4	2300	2110	1100	1.40	[48]
$Al_2O_3.2SiO_2$ composite	2520	2290	1050	1.20	[44]
ZrO_2 composite	2830	2560	940	0.80	[44]
Al_2O_3	2580	2340	1200	2.50	[46]
μ-n $BaTiO_3$	3690	3370	3300	1.00	[47]
wax polymer binder	870	700	1240	0.20	[43]

Table 2.5. Experimental feedstock viscosity for various temperatures and shear rate

feedstock	viscosity, Pa.s						reference #
	415 K			425 K			
shear rate s^{-1}	10^1	10^2	10^3	10^1	10^2	10^3	
μ SiC	7100	1030	150	6600	960	140	[43]
μ-n SiC	15550	1820	210	14960	1760	200	[43]
μ AlN	1470	350	80	1380	330	80	[43], [45]
μ-n AlN	34620	3910	440	33980	3840	430	[43], [45]
μ-n Si_3N_4	45220	5080	570	40330	4530	510	[48]
$Al_2O_3.2SiO_2$ composite	19950	2080	220	19850	2070	220	[44]
ZrO_2 composite	11820	1320	150	11630	1300	140	[44]
Al_2O_3	4680	800	130	4330	740	120	[46]
μ-n $BaTiO_3$	6330	790	90	5640	730	90	[47]
wax polymer binder	140	40	10	60	30	10	[43]

Table 2.6. Experimental feedstock specific volume for various temperatures and pressures

feedstock	specific volume, $X10^3$ m^3/kg						reference #
	0 MPa			100 MPa			
temperature, K	300	330	390	300	330	390	
μ SiC	0.50	0.51	0.53	0.49	0.50	0.51	[43]
μ-n SiC	0.46	0.47	0.49	0.45	0.46	0.47	[43]
μ AlN	0.47	0.49	0.50	0.46	0.47	0.48	[43], [45]
μ-n AlN	0.43	0.44	0.46	0.42	0.43	0.44	[43], [45]
μ-n Si_3N_4	0.43	0.45	0.46	0.42	0.43	0.45	[48]
20%ZrO_2-80%$Al_2O_3.2SiO_2$	0.40	0.40	0.42	0.38	0.39	0.41	[44]
57%ZrO_2-43%$Al_2O_3.2SiO_2$	0.35	0.36	0.38	0.34	0.35	0.36	[44]
Al_2O_3	0.39	0.40	0.41	0.38	0.39	0.40	[46]
μ-n $BaTiO_3$	0.27	0.28	0.29	0.26	0.27	0.28	[47]
wax polymer binder	1.15	1.22	1.33	1.11	1.14	1.24	[43]

Table 2.7. Models used in the present study to estimate feedstock properties

property	empirical equation	equation #	reference #
density	$\frac{1}{\rho_c} = \frac{X_b}{\rho_b} + \frac{X_p}{\rho_p}$	1	[40]
volume fraction	$\phi_p = \frac{X_p/\rho_p}{X_p/\rho_p + X_b/\rho_b}$ $\phi_b = \frac{X_b/\rho_b}{X_p/\rho_p + X_b/\rho_b}$	2 3	[40]
specific heat	$C_{p_c} = \left[C_{p_b}X_b + C_{p_p}X_p\right] * \left[1 + A * X_b X_p\right]$	4	[40]
thermal conductivity	$1 - \phi_p = \left(\frac{\lambda_p - \lambda_c}{\lambda_p - \lambda_b}\right)\left(\frac{\lambda_b}{\lambda_c}\right)^{1/3}$	5	[40]
viscosity	$\eta_c = \frac{\eta_b}{\left[1 - \frac{\phi_p}{\phi_{max}}\right]^2}$	6	[40]
specific volume	$v_c = X_p v_p + v_b(1 - X_p)$	9	[40]

Table 2.8. Literature filler properties of different ceramic systems at 300 K

filler	solid density, kg/m^3	specific heat, J/kg.K	thermal conductivity, W/m.K	reference #
SiC	3200±50	720±70	110±20	[3], [55], [63]–[76]
AlN	3300±50	800±30	230±70	[3], [21], [55], [64], [77]–[92]
Si_3N_4	3200±15	730±90	30±5	[3], [55], [57], [64], [93]–[98]
$3Al_2O_3.2SiO_2$	3000±20	760±10	5.1±1.1	[3], [44], [55], [63], [73], [99]–[105]
Al_2O_3	3900±10	800±20	30±10	[3], [55], [56], [63], [64], [72], [73], [80], [106]–[113]
$BaTiO_3$	5900±10	420±30	2.7±0.1	[56], [73], [102], [114]–[118]

Table 2.9. Coefficient of determination for different ceramic feedstock material properties

property	R^2
density	0.96
specific heat	0.64
thermal conductivity	0.23
viscosity	0.61
specific volume	0.97

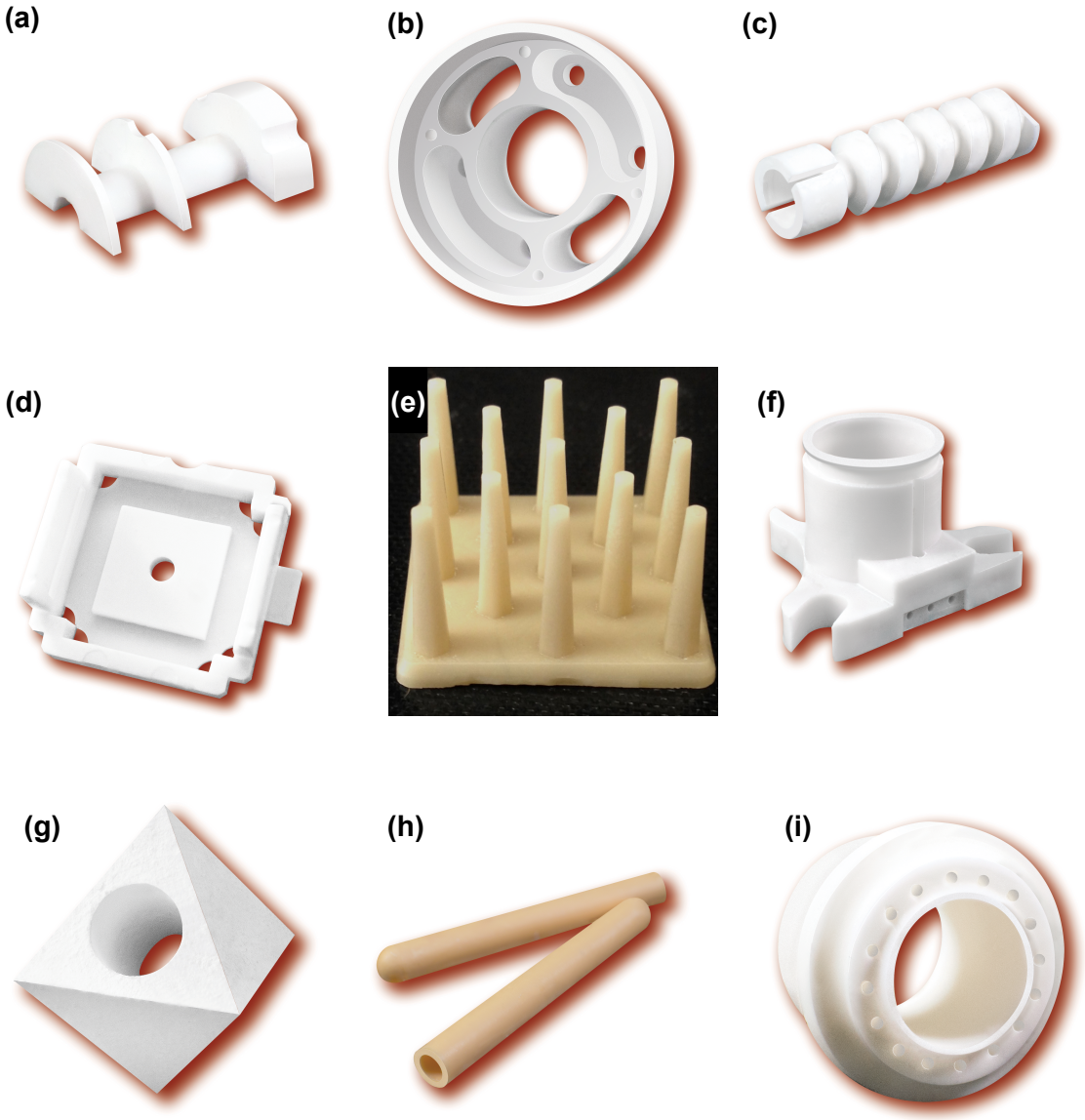

Figure 2.1. Various applications of PIM ceramic parts (© Ceramco, used with permission) (a) bobbin made from alumina, (b) detector component made from alumina, (c) auger bit made from alumina, (d) circuit coverlid made from alumina, (e) PIM heat sink geometry made from aluminum nitride, (f) mounting bracket made from zirconia, (g) octahedron made mullite, (h) sensor caps made from zirconia, and (i) swirl baffle made from alumina

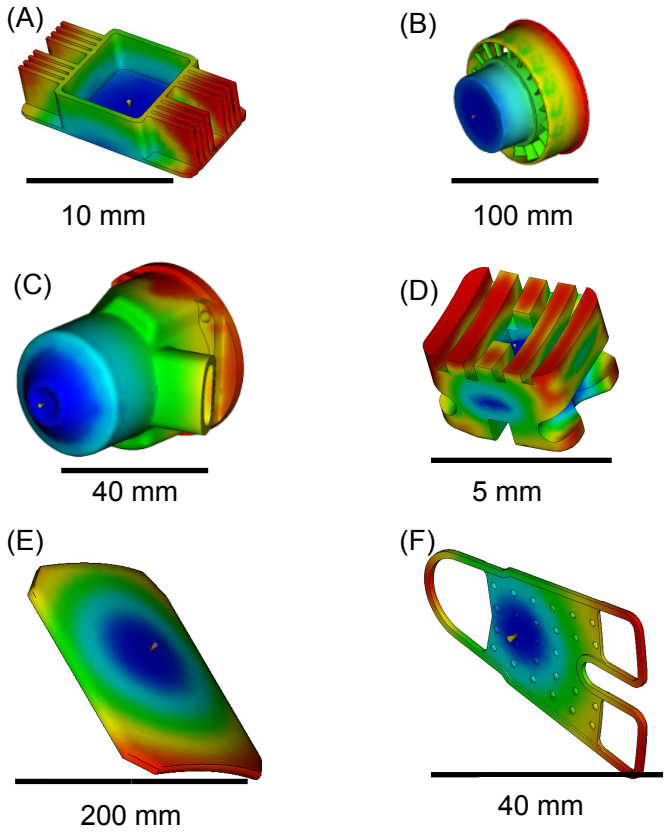

Figure 2.2. Examples of studies on mold –filling simulations for several applications and material systems (A) AlN heat sink[42], (B) mullite miniature turbine stator [8], (C) Si_3N_4 engine component [51], and (D) Al_2O_3 dental bracket [54] (E) SiC armor plate (F) ZrO_2 composite recuperator plate

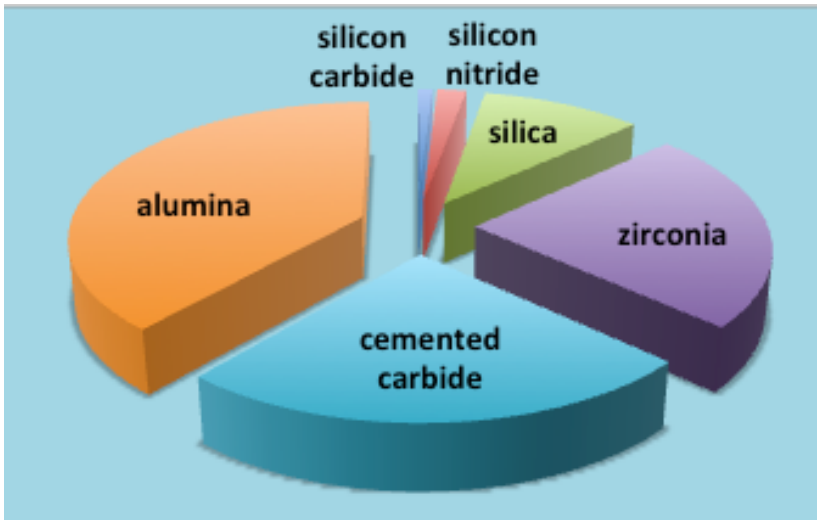

Figure 2.3. Relative CIM market based on the type of material used [50]

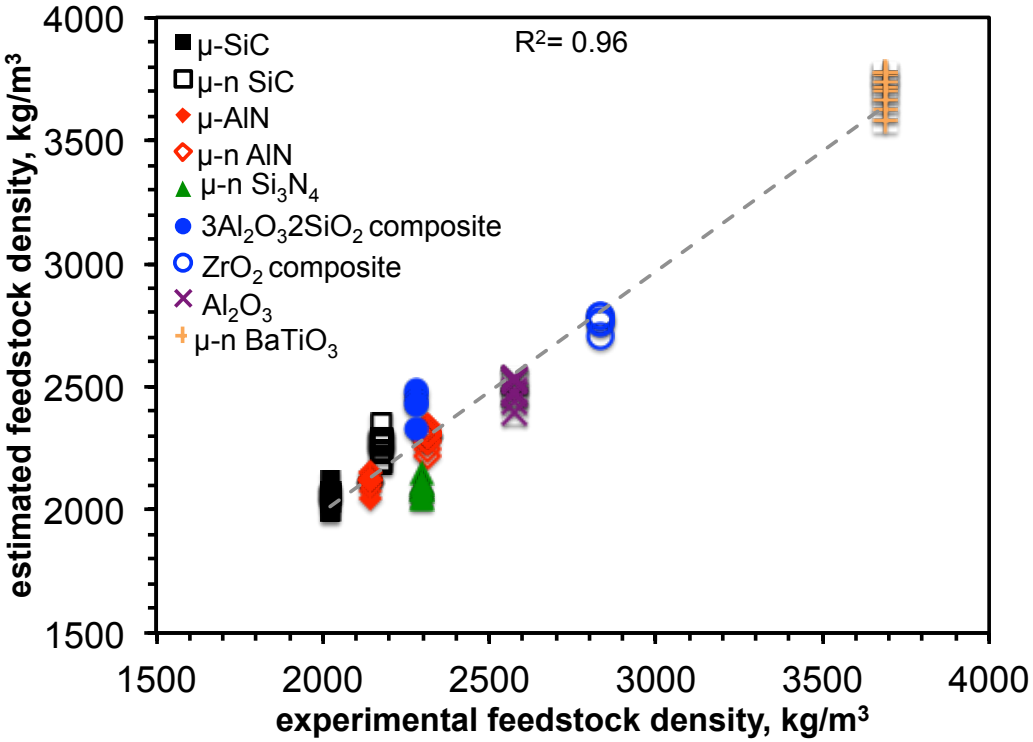

Figure 2.4. Comparison of experimental with estimated feedstock density of different ceramic feedstocks at 300 K based on data in Table 2.4 and 8; the dotted line is a regression line that has an R^2 of 0.96.

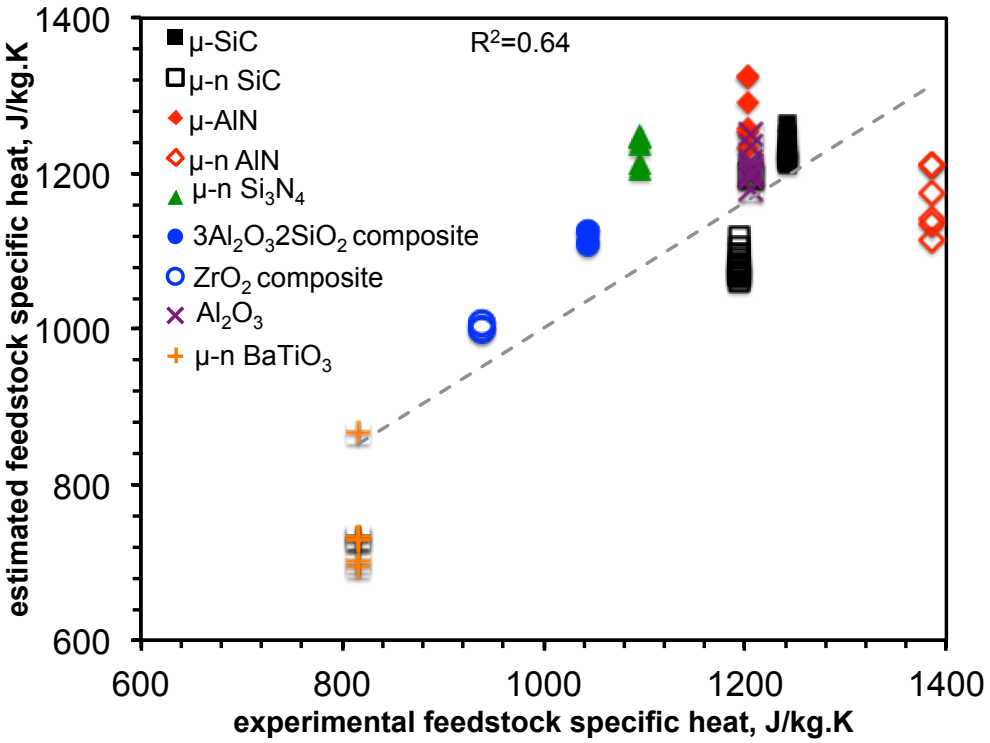

Figure 2.5. Comparison of experimental with estimated feedstock specific heat of different ceramic feedstocks at 300K based on data in Table 2.4 and 8; the dotted line is a regression line that has an R^2 of 0.64

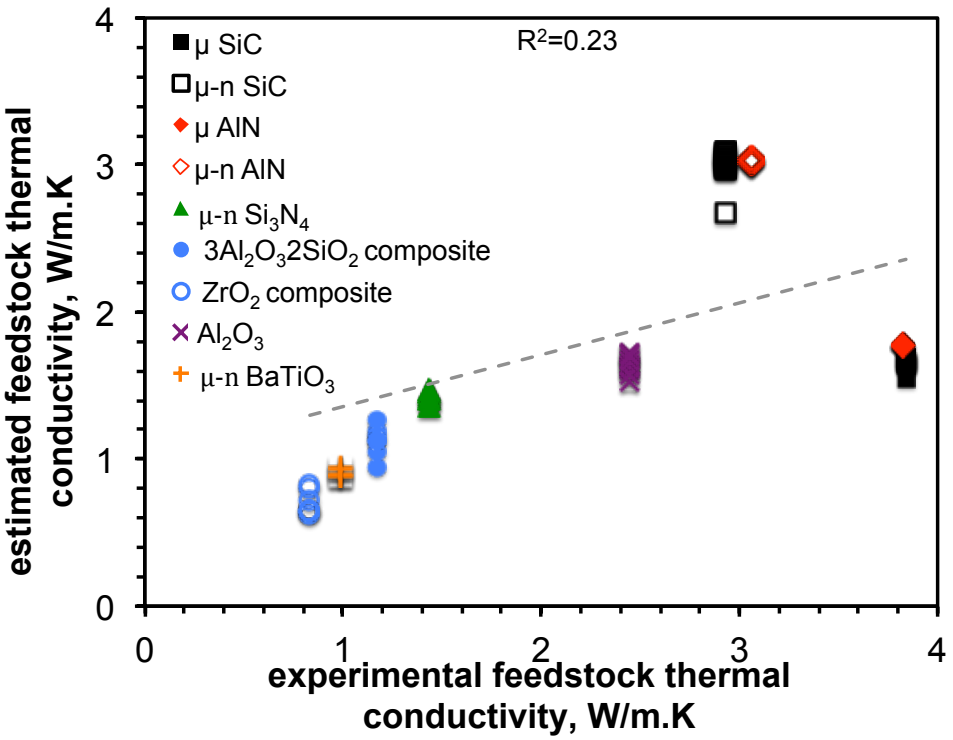

Figure 2.6. Comparison of experimental with estimated feedstock thermal conductivity of different ceramic feedstocks at 340K based on data in Table 2.4 and 8; the dotted line is a regression line that has an R^2 of 0.23

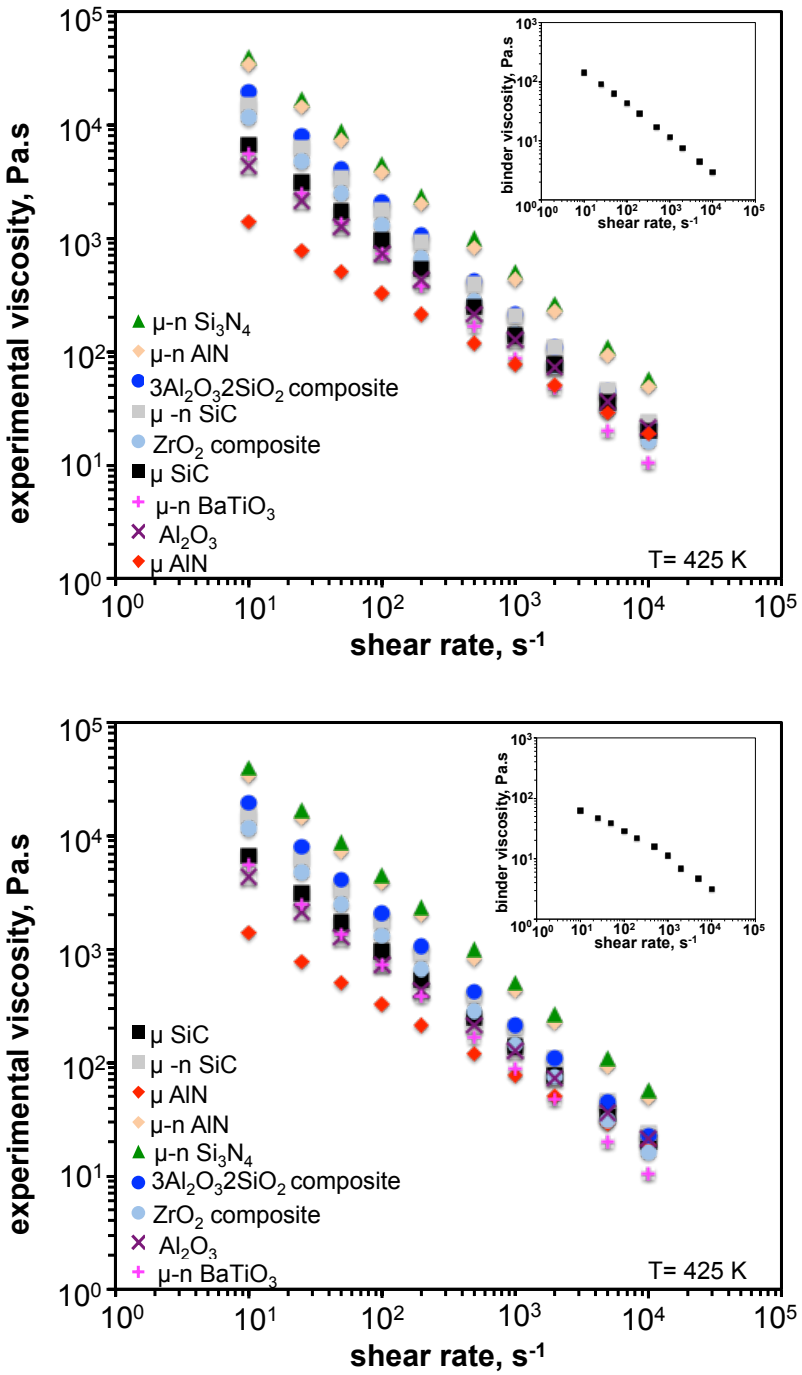

Figure 2.7. Plot of experimental viscosity as a function of shear rate for different ceramic feedstocks at 415 and 425 K and inset experimental binder viscosity as a function of shear rate based on data in **Table 2.5**

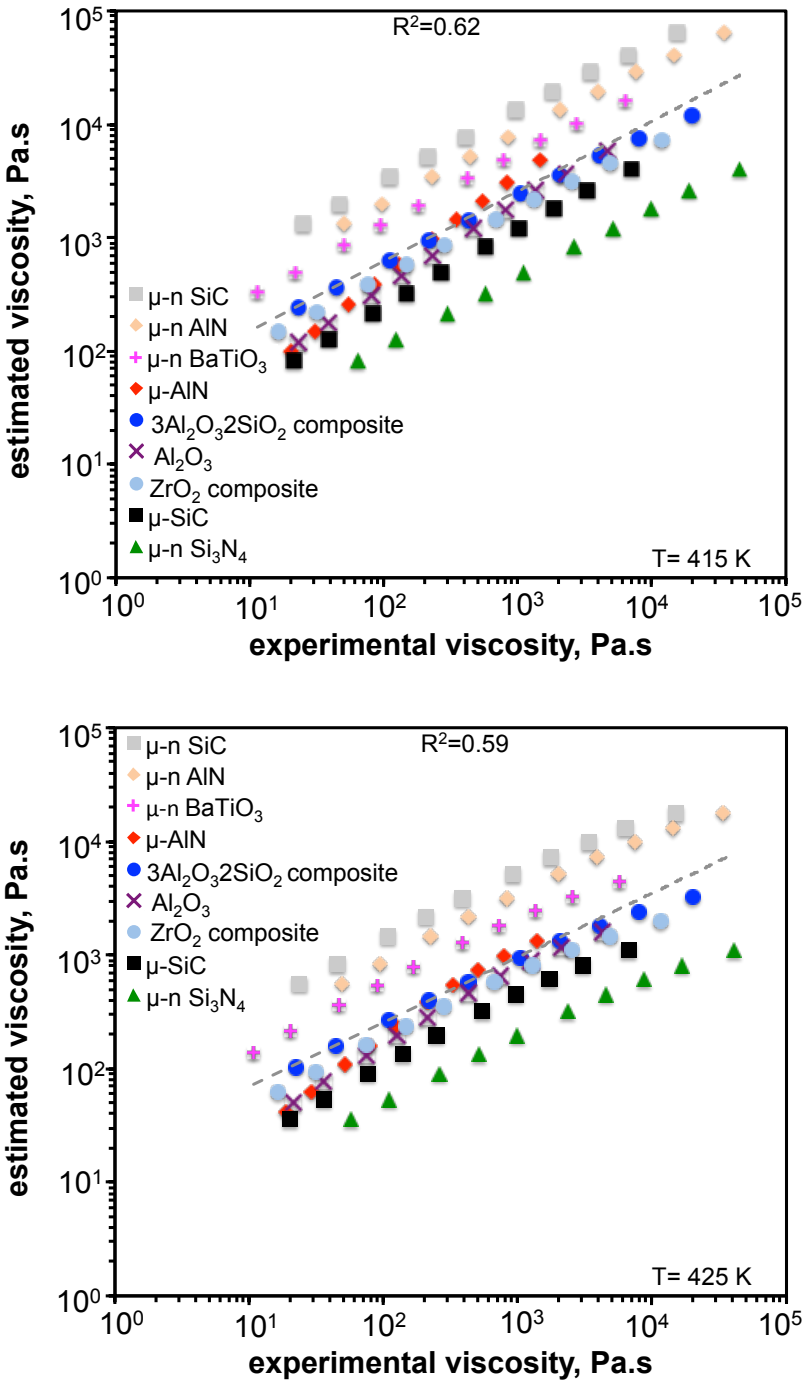

Figure 2.8. Comparison of experimental with estimated viscosity of different ceramic feedstocks at (a) 415 K, (b) 425 K for shear rate range of 10 to 10000s^{-1} based on data in Table 2.5 and the dotted line is a regression line that has an R^2 of (a) 0.62 for 415 K and (b) 0.58 for 425 K

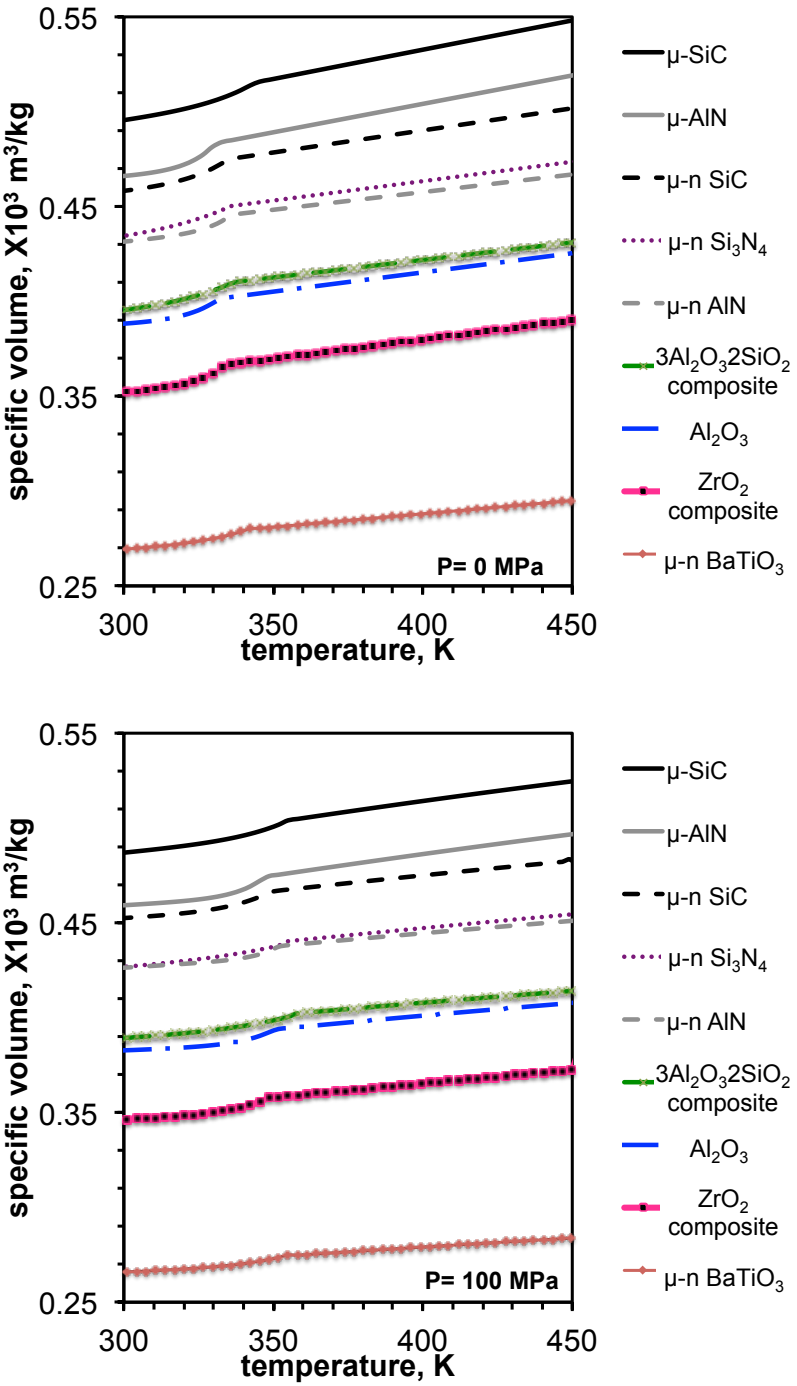

Figure 2.9. Plot of experimental feedstock specific volume as a function of temperature for various ceramic feedstocks at 0 and 100 MPa pressure based on data in **Table 2.6**

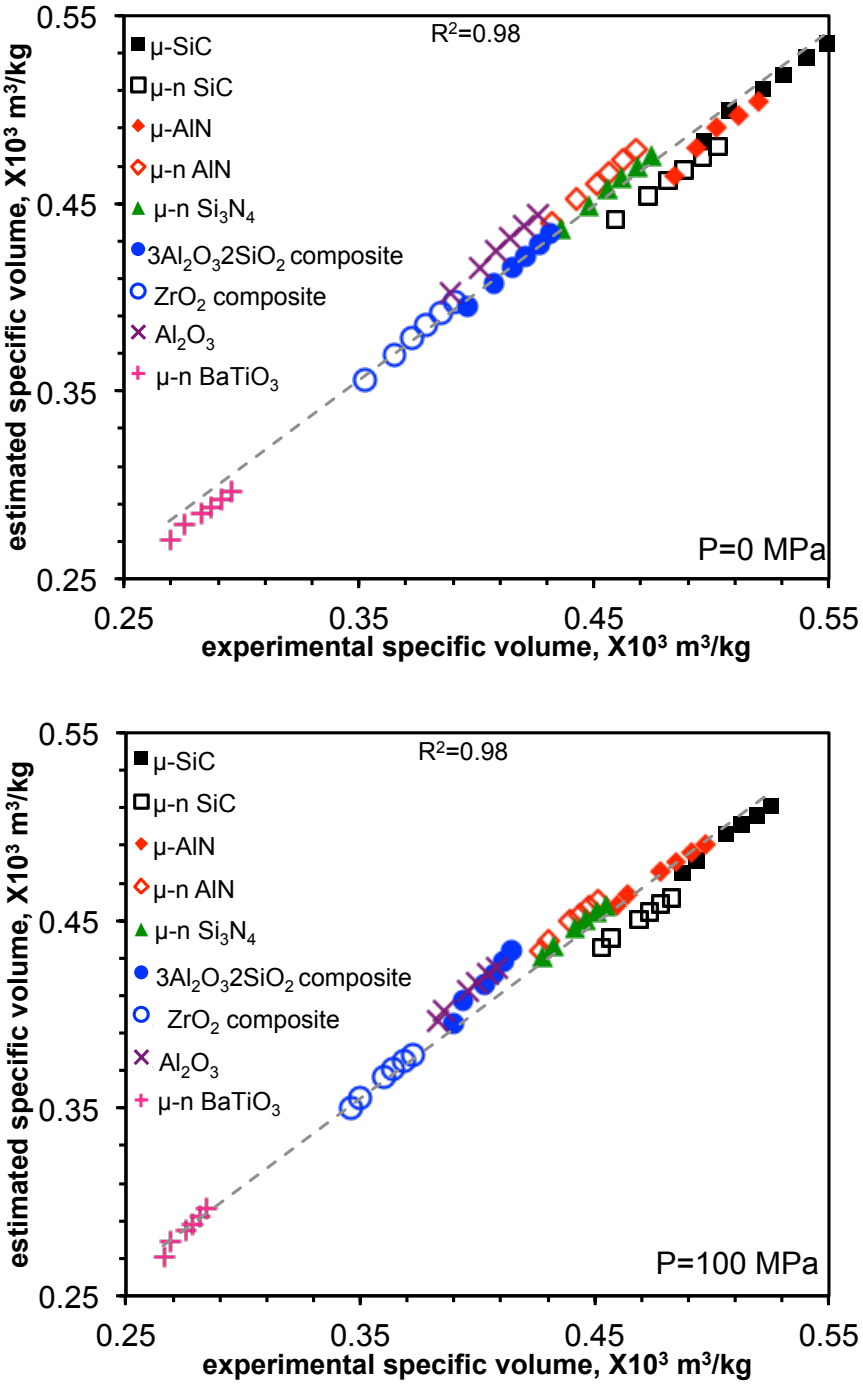

Figure 2.10. Comparison of experimental with estimated specific volume of different ceramic feedstocks at 300 K for (a) 0 MPa (b) 100 MPa pressure based on data in Table 2.4, 6, and 8; the dotted line is a regression line that has an R^2 of (a) 0.98 for 0 MPa and (b) 0.98 for 100 MPa

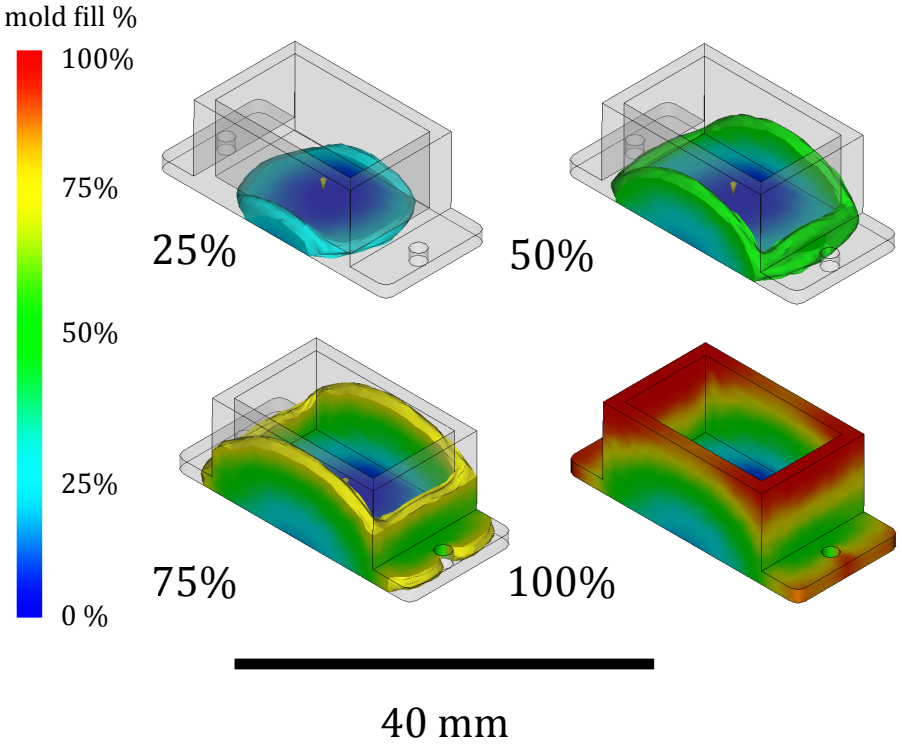

Figure 2.11. Progressive mold filling in a heat sink geometry using Autodesk MoldFlow Insight for experimental μ-AlN feedstocks

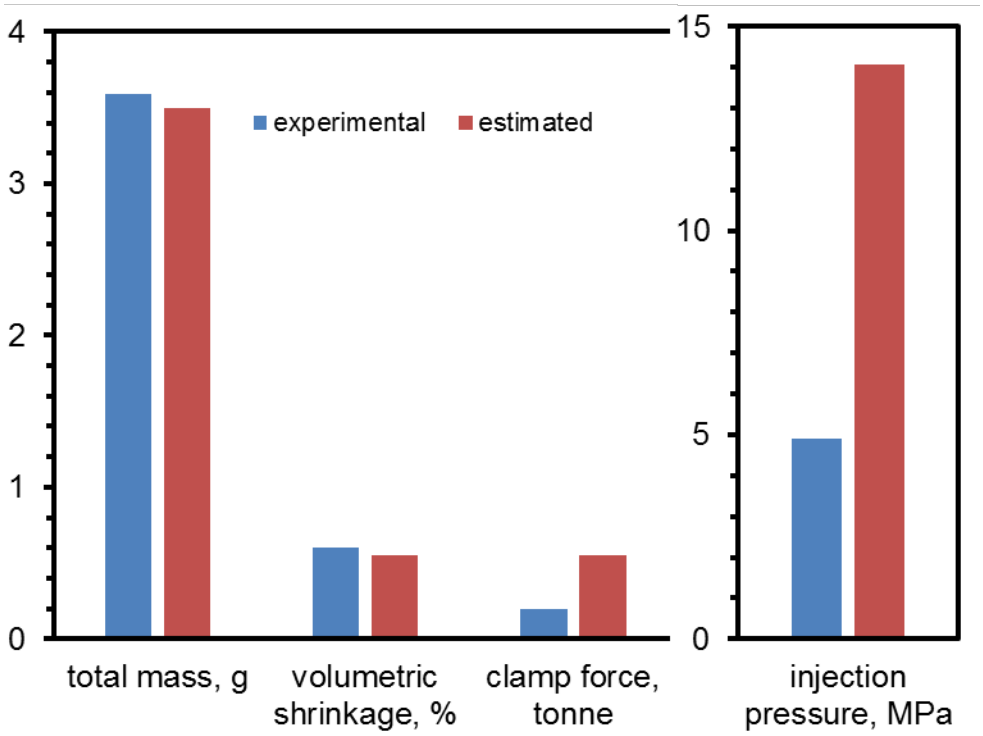

Figure 2.12. Injection molding simulations output parameters using experimental and estimated average values of μ-AlN feedstocks

Chapter 3: Influence of feedstock property measurements and estimates on ceramic injection molding simulations for aluminum nitride

Abstract

Powder injection molding (PIM) simulations are useful to identify appropriate material, process, and geometry variables required for injection molding. PIM simulations can also be crucial for achieving high production rates when changes made to feedstock composition or geometry design. PIM simulations require physical, thermal, and rheological feedstock properties as input data. However, there is a limited availability of experimental data for such properties and measuring them for each composition is quite time consuming and expensive. Recent work by our group developed a method to estimate feedstock properties using filler properties and semi-empirical models from literature. The present work estimated physical, thermal, and rheological feedstock properties based on this approach and compared the estimates with experimental measurements for an aluminum nitride feedstock. Mold-filling simulations were performed for a set of process input parameters and heat-sink substrate geometries to compare the differences in the output of PIM simulations based on the input feedstock property data from experiments and estimates. The results helped identify the differences in estimated and experimental values of feedstock properties that contributed the most to variations in the predictions from PIM simulations.

3.1 Introduction

Powder injection molding is a near-net shaping process used to manufacture parts with complex shapes at high production volumes with metals or ceramics. Computer aided engineering (CAE) tools early in the design stage can enable the growth in the $2 billion industry [1]. CAE tools are useful to evaluate appropriate process settings, mold geometry design, and feedstock properties necessary to manufacture quality parts with no defects [2]–[6]. Common CAE tools include Autodesk Moldflow, Sigmasoft, PIMsolver, and Modelx3D. CAE design tools depend on the availability of feedstock property data such as density, specific heat, viscosity, thermal conductivity, viscosity, and specific volume. One approach is to measure these feedstock properties for a particular powder-polymer composition required to perform PIM simulations. Mold geometry is designed and used along with the feedstock catalog file to perform injection molding simulations. Complications arise when simulation results detect poor moldability, or defects in the molded geometry, even after varying the process settings. The general approach to address these issues would be to modify mold geometry design or vary the feedstock composition. However, changes in feedstock composition require a new set of experiments and fresh measurements of feedstock properties.

A recent paper from our research group evaluated several models to estimate feedstock properties for any feedstock composition [4]. That study identified models that appear to best predict thermal, physical, and rheological properties based on existing literature data on filled polymers. The present study uses aluminum nitride (AlN) feedstock property estimates based on literature values for filler properties. These estimates were compared to experimental measurements of AlN feedstock properties. The goal of the present paper is to understand the influence of feedstock properties from experiments and estimates on predictions derived from mold-filling simulations.

The current work is divided into three parts. Firstly, aluminum nitride (AlN) feedstock and a wax-polymer binder system were mixed and experimental measurements were made for density, specific heat, thermal conductivity, viscosity, and pressure-volume-temperature parameters [7]. Secondly, estimates were then made for density, specific heat, thermal conductivity, viscosity, and pressure-volume-temperature parameters for AlN feedstock properties. Thirdly, the experimental and estimated feedstock properties were used to conduct injection molding simulations to compare the differences in predicting mold-filling behavior.

3.2 Injection molding simulations requirements

Powder injection molding simulations requires base feedstock properties, 3D part geometry, and process settings. Feedstock properties critical for PIM simulations include solid and melt density; thermal conductivity and specific heat as a function of temperature; viscosity as a function of temperature and shear rate; and specific volume as a function of temperature and pressure. Typically, experimental measurements are made for these feedstock properties and cataloged into simulation software packages such as Autodesk Moldflow, Sigmasoft, PIMsolver or Modelx3D. The 3D part geometry is prepared according to design requirements with a 3D modeling software such as Solidworks and imported into the PIM simulation software. Process settings for injection molding simulations include fill time, injection pressure, along with mold and melt temperatures are specified to obtain mold filling predictions.

3.3 Experimental methods

AlN feedstock and a wax-polymer binder were mixed using a 27 mm twin-screw extruder with length-to-diameter (L/D) ratio of 40. [7], [8] The AlN feedstock consisted of a powder–polymer mixture with 80.5 wt.% AlN powders (median particle size 1.1 μm) and 19.5 wt.% binder. The binder comprised of paraffin wax, a low-density polyethylene, a modified polypropylene, and stearic acid. Details of the binder composition and feedstock compounding are provided

elsewhere. [7], [8] Material property measurements were made for the AlN feedstock and the unfilled wax-polymer binder for density, thermal conductivity, specific heat, viscosity, and PVT parameters at Datapoint Labs (Ithaca, NY).

The solid density was measured according to Archimedes principle and ASTM D792 standard. The melt density measurement was done using a capillary rheometer in accordance with ASTM D3835 [7, 8]. The specific heat was measured with ASTM E1269 using differential scanning calorimetry (DSC) [7, 8]. The thermal conductivity was measured based on ASTM D5930 using a transient line-source technique [7, 8]. The viscosity was measured using ASTM D3835 on a capillary rheometer [7, 8]. The pressure-volume-temperature values (PvT) were measured according to ASTM D792 using a high pressure dilatometer [7, 8].

3.3.1 Feedstock property estimation requirements

Aluminum nitride feedstock properties were estimated for density, thermal conductivity, specific heat, viscosity, and PVT parameters. Select semi-empirical equations were used that estimate feedstock properties as a function of composition, AlN filler, and binder property values. Several literature reports were studied to gather AlN filler property data for density, specific heat, and thermal conductivity. Filler properties collected from literature were reported for 300 K **(Table 3.1)**. Twenty-two values of density for AlN were gathered from the literature [1-15]. It can be observed from **Table 3.1** that the AlN filler density was 3300 ± 50 kg/m^3. The reciprocal of the density values were also used to estimate the filler specific volume for AlN. Six data points of specific heat for AlN were gathered from literature [10, 22-24]. It can be observed from **Table 3.1** that AlN filler specific heat was 800 ± 30 J/kg-K. Eighteen values of thermal conductivity for AlN were gathered from literature [10, 13, 15, 19–21, 25–28]. It can be observed from **Table 3.1** that AlN filler thermal conductivity was 230 ±70 W/m-K.

Experimentally measured feedstock properties were compared to estimations based on filler property values for each physical, thermal, and rheological property using models described in the rest of the sections.

3.3.2 Density

Density measurements are required in injection molding simulations to predict part weight and variations in density that occur inside the mold geometry.

Density measurements

Table 3.2 summarizes the experimental density of AlN feedstock used in this study. The solid density of AlN feedstock was experimentally measured to be 2150 kg/m^3 and melt density was experimentally measured as 1940 kg/m^3**.** The solid and melt densities of the wax-polymer binder were measured to be 870 and 700 kg/m^3, respectively [7], [8].

Density estimates

An inverse rule of mixture (**Equation 3.1**) was used to estimate solid and melt density of AlN feedstock. This Equation 3.has been previously evaluated to be suiTable 3.for predicting powder-polymer density at higher weight fractions of fillers [9]. **Equation 3.1** provides a coefficient of determination (R^2) of 0.97 when fitted to literature data on measured powder-polymer densities (50-70 wt%).

$$\frac{1}{\rho_c} = \frac{X_b}{\rho_{b\ exp}} + \frac{X_p}{\rho_p} \qquad 3.1$$

X_p is weight fraction of AlN filler (0.805), X_b is weight fraction of wax-polymer binder (1- X_p) and ρ_c, $\rho_{b\ exp}$, and ρ_p represent density of composite, binder, and filler respectively.

The AlN filler density (ρ_p) values were obtained from literature as listed in **Table 3.1**. The binder density ($\rho_{b\ exp}$) value was used from the experimental value in **Table 3.2**. The solid and melt density of AlN feedstock was estimated for 22 data points of AlN filler density (**Table 3.1**). In **Table 3.1** the bold numbers

represent experimentally measured values of ρ_c and $\rho_{b\,exp}$. The estimated values of average solid and melt density ($\rho_{c\,avg}$) were 2120 kg/m^3 and 1940 kg/m^3. The estimated minimum values for solid and melt density ($\rho_{c\,min}$) were 2050 kg/m^3 and 1880 kg/m^3. The estimated maximum values for solid and melt density ($\rho_{c\,max}$) were 2150 kg/m^3 and 1960 kg/m^3. The estimated average ($\rho_{c\,avg}$), maximum ($\rho_{c\,min}$) and minimum ($\rho_{c\,max}$) density values from **Table 3.2** were used to create the dataset necessary for performing mold-filling simulations.

The composition of the AlN feedstock is experimentally determined by weighing the components prior to mixing. Therefore it is useful to report these values on a on a weight-fraction basis. However, several material properties such as viscosity and thermal conductivity require volume fraction as basis [9]. To calculate volume fraction the feedstock solid and binder density in **Table 3.1** were used in conjunction with **Equations 2** and **3**.

$$\phi_p = \frac{X_p/\rho_p}{X_p/\rho_p + X_b/\rho_{b\,exp}} \tag{3.2}$$

$$\phi_b = \frac{X_b/\rho_b}{X_p/\rho_p + X_b/\rho_{b\,exp}} \tag{3.3}$$

ϕ_p and ϕ_b are binder and powder volume fractions. ϕ_p was calculated as 0.52 and ϕ_b was calculated as 0.48.

3.3.3 Specific heat

Specific heat measurements are required in injection molding simulations to model the heat transfer during mold filling, packing, and cooling stages.

Specific heat measurements

Specific heat measurements were made for the AlN feedstock and the wax-polymer binder for a temperature range between 280 and 430 K. The data is represented in **Table 3.3**. It was observed that the specific heat of the wax-polymer binder initially increased up to the transition temperature of the binder

(320K) and showed a decrease in specific heat with further increase in temperature. The specific heat measurements of AlN feedstock followed a similar trend to the wax binder system. Specific heat of wax-polymer binder ($C_{p_{b\,exp}}$) ranged between 2080 and 4900 J/kg-K and AlN feedstock ($C_{p_{c\,exp}}$) ranged between 920 and 2810 J/kg-K [7, 8].

Specific heat estimates

Several mathematical models have been published in literature that can estimate specific heat of a powder-polymer mixture [9]. In the present study, a modified rule-of-mixtures model (**Equation 3.4**) was used to estimate specific heat. **Equation 3.4** provides R^2 values ranging from 0.92-0.97 when fitted to literature data on measured specific heats of five 47-75 wt.% filled-polymer systems [9]. The specific heat of AlN feedstock was estimated using **Equation 3.4** for 80.5 wt.% AlN feedstock.

$$C_{p_c} = \left[C_{p_{b\,exp}} X_b + C_{p_p} X_p\right] * \left[1 + A * X_b X_p\right] \qquad 3.4$$

X_p is weight fraction of AlN feedstock (0.805) and X_b is weight fraction of wax-polymer binder. C_{p_c}, $C_{p_{b\,exp}}$, and C_{p_p} represent specific heats of composite, binder, and filler respectively. A is a fitting constant for spherical powders with a value of 0.2.

To make estimates, the specific heat of AlN feedstock for a temperature range of 280 to 430 K and the polymer binder specific heat ($C_{p_{b\,exp}}$) for corresponding temperatures was taken from **Table 3.1** [7, 8]. There is a lack of literature data for specific heat values of AlN over the temperature range of interest. It was therefore assumed that specific heat of AlN filler remained constant between 280 and 430 K.

The values for AlN filler specific heats (C_{p_p}) were obtained from literature and are reported in **Table 3.1**.The binder specific heat ($C_{p_{b\,exp}}$) value for temperatures between 283 and 423 K were experimentally measured and

reported in **Table 3.3**. The specific heat of AlN feedstock was estimated for 6 data points of AlN filler specific heat (**Table 3.1**). The estimated average ($C_{p_{c\ avg}}$), maximum ($C_{p_{c\ max}}$) and minimum ($C_{p_{c\ min}}$) specific heat values from **Table 3.3** were used to create a dataset necessary for performing mold-filling simulations.

3.3.4 Thermal conductivity

Thermal conductivity measurements are required in injection molding simulations to model the heat transfer during mold filling, packing, and cooling stages.

Thermal conductivity measurements

Thermal conductivity measurements for AlN feedstock and the wax-polymer binder were made for a temperature range between 310 and 440 K. Representative experimental measurements are shown as bold values in **Table 3.4**. It was observed that the thermal conductivity of the wax-polymer binder decreased with an increase in temperature. The thermal conductivity measurements of AlN feedstock followed a similar trend. The thermal conductivity of the wax-polymer binder ($\lambda_{b\ exp}$) ranged between 0.162 and 0.195 W/m-K. The AlN feedstock ($\lambda_{b\ exp}$) ranged between 2.20 and 4.26 W/m-K [7, 8].

Thermal conductivity estimates

The Maxwell model, Bruggeman model, and a modified Lichtenecker model have been previously used to estimate thermal conductivity [9]. In the present study the Bruggeman model (**Equation 3.5**) was used to estimate thermal conductivity of 52 vol.% AlN feedstock [9].

$$1 - \phi_p = \left(\frac{\lambda_p - \lambda_c}{\lambda_p - \lambda_{b\ exp}}\right)\left(\frac{\lambda_b}{\lambda_c}\right)^{1/3} \qquad 3.5$$

ϕ_p is the volume fraction of AlN feedstock (0.52). λ_c, $\lambda_{b\ exp}$, and λ_p represent thermal conductivities of the composite, binder, and filler respectively.

In order to estimate the thermal conductivity of AlN feedstock for a temperature range of 310 to 440 K, the binder thermal conductivity ($\lambda_{b\ exp}$) were taken from **Table 3.4** [7, 8]. The values for AlN filler thermal conductivities (λ_p) were obtained from literature and taken from **Table 3.1**. There is limited availability of literature data for thermal conductivity of AlN filler for a range of temperature. It was assumed that thermal conductivity of AlN filler remains constant between 310 and 440 K. The thermal conductivity of AlN feedstock was estimated for 18 data points of AlN filler thermal conductivity (**Table 3.1**). **Table 3.4** shows the estimated thermal conductivity as a function of experimental thermal conductivity for a range of temperatures of AlN feedstock. The estimated average ($\lambda_{c\ avg}$), maximum ($\lambda_{c\ max}$), and minimum ($\lambda_{c\ min}$) thermal conductivity values from **Table 3.4** were used to create datasets necessary for performing mold-filling simulations.

3.3.5 Viscosity

Viscosity measurements are required in injection molding simulations to understand the flow characteristics of the feedstock melt. It is one of most important properties required to predict output parameters such as injection pressure and clamp force.

Viscosity measurements

Viscosity measurements for the AlN feedstock and the wax-polymer binder were performed for temperatures of 415, 420, 425, and 430 K and shear rates from 10 to 10^4 s^{-1} are represented in **Figure 3.1**. It was observed that the viscosity of the wax-polymer binder and AlN feedstock decreased with an increase in shear rate and temperature **(Figure 3.1)**. A representative version of AlN feedstock viscosity data from **Figure 3.1** is shown in **Table 3.5.**

Viscosity estimates

The Chong model, Eiler model, Mooney model, and Krieger Dougherty model have be used to estimate viscosity [9]. In the present study, a simplified Krieger

Dougherty model (**Equation 3.6**) was used to estimate viscosity. **Equation 3.6** provides R^2 values ranging from 0.94-0.99 when fitted to literature data on measured viscosity of three 50-60 vol.% filled-polymer systems.

$$\eta_c = \frac{\eta_{b\,exp}}{\left[1 - \frac{\phi_p}{\phi_{max}}\right]^2} \qquad 3.6$$

$\eta_{b\,exp}$ is the viscosity of binder, η_c is the viscosity of feedstock, ϕ_p is volume fraction of feedstock, and ϕ_{max} is the volume fraction of critically loaded feedstock.

Viscosity of the AlN feedstock was estimated for 40 different shear rates in ranges between 10 and 10^4 s^{-1} and for temperatures 415, 420, 425 and 430 K using **Equation 3.6** and polymer binder viscoisty ($\eta_b\ exp$) values from **Figure 3.1.** The volume fraction of AlN feedstock (ϕ_p) was calculated to be 0.52 using **Equation 3.2**. Viscosity was estimated for ϕ_{max} of 0.6, 0.64, and 0.68 critical filler content.

To perform mold-filling simulations, the viscosity of had to be represented in terms of fitted constants. A Cross-WLF Equation 3.**(Equation 3.7)** was used to extract fitted constants for ϕ_{max} of 0.6, 0.64, and 0.68.

$$\eta = \frac{\eta_0}{1 + \left(\frac{\eta_0 \gamma}{\tau^*}\right)^{1-n}} \qquad 3.7$$

η is the melt viscosity (Pa-s), η_0 is the zero shear viscosity, γ is the shear rate (1/s), τ^* is the critical stress level at the transition to shear thinning and is determined by curve fitting, and n is the power law index in the high shear rate regime. Power law index, n is also determined by curve fitting.

The temperature dependence of viscosity of any powder-polymer mixture can be calculated using **Equation 3.8**.

$$\eta_0 = D_1 exp\left[-\frac{A_1(T - T^*)}{A_2 + (T - T^*)}\right] \quad 3.8$$

T is the temperature (K). T^*, D_1 and A_1, are curve fitted coefficients. A_2 is the WLF constant and is assumed to be 51.6 K.

Table 3.6 presents the Cross-WLF constants extracted from experimental viscosity data of wax-polymer binder ($\eta_{b\ exp}$) and from estimated viscosity data using **Equations 7** and **8**. The values of these constants were obtained by curve- fitting the estimated viscosity for ϕ_{max} of 0.6, 0.64 and 0.68 and are represented as $\eta_{c\ max}$, $\eta_{c\ avg}$, and $\eta_{c\ min}$ respectively in **Table 3.6**.

3.3.6 Specific volume

Specific volume measurements are required in injection molding simulations to calculate the shrinkage that occurs when a feedstock is cooled from melt temperature to ambient temperature.

Specific volume measurements

Mold-filling simulations require specific volume data of feedstocks typically for temperature range between 298 and 453 K and pressure range between 0 and 200 MPa. Experimentally measured values of specific volume for these temperature and pressure ranges of AlN feedstock and a wax-based polymer-binder were obtained. **Figure 3.2** shows specific volume of AlN feedstock and a wax-polymer binder for various temperatures and at 100 MPa pressure. A representative version of AlN feedstock viscosity data from **Figure 3.2** is shown in **Table 3.7.**

Specific volume estimates

A rule-of-mixtures (**Equation 3.9**) was used to estimate specific volume of AlN feedstock. It has been found to be suiTable 3.for predicting the powder-polymer specific volume at higher weight fractions of fillers [9]. **Equation 3.9** provided an R^2 value of 0.99 when fitted to literature data on measured specific volume for two 20-80 wt.% filled material systems [9]. To estimate specific volume for a

range of temperature and pressure of AlN feedstock a simple empirical Equation 3.**(Equation 3.9)** was used.

$$v_c = X_p v_{\,p} + v_{b\,exp}\left(1 - X_p\right) \tag{3.9}$$

To calculate the specific volume of AlN filler, the reciprocal of density of AlN filler was used **(Table 3.1)**. The density of AlN were gathered at 300 K from 22 values in the literature. **Table 3.7** shows estimated and experimental specific volumes of AlN feedstock as a function of temperatures and pressure. In order to estimate specific volume of AlN feedstock for a range of temperatures and pressures, it was assumed that specific volume of AlN filler doesn't change with temperature and pressure.

The specific volume for AlN feedstocks was estimated for average, maximum, and minimum values of AlN filler specific volume. The specific volume of AlN filler was calculated from the inverse of AlN filler density values from **Table 3.1**. Additionally, to perform mold-filling simulations in Moldflow Insight software, specific volume of AlN feedstock needs to be represented in terms of fitted constants. A Dual-domain Tait Equation 3.**(Equation 3.10)** was used to extract these fitted constants for average, maximum, and minimum AlN feedstocks specific volumes. **Table 3.8** presents the Dual-domain Tait constants extracted for estimated average $v_{c\,\mathrm{avg}}$, estimated maximum $v_{c\,\mathrm{max}}$, and estimated minimum $v_{c\,\mathrm{min}}$ specifc volume. These values were obtained using **Equation 3.10**

$$v(T,p) = v_o(T)\left[1 - Cln\left(1 + \frac{p}{B(T)}\right) + v_t(T,p)\right] \tag{3.10}$$

$v(T,p)$ is the specific volume at a given temperature and pressure, v_o is the specific volume at zero gauge pressure, T is temperature in K, p is pressure in Pa, and *C* is a constant assumed as 0.0894. The parameter *B* accounts for the pressure sensitivity of the material and is separately defined for the solid and melt regions. For the upper bound when $T > T_t$ (volumetric transition temperature), *B* is given by **Equation 3.11.**

$$v_o = b_{1m} + b_{2m}(T - b_5); \quad B(T) = b_{3m}e^{[-b_{4m}(T-b_5)]}; \quad v_t(T,p) = 0 \qquad 3.11$$

b_{1m}, b_{2m}, b_{3m}, b_{4m}, and b_5 are curve-fitted coefficients. For the lower bound, when $T < T_t$, the parameter, B, is given by **Equation 3.12.**

$$v_o = b_{1s} + b_{2s}(T - b_5); \quad B(T) = b_{2s}e^{[-b_{4s}(T-b_5]}; \quad v_t(T,p) = b_7e^{[b_8(T-b_5)-(b_9p)]} \qquad 3.12$$

b_{1s}, b_{2s}, b_{3s}, b_{4s}, b_5, b_7, b_8, and b_9 are curve-fitted coefficients. The dependence of the volumetric transition temperature T_t on pressure can be given by **Equation 3.13**

$$T_t(p) = b_5 + b_6(p) \qquad 13$$

Dual-domain Tait constants from **Table 3.8** were further used to create a dataset necessary for performing mold-filling simulations.

3.4 Mold-filling simulations

Mold-filling simulations were performed using Autodesk Moldflow software. The software is capable of simulating results in three-dimension (3-D) and uses a finite element method (FEM) for calculating velocity, temperature, and pressure profiles in defined geometry. To analyze FEM results the defined geometry is dived into smaller elements that are joined together by the means of a mesh. Results are calculated for each element in the mesh. The typical mesh types are mid-plane, dual-domain, and 3D in Autodesk Moldflow. Mold-filling simulations were performed using estimated and experimental feedstock properties of AlN to understand the influence of scatter in feedstock property estimates on mold-filling behavior. To understand the effect of complexity of shapes on mold-filling behavior, two different heats sink geometries were used for the current study.

3.4.1 Design geometry

Two types of heat-sink substrate geometries were chosen to conduct mold-filling **(Figure 3.3)** simulations. Solidworks software was used to design these heat-sink substrate geometries. A heat-sink substrate without fins **(Figure 3.3a)**

and a heat-sink substrate with fins **(Figure 3.3b)** were designed to understand the influence of geometry design on injection molding output parameters and feedstock properties.

3.4.2 Simulation procedure

The two heat-sink substrate geometries described above were imported into the Autodesk Moldflow software and meshed using a "3D" mesh type to conduct mold-filling simulations. A 3D mesh type was selected as it provides most accurate 3D representation of results in thick or thin solid regions in the part when compared to mid-plane and dual-domain mesh types. A ".udb" catalog file was created for experimental and estimated AlN feedstock properties presented in **Tables 2, 3, 4**, **6 and 8.** For the current study, 7 datasets of AlN feedstock properties were cataloged and their details are listed in **Table 3.9.** To perform simulations for each of the 7 datasets, a set of process input parameters were identified. An injection location was selected at the bottom face of the heat-sink substrate since it provides uniform flow distribution of melted feedstock throughout the geometry. Injection molding simulations were performed for each the 7 datasets presented in **Table 3.9.**

3.4.3 Process input parameters

The selected input parameters for the current simulation study are represented in **Table 3.10**. Injection time was set at 0.1 s, mold and melt temperatures were set at 308 K and 423 K while velocity to pressure switchover (V/P) point was selected as 99%. This set of process input parameters were selected as the injection pressure and volumetric shrinkage results for experimental AlN feedstock dataset lie in the optimum processing range for both heat-sink substrate geometries.

3.4.4 Process output parameters

The first set of injection mold simulation comparisons were conducted for the experimental AlN feedstock property dataset and estimated AlN feedstock

property datasets 1-3 (**Table 3.9**). The process simulation results are divided into flow, temperature, and pressure related output parameter. Dataset 1 in **Table 3.9** represents average estimated feedstock properties for AlN. Dataset 2 in **Table 3.9** represents minimum (lowest) estimated feedstock properties for AlN and Dataset 3 in **Table 3.9** represents maximum (highest) estimated feedstock properties for AlN. It was observed that flow and temperature related output parameters of estimated Datasets 1-3 had a close match to that of experimental output parameters. Pressure related output parameters for Datasets 1-3 were overestimated by a factor of 10 when compared with experimental dataset output parameters. As suggested in a previous work by our research group, the cause for such overestimation can be attributed to sensitivity of viscosity estimates towards pressure related output parameters [2]. To understand the sensitivity of viscosity on pressure-related output parameters, Datasets 4-6 were created by substituting estimated feedstock viscosity with experimental feedstock viscosity data (**Table 3.9**). The defect evolution was studied by analyzing location of air traps and weld lines.

Flow-related output parameters

The progressive mold-filling behavior observed by using the experimental feedstock property dataset for the heat-sink substrate without fin is shown in **Figure 3.4a** while progressive mold filling for heat-sink substrate without fin is shown in **Figure 3.4b**. A similar progressive mold-filling behavior was observed for simulations using estimated AlN feedstock property Datasets 1-3 (**Table 3.9**) for both the heat-sink substrate geometries.

Temperature-related output parameters

Part weights result comparisons for heat-sink substrate with and without fins are presented in **Figure 3.5.** The part weight was determined from the room temperature density value (**Table 3.2**) and the total volume defined for the meshed geometry (**Figure 3.3**). It was observed that part weights both for experimental AlN feedstock property dataset (**Table 3.9**) and estimated AlN

feedstock property Datasets 1-3 (**Table 3.9**) were higher for the heat-sink substrate with fins. This increase in part weights for heat-sink substrate with fins can be attributed to the increase in part volume due to the addition of fins. Part weights for the experimental dataset and estimated Dataset 1 were comparatively similar with an error of 2 % for both the heat-sink substrate geometries. It was observed that part weight increases with a decrease in feedstock property estimates. The maximum feedstock property estimate, Dataset 3 (**Table 3.9**), has the lowest part weight while the minimum feedstock property estimate Dataset 2 (**Table 3.9**) has the highest part weight **(Figure 3.5)**.

Percent volumetric shrinkage result comparisons for the heat-sink substrate without fins and with fins are presented in **Figure 3.6.** The volumetric shrinkage calculations were based on the difference between the PVT state during molding and the reference state where pressure (P) is 0 MPa and temperature (T) is at ambient temperature of 298 K (**Figure 3.2**). For ceramic-filled polymers, the percent volumetric shrinkages has been reported to range between 1.2 and 2.4 % [29]. It can be observed from **Figure 3.6** that volumetric shrinkage for the experimental AlN feedstock property dataset is ~ 1.2 % while volumetric shrinkage from the estimated AlN feedstock property Datasets 1-3 are in the range of 0.98-1.3%. The percent volumetric shrinkage for experimental dataset and estimated Dataset 1 are comparatively similar with an error of 0.8 % for the heat-sink geometry without fin and an error of 6% for the heat-sink substrate with fins. It was observed that shrinkage decreases with a decrease in feedstock property estimates. The maximum feedstock property estimates, Dataset 3 (**Table 3.9**), had the lowest shrinkage while the minimum feedstock property estimates, Dataset 2 (**Table 3.9**), had the highest shrinkage **(Figure 3.6)**.

Packing times result comparisons for heat-sink substrate without fins and with fins are presented in **Figure 3.7.** Packing time in injection molding starts when

the mold is filled completely and ends when the packing pressure is released. In the packing stage, pressure is applied to the feedstock melt to compress the polymer so that more feedstock gets filled into the mold. Packing times are dependent on the heat transfer rate and amount of heat needed to cool the feedstock from melting temperature to ambient temperature. It can be observed from **Figure 3.7** that packing times for experimental feedstock property dataset (**Table 3.9**) and estimated feedstock property datasets 1-3 (**Table 3.9**) were comparatively same for both heat-sink substrate geometries. Packing times showed no sensitivity for estimated datasets 1-3 indicating that variation in thermal conductivity and specific heat estimates do not correspond to variations in packing times. If thermal conductivity and specific heat are estimated in same order of magnitude as that of experimental measurements then the corresponding packing time estimates can be predicted reasonably well. Additionally, it was observed that heat-sink substrate with fins have higher packing times due to their higher volumes.

Pressure-related output parameters

Injection pressure comparisons for both the heat-sink substrate geometries are presented in **Figure 3.8.** Injection pressure is the pressure applied to the feedstock melt by the ram during the mold filling stage that causes the material to flow inside the cavity and later during packing stage to compress the feedstock melt inside the cavity. The maximum pressure at the nozzle during the filling phase when the switch over occurs from velocity filled to pressure filled (**Table 3.10**) is referred to as the injection pressure in simulations. Large pressure gradients during mold filling stage are a sign of flow imbalance due to improper gate location and very small or very high fill times [30]. Therefore, identifying minimum injection pressures that provide the least amount of shrinkage are best for obtaining a quality part with no defects. It can be observed in **Figure 3.8a** that injection pressures for estimated feedstock property Datasets 1-3 are higher by a factor of 10 when compared with injection

pressures obtained from experimental feedstock property dataset (**Table 3.9**) for both heat-sink substrate geometries.

To account for the overestimation in injection pressure, the viscosity estimates were substituted with experimental values from viscosity measurements and Datasets 4-6 were created [2]. It can be observed from **Figure 3.8b** that the injection pressures for Datasets 4-6 were comparatively close to the injection pressure obtained from using the experimental feedstock dataset (**Table 3.9**). Therefore, an improvement in viscosity estimates is necessary to obtain accurate injection pressure estimates and is a part of our future study.

Clamp force is another pressure-related output parameter. It is the maximum force required to keep the mold closed during the filling stage. Clamp force is a function of injection pressure and the area of the part projected onto the XY plane. It can be observed in **Figure 3.9a** that the clamp force for estimated feedstock property Datasets 1-3 were higher by a factor of ~ 10 when compared with clamp force obtained from experimental feedstock property dataset (**Table 3.9**) for both the heat-sink substrate geometries.

To account for the overestimation in clamp force, the viscosity estimates were substituted with experimental values from viscosity measurements and Datasets 4-6 were created due to sensitivity of clamp force towards viscosity [2]. It can be observed from **Figure 3.9b** that clamp force for Datasets 4-6 were comparatively close to the clamp force obtained by using the experimental feedstock dataset (**Table 3.9**). A further improvement in viscosity estimates is therefore necessary in order to obtain accurate clamp force estimates and is a part of our future study.

Defect formation

Air-trap locations observed by using the experimental feedstock property dataset for the heat-sink substrate without fins are shown in **Figure 3.10a** while air-trap locations for the heat-sink substrate with fins is shown in **Figure 3.10b**.

A similar pattern of air-trap locations were observed for simulations using estimated AlN feedstock property Datasets 1-3 (**Figure 3.10 c-d**) for both the heat-sink substrate geometries. Air traps are caused due to trapping of air from converging flow fronts that causes a surface blemish. The air-trap locations correspond well with the flow front convergence as observed in **Figure 3.4**.

Weld-line locations observed by using experimental feedstock property dataset for the heat-sink substrate without fins is shown in **Figure 3.11a** while no weld lines were observed for heat-sink substrate without fins is shown in **Figure 3.11b**. Similar pattern of weld line locations were observed for simulations using estimated AlN feedstock property Datasets 1-3 (**Figure 3.11 c-d**) for both the heat-sink substrate geometries. The absence of weld line formation in the heat sink geometry without fins can be attributed to the absence of flow front convergence and can be traced back to **Figure 3.4b.**

3.5 Conclusions

The present study can be used for a variety of material systems and geometries early in the PIM design stage. The approach developed in the present study was found to have the following key attributes:

1. Literature filler properties can be used in conjunction with mixture models to estimate physical, thermal, and rheological properties of AlN feedstocks.
2. The mold-filling simulation results clearly indicate that a scatter in feedstock property estimates showed no sensitivity towards predicting flow-related output parameters and defect formations.
3. Temperature-related output parameters such as part weight, volumetric shrinkage, and packing time can be predicted with reasonably good accuracy and an error ranging between 1 to 6%. This further indicates that a scatter in thermal feedstock property estimates has little sensitivity towards predicting temperature-related output parameters.
4. Pressure-related output parameters are overestimated by a factor of 10 indicating that a further improvement in estimation of viscosity is needed.

Acknowledgements

The authors thank the financial support obtained from the National Science Foundation (CMMI 1200144).

3.6 References

[1] R. M. German and S. V. Atre, “PIM 2013 Market Study,” New York, SciPiVision, 2013.

[2] S. V. Atre, S.-J. Park, R. Zauner, and R. M. German, “Process simulation of powder injection moulding: identification of significant parameters during mould filling phase,” *Powder Metall.*, vol. 50, no. 1, pp. 76–85, Mar. 2007.

[3] R. Urval, S. Lee, S. V. Atre, S.-J. Park, and R. M. German, “Optimisation of process conditions in powder injection moulding of microsystem components using a robust design method: part I. primary design parameters,” *Powder Metall.*, vol. 51, no. 2, pp. 133–142, Jun. 2008.

[4] K. H. Kate, V. P. Onbattuvelli, R. K. Enneti, S. W. Lee, S.-J. Park, and S. V. Atre, “Measurements of Powder–Polymer Mixture Properties and Their Use in Powder Injection Molding Simulations for Aluminum Nitride,” *JOM*, vol. 64, no. 9, pp. 1048–1058, Sep. 2012.

[5] S. Ahn, S. T. Chung, S. V. Atre, S. J. Park, and R. M. German, “Integrated filling, packing and cooling CAE analysis of powder injection moulding parts,” *Powder Metall.*, vol. 51, no. 4, pp. 318–326, Dec. 2008.

[6] S.-J. Park, S. Ahn, T. G. Kang, S. T. Chung, Y. S. Kwon, S. H. Chung, S. G. Kim, S. V. Atre, S. Lee., and R. M. German, “A review on computer simulations in powder injection molding,” *Int. J. Powder Metall.*, vol. 46, no. 3, pp. 37–46, 2010.

[7] V. P. Onbattuvelli, R. K. Enneti, S.-J. Park, and S. V. Atre, “The effects of nanoparticle addition on SiC and AlN powder–polymer mixtures: Packing and flow behavior,” *Int. J. Refract. Met. Hard Mater.*, vol. 36, pp. 183–190, Jan. 2013.

[8] V. P. Onbattuvelli, “The effects of nanoparticle addition on the processing, structure and properties of SiC and AlN,” 2010.

[9] K. H. Kate, R. K. Enneti, S.-J. Park, R. M. German, and S. V. Atre, “Predicting Powder-Polymer Mixture Properties for PIM Design,” *Crit. Rev. Solid State Mater. Sci.*, vol. 39, no. 3, pp. 197–214, Mar. 2014.

[10] M. F. Ashby, *Materials Selection in Mechanical Design*. Butterworth-Heinemann, 2010.

[11] J. R. Groza and A. Zavaliangos, “Sintering activation by external electrical field,” *Mater. Sci. Eng. A*, vol. 287, no. 2, pp. 171–177, Aug. 2000.

[12] K. Biswas, J. Schneider, G. Rixecker, and F. Aldinger, “Comparative bending creep behaviour of silicon carbide sintered with oxynitride additives,” *Scr. Mater.*, vol. 53, no. 5, pp. 591–596, Sep. 2005.

[13] J. Gu, Q. Zhang, J. Dang, J. Zhang, and Z. Yang, “Thermal conductivity and mechanical properties of aluminum nitride filled linear low-density polyethylene composites,” *Polym. Eng. Sci.*, vol. 49, no. 5, pp. 1030–1034, May 2009.

[14] R. Kochetov, T. Andritsch, U. Lafont, P. H. F. Morshuis, S. J. Picken, and J. J. Smit, “Preparation and dielectric properties of epoxy - BN and epoxy - AlN nanocomposites,” in *IEEE Electrical Insulation Conference, 2009. EIC 2009*, 2009, pp. 397–400.

[15] W. Zhou, “Thermal and dielectric properties of the AlN particles reinforced linear low-density polyethylene composites,” *Thermochim. Acta*, vol. 512, no. 1–2, pp. 183–188, Jan. 2011.

[16] B. L. Zhu, J. Ma, J. Wu, K. C. Yung, and C. S. Xie, “Study on the properties of the epoxy-matrix composites filled with thermally conductive AlN and BN ceramic particles,” *J. Appl. Polym. Sci.*, vol. 118, no. 5, pp. 2754–2764, Dec. 2010.

[17] S. H. Risbud, J. R. Groza, and M. J. Kim, “Clean grain boundaries in aluminium nitride ceramics densified without additives by a plasma-activated sintering process,” *Philos. Mag. Part B*, vol. 69, no. 3, pp. 525–533, 1994.

[18] K. A. Khor, K. H. Cheng, L. G. Yu, and F. Boey, “Thermal conductivity and dielectric constant of spark plasma sintered aluminum nitride,” *Mater. Sci. Eng. A*, vol. 347, no. 1–2, pp. 300–305, Apr. 2003.

[19] M. Medraj, “Understanding AlN sintering through computational thermodynamics combined with experimental investigation,” *J. Mater. Process. Tech*, vol. 161, no. 3, pp. 415–422.

[20] L. Qiao, H. Zhou, and R. Fu, “Thermal conductivity of AlN ceramics sintered with CaF2 and YF3,” *Ceram. Int.*, vol. 29, no. 8, pp. 893–896, 2003.

[21] F. Miyashiro, N. Iwase, A. Tsuge, F. Ueno, M. Nakahashi, and T. Takahashi, “High thermal conductivity aluminum nitride ceramic substrates and packages,” *IEEE Trans. Compon. Hybrids Manuf. Technol.*, vol. 13, no. 2, pp. 313–319, 1990.

[22] W. M. Haynes, *CRC Handbook of Chemistry and Physics, 95th Edition*. CRC Press, 2014.

[23] F. Cardarelli, *Materials Handbook: A Concise Desktop Reference*. Springer Science & Business Media, 2008.

[24] P. U. T. P. R. Center, *Thermophysical Properties of Matter: Specific heat: metallic elements and alloys, by Y. S. Touloukian and E. H. Buyco*. IFI/Plenum, 1970.

[25] T. B. Jackson, A. V. Virkar, K. L. More, R. B. Dinwiddie, and R. A. Cutler, “High-Thermal-Conductivity Aluminum Nitride Ceramics: The Effect of Thermodynamic, Kinetic, and Microstructural Factors,” *J. Am. Ceram. Soc.*, vol. 80, no. 6, pp. 1421–1435, Jun. 1997.

[26] J.-W. Bae, W. Kim, S.-H. Cho, and S.-H. Lee, “The properties of AlN-filled epoxy molding compounds by the effects of filler size distribution,” *J. Mater. Sci.*, vol. 35, no. 23, pp. 5907–5913, Dec. 2000.

[27] M. Bauccio, *ASM engineered materials reference book*. ASM International, 1994.

[28] H. Nakano, K. Watari, H. Hayashi, and K. Urabe, “Microstructural Characterization of High-Thermal-Conductivity Aluminum Nitride Ceramic,” *J. Am. Ceram. Soc.*, vol. 85, no. 12, pp. 3093–3095, Dec. 2002.

[29] W. J. Smothers, *1981 New England Section Topical Meeting on Nonoxide Ceramics: Ceramic Engineering and Science Proceedings, Volume 3, Number 1/2*. John Wiley & Sons, 2009.

[30] J. Shoemaker, *Moldflow Design Guide: ’A Resource for Plastics Engineers*. Munich : Cincinnati: Hanser Publications, 2006.

[31] “Granta’s CES EduPack and teaching resources: supporting Materials Education.” [Online]. Available: http://www.grantadesign.com/education/. [Accessed: 27-Sep-2013].

[32] T. B. Jackson, A. V. Virkar, K. L. More, R. B. Dinwiddie, and R. A. Cutler, “High-Thermal-Conductivity Aluminum Nitride Ceramics: The Effect of Thermodynamic, Kinetic, and Microstructural Factors,” *J. Am. Ceram. Soc.*, vol. 80, no. 6, pp. 1421–1435, 1997.

[33] G. A. Slack, “Thermal Conductivity of Pure and Impure Silicon, Silicon Carbide, and Diamond,” *J. Appl. Phys.*, vol. 35, no. 12, p. 3460, Dec. 1964.

[34] W. M. Yim and R. J. Paff, “Thermal expansion of AlN, sapphire, and silicon,” *J. Appl. Phys.*, vol. 45, no. 3, p. 1456, Mar. 1974.

[35] L. Qiao, H. Zhou, H. Xue, and S. Wang, “Effect of Y2O3 on low temperature sintering and thermal conductivity of AlN ceramics,” *J. Eur. Ceram. Soc.*, vol. 23, no. 1, pp. 61–67, Jan. 2003.

[36] L. Qiao, H. Zhou, K. Chen, and R. Fu, “Effects of Li2O on the low temperature sintering and thermal conductivity of AlN ceramics,” *J. Eur. Ceram. Soc.*, vol. 23, no. 9, pp. 1517–1524, Aug. 2003.

3.7 List of Tables

3.8 LIst of Figures

Table 3.1. Literature filler properties of AlN fillers at 300 K

filler	solid density* ρ_p, kg/m^3	specific heat+ C_{p_p}, J/kg-K	thermal conductivity++ λ_p, W/m-K	reference #
AlN	3250±50	800±30	230±70	[5]–[15], [17], [19]–[26]

*ρ_f has 22 data points; +C_{p_f} has 6 data points; ++λ_f has 18 data points

Table 3.2. Density of AlN feedstock and wax-polymer binder at 300 K

density, m^3/kg	$\rho_{b\ \text{exp}}$*	$\rho_{c\ \text{exp}}$*	$\rho_{c\ \text{est}}$+
solid	**880**	**2150**	2130±20
melt	**730**	**1940**	1940±20

*measured experimentally; +estimated using **Equation 3.1** for 22 data points of ρ_f from **Table 3.1**

Table 3.3. Specific heat of AlN feedstock and wax-polymer binder for temperature between 283 and 423 K

specific heat C_p, J/kg-K	temperature, K				
	283	298	331	374	423
$C_{p_{b\ \text{exp}}}$*	**2080**	**3360**	**4640**	**3490**	**2530**
$C_{p_{c\ \text{exp}}}$*	**920**	**1110**	**1090**	**1130**	**1210**
$C_{p_{c\ \text{est}}}$+	1050±35	1240±35	1570±35	1850±35	1150±35

*measured experimentally; +estimated using **Equation 3.4** for 6 data points of C_{p_f} from **Table 3.1**

Table 3.4. Thermal conductivity of AlN feedstock and wax-polymer binder for temperature between 316 and 436 K

thermal conductivity, W/m-K	temperature, K				
	316	356	377	397	436
$\lambda_{b\ \text{exp}}$*	**0.195**	**0.182**	**0.176**	**0.171**	**0.162**
$\lambda_{c\ \text{exp}}$*	**4.26**	**2.23**	**2.66**	**2.06**	**2.50**
$\lambda_{c\ \text{est}}$+	1.82 ±0.01	1.71 ±0.01	1.67 ±0.06	1.62 ±0.08	1.55 ±0.10

*measured experimentally; +estimated using **Equation 3.5** for 18 data points of λ_f from **Table 3.1**

Table 3.5. Viscosity of AlN feedstock as a function of shear rate between 10^1 and 10^4 s^{-1} and a temperature range of 415 - 430 K

shear rate s^{-1}	viscosity η_c, Pa.s @ T= 415 K			
	$\eta_{c\ exp}$ *	$\eta_{c\ min}$ + @ ϕ_{max} = 0.68	$\eta_{c\ avg}$ + @ ϕ_{max} = 0.64	$\eta_{c\ max}$ + @ ϕ_{max} = 0.60
10^1	**1470**	2930	4830	10500
10^2	**350**	890	1460	3170
10^3	**80**	240	390	840
10^4	**20**	60	100	210

shear rate s^{-1}	viscosity η_c, Pa.s @ T= 425 K			
	$\eta_{c\ exp}$ *	$\eta_{c\ min}$ + @ ϕ_{max} = 0.68	$\eta_{c\ avg}$ + @ ϕ_{max} = 0.64	$\eta_{c\ max}$ + @ ϕ_{max} = 0.60
10^1	**1380**	810	1330	2890
10^2	**330**	330	540	1170
10^3	**80**	100	160	350
10^4	**20**	30	40	90

shear rate s^{-1}	viscosity η_c, Pa.s @ T= 430 K			
	$\eta_{c\ exp}$ *	$\eta_{c\ min}$ + @ ϕ_{max} = 0.68	$\eta_{c\ avg}$ + @ ϕ_{max} = 0.64	$\eta_{c\ max}$ + @ ϕ_{max} = 0.60
10^1	**1340**	400	660	1430
10^2	**320**	190	890	690
10^3	**80**	60	100	230
10^4	**20**	20	30	60

*measured experimentally; +estimated using **Equation 3.6**

Table 3.6. Cross-WLF constants for AlN feedstock

Cross WLF constants	η_c exp*	η_c min+ @ ϕ_{max} = 0.68	η_c avg+ @ ϕ_{max} = 0.64	η_c max+ @ ϕ_{max} = 0.60
n	**0.38**	0.40	0.40	0.40
τ*, Pa	**180**	58300	26860	16300
D_1, Pa.s	**$8.78X10^{10}$**	$2.23X10^{15}$	$2.23X10^{15}$	$2.23X10^{15}$
D_2, K	**263**	361.95	360.93	360.17
A_1, K/Pa	**14.24**	48.49	49.55	50.19
A_2, K	**51.60**	51.60	51.60	51.60

*calculated from **Equation 3.7, 8** and experimental (η_c) values from **Table 3.5**;

+calculated from **Equation 3.7, 8** and estimated (η_c) values from **Table 3.5**

Table 3.7. Specific volume of AlN feedstock as a function of pressures between 0 to 200 MPa and temperature range of 300 to 450 K

temperature, K	specific volume ν_c X10^{-3}, m^3/kg @ P = 0 MPa			
	$\nu_{c\ exp}$ *	$\nu_{c\ min}$ + @ ν_f=0.30	$\nu_{c\ avg}$ + @ ν_f=0.32	$\nu_{c\ max}$ + @ ν_f=0.44
300	**0.47**	0.47	0.48	0.58
350	**0.49**	0.49	0.50	0.60
400	**0.50**	0.50	0.51	0.61
450	**0.52**	0.52	0.53	0.63

temperature, K	specific volume ν_c X10^{-3}, m^3/kg @ P = 100 MPa			
	$\nu_{c\ exp}$ *	$\nu_{c\ min}$ + @ ν_f=0.30	$\nu_{c\ avg}$ + @ ν_f=0.32	$\nu_{c\ max}$ + @ ν_f=0.44
300	**0.46**	0.46	0.47	0.57
350	**0.48**	0.48	0.49	0.59
400	**0.49**	0.49	0.50	0.60
450	**0.50**	0.49	0.50	0.60

temperature, K	specific volume ν_c X10^{-3}, m^3/kg @ P = 200 MPa			
	$\nu_{c\ exp}$ *	$\nu_{c\ min}$ + @ ν_f=0.30	$\nu_{c\ avg}$ + @ ν_f=0.32	$\nu_{c\ max}$ + @ ν_f=0.44
300	**0.45**	0.45	0.46	0.57
350	**0.46**	0.46	0.47	0.59
400	**0.47**	0.48	0.49	0.60
450	**0.48**	0.48	0.49	0.60

*measured experimentally; +estimated using **Equation 3.9**

Table 3.8. Dual-domain Tait constants for AlN feedstock

Dual-domain Tait constants	$\nu_{c\ exp}$ *	$\nu_{c\ min}$ + @ ν_f=0.30	$\nu_{c\ avg}$ + @ ν_f=0.32	$\nu_{c\ max}$ + @ ν_f=0.44
b_5, K	**331**	331	331	331
b_6, K/Pa	**1.30X10^{-7}**	1.30X10^{-7}	1.30X10^{-7}	1.30X10^{-7}
b_{1m}, m^3/kg	**4.64X10^{-4}**	4.75X10^{-4}	5.77X10^{-4}	4.64X10^{-4}
b_{2m}, m^3/kg.K	**1.87X10^{-7}**	1.88X10^{-7}	1.95X10^{-7}	1.87X10^{-7}
b_{3m}, Pa	**2.05X10^{9}**	1.79X10^{9}	2.17X10^{9}	1.65X10^{9}
b_{4m}, 1/K	**4.60X10^{-3}**	3.58X10^{-3}	6.15X10^{-3}	2.25X10^{-3}
b_{1s}, m^3/kg	**4.55X10^{-4}**	4.67X10^{-4}	5.69X10^{-4}	4.56X10^{-4}
b_{2s}, m^3/kg.K	**2.05X10^{-7}**	2.05X10^{-7}	2.05X10^{-7}	2.05X10^{-7}
b_{3s}, Pa	**2.52X10^{9}**	1.56X10^{9}	1.63X10^{9}	1.31X10^{9}
b_{4s}, 1/K	**3.01X10^{-3}**	5.88X10^{-3}	6.35X10^{-3}	4.21X10^{-3}
b_7, m^3/kg	**5.08X10^{-5}**	4.73X10^{-5}	5.34X10^{-5}	4.09X10^{-5}
b_8, 1/K	**8.54X10^{-1}**	8.62X10^{-1}	8.97X10^{-1}	8.17X10^{-1}
b_9, 1/Pa	**5.06X10^{-6}**	5.25X10^{-6}	3.53X10^{-5}	5.19X10^{-6}

*calculated from **Equation 3.10-13** and experimental (ν_c) values from **Table 3.7**;

+calculated from **Equation 3.1-13** and estimated (ν_c) values from **Table 3.7**

Table 3.9. AlN feedstock datasets used for injection molding simulations

AlN feedstock dataset	density* ρ_c, kg/m^3	specific heat** C_{p_c}, J/kg-K	thermal conductivity+ λ_c, W/m-K	Cross WLF constants++	Dual-domain Tait constants*+
experimental	$\boldsymbol{\rho_{c\ exp}}$	$\mathbf{C_{p_{c\ exp}}}$	$\boldsymbol{\lambda_{c\ exp}}$	$\boldsymbol{\eta_{c\ exp}}$	$\boldsymbol{\nu_{c\ exp}}$
1	$\rho_{c\ avg}$	$C_{p_{c\ avg}}$	$\lambda_{c\ avg}$	$\eta_{c\ avg}$	$\nu_{c\ avg}$
2	$\rho_{c\ min}$	$C_{p_{c\ min}}$	$\lambda_{c\ min}$	$\eta_{c\ min}$	$\nu_{c\ min}$
3	$\rho_{c\ max}$	$C_{p_{c\ max}}$	$\lambda_{c\ max}$	$\eta_{c\ max}$	$\nu_{c\ max}$
4	$\rho_{c\ avg}$	$C_{p_{c\ avg}}$	$\lambda_{c\ avg}$	$\boldsymbol{\eta_{c\ exp}}$	$\nu_{c\ avg}$
5	$\rho_{c\ min}$	$C_{p_{c\ min}}$	$\lambda_{c\ min}$	$\boldsymbol{\eta_{c\ exp}}$	$\nu_{c\ min}$
6	$\rho_{c\ max}$	$C_{p_{c\ max}}$	$\lambda_{c\ max}$	$\boldsymbol{\eta_{c\ exp}}$	$\nu_{c\ max}$

*data from **Table 3.2**; **data from **Table 3.3**; +data from **Table 3.4**;
++data from **Table 3.6**; and *+data from **Table 3.8**

Table 3.10. Process input parameters for injection molding simulations

input parameters	**values**
fill time	0.1 s
velocity to pressure switch over	99%
mold temperature	308 K
melt temperature	423 K

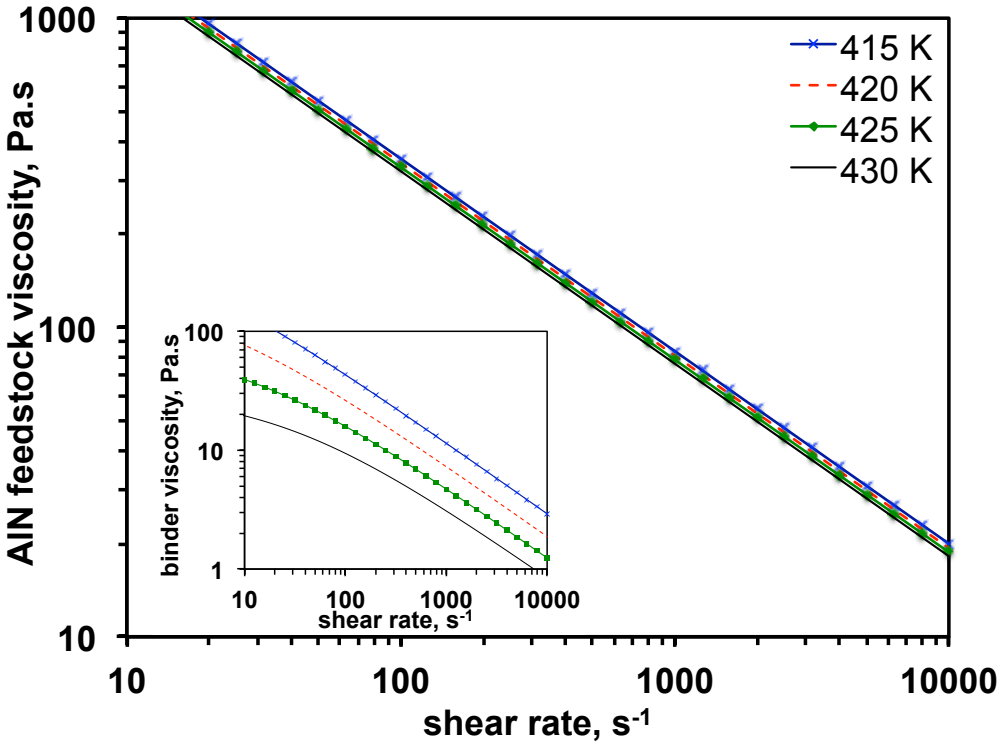

Figure 3.1. Viscosity of AlN feedstock and wax-polymer binder (inset) for a shear rate range of 10 to 10^4 s^{-1} and a temperature range between 415 and 430 K.

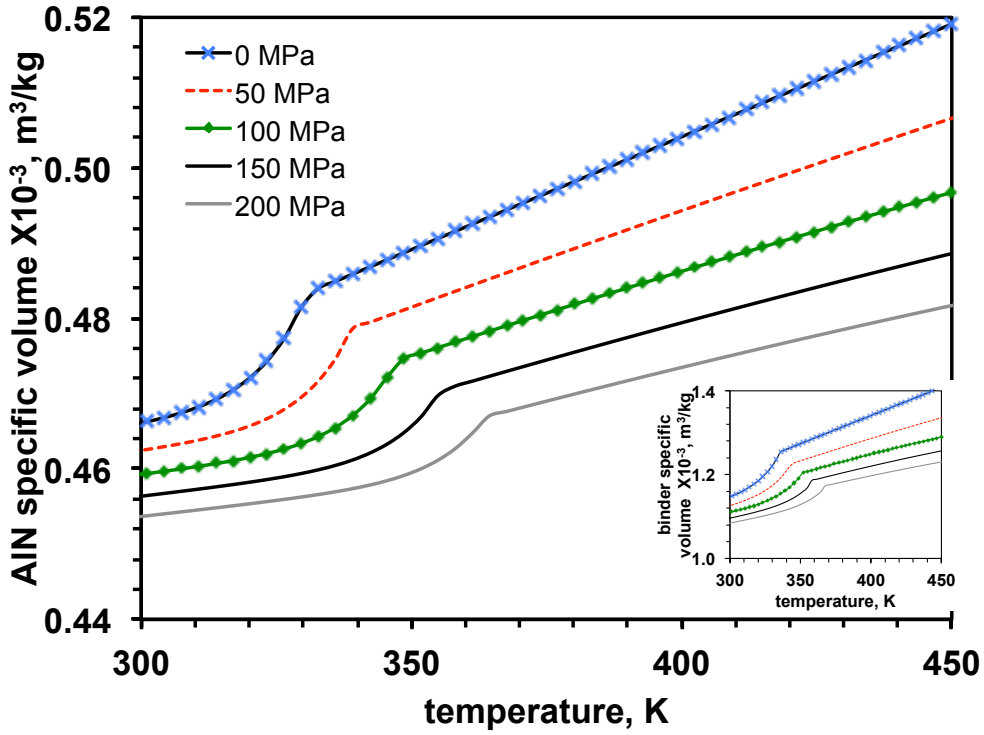

Figure 3.2. Specific volume of AlN feedstock for a temperature range of 300 to 450 K and pressures between 0 and 200 MPa.

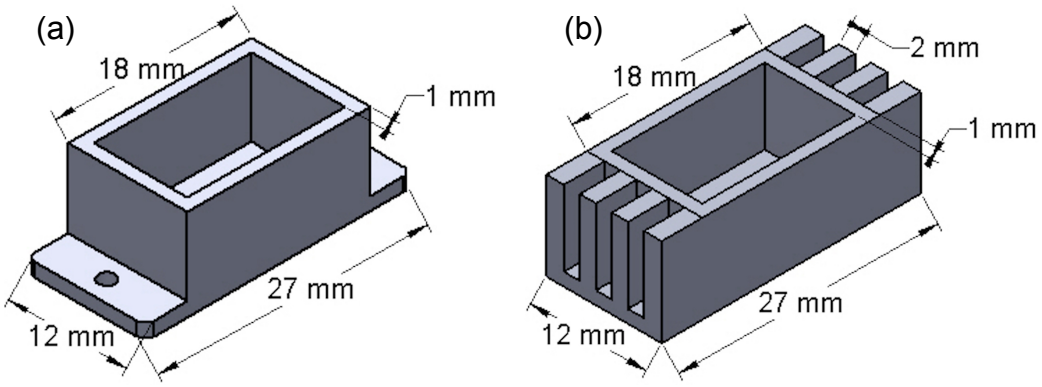

Figure 3.3. Mold geometry used for injection molding simulation (a) heat-sink substrate without fins and (b) heat-sink substrate with fins.

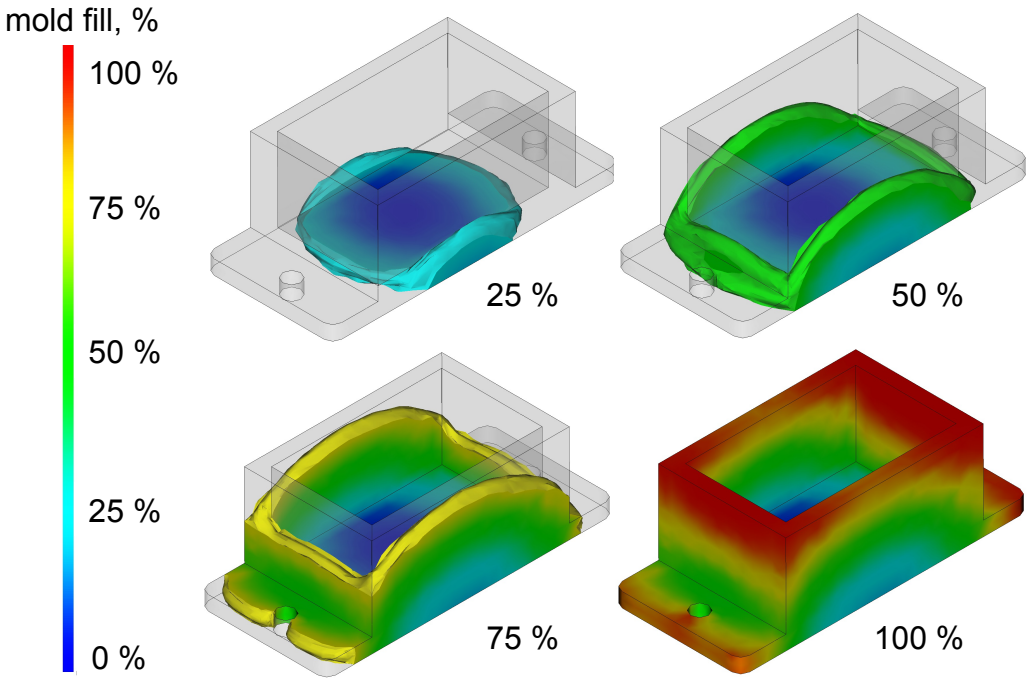

Figure 3.4a. General progressive mold-filling behavior observed for heat-sink substrate without fins.

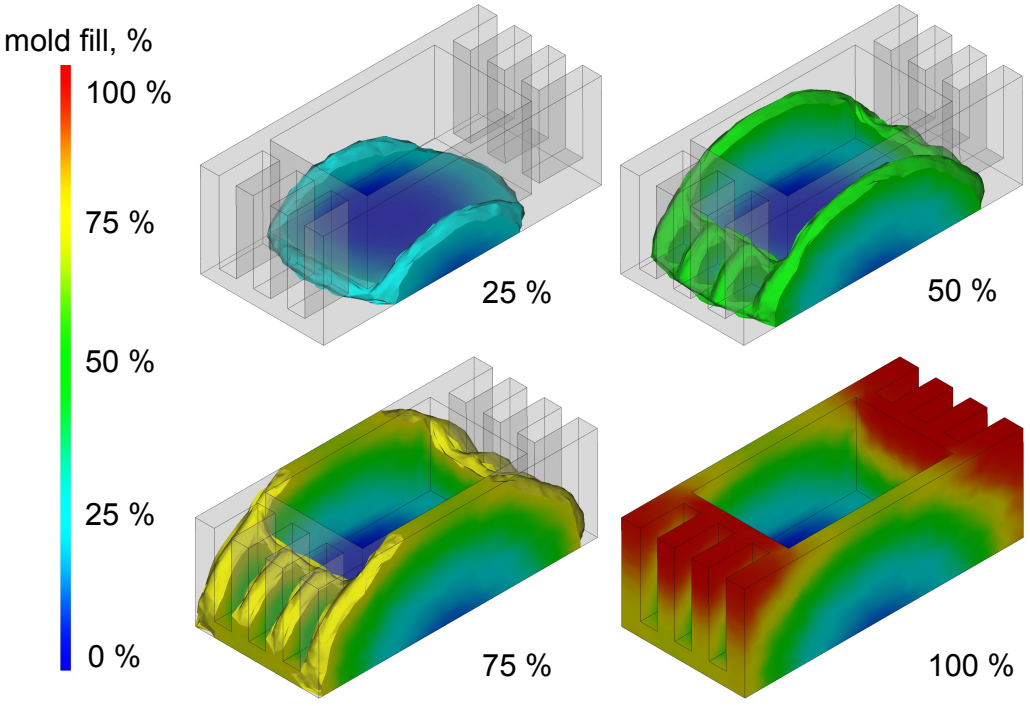

Figure 3.4b. General progressive mold-filling behavior observed for heat-sink substrate with fins.

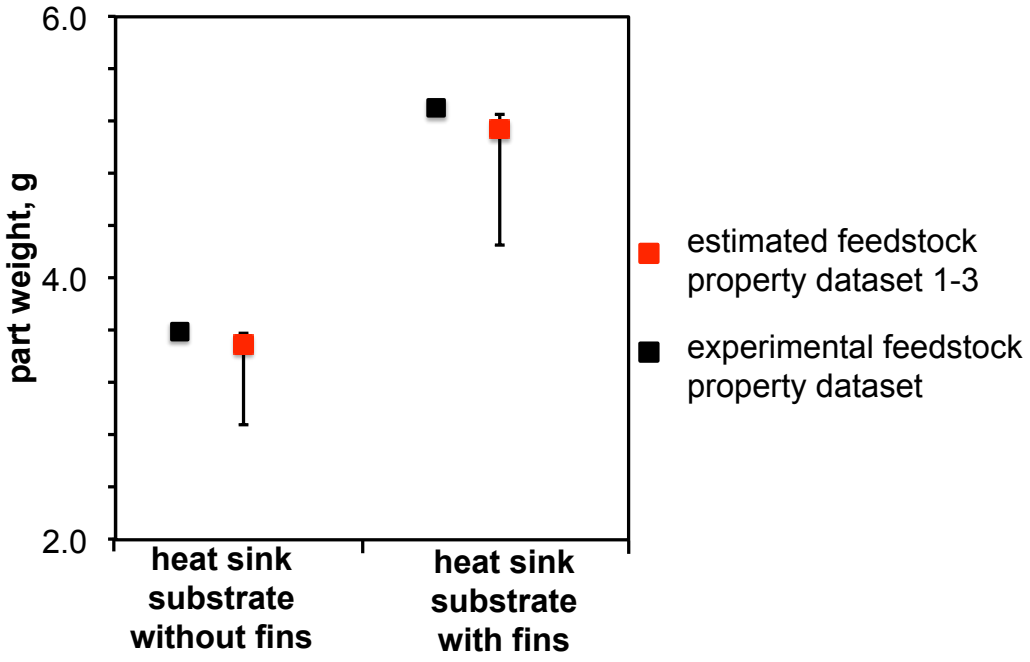

Figure 3.5. Comparison of part weight for heat-sink substrates with fins and without fins using the experimental feedstock property dataset and estimated feedstock property Datasets 1-3 (**Table 3.9**).

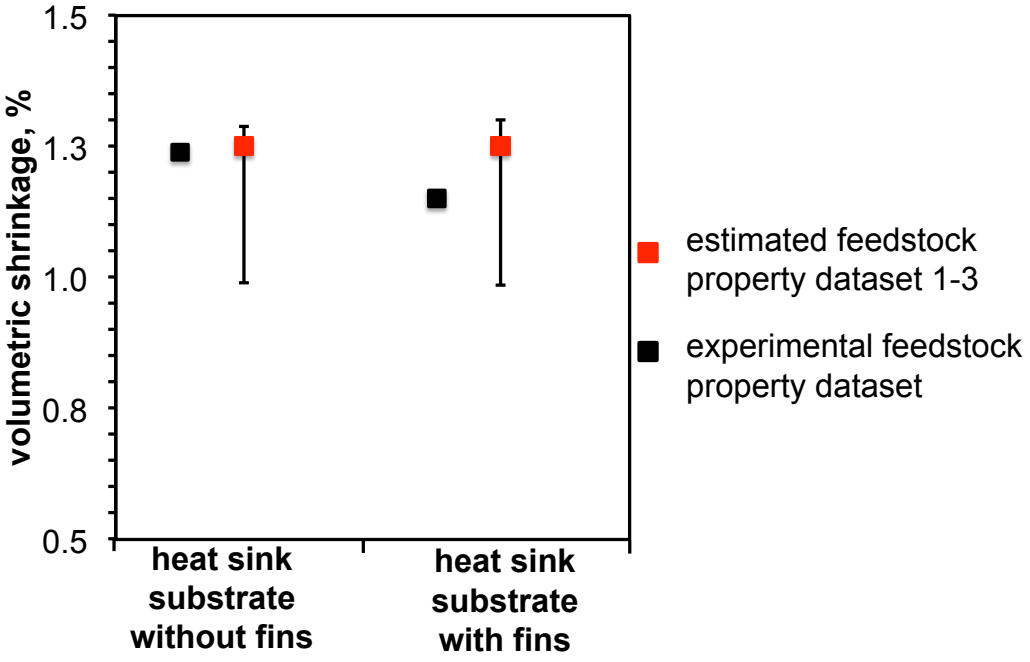

Figure 3.6. Comparison of percent volumetric shrinkage for heat-sink substrates with fins and without fins using the experimental feedstock property dataset and estimated feedstock property Datasets 1-3 (**Table 3.9**).

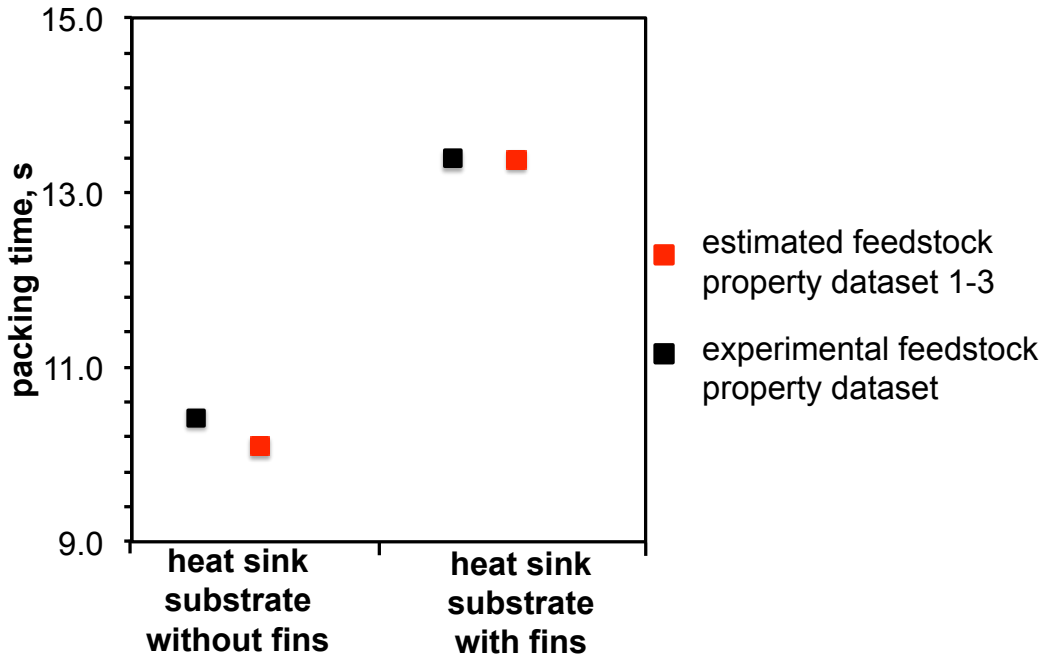

Figure 3.7. Comparison of packing time for heat-sink substrates with fins and without fins using the experimental feedstock property dataset and estimated feedstock property Datasets 1-3 (**Table 3.9**).

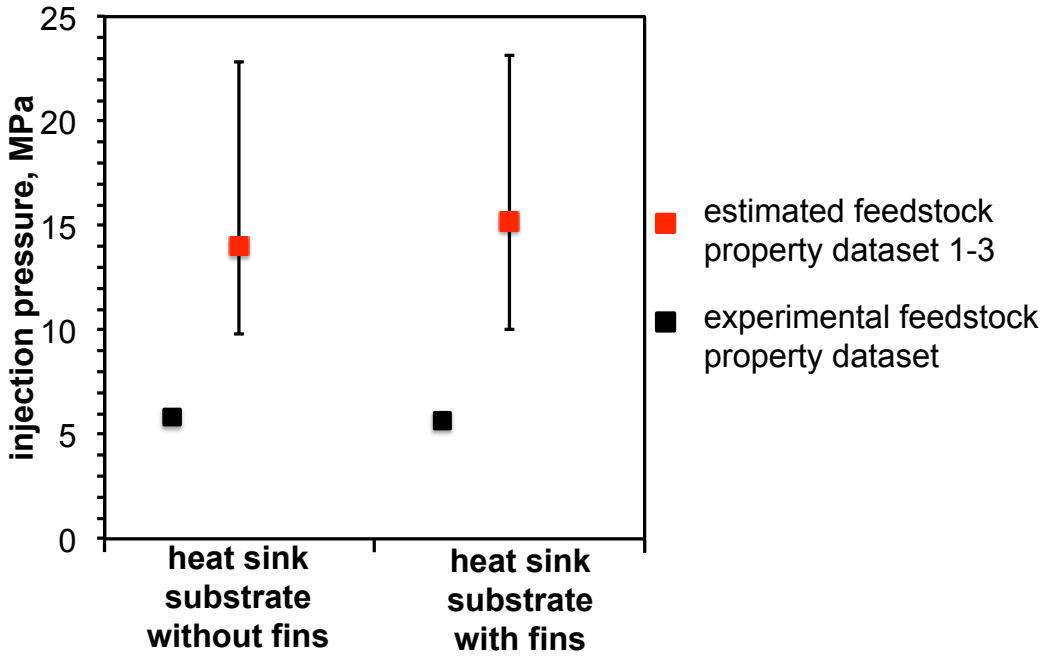

Figure 3.8a. Comparison of injection pressure for heat-sink substrates with fins and without fins using the experimental feedstock property dataset and estimated feedstock property Datasets 1-3 (**Table 3.9**).

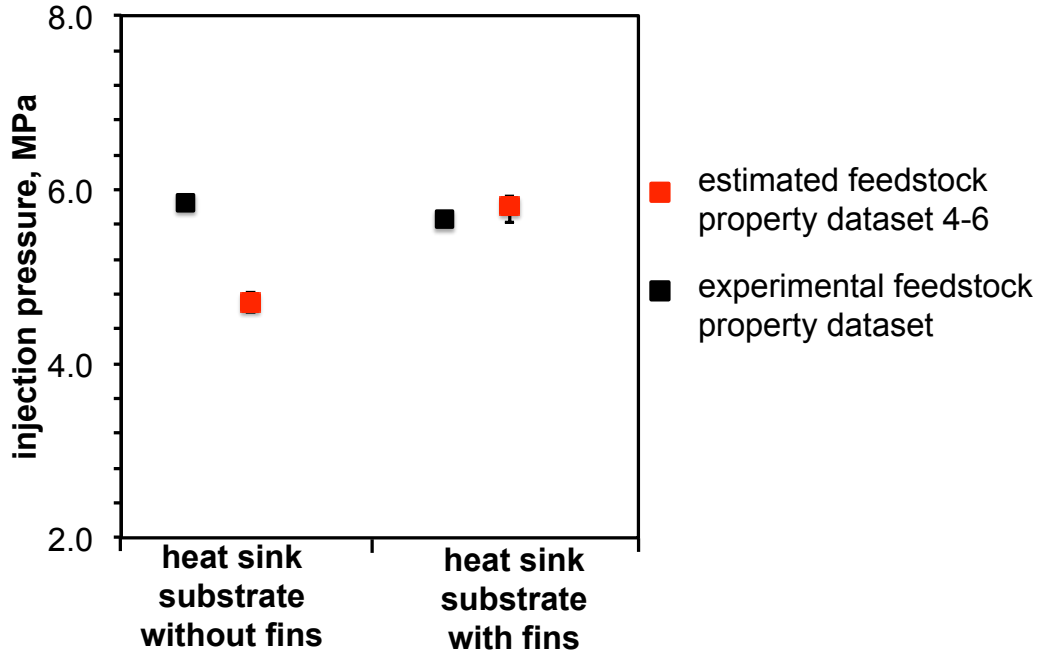

Figure 3.8b. Comparison of injection pressure for heat-sink substrates with fins and without fins geometry using the experimental feedstock property dataset and estimated feedstock property Datasets 4-6 (**Table 3.9**).

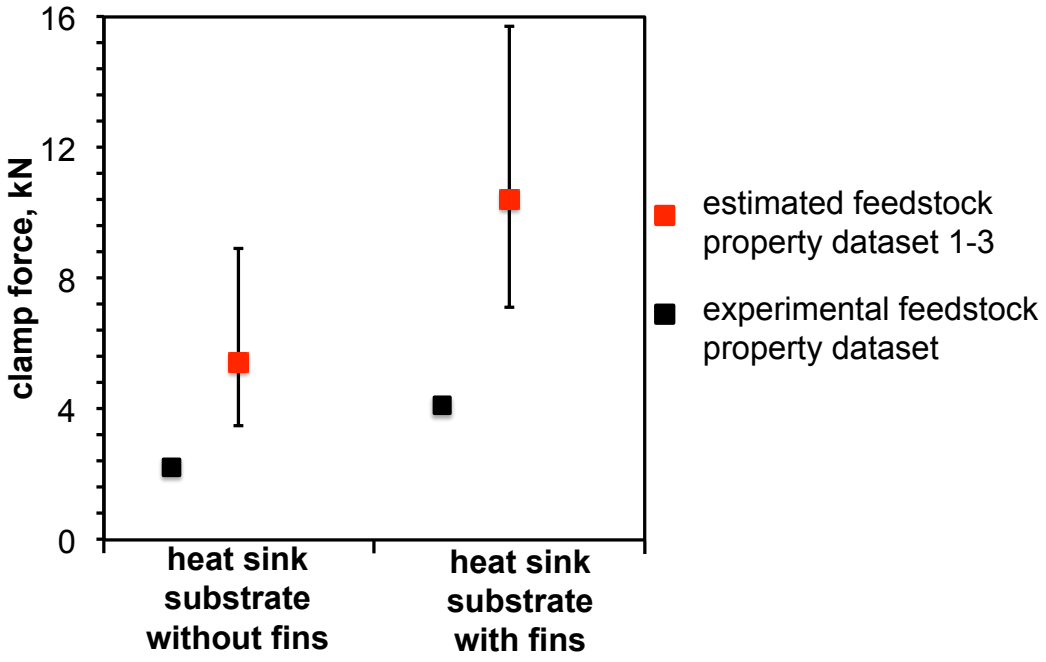

Figure 3.9a. Comparison of clamp force for heat-sink substrates with fins and without fins using the experimental feedstock property dataset and estimated feedstock property Datasets 1-3 (**Table 3.9**).

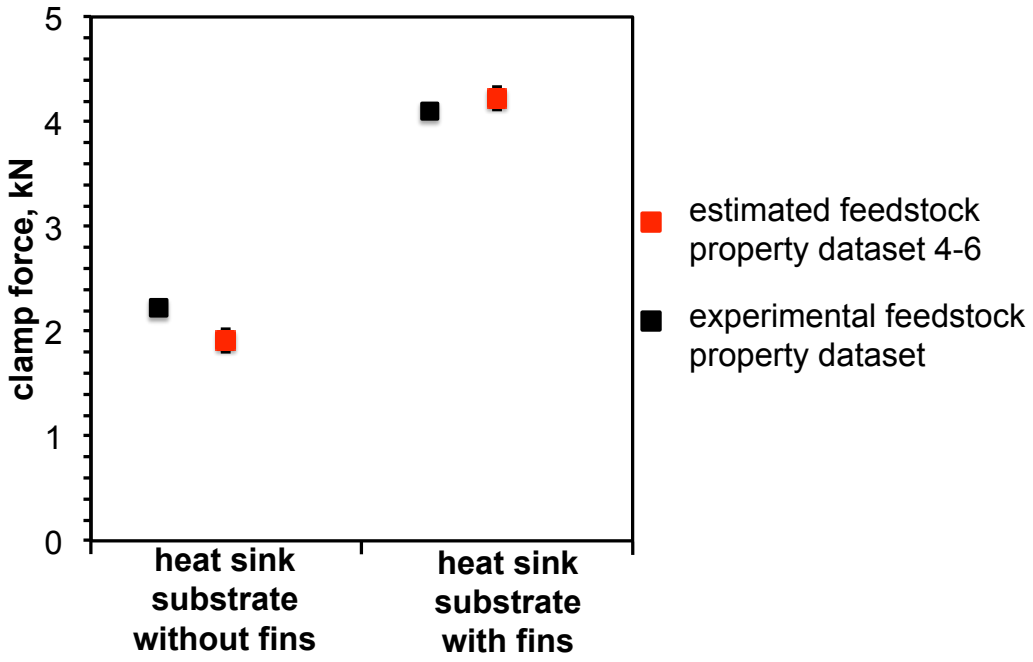

Figure 3.9b. Comparison of clamp force for heat-sink substrates with fins and without fins using the experimental feedstock property dataset and estimated feedstock property Datasets 4-6 (**Table 3.9**).

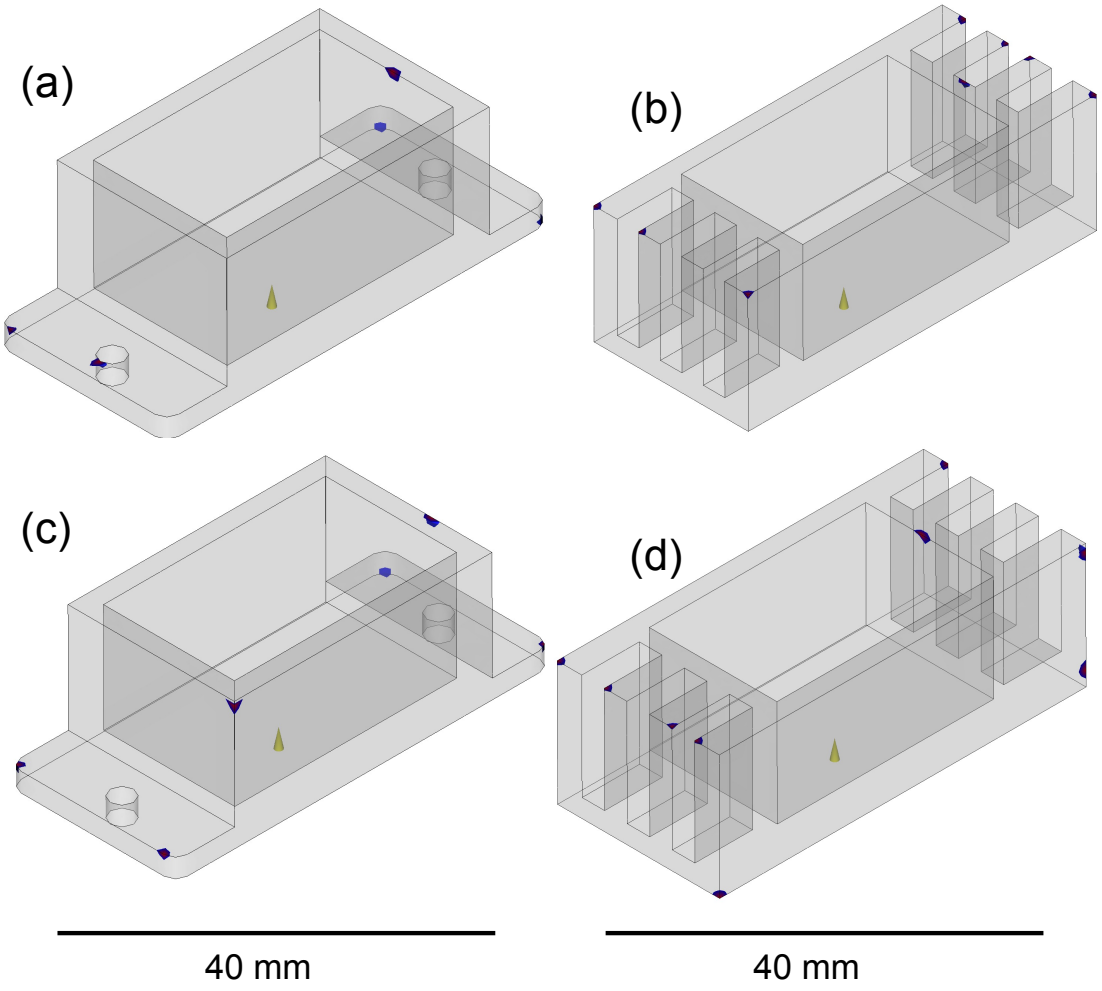

Figure 3.10. Air-trap locations in heat-sink substrates with fins and without fins. (a,b) for the experimental AlN feedstock dataset and (c,d) for the estimated AlN feedstock Dataset 1.

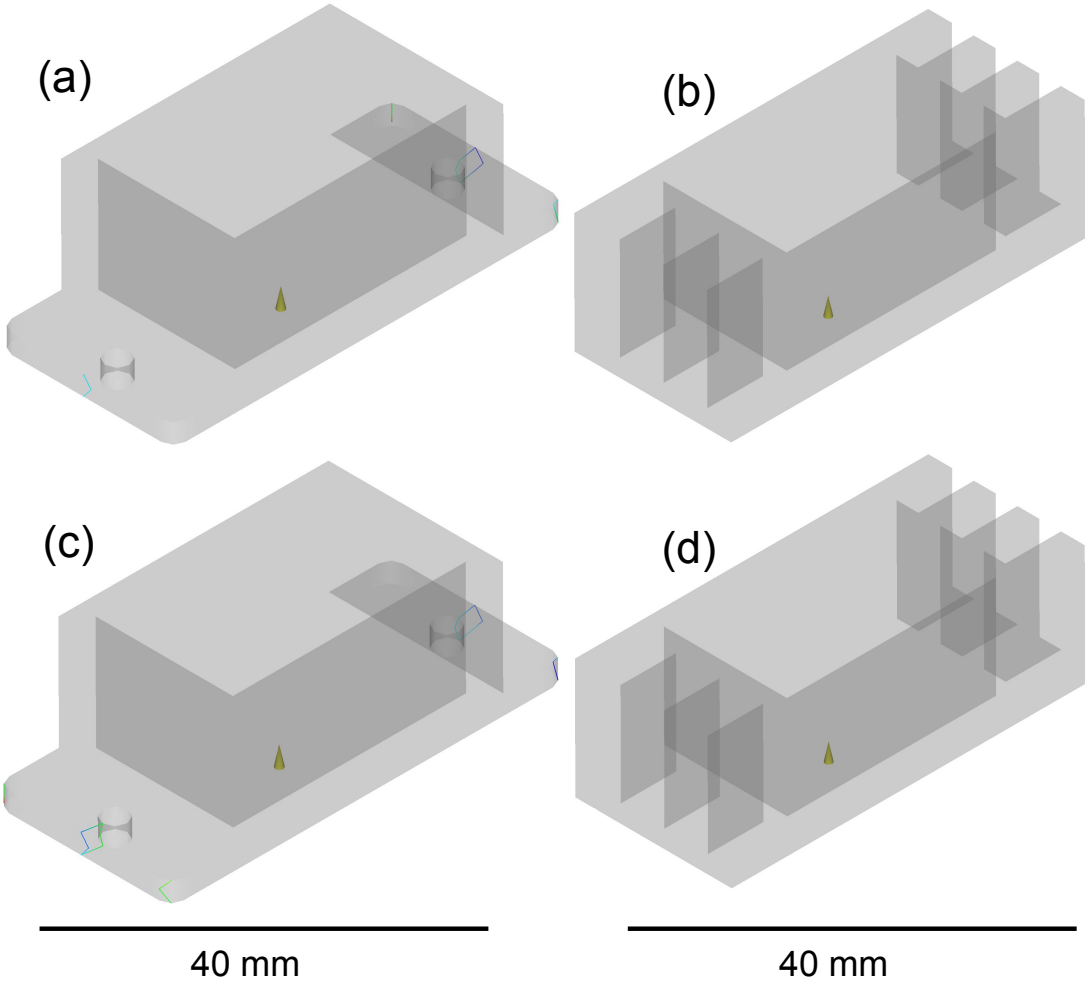

Figure 3.11. Weld-line locations in heat-sink substrates with fins and without fins. (a,b) for the experimental AlN feedstock dataset and (c,d) for the estimated AlN feedstock Dataset 1.

Chapter 4: Simulations And Injection Molding Experiments For Aluminum Nitride Feedstock

Abstract

Powder injection molding (PIM) simulations are useful at predicting mold-filling behavior as they aid material, process and part design. To perform PIM simulations, measurements for feedstock properties such as physical, thermal, and rheological are required as inputs. The availability of data for such feedstock properties is limited and fresh measurements are often required in order to perform PIM simulations for variations in feedstock composition. A recent study by our group presented a procedure to estimate feedstock properties and use them in mold-filling simulations. The present work compares the predictions of PIM mold-filling simulations using experimental and estimated feedstock properties with injection-molding experiments. Aluminum nitride (AlN) feedstock of 80.5 wt.% was compounded using a twin-screw extruder and injection-molded as tensile bars. Injection-molding experiments were performed using the AlN feedstock at various melt temperatures and injection pressures to obtain complete and partially filled parts. Simulations were performed using measured and estimated AlN feedstock properties on the tensile-bar geometry used during injection molding experiments. Melt temperature inputs were varied while performing simulations to obtain a process window for complete and

4.1 Introduction

Powder injection molding (PIM) is a multi-step process that can be divided into four basic steps: 1) ceramic or metal powders are mixed with polymer binders to form a homogenous feedstock using a twin-screw extruder, 2) the feedstock is injection molded into desired geometries using an injection molding machine, 3) the binder phase is debinded from the molded parts by thermal or solvent based techniques, and 4) debinded parts are sintered to achieve final parts. The PIM simulations are generally performed typically after feedstock compounding to identify appropriate process and geometry attributes for optimum molding. To perform PIM simulations, feedstock property measurements for density, thermal conductivity, and specific heat are required for a range of temperatures, viscosity measurements are required for a range of shear rates and temperatures, while specific volume measurements are required for a range of temperatures and pressures [1–4]. Availability of such feedstock property data is limited and properties are typically measured for a particular composition.

Powder injection molding (PIM) is a multi-step process that can be divided into four basic steps: 1) ceramic or metal powders are mixed with polymer binders to form a homogenous feedstock using a twin-screw extruder, 2) the feedstock is injection molded into desired geometries using an injection molding machine, 3) the binder phase is debinded from the molded parts by thermal or solvent based techniques, and 4) debinded parts are sintered to achieve final parts. The PIM simulations are generally performed typically after feedstock compounding to identify appropriate process and geometry attributes for optimum molding [1]–[12]. Common injection molding simulation tools include Autodesk Moldflow, Sigmasoft, PIMsolver, and Modlex3D.

To perform PIM simulations, feedstock property measurements for density, thermal conductivity, and specific heat are required for a range of temperatures, viscosity measurements are required for a range of shear rates and

temperatures, while specific volume measurements are required for a range of temperatures and pressures [1–4]. Availability of such feedstock property data is limited and properties are typically measured for a particular composition.

A recent work by our group suggests a design method that uses empirical equations and estimate feedstock properties as a function of composition, filler properties, and binder properties [17]. This design method employs the use of available literature filler and binder properties to estimate physical, thermal and rheological properties for nine different ceramic feedstocks [17]. An extension of this work outlines a procedure to use feedstock property estimates and perform mold-filling simulations. It further studies the effect of scatter in estimates to predict mold filling behavior [18].

In the current work, 80.5-weight percent aluminum nitride (AlN) feedstock was extruded and injection molded into a tensile geometry. Injection molding was performed as a function of melt temperatures and injection pressures in order to get parts with partial and complete mold fills. Feedstock properties for AlN were measured at Datapoint Labs and estimated using our design procedure for PIM simulations [5, 6]. To perform PIM simulations a tensile geometry was designed according to the mold tool dimensions. Simulations were performed using measured and estimated AlN feedstock properties at various melt temperatures and injection pressures to obtain complete and partially filled parts. Comparisons of melt temperatures for simulation and experiments were made to understand the effectiveness of PIM simulations in predicting mold-filling behavior.

4.2 Experimental Methods

Commercially available aluminum nitride (AlN) powder (median particle size of 1 μm) and a wax-polymer binder were used as starting materials. The binder is composed of paraffin wax, low-density polyethylene, polypropylene, and stearic acid. Details of the binder composition and feedstock compounding are

provided [19], [20]. A feedstock with 80.5 wt.% AlN powder was compounded using a 27 mm twin-screw extruder with a length to diameter (L/D) ratio of 40.

Material property measurements were made at Datapoint Labs (Ichata, NY) for the AlN feedstock and a wax-polymer binder [7, 8]. Solid density measurements were made for AlN feedstock and wax-polymer binder using Archimedes principle as laid out in ASTM standard D792. The melt density measurement was done using a Gottfert Rheograph capillary rheometer in accordance with ASTM D3835 for AlN feedstock and a wax-polymer binder. A Perkin Elmer differential scanning calorimetry (DSC) was used to measure specific heats for AlN feedstock and a wax-polymer binder in accordance with ASTM E1269 standard. Thermal conductivity measurements for AlN feedstock and the wax-polymer binder were made using a K-System II thermal conductivity system in accordance with ASTM standard D5930. Viscosity for AlN feedstock and the wax-polymer binder was measured according to ASTM D3835 using a Gottfert Rheograph capillary rheometer. Pressure-volume-temperature (PVT) measurements for AlN feedstock and the wax-polymer binder were made with a Gnomix PVT apparatus in accordance with ASTM D792 [7, 8]. The feedstock property measurements were compared to values estimated using models listed in **Table 4.1**.

The AlN feedstock was injection molded into a tensile geometry using an Arburg 221M injection-molding machine. An injection gate with a size of 6.5 mm was used to inject the AlN feedstock into the mold cavity. Injection molding experiments were performed at a set of melt temperatures and injection pressures to obtain parts with complete and incomplete mold fill (**Table 4.2**). In the first molding experiment (**Table 4.2**) the injection pressure (P_i) was set at 38 MPa and melt temperature (T_m) was set at 455 K. A total of 50 parts with no defects were molded during this experiment and a specimen part is shown in **Figure 4.1a.** To understand the effect of decreases in injection pressure and melt temperature on the molding behavior, experiments # 2-4 were performed

(**Table 4.2**). For Experiments 2-4 the melt temperatures was decreased from 444 K to 422 K while keeping injection pressure constant at 14 MPa to obtain parts with incomplete mold fill (short-shot). A total of four to five specimens were injection molded in each of the experiments 2-4 and sample molded specimens are presented in **Figure 4.2b-d**. All injection molding experiments listed in **Table 4.2** were performed at injection speed of 33 cm^3/s, the initial packing pressure was set at 100% of the injection pressure value for the first second and then it was reduced to 65% of the injection pressure value for the next 1.2 s. To calculate the percentage of part filled of the incompletely filled samples, their weights were compared to those of the filled samples.

To perform mold-filling simulations, the tensile geometry model was imported into the Autodesk Moldflow software. The tensile geometry was meshed using an automated solid 3D meshing protocol based on finite element analysis. A gate size of 6.5 mm was set to perform molding simulations. A fill-and-pack type process module was selected to perform simulations. Simulations were performed using measured and estimated AlN feedstock property values.

Simulations were performed on a 3D tensile geometry model designed using Solidworks in accordance with mold tool design. Dimensions for the tensile geometry are shown in **Figure 4.2**. Initial simulations were performed using Autodesk Moldflow software for injection molding conditions listed in **Table 4.2.** Additional simulations for lower values of melt temperature were performed in case short-shots were not obtained at the melt temperature of 422 K.

4.3 Results and Discussion

4.3.1 Properties

The physical, thermal and rheological properties of AlN feedstock were estimated using selected empirical models presented in **Table 4.1**. The empirical models estimate material properties of feedstocks as a function of feedstock composition and filler and binder properties. The empirical models

were selected by performing an in-depth statistical analysis on various published models that were fitted to literature data on experimentally measured properties of powder-polymer mixtures [13]. Description of the symbols used in **Table 4.1** and throughout this paper is presented in **Table 4.2**. The thermal, physical and rheological properties of the wax-polymer binder and thermal and physical properties of AlN filler were collected from literature. Filler properties collected from literature were reported for 300 K.

The solid and melt density of AlN feedstock was estimated using **Equation 4.1** for the 22 data points of AlN filler density (3300±50 kg/m^3) [13–27]. Estimations were made for the wax-polymer solid and melt density values of 870 and 700 kg/m^3 respectively and details for estimation procedure are reported elsewhere [17–19, 33]. The experimentally measured and estimated values of solid and melt densities for the AlN feedstock are presented in **Table 4.4.** The average values of density estimates and measured values of density from **Table 4.4** were used to create a dataset necessary for performing mold-filling simulations.

Furthermore, the densities values of AlN filler and the wax-polymer binder in conjunction with **Equation 4.2** and **3** were used to calculate volume fraction of the AlN feedstock. Volume fraction values are required to estimate material properties like viscosity and thermal conductivity.

The specific heat of the AlN feedstock was estimated using **Equation 4.4** as a function of temperature for the six data points of filler specific heats (800±30 J/kg.K) [34–36]. Estimations were made for the wax-polymer binder specific heats reported for temperature between 283 and 430 K. The specific heat values of the wax-polymer binder used for this estimation ranged between 2080 and 4640 J/kg.K and details for the estimation procedure are reported elsewhere [17–19, 33]. The experimentally measured and estimated values of specific heats for the AlN feedstock are presented in **Table 4.5.** The average values of specific heat estimates and measured values of specific heats from

Table 4.5 were used to create a dataset necessary for performing mold-filling simulations.

The thermal conductivity of the AlN feedstock was estimated using **Equation 4.5** as a function of temperature for the 18 data points of filler specific heats (230±70 W/m.K) [21], [24], [26], [30]–[32], [37]–[40] Estimations were made for the wax-polymer binder thermal conductivity reported for temperature between 310 and 440 K. The thermal conductivity values of the wax-polymer binder used for this estimation ranged between 0.162 and 0.195 W/m.K and details for the estimation procedure are reported elsewhere [17–19, 33]. The experimentally measured and estimated values of thermal conductivity for the AlN feedstock are presented in **Table 4.6.** The average values of thermal conductivity estimates and measured values of thermal conductivity from **Table 4.6** were used to create a dataset necessary for performing mold-filling simulations.

In the present study, a Simplified Krieger Dougherty model (**Equation 4.6**) was used to estimate viscosity. The viscosity of the AlN feedstock was estimated for 40 different shear rates in ranges between 10 and 10^4 s^{-1} and for temperatures of 415, 420, 425 and 430 K using **Equation 4.6** and polymer binder viscosity ($\eta_{b\ exp}$) values from **Figure 4.3.** The viscosity data for the wax-polymer binder was gathered from literature [19]. The volume fraction of the AlN feedstock (ϕ_p) was calculated to be 0.52 using **Equation 4.2**. Viscosity was estimated for a ϕ_{max} of 0.64 critical filler content and details for the estimation procedure are reported elsewhere [17–19, 33]. The representative values for the estimated and experimental AlN feedstock viscosities are shown in **Table 4.7.**

To perform mold-filling simulations the viscosity of the AlN feedstock has to be represented in terms of fitted constants. The Cross-WLF Equation 4.**(Equation 4.7** and **Equation 4.8)** was used to extract fitted constants for the measured and estimated AlN feedstock viscosity (**Table 4.8)** and details for the extraction procedure are reported elsewhere [17–19, 33]. The Cross-WLF constants from

Table 4.8 were further used to create a dataset necessary for performing mold filling simulations.

A rule-of-mixtures model (**Equation 4.9**) was used to estimate specific volume of AlN feedstock. To calculate the specific volume of AlN filler, the reciprocals of the densities of the AlN filler were used. The specific volume of the AlN feedstock was estimated for 20 different temperatures in ranges between 300 and 453 K and for pressures of 0, 50, 100, 150, and 200 MPa using **Equation 4.9** and polymer binder specific volume ($v_{b\ exp}$) values from **Figure 4.4.** The specific volume data for the wax-polymer binder was gathered from literature [19]. The average value for the AlN filler specific volume was used to estimate the AlN feedstock specific volume and details for the estimation procedure are reported elsewhere [17–19, 33]. The representative values for the estimated and experimental AlN feedstock specific volumes are shown in **Table 4.9.**

To perform mold-filling simulations, the specific volume of the AlN feedstock needs to be represented in terms of fitted constants. A Dual-domain Tait Equation 4.**(Equation 4.10-13)** was used to extract these fitted constants for the estimated and measured AlN feedstock specific volumes (**Table 4.10**) and details for the extraction procedure are reported elsewhere [17–19, 33]. The Dual-domain Tait constants from **Table 4.10** were further used to create a dataset necessary for performing mold filling simulations.

4.3.2 Injection molding results

The first injection molding experiment listed in **Table 4.1** was performed for an injection pressure of 38 MPa and a melt temperature of 455 K with the AlN feedstock. This particular combination of injection pressure and melt temperature resulted in 100% filled parts (**Figure 4.1a**). Additional injection molding experiments with an increase in injection pressure to a value of 48 MPa also resulted in a 100% filled parts. This behavior indicated that an increase in injection pressure from 30 to 48 MPa showed no sensitivity towards part filling.

Injection molding experiments 2-4 listed in **Table 4.1** were performed at a lower injection pressure of 14 MPa and melt temperature was decreased from 444K to 389 K. Experiments # 2-4 were performed to investigate the sensitivity of variation in injection pressure and melt temperature towards part filling. Specimen images of molded parts for experiments # 2-4 are represented in **Figure 4.1b-d**. Molding experiment #2 performed at a melt temperature of 444 K resulted in a 100% filled part (**Figure 4.1b**), molding experiment # 3 performed at a melt temperature of 433 K resulted in a 89 % filled part (**Figure 4.1c**), and molding experiment #3 performed at a melt temperature of 389 K resulted in 71 % filled part (**Figure 4.1d**). The onset of an incomplete mold filling (short-shot) was observed at a melt temperature of 433 K (**Figure 4.1c**).

The PIM simulations were performed using the AlN feedstock property datasets 1-3 presented in **Table 4.10**. Dataset 1 comprises of experimentally measured physical, thermal and rheological feedstock properties, dataset 2 comprises of estimated physical, thermal and rheological properties, and dataset 3 comprises of estimated physical, thermal properties, and experimentally measured rheological properties.

In order to study the effectiveness of the PIM simulations in predicting mold filling behavior, simulations were performed for the experimental processing conditions listed in **Table 4.1**. **Figure 4.5** show a typical progressive mold filling behavior for a PIM simulation performed at an injection pressure of 38 MPa and melt temperature of 455 K using dataset 1 feedstock properties. A similar progressive mold filling behavior was observed for simulations performed with dataset 2 and 3 feedstock properties at an injection pressure of 38 MPa.

Simulations performed at a lower injection pressure of 14 MPa and melt temperature of 444K using datasets 1-3 also displayed a filling profile similar to that observed in **Figure 4.5**. For instance, **Figure 4.6a** shows a filling profile simulated for an injection pressure of 14 MPa and melt temperature of 444K using dataset-1 feedstock properties. In order to study well how PIM simulations

predict the melt temperature at which the short-shot occurs, the melt temperature inputs were lowered until a short-shot occurred. The onset of short-shot for simulation with dataset 1 occurred at a melt temperature of 333 K (**Figure 4.6b**). Simulations with dataset 2 resulted in complete mold fills for melt temperatures until 430K and a short-shot occurred at a melt temperature of 420K (**Figure 4.6c**). Simulations with dataset 3 resulted in complete mold fills for melt temperatures until 353K and a short-shot occurred at a melt temperature of 333K (**Figure 4.6c**).

A plot of percent mold fill with melt temperature for injection molding experiments and simulations is presented in **Figure 4.7**. Simulations with datasets 1-3 predict a complete mold fill for process input conditions set according to experiment #1 and #2 (**Table 4.1**). This behavior was also observed for the injection molding experiments. However, as the melt temperature values were lowered, the PIM simulations couldn't predict the onset of short-shot accurately.

A plot of part weight with melt temperature for injection molding experiments and simulations are presented in **Figure 4.8**. Part weights for injection molding experiments with complete mold fill were typically around ~9.95g and had a standard deviation of ±0.02. Simulations with datasets 1-3 predict part weights with reasonable accuracy for process input conditions set according to experiment #1 and #2 (**Table 4.1**). Simulations with dataset 3 for a melt temperature of 450K showed the highest deviation of 8% in predicted part weight. However, as the melt temperature values were lowered to 389K the deviation of part weight predictions from the experiments increased by 31% for simulations using dataset 2.

A plot of percent-linear shrinkage with melt temperature for injection molding experiments and simulations is presented in **Figure 4.9**. Percent linear shrinkages for injection molding experiments with complete mold fill were typically around 0.8% and had a standard deviation of ±0.15. Simulations with

datasets 1-3 predict percent linear shrinkages with reasonable accuracy for process input conditions set according to experiment #1 and #2 (**Table 4.1**). For ceramic-filled polymers, the percent linear shrinkages has been reported to range between 0.4 and 0.8 % [41]. The predicted and experimental values of percent-linear shrinkage are on the same order of magnitude as observed in literature for ceramic-filled polymers.

A plot of injection pressure and melt temperature for injection molding experiments and simulations are presented in **Figure 4.10**. The injection-molding experiments were conducted by setting an injection pressure to a desired value. The feedstock melt was injected at this pressure and a set flow rate of 33 cm^3/s. The PIM simulations also allow setting of a specific value for injection pressure and flow rate. The simulation tries to attain this injection pressure value by filling the mold cavity at the desired flow rate.

Figure 4.10 shows the simulated values for the maximum injection pressure that can be attained during the mold filling process. It can be observed from **Figure 4.10** that simulations with datasets 1-3 underestimate injection pressures by a factor of 30 and 10 for process input conditions set according to experiment #1 and #2 respectively. (**Table 4.1**). For simulations performed with dataset 2 and for process input conditions set according to experiment #3 and #4 (**Table 4.1**), the injection pressure values are close to that of the actual experiments. A cause for this behavior is not presently understood. In the future, simulations using a different PIM simulation software package based on alternative constitutive models need to be studied.

Conclusions

The present study can be used as a design approach to perform PIM simulations by estimating feedstock properties and study a wide variety of material systems The current investigation was found to have the following key attributes:

1. Literature filler properties can be used in conjunction with mixture models to estimate physical, thermal, and rheological properties of AlN feedstocks.

2. Mold-filling behavior for injection molding experiments and PIM simulations are similar for parts that showed 100% mold filling. Short shot predictions using simulations were however not in agreement with injection-molding experiments.

3. Part weight predictions by PIM simulations for injection pressures of 38 and 14 MPa and melt temperature of 455K and 444K respectively, showed reasonably good accuracy with a maximum error of 8%.

4. Percent linear shrinkages for PIM simulations ranged between 0.3-1.4% and showed reasonable agreement with injection molding experiments that ranged between 0.65-0.95%.

5. Injection pressure predictions by simulations are poor and further investigation of PIM simulations using other PIM software packages is needed.

Acknowledgements

The authors thank the financial support obtained from the National Science Foundation (CMMI 1200144).

4.4 References

[1] R. Urval, S. Lee, S. V. Atre, S.-J. Park, and R. M. German, “Optimisation of process conditions in powder injection moulding of microsystem components using a robust design method: part I. primary design parameters,” *Powder Metall.*, vol. 51, no. 2, pp. 133–142, Jun. 2008.

[2] R. Urval, S. Lee, S. V. Atre, S.-J. Park, and R. M. German, “Optimisation of process conditions in powder injection moulding of microsystem components using robust design method Part 2 – Secondary design parameters,” *Powder Metall.*, vol. 53, no. 1, pp. 71–81, Mar. 2010.

[3] J. Kim, S. Ahn, S. V. Atre, S. J. Park, T. G. Kang, and R. M. German, “Imbalance filling of multi-cavity tooling during powder injection molding,” *Powder Technol.*, vol. 257, pp. 124–131, May 2014.

[4] R. K. Enneti, S. J. Park, J. Palagi de Souza, and S. V. Atre, “Critical Issues In Manufacturing Dental Brackets By Powder Injection Molding,” *Int. J. Powder Metall.*, vol. 48, no. 2, pp. 23–39, 2012.

[5] S. Laddha, C. Wu, G. K. lingam, K. Simmons, S. vallury, S. Lee, S. J. Park, R. M. German, P. Vilma, A. Varez, and S. V. Atre, “Characterization of Alumina Feedstock with Polyacetal and Wax-Polymer Binder Systems for Micro Powder Injection Moulding,” *PIM International*, vol. 3, no. 3, pp. 64–70, 2009.

[6] S. J. Park, S. Y. Ahn, T. G. Kang, S. T. Chung, Y. S. Kwon, S. Chung, S. G. Kim, S. Kim, S. V. Atre, S. Lee, and R. M. German, “Computer Simulations in Powder Injection Molding,” *Int. J. Powder Metall.*, vol. 46, no. 3, pp. 37–46, 2010.

[7] R. Urval, C. Wu, S. V. Atre, S. J. Park, and R. M. German, “CAE-Based Process Design for Microfluidic Components,” Powder Injection Molding Internationa,” *PIM International*, no. I, pp. 48–54, 2007.

[8] S. Laddha, C. Wu, S. J. Park, S. Lee, S. Ahn, R. M. German, and S. V. Atre, “Analysis of Macroscale Mold Filling Defects in Micro Powder Injection Molding,” *Int. J. Powder Metall.*, vol. 46, no. 3, pp. 49–59, 2010.

[9] S. V. Atre, S.-J. Park, R. Zauner, and R. M. German, “Process simulation of powder injection moulding: identification of significant parameters during mould filling phase,” *Powder Metall.*, vol. 50, no. 1, pp. 76–85, Mar. 2007.

[10] S. Ahn, S. T. Chung, S. V. Atre, S. J. Park, and R. M. German, “Integrated filling, packing and cooling CAE analysis of powder injection moulding parts,” *Powder Metall.*, vol. 51, no. 4, pp. 318–326, Dec. 2008.

[11] S. W. Lee, S. Ahn, C. J. Whang, S. J. Park, S. V. Atre, J. Kim, and R. M. German, “Effects of process parameters in plastic, metal, and ceramic injection molding processes,” *Korea-Aust. Rheol. J.*, vol. 23, no. 3, pp. 127–138, Sep. 2011.

[12] S. Ahn, S. J. Park, S. Lee, S. V. Atre, and R. M. German, “Effect of powders and binders on material properties and molding parameters in iron and stainless steel powder injection molding process,” *Powder Technol.*, vol. 193, no. 2, pp. 162–169, Jul. 2009.

[13] K. H. Kate, R. K. Enneti, S.-J. Park, R. M. German, and S. V. Atre, “Predicting Powder-Polymer Mixture Properties for PIM Design,” *Crit. Rev. Solid State Mater. Sci.*, vol. 39, no. 3, pp. 197–214, Mar. 2014.

[14] K. H. Kate, R. K. Enneti, V. P. Onbattuvelli, and S. V. Atre, “Feedstock properties and injection molding simulations of bimodal mixtures of nanoscale and microscale aluminum nitride,” *Ceram. Int.*, vol. 39, no. 6, pp. 6887–6897, Aug. 2013.

[15] K. H. Kate, V. P. Onbattuvelli, R. K. Enneti, S. W. Lee, S.-J. Park, and S. V. Atre, “Measurements of Powder–Polymer Mixture Properties and Their Use in Powder Injection Molding Simulations for Aluminum Nitride,” *JOM*, vol. 64, no. 9, pp. 1048–1058, Sep. 2012.

[16] J. Lenz, R. K. Enneti, V. Onbattuvelli, K. Kate, R. Martin, and S. Atre, “Powder Injection Molding of Ceramic Engine Components for Transportation,” *JOM*, vol. 64, no. 3, pp. 388–392, Mar. 2012.

[17] K. H. Kate, M. Winseck, R. K. Enneti, R. M. German, and S. V. Atre, “Material Property Design in Ceramic Injection Molding,” *Manuscr. Prep. Int. Mater. Rev.*, 2015.

[18] K. H. Kate, R. K. Enneti, and S. V. Atre, “Influence of feedstock property measurements and estimates on ceramic injection molding simulations for aluminum nitride,” *Manuscr. Prep.*, 2015.

[19] V. P. Onbattuvelli, R. K. Enneti, S.-J. Park, and S. V. Atre, “The effects of nanoparticle addition on SiC and AlN powder–polymer mixtures: Packing and flow behavior,” *Int. J. Refract. Met. Hard Mater.*, vol. 36, pp. 183–190, Jan. 2013.

[20] V. P. Onbattuvelli, “The effects of nanoparticle addition on the processing, structure and properties of SiC and AlN,” 2010.

[21] M. F. Ashby, *Materials Selection in Mechanical Design*. Butterworth-Heinemann, 2010.

[22] J. R. Groza and A. Zavaliangos, “Sintering activation by external electrical field,” *Mater. Sci. Eng. A*, vol. 287, no. 2, pp. 171–177, Aug. 2000.

[23] K. Biswas, J. Schneider, G. Rixecker, and F. Aldinger, “Comparative bending creep behaviour of silicon carbide sintered with oxynitride additives,” *Scr. Mater.*, vol. 53, no. 5, pp. 591–596, Sep. 2005.

[24] J. Gu, Q. Zhang, J. Dang, J. Zhang, and Z. Yang, “Thermal conductivity and mechanical properties of aluminum nitride filled linear low-density polyethylene composites,” *Polym. Eng. Sci.*, vol. 49, no. 5, pp. 1030–1034, May 2009.

[25] R. Kochetov, T. Andritsch, U. Lafont, P. H. F. Morshuis, S. J. Picken, and J. J. Smit, “Preparation and dielectric properties of epoxy - BN and epoxy - AlN nanocomposites,” in *IEEE Electrical Insulation Conference, 2009. EIC 2009*, 2009, pp. 397–400.

[26] W. Zhou, “Thermal and dielectric properties of the AlN particles reinforced linear low-density polyethylene composites,” *Thermochim. Acta*, vol. 512, no. 1–2, pp. 183–188, Jan. 2011.

[27] B. L. Zhu, J. Ma, J. Wu, K. C. Yung, and C. S. Xie, “Study on the properties of the epoxy-matrix composites filled with thermally conductive AlN and BN ceramic particles,” *J. Appl. Polym. Sci.*, vol. 118, no. 5, pp. 2754–2764, Dec. 2010.

[28] S. H. Risbud, J. R. Groza, and M. J. Kim, “Clean grain boundaries in aluminium nitride ceramics densified without additives by a plasma-activated sintering process,” *Philos. Mag. Part B*, vol. 69, no. 3, pp. 525–533, 1994.

[29] K. A. Khor, K. H. Cheng, L. G. Yu, and F. Boey, “Thermal conductivity and dielectric constant of spark plasma sintered aluminum nitride,” *Mater. Sci. Eng. A*, vol. 347, no. 1–2, pp. 300–305, Apr. 2003.

[30] M. Medraj, “Understanding AlN sintering through computational thermodynamics combined with experimental investigation,” *J. Mater. Process. Tech*, vol. 161, no. 3, pp. 415–422.

[31] L. Qiao, H. Zhou, and R. Fu, “Thermal conductivity of AlN ceramics sintered with CaF2 and YF3,” *Ceram. Int.*, vol. 29, no. 8, pp. 893–896, 2003.

[32] F. Miyashiro, N. Iwase, A. Tsuge, F. Ueno, M. Nakahashi, and T. Takahashi, “High thermal conductivity aluminum nitride ceramic substrates and packages,” *IEEE Trans. Compon. Hybrids Manuf. Technol.*, vol. 13, no. 2, pp. 313–319, 1990.

[33] V. Onbattuvelli and S. Atre, “Review of Net Shape Fabrication of Thermally Conducting Ceramics,” *Mater. Manuf. Process.*, vol. 26, no. 6, pp. 832–845, Jun. 2011.

[34] “Granta’s CES EduPack and teaching resources: supporting Materials Education.” [Online]. Available: http://www.grantadesign.com/education/. [Accessed: 27-Sep-2013].

[35] W. M. Haynes, *CRC Handbook of Chemistry and Physics, 95th Edition*. CRC Press, 2014.

[36] P. U. T. P. R. Center, *Thermophysical Properties of Matter: Specific heat: metallic elements and alloys, by Y. S. Touloukian and E. H. Buyco*. IFI/Plenum, 1970.

[37] T. B. Jackson, A. V. Virkar, K. L. More, R. B. Dinwiddie, and R. A. Cutler, “High-Thermal-Conductivity Aluminum Nitride Ceramics: The Effect of Thermodynamic, Kinetic, and Microstructural Factors,” *J. Am. Ceram. Soc.*, vol. 80, no. 6, pp. 1421–1435, Jun. 1997.

[38] J.-W. Bae, W. Kim, S.-H. Cho, and S.-H. Lee, “The properties of AlN-filled epoxy molding compounds by the effects of filler size distribution,” *J. Mater. Sci.*, vol. 35, no. 23, pp. 5907–5913, Dec. 2000.

[39] M. Bauccio, *ASM engineered materials reference book*. ASM International, 1994.

[40] H. Nakano, K. Watari, H. Hayashi, and K. Urabe, “Microstructural Characterization of High-Thermal-Conductivity Aluminum Nitride Ceramic,” *J. Am. Ceram. Soc.*, vol. 85, no. 12, pp. 3093–3095, Dec. 2002.

[41] W. J. Smothers, *1981 New England Section Topical Meeting on Nonoxide Ceramics: Ceramic Engineering and Science Proceedings, Volume 3, Number 1/2*. John Wiley & Sons, 2009.

4.5 List of Tables

4.7 List of Figures

Table 4.1. Models used in present study to estimate the feedstock properties

property	empirical relations	#
density	$\frac{1}{\rho_c} = \frac{X_b}{\rho_{b\,exp}} + \frac{X_p}{\rho_p}$	1
volume fraction	$\phi_p = \frac{X_p/\rho_p}{X_p/\rho_p + X_b/\rho_{b\,exp}}$	2
	$\phi_b = \frac{X_b/\rho_b}{X_p/\rho_p + X_b/\rho_{b\,exp}}$	3
specific heat	$C_{p_c} = \left[C_{p_{b\,exp}} X_b + C_{p_p} X_p\right] * \left[1 + A * X_b X_p\right]$	4
thermal conductivity	$1 - \phi_p = \left(\frac{\lambda_p - \lambda_c}{\lambda_p - \lambda_{b\,exp}}\right)\left(\frac{\lambda_b}{\lambda_c}\right)^{1/3}$	5
viscosity	$\eta_c = \frac{\eta_{b\,exp}}{\left[1 - \frac{\phi_c}{\phi_{max}}\right]^2}$	6
	$\eta_c = \frac{\eta_0}{1 + \left(\frac{\eta_0 \gamma}{\tau^*}\right)^{1-n}}$	7
	$\eta_0 = D_1 exp\left[-\frac{A_1(T - T^*)}{A_2 + (T - T^*)}\right]$	8
specific volume	$v_c = X_p v_{\,p} + v_{b\,exp}(1 - X_p)$	9
	$v(T,p) = v_o(T)\left[1 - Cln\left(1 + \frac{p}{B(T)}\right) + v_t(T,p)\right]$	10
	for T>T_t $v_o = b_{1m} + b_{2m}(T - b_5); \quad B(T) = b_{3m} e^{[-b_{4m}(T - b_5)]};$ $v_t(T,p) = 0$	11
	for T<T_t; $v_o = b_{1s} + b_{2s}(T - b_5); \quad B(T) = b_{2s} e^{[-b_{4s}(T - b_5]};$ $v_t(T,p) = b_7 e^{[b_8(T - b_5) - (b_9 p)]}$	12
	$T_t(p) = b_5 + b_6(p)$	13

Table 4.2. Description of symbols used in the paper

symbol	description
T_m	melt temperature
X_c	mass fraction of feedstock
X_b	mass fraction of binder
X_p	mass fraction of filler
ρ_c	density of feedstock
ρ_b	measured density of binder
ρ_p	density of filler
$\rho_{c\,est}$	estimated average density of feedstock
C_{p_c}	specific heat of feedstock
$C_{p_{b\,exp}}$	measured specific heat of binder
C_{p_p}	specific heat of filler
A	=0.2 fitting constant for spherical powders
$C_{p_{c\,est}}$	estimated average specific heat of feedstock
λ_c	thermal conductivity of feedstock
$\lambda_{b\,exp}$	measured thermal conductivity of binder
λ_p	thermal conductivity of filler
$\lambda_{c\,est}$	estimated average thermal conductivity of feedstock
ϕ_c	volume fraction of feedstock
ϕ_b	volume fraction of binder
ϕ_p	volume fraction of filler

Table 4.2 Continued. Description of symbols used in the paper

symbol	description
$\eta_{b\ exp}$	viscosity of binder
η_c	viscosity of feedstock
ϕ_{max}	(0.64) volume fraction of critical solids loading of feedstock
$\eta_{c\ est}$	estimated average viscosity of feedstock at ϕ_{max} =0.64
η_0	is the zero shear viscosity
γ	shear rate
τ^*	critical stress level at the transition to shear thinning determined by curve fitting
n	power law index in the high shear rate regime
T	temperature
$T^*\ D_1\ and\ A_1$	curve fitted coefficients
A_2	(51.6 K) WLF constant
υ_c	specific volume of feedstock
$\upsilon_{b\ exp}$	measured specific volume of binder
υ_p	specific volume of filler
$\nu_{c\ est}$	estimated average specific volume of feedstock
$\upsilon\ (T\ p)$	specific volume at a given temperature and pressure
υ_o	specific volume at zero gauge pressure
p	pressure
C	(0.0894) constant
$b_{1s}\ b_{2s}\ b_{3s}\ b_{4s}$ $b_5\ b_7\ b_8\ and\ b_9$	curve-fitted coefficients
$b_{1m}\ b_{2m}\ b_{3m}$ $b_{4m}\ b_5\ and\ b_6$	curve-fitted coefficients
$B\ (T)$	pressure sensitivity material as a function of temperature

Table 4.3. Molding parameters for AlN tensile geometry

molding parameters	experiment number, #			
	# 1	# 2	# 3	# 4
mold temperature, K	297	297	297	297
melt temperature, K	444	433	422	455
injection speed, cm^3/s	33	33	33	33
injection pressure, MPa	14	14	14	38
packing pressure 1, MPa for 1 s	14	14	14	38
packing pressure 2, MPa for 1.2 s	9	9	9	25

*variation in temperature profile; **variation in pressure profile

Table 4.4. Density of the AlN feedstock and wax-polymer binder at 300 K

density, m^3/kg	$\rho_{c\,\mathrm{exp}}{}^{*}$	$\rho_{c\,\mathrm{est}}{}^{+}$
solid	**2150**	2130±20
melt	**1940**	1940±20

*measured experimentally; +estimated using **Equation 4.1** for 22 data points of ρ_p

Table 4.5. Specific heat of the AlN feedstock and wax-polymer binder for temperature between 283 and 423 K

specific heat C_p, J/kg-K	temperature, K				
	283	298	331	374	423
$C_{p_{c\ \mathrm{exp}}}{}^{*}$	**920**	**1110**	**1090**	**1130**	**1210**
$C_{p_{c\ \mathrm{est}}}{}^{+}$	1050±35	1240±35	1570±35	1850±35	1150±35

*measured experimentally; +estimated using **Equation 4.4** for 6 data points of C_{p_p}

Table 4.6. Thermal conductivity of AlN feedstock and wax-polymer binder for temperature between 316 and 436 K

thermal conductivity, W/m-K	temperature, K				
	316	356	377	397	436
$\lambda_{c\ \mathrm{exp}}{}^{*}$	**4.26**	**2.23**	**2.66**	**2.06**	**2.50**
$\lambda_{c\ \mathrm{est}}{}^{+}$	1.82 ±0.01	1.71 ±0.01	1.67 ±0.06	1.62 ±0.08	1.55 ±0.10

*measured experimentally; +estimated using **Equation 4.5** for 18 data points of λ_p

Table 4.7. Viscosity of the AlN feedstock as a function of shear rate between 10^1 and 10^4 s^{-1} for a temperature range of 415 to 430 K

shear rate s^{-1}	viscosity η_c, Pa.s @ ϕ_{max} = 0.64					
	T = 415 K		T = 425 K		T = 430 K	
	$\eta_{c\ exp}$*	$\eta_{c\ est}$+	$\eta_{c\ exp}$*	$\eta_{c\ est}$+	$\eta_{c\ exp}$*	$\eta_{c\ est}$+
10^1	**1470**	4830	**1380**	1330	**1340**	660
10^2	**350**	1460	**330**	540	**320**	890
10^3	**80**	390	**80**	160	**80**	100
10^4	**20**	100	**20**	40	**20**	30

*measured experimentally; +estimated using **Equation 4.6**

Table 4.8. Cross-WLF constants for the AlN feedstock

Cross WLF constants	$\eta_{c\ exp}$*	$\eta_{c\ est}$+
n	**0.38**	0.40
τ*, Pa	**180**	26860
D_1, Pa.s	**$8.78X10^{10}$**	$2.23X10^{15}$
D_2, K	**263**	360.93
A_1, K/Pa	**14.24**	49.55
A_2, K	**51.60**	51.60

*calculated from **Equation 4.7, 8** and experimental (η_c) values from **Table 4.7**;
+calculated from **Equation 4.7, 8** and estimated (η_c) values from **Table 4.7**

Table 4.9. Specific volume of the AlN feedstock as a function of pressure between 0 MPa and 200 MPa for a temperature range of 300 to 450 K

temperature, K	specific volume X10^{-3}, m^3/kg					
	P = 0 MPa		P = 100 MPa		P = 200 MPa	
	$v_{c\ exp}$*	$v_{c\ est}$+	$v_{c\ exp}$*	$v_{c\ est}$+	$v_{c\ exp}$	$v_{c\ est}$+
300	**0.47**	0.48	**0.46**	0.47	**0.45**	0.46
350	**0.49**	0.50	**0.48**	0.49	**0.46**	0.47
400	**0.50**	0.51	**0.49**	0.50	**0.47**	0.49
450	**0.52**	0.53	**0.50**	0.50	**0.48**	0.49

*measured experimentally; +estimated using **Equation 4.9**

Table 4.10. Dual-domain Tait constants for the AlN feedstock

Dual-domain Tait constants	$\nu_{c\ exp}$ *	$\nu_{c\ est}$ +
b_5, K	**331**	331
b_6, K/Pa	**1.30X10^{-7}**	1.30X10^{-7}
b_{1m}, m^3/kg	**4.64X10^{-4}**	5.77X10^{-4}
b_{2m}, m^3/kg.K	**1.87X10^{-7}**	1.95X10^{-7}
b_{3m}, Pa	**2.05X10^{9}**	2.17X10^{9}
b_{4m}, 1/K	**4.60X10^{-3}**	6.15X10^{-3}
b_{1s}, m^3/kg	**4.55X10^{-4}**	5.69X10^{-4}
b_{2s}, m^3/kg.K	**2.05X10^{-7}**	2.05X10^{-7}
b_{3s}, Pa	**2.52X10^{9}**	1.63X10^{9}
b_{4s}, 1/K	**3.01X10^{-3}**	6.35X10^{-3}
b_7, m^3/kg	**5.08X10^{-5}**	5.34X10^{-5}
b_8, 1/K	**8.54X10^{-1}**	8.97X10^{-1}
b_9, 1/Pa	**5.06X10^{-6}**	3.53X10^{-5}

*calculated from **Equation 4.10-13** and experimental (ν_c) values from **Table 4.9**;
+calculated from **Equation 4.1-13** and estimated (ν_c) values from **Table 4.9**

Table 4.11. AlN feedstock dataset used for injection molding simulations

AlN feedstock dataset	density* ρ_c, kg/m^3	specific heat** C_{p_c}, J/kg-K	thermal conductivity+ λ_c, W/m-K	Cross WLF constants++	Dual-domain Tait constants*+
1	$\rho_{c\ exp}$	$C_{p_{c\ exp}}$	$\lambda_{c\ exp}$	$\eta_{c\ exp}$	$\nu_{c\ exp}$
2	$\rho_{c\ est}$	$C_{p_{c\ est}}$	$\lambda_{c\ est}$	$\eta_{c\ est}$	$\nu_{c\ est}$
3	$\rho_{c\ est}$	$C_{p_{c\ est}}$	$\lambda_{c\ est}$	$\eta_{c\ exp}$	$\nu_{c\ est}$

*data from **Table 4.4**; **data from **Table 4.5**; +data from **Table 4.6;**
++data from **Table 4.8**; and *+data from **Table 4.10**

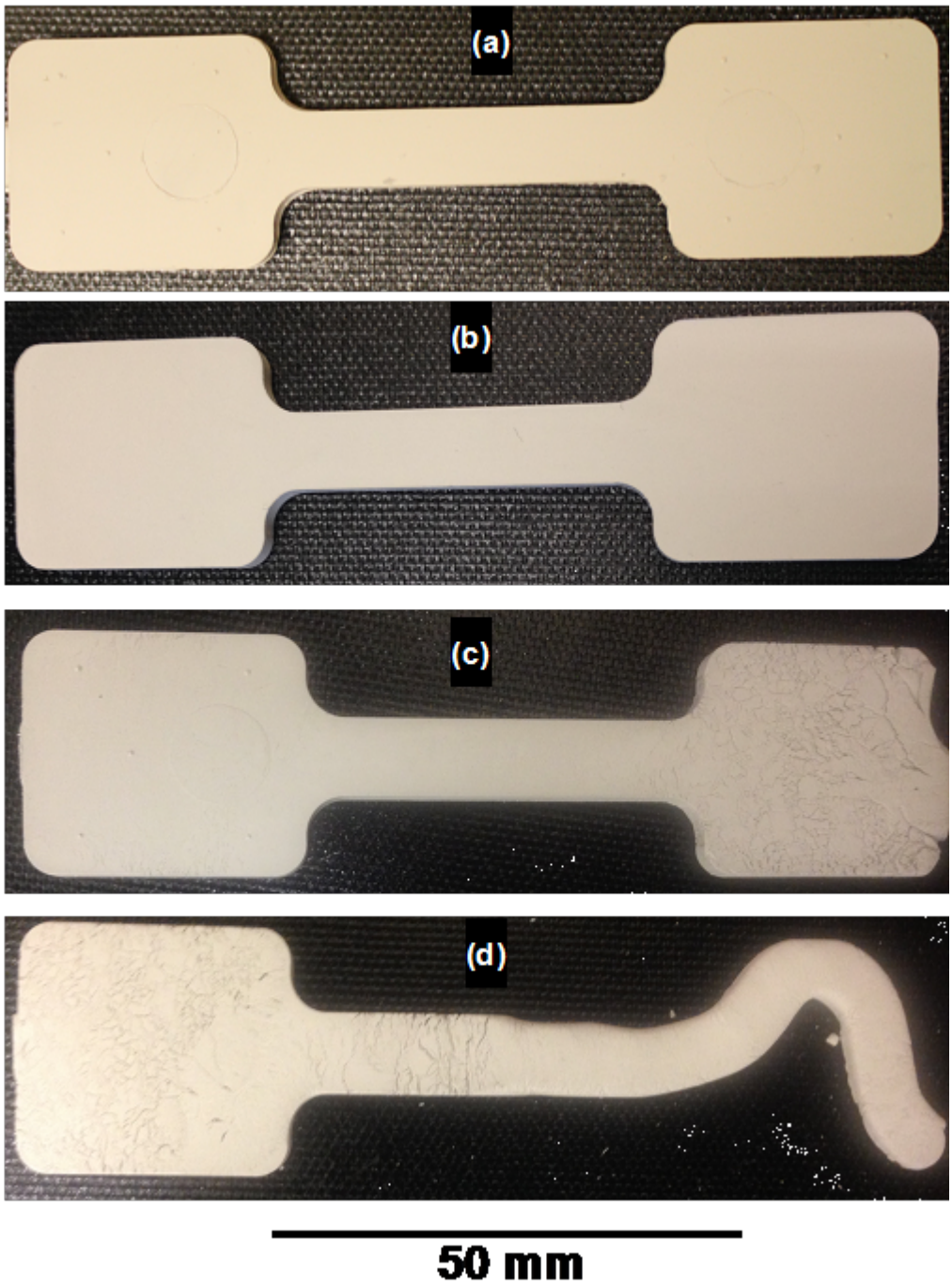

Figure 4.1. Injection molded AlN tensile bar geometry for (a) experiment # 1 with 100% mold fill, (b) experiment # 2 with 89% mold fill, (c) experiment # 3 with 71% mold fill, and (d) experiment # 4 with 100% mold fill.

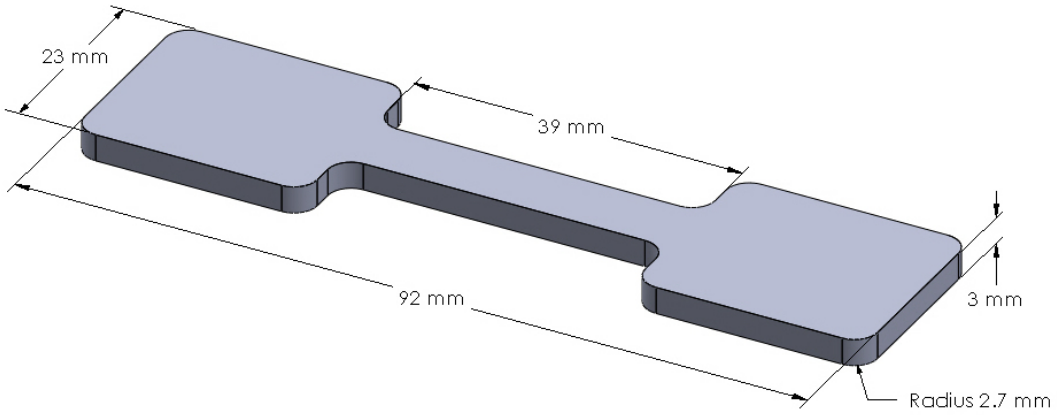

Figure 4.2. Tensile bar geometry used for injection molding experiments and simulations.

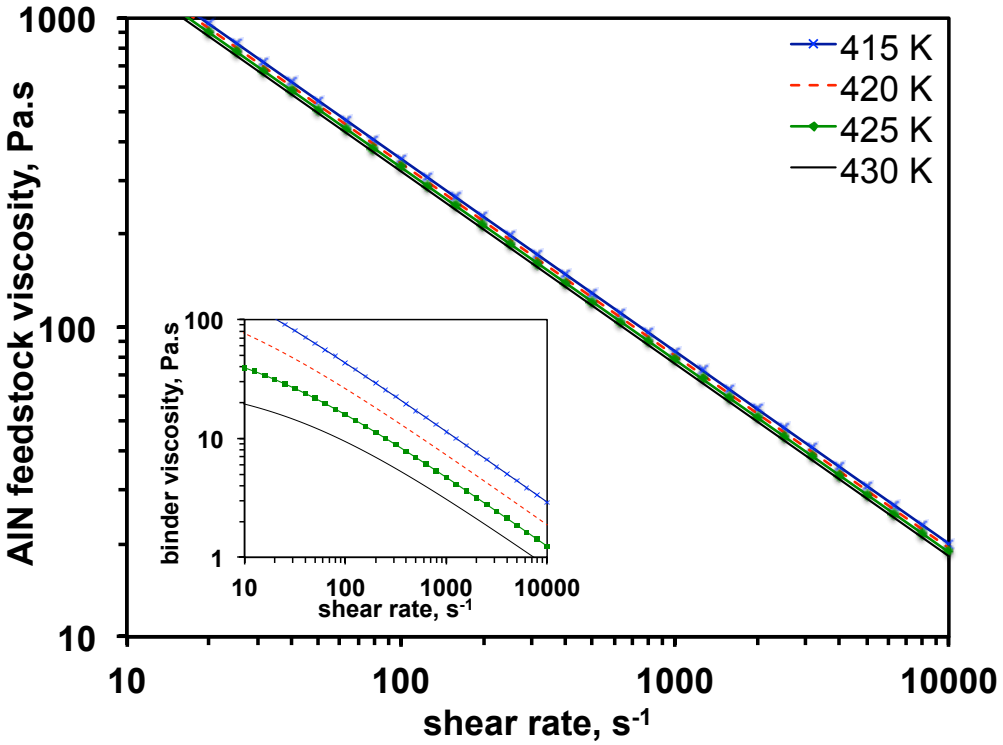

Figure 4.3. Viscosity of AlN feedstock and wax-polymer binder (inset) for a shear rate range of 10 to $10^4 s^{-1}$ and temperatures between 415 and 430 K.

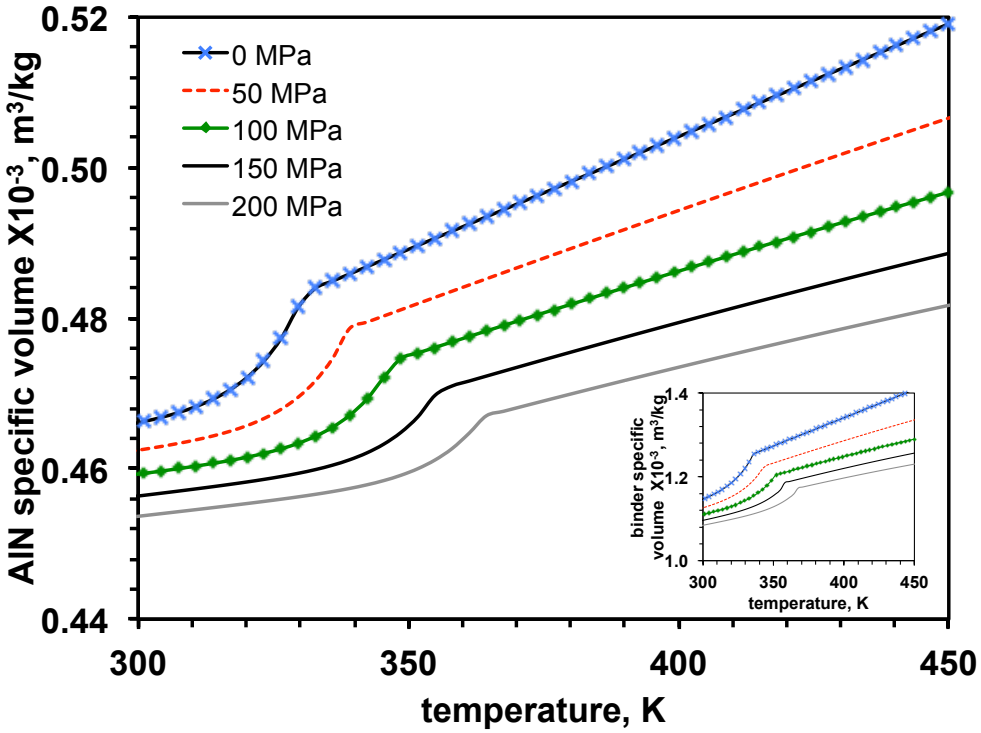

Figure 4.4. Specific volume of AlN feedstock for a temperature range of 300 to 450 K and pressures between 0 and 200 MPa

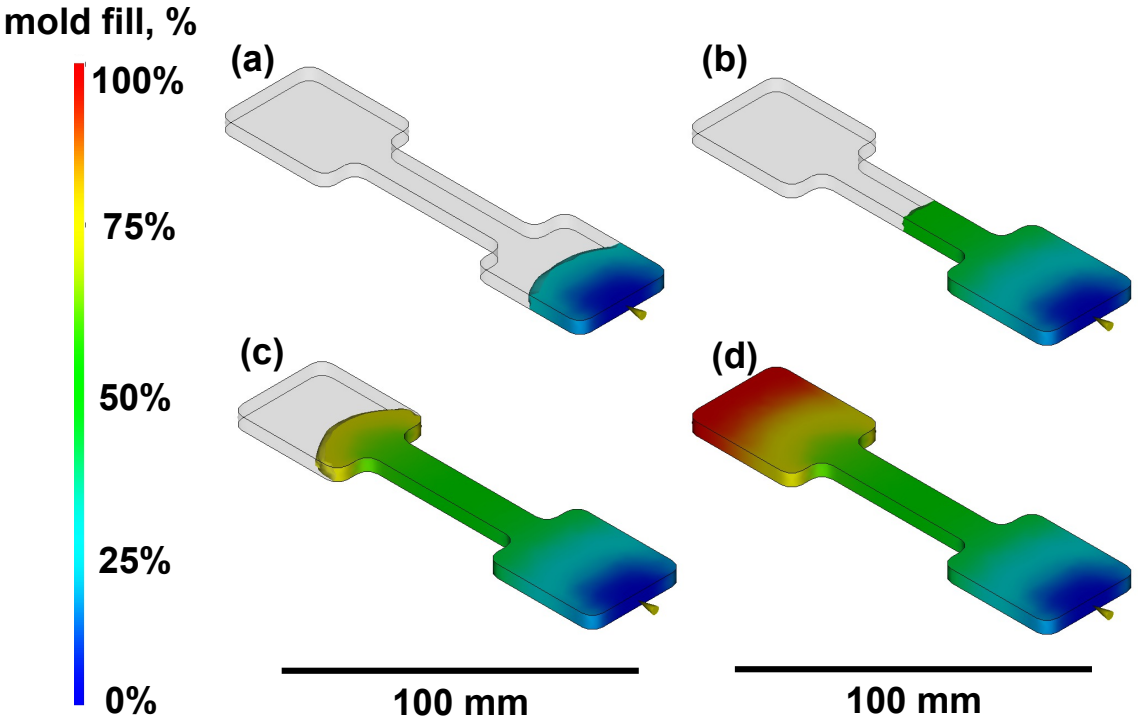

Figure 4.5. Progressive mold filling behavior for simulations performed with dataset 1 at an injection pressure of 38MPa. Progressive fill patterns for (a) 25% mold fill (b) 50% mold fill (c) 75% mold fill, and (d) 100% mold fill

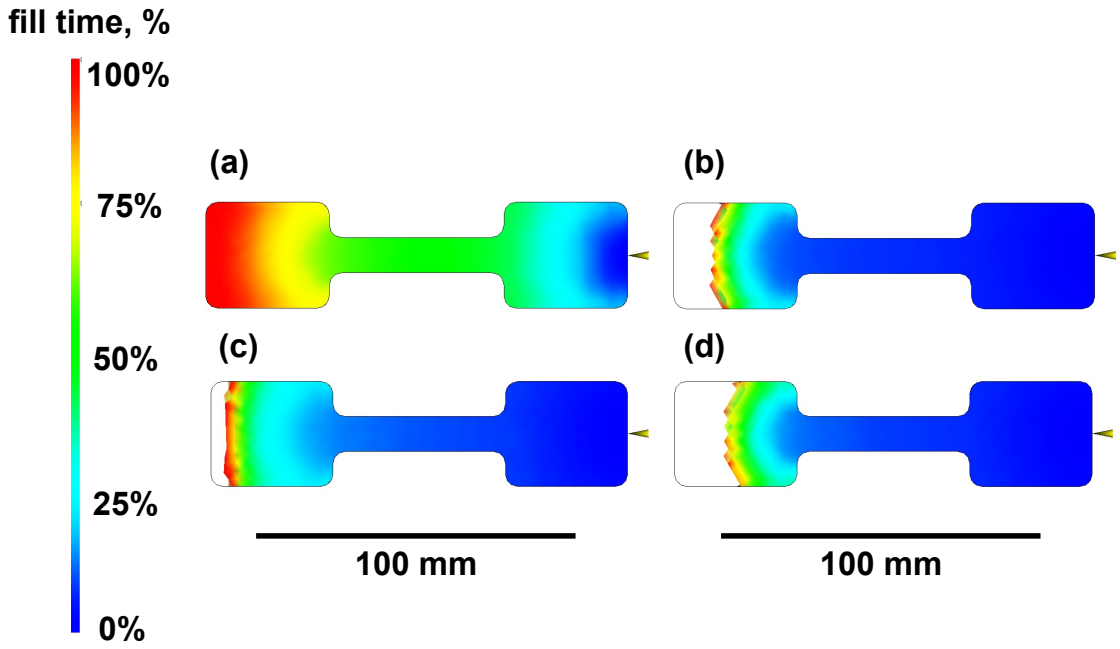

Figure 4.6. Mold fills for AlN tensile geometry for (a) simulations for dataset 1 at 444 K melt temperature with 100 % mold fill (b) simulations for dataset 1 at 330 K melt temperature with 89 % mold fill (c) simulations for dataset 2 at 430 K melt temperature with 97 % mold fill, (d) simulations for dataset 3 at 330 K melt temperature with 84 % mold fill

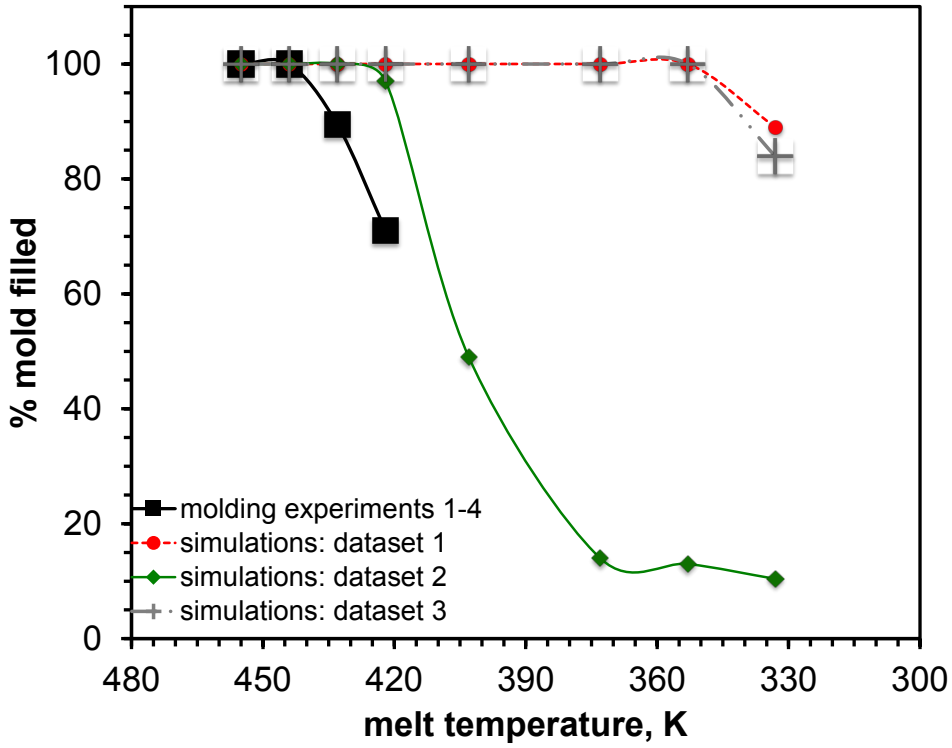

Figure 4.7. Melt temperature versus percent mold fill for injection molding experiments 1-4 and simulations

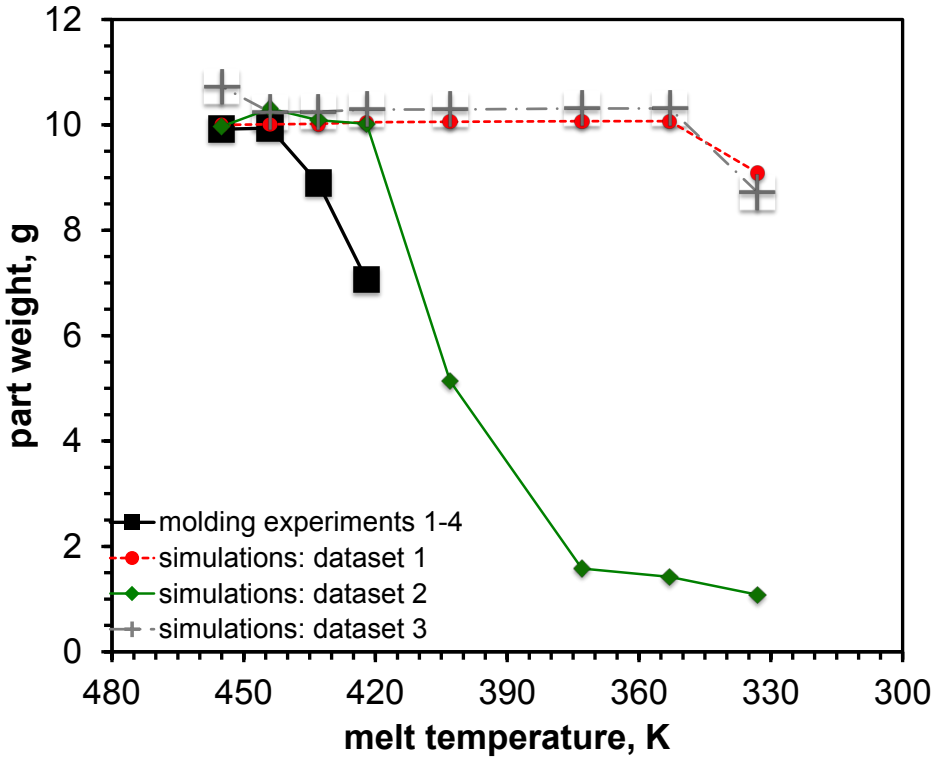

Figure 4.8. Melt temperature versus part weight for injection molding experiments 1-4 and simulations

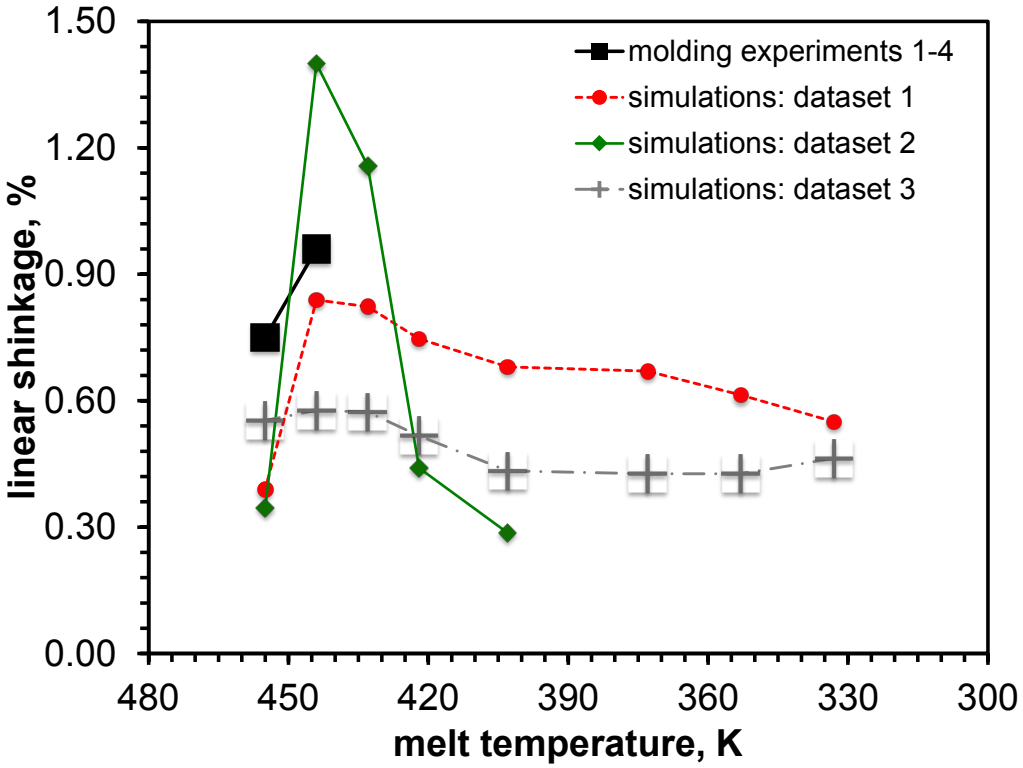

Figure 4.9. Melt temperature versus percent linear shrinkage for injection molding experiments 1-4 and simulations

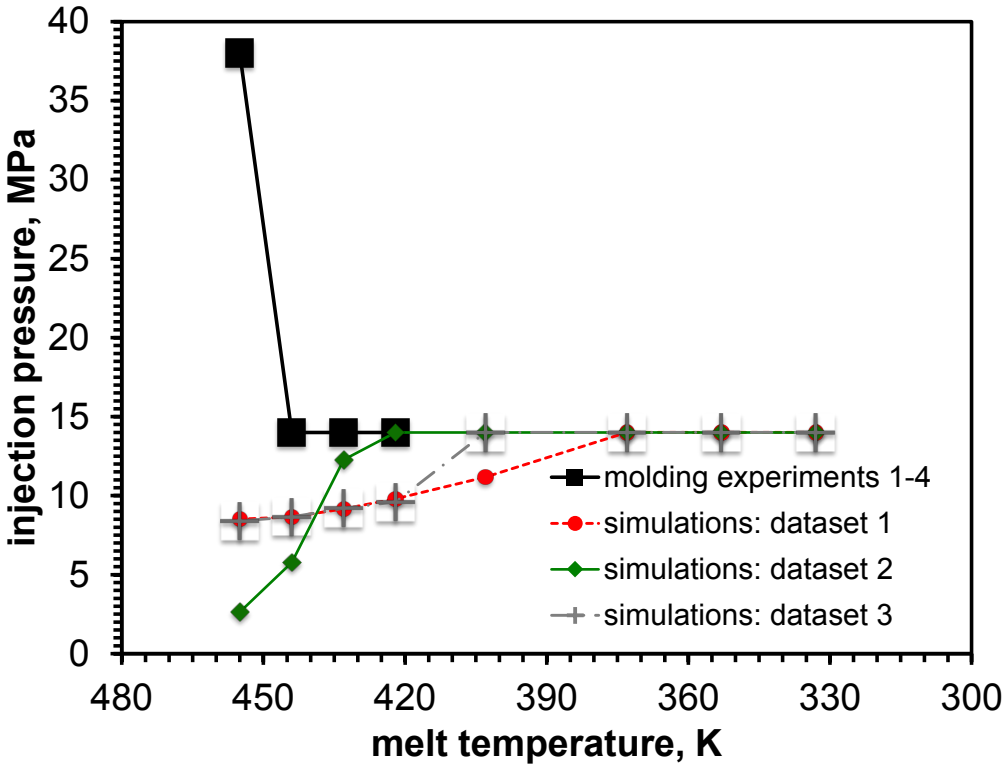

Figure 4.10. Melt temperature versus injection pressure for injection molding experiments 1-4 and simulations

Chapter 5: Conclusions and Future Work

5.1 Conclusions

The present study provides a design methodology that can be used to estimate critical feedstock properties for a variety of material systems and to perform ceramic injection molding (CIM) simulations. The method developed in the present study was found to have the following key attributes:

1. Literature filler properties can be used in conjunction with mixture models to estimate physical, thermal, and rheological properties for nine different ceramic feedstocks that constitute the majority of ceramics used in CIM.
    a. Regression analysis indicated the suitability of models for estimating material properties such as density, specific heat capacity, specific volume, and viscosity.
    b. Additional experimentation and model development will be required for properties such as thermal conductivity and viscosity.
2. Comparative mold filling simulations performed for an aluminum nitride (AlN) feedstock using a set of process input parameters and heat-sink substrate geometries identified the differences between estimated and experimental values of feedstock properties that contributed the most to variations in the predictions from PIM simulations.
    a. The mold filling simulations for the AlN feedstock results clearly indicate that a scatter in feedstock property estimates showed no sensitivity towards predicting mold filling behavior and defect evolutions.
    b. Part weight, volumetric shrinkage, and packing time output parameters can be predicted with reasonably good accuracy and an error ranging from 1 to 6%.
    c. Injection pressure and clamp force are overestimated by a factor of 10 indicating that a further improvement in the estimation of viscosity is needed.

3. Comparative injection molding experiments and simulations performed for the AlN feedstock helped identify the effectiveness of using CIM simulations to predict mold filling behavior.
    a. Mold filling behavior for injection molding experiments and CIM simulations are similar for parts that showed 100% mold filling. Short shot predictions using simulations were however not in agreement with injection-molding experiments.
    b. Part weight predictions by CIM simulations for completely filled parts showed reasonably good accuracy with a maximum error of 8%.
    c. Percent linear shrinkages for the CIM simulations showed reasonable agreement with injection molding experiments and ranged between 0.3-1.4%
    d. Injection pressure predictions by simulations are poor and further investigation of CIM simulations using other software packages is needed.

5.2 Future work

5.2.1 Method to estimate viscosity of ceramic feedstocks for CIM simulations

Viscosity measurements are required in injection molding simulations to understand the flow characteristics of the feedstock melt. It is one of most important properties required to predict output parameters such as injection pressure and clamp force. A Simplified Krieger Dougherty model can be used to estimate viscosity for various ceramic feedstock as discussed in **Chapter 2**.

The coefficient of determination (R^2) value of 0.6 supports the general applicability of the approach to predict the viscosity of PIM feedstocks but pressure related output parameters in PIM simulations like injection pressure and clamp force are overestimated by a factor of 10. Improvements in viscosity predictions are necessary in order to predict pressure related output parameters with higher accuracy. A procedure to estimate viscosity and maximum filler

content (ϕ_{max}) for a range of shear rates and temperatures is discussed in **Appendix C**. It can be observed from **Appendix C** calculations that ϕ_{max} increases with increase in shear rate. One way to improve viscosity estimations based on this observation is to use a range of ϕ_{max} values across all shear rate and temperature ranges. Further investigations on extracting ϕ_{max} for a variety of PIM feedstock and comparing their sensitivity to compositions will help improve viscosity predictions.

To perform mold-filling simulations, the viscosity had to be represented in terms of fitted constants. A Cross-WLF equation (**Chapter 3**) can be used to extract constants from viscosity data. There are no detailed reports on how viscosity for PIM feedstocks (measured or estimated) and the required Cross-WLF constants are determined. As an example, a detailed procedure to extract WLF constant is discussed in **Appendix C.** Further work on extracting WLF constants for a variety of PIM feedstocks and comparing their sensitivities to their compositions will help improve their predictions.

5.2.2 Method to estimate PVT parameters of ceramic feedstock for CIM simulations

Specific volume measurements are required in injection molding simulations to calculate the shrinkage that occurs when a feedstock is cooled from melt temperature to ambient temperature. To estimate specific volume for a range of temperatures and pressures of ceramic feedstock a simple empirical equation can be used as discussed in **Chapter 3.**

To perform mold-filling simulations, the specific volume of the ceramic feedstock needs to be represented in terms of fitted constants. A Dual-domain Tait equation can used to extract these fitted constants (**Appendix D)**

There are no detailed reports on how the viscosity for PIM feedstocks (measured or estimated) and the required Dual-domain Tait are determined. Further work on extracting Dual-domain Tait constants for a variety of PIM

feedstocks and comparing their sensitivities to their compositions will help improve their predictions.

5.2.3 Injection molding of complex geometries for aluminum nitride and variation in powder size distribution

Two factors that were kept constant in the current work were the use of a simple tensile geometry and an AlN feedstock with a single powder size distribution. In order to study the effect of shape complexity a prototype micro-channel featured part and a heat sink geometry having an array of fins were injection molded. (**Figure 5.1**)

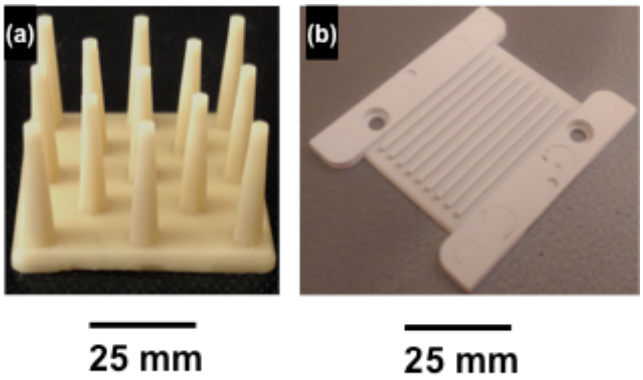

Figure 5.1. Protoype injection molded AlN injection molded parts (a) a heat sink substrate with hexagonal fins (b) a micro-channel heat sink part

Further experiments on injection molding the complex geometries shown in **Figure 5.1** need to be performed. To study the effect of a variation in powder size distribution, an AlN feedstock with bimodal distribution will be compounded and injection molded in the future.

5.2.4 Effect of sintering additives on final part properties of AlN injection molded parts

In addition to the CIM design methodology discussed in the previous section, achieving a high sintered density is crucial to obtaining desired final part properties. The addition of sintering additives is one way in which high sintered densities can be achieved.[1] The addition of Y_2O_3 as a sintering aid has previously been identified in our research group as a promising candidate to

achieve higher sintered densities in injection molded AlN. However, there are few studies focused on understanding the effect of varying the amount of Y_2O_3 on sintered densities and thermal properties of AlN.[1], [2] In this work, the effect of varying sintering conditions and sintering aids on the properties of injection molded AlN will be studied. AlN feedstocks with 0, 3 and 5 wt.% Y_2O_3 added were extruded using a twin-screw extruder. The AlN feedstock was further injection molded into tensile geometries as presented in **Figure 5.2.**

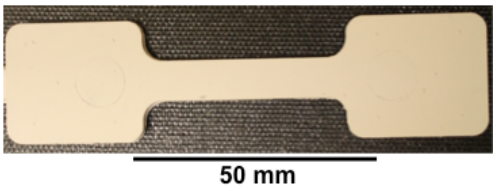

Figure 5.2. AlN injection molded tensile geometry

Sintering of the injection molded AlN parts will be conducted for different time-temperature conditions. Sintered property measurements will be performed to study the influence of sintering aid and sintering conditions on AlN injection molded final part properties. Further sintering experiments need to be performed to understand the influence of varying amount of sintering additives has on microstructure, sintering behavior, and properties.

5.2.5 Micro-scale features on AlN injection molded parts

This work focuses on the feasibility and effectiveness of fabrication of three-dimensional (3D) micro-scale features on ceramics by combining the green micromachining (GMM) and CIM processes. In this work, injection molded AlN parts were green micro-machined **(Figure 5.3)** by Dr. Ozdoganlar's research group at Carnegie Mellon University.

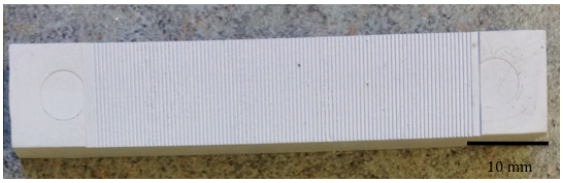

Figure 5.3. AlN green micro-machined part

The GMM parts were received and sintered at different times and temperatures to study the influence of micro-features and green micro machining on final part quality. **Figure 5.4** shows a scanning electron microscope (SEM) image of a typical green micro-machined AlN part.

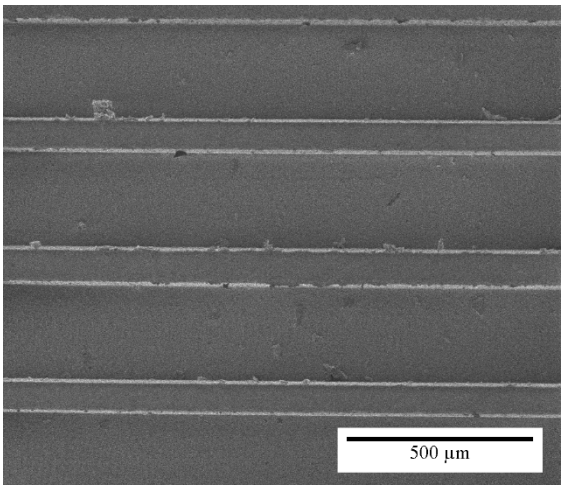

Figure 5.4. SEM image of a typical injection molded AlN micro-machined part sintered 1700^{o}C for 1 hour in N_2

Further experimentation on sintering time-temperature conditions needs to be performed to understand the influence of sintering conditions on defect evolutions and shape retentions of the mirco-scale features and properties. Additional SEM images of GMM parts can be found in **Appendix E.**

5.3 References

[1] V. P. Onbattuvelli, “The effects of nanoparticle addition on the processing, structure and properties of SiC and AlN,” 2010.

[2] M. Medraj, “Understanding AlN sintering through computational thermodynamics combined with experimental investigation,” *J. Mater. Process. Tech*, vol. 161, no. 3, pp. 415–422.

BIBLIOGRAPHY

Bibliography

[1] R. M. German and A. Bose, *Injection Molding of Metals and Ceramics*. Metal Powder Industries Federation, 1997.

[2] Jahanmir, *Machining of Ceramics and Composites*. CRC Press, 1999.

[3] F. Cardarelli, *Materials Handbook: A Concise Desktop Reference*. Springer Science & Business Media, 2008.

[4] R., William Davidge, *Mechanical behaviour of ceramics*. Cambridge ; New York : Cambridge University Press, 1979.

[5] A. Koller and M. Štulíková, *Structure and properties of ceramics*. Amsterdam; London [etc.]: Elsevier, 1994.

[6] D. Whittaker, “Powder injection moulding looks to automotive applications for growth and stability,” *PIM Int.*, vol. 1, no. 2, pp. 14–22, 2007.

[7] J. Neil, G. Bandopadhyay, D. Sordelet, and M. Mahoney, “Development in injection molding silicon nitride turbine components,” in *Proceeding of Gas Turbine and Aeroengine Congress and Exposition*, Brussels, Belgium, vol. 2, p. 186.

[8] T. Ayers and J. M. Hoffman, “Micromini ceramics sport SUPERSIZED PROPERTIES,” *Mach. Des.*, vol. 75, no. 9, p. 59, May 2003.

[9] H.-J. Sterzel, “Spritzgießen keramischer Bauteile,” *Mater. Werkst.*, vol. 28, no. 11, pp. 534–542.

[10] H. Ş. Soykan and Y. Karakaş, “Injection moulding of thin walled zirconia tubes for oxygen sensors,” *Adv. Appl. Ceram.*, vol. 104, no. 6, pp. 285–290, Dec. 2005.

[11] R. M. German, “Powder injection moulding in the aerospace industry: opportunities and challenges,” *PIM International*.

[12] Anonym, “MIM and CIM parts used in Cochlear hearing implant devices,” *PIM International*, Apr-2011.

[13] J. Yang, K. Wang, G. Liu, and D. Wang, “Fracture resistance of inter-joined zirconia abutment of dental implant system with injection molding technique,” *Clin. Oral Implants Res.*, vol. 24, no. 11, pp. 1247–1250, Nov. 2013.

[14] J. L. Johnson and D. F. Heaney, “Processing of biocompatible materials via metal and ceramic injection molding,” *Med. Device Mater. II*, pp. 325–330, 2005.

[15] Anonym, “Amedica signs agreement with Kyocera for silicon nitride medical devices,” *PIM Int.*, vol. 8, no. 1, p. 11, 2014.

[16] Anonym, “BioBone Research Network looks to CIM for promising candidate components for osseointegration,” *PIM Int.*, vol. 7, no. 4, p. 25, 2013.

[17] Anonym, “Formatec reports growth in demand for MicroCIM components,” *PIM International*, Feb-2012.

[18] B. Lin, M. Zhang, C. Wu, and F. Liu, “Optimization and Simulation for Ceramic Injection Mould of ZrO2 Fiber Ferrule,” in *Some Critical Issues for Injection Molding*, Dr. Jian Wang (Ed.)., 2012.

[19] S. I.-E. Lin, “Near-net-shape forming of zirconia optical sleeves by ceramics injection molding,” *Ceram. Int.*, vol. 27, no. 2, pp. 205–214, 2001.

[20] “HB-LED grade aluminum nitride meets thermal needs of today’s LEDs | Solid State Technology.” .

[21] F. Miyashiro, N. Iwase, A. Tsuge, F. Ueno, M. Nakahashi, and T. Takahashi, “High thermal conductivity aluminum nitride ceramic substrates and packages,” *IEEE Trans. Compon. Hybrids Manuf. Technol.*, vol. 13, no. 2, pp. 313–319, 1990.

[22] T. Moritz, “Two-component CIM parts for the automotive and railway sectors’,” *PIM Int.*, vol. 2, no. 4, pp. 38–39, 2008.

[23] M. Pidria, E. Merlone, F. Parussa, J. Handelsman, and A. Gorodnev, “Near Net Shape, Low Cost Ceramic Valves for Advanced Engine Applications,” *Mater. Sci. Forum*, vol. 426–432, pp. 2321–2326, 2003.

[24] J. W. Macbeth, “Ceramic engine components reduce wear, friction,” *Ceram. Ind.*, vol. 7, pp. 33–45, 1984.

[25] S. Kamiya, M. Murachi, H. Kawamoto, S. Kato, S. Kawakami, and Y. Suzuki, “Silicon Nitride Swirl Lower-Chamber for High Power Turbocharged Diesel Engines,” SAE International, Warrendale, PA, SAE Technical Paper 850523, Feb. 1985.

[26] Anonym, “Morgan Technical Ceramics highlights potential for CIM in energy efficient motors,” *PIM International*, 2012.

[27] I. Santacruz, “Aqueous injection moulding of porcelains,” *J. Eur. Ceram. Soc.*, vol. 23, no. 12, pp. 2053–2060.

[28] J. Ter-Maat, M. Blömacher, A. Kern, and A. Thom, “Ceramic injection moulded zirconia products enjoy success in high-value luxury applications,” *PIM Int.*, vol. 4, no. 4, pp. 33–37, 2010.

[29] B. Williams, “Oeschler AF proves its competence in ceramic injection moulding with new BMW applications,” *PIM Int.*, vol. 3, no. 2, pp. 31–35, 2009.

[30] R. Urval, S. Lee, S. V. Atre, S.-J. Park, and R. M. German, “Optimisation of process conditions in powder injection moulding of microsystem components using robust design method Part 2 – Secondary design parameters,” *Powder Metall.*, vol. 53, no. 1, pp. 71–81, Mar. 2010.

[31] S. J. Park, S. Y. Ahn, T. G. Kang, S. T. Chung, Y. S. Kwon, S. Chung, S. G. Kim, S. Kim, S. V. Atre, S. Lee, and R. M. German, “Computer Simulations in Powder Injection Molding,” *Int. J. Powder Metall.*, vol. 46, no. 3, pp. 37–46, 2010.

[32] R. K. Enneti, S. J. Park, J. Palagi de Souza, and S. V. Atre, “Critical Issues In Manufacturing Dental Brackets By Powder Injection Molding,” *Int. J. Powder Metall.*, vol. 48, no. 2, pp. 23–39, 2012.

[33] J. Kim, S. Ahn, S. V. Atre, S. J. Park, T. G. Kang, and R. M. German, “Imbalance filling of multi-cavity tooling during powder injection molding,” *Powder Technol.*, vol. 257, pp. 124–131, May 2014.

[34] R. Urval, C. Wu, S. V. Atre, S. J. Park, and R. M. German, “CAE-Based Process Design for Microfluidic Components,” Powder Injection Molding Internationa,” *PIM International*, no. I, pp. 48–54, 2007.

[35] S. Laddha, C. Wu, G. K. lingam, K. Simmons, S. vallury, S. Lee, S. J. Park, R. M. German, P. Vilma, A. Varez, and S. V. Atre, “Characterization of Alumina Feedstock with Polyacetal and Wax-Polymer Binder Systems for Micro Powder Injection Moulding,” *PIM International*, vol. 3, no. 3, pp. 64–70, 2009.

[36] S. Laddha, C. Wu, S. J. Park, S. Lee, S. Ahn, R. M. German, and S. V. Atre, “Analysis of Macroscale Mold Filling Defects in Micro Powder Injection Molding,” *Int. J. Powder Metall.*, vol. 46, no. 3, pp. 49–59, 2010.

[37] S. V. Atre, S.-J. Park, R. Zauner, and R. M. German, “Process simulation of powder injection moulding: identification of significant parameters during mould filling phase,” *Powder Metall.*, vol. 50, no. 1, pp. 76–85, Mar. 2007.

[38] S. Ahn, S. T. Chung, S. V. Atre, S. J. Park, and R. M. German, “Integrated filling, packing and cooling CAE analysis of powder injection moulding parts,” *Powder Metall.*, vol. 51, no. 4, pp. 318–326, Dec. 2008.

[39] S. W. Lee, S. Ahn, C. J. Whang, S. J. Park, S. V. Atre, J. Kim, and R. M. German, “Effects of process parameters in plastic, metal, and ceramic injection molding processes,” *Korea-Aust. Rheol. J.*, vol. 23, no. 3, pp. 127–138, Sep. 2011.

[40] K. H. Kate, R. K. Enneti, S.-J. Park, R. M. German, and S. V. Atre, “Predicting Powder-Polymer Mixture Properties for PIM Design,” *Crit. Rev. Solid State Mater. Sci.*, vol. 39, no. 3, pp. 197–214, Mar. 2014.

[41] K. H. Kate, R. K. Enneti, V. P. Onbattuvelli, and S. V. Atre, “Feedstock properties and injection molding simulations of bimodal mixtures of nanoscale and microscale aluminum nitride,” *Ceram. Int.*, vol. 39, no. 6, pp. 6887–6897, Aug. 2013.

[42] K. H. Kate, V. P. Onbattuvelli, R. K. Enneti, S. W. Lee, S.-J. Park, and S. V. Atre, “Measurements of Powder–Polymer Mixture Properties and Their Use in Powder Injection Molding Simulations for Aluminum Nitride,” *JOM*, vol. 64, no. 9, pp. 1048–1058, Sep. 2012.

[43] V. P. Onbattuvelli, “The effects of nanoparticle addition on the processing, structure and properties of SiC and AlN,” 2010.

[44] R. A. Martin, “Development of mullite-zirconia composite feedstocks for powder injection molding,” oregon state university, Corvallis Oregon, 2013.

[45] K. H. Kate, “Models for predicting powder-polymer properties and their use in injection molding simulations of aluminum nitride,” 2012.

[46] S. Laddha, “The effect of feedstock composition on defect evolution in powder injection molded ceramic microarrays using simulations and experiments,” Thesis, oregon state university, Corvallis Oregon, 2008.

[47] V. Onbattuvelli, R. K. Enneti, S. B. Sohn, T. McCabe, S. J. Park, and S. V. Atre, “Micro-powder injection molding of barium titanate,” *PIM Int.*, vol. 5, no. 1, pp. 59–65, 2011.

[48] J. H. (Juergen H. Lenz, “Materials and process design for powder injection molding of silicon nitride for the fabrication of engine components,” Mar. 2012.

[49] R. A. Martin, “Development of mullite-zirconia composite feedstocks for powder injection molding,” Jun. 2013.

[50] R. M. German and S. V. Atre, “PIM 2013 Market Study,” New York, SciPiVision, 2013.

[51] J. Lenz, R. K. Enneti, V. Onbattuvelli, K. Kate, R. Martin, and S. Atre, “Powder Injection Molding of Ceramic Engine Components for Transportation,” *JOM*, vol. 64, no. 3, pp. 388–392, Mar. 2012.

[52] V. P. Onbattuvelli, R. K. Enneti, S.-J. Park, and S. V. Atre, “The Effect of Nanoparticle Addition on SiC and AlN Powder-Polymer Mixtures: Part I. Packing & Flow Behavior,” *The effects of nanoparticle addition on SiC and AlN powder–polymer mixtures: Packing and flow behavior*, Jan. 2013.

[53] K. H. Kate, “Models for predicting powder-polymer properties and their use in injection molding simulations of aluminum nitride,” Dec. 2012.

[54] R. K. Enneti, S.-J. Park, J. Palagi de Souza, and S. V. Atre, “Critical issues in manufacturing dental brackets by powder injection molding,” *Int. J. Powder Metall.*, vol. 48, no. 2, pp. 23–29, 2012.

[55] M. Bauccio, *ASM engineered materials reference book*. ASM International, 1994.

[56] Y. S. Touloukian, *Thermophysical Properties of Matter: Thermal conductivity : nonmetallic solids*. IFI/Plenum, 1970.

[57] J. F. Shackelford and W. Alexander, *CRC Materials Science and Engineering Handbook, Third Edition*. CRC Press, 2000.

[58] A. J. Pigram and R. Freer, “The production of Mn-Zn ferrite ceramics by injection moulding,” *J. Mater. Sci.*, vol. 29, no. 24, pp. 6420–6426, Jan. 1994.

[59] S. Liu, V. A. Merrick, and N. Newman, “Structural, chemical and dielectric properties of ceramic injection moulded Ba(Zn1/3Ta2/3)O3 microwave dielectric ceramics,” *J. Eur. Ceram. Soc.*, vol. 26, no. 15, pp. 3273–3278, 2006.

[60] G. Schlieper, “Philips Lighting: The evolution of PIM HID lighting components and the potential for transparent alumina products,” *PIM Int.*, vol. 6, no. 4.

[61] Ç. Toy, Y. Palaci, and T. Baykara, “A new ceramic thread-guide composition via low-pressure injection molding,” *J. Mater. Process. Technol.*, vol. 51, no. 1–4, pp. 211–222, Apr. 1995.

[62] Anonym, “Ceramic inkjet printhead,” *PIM International*, vol. 2, no. 4, p. 26, 2008.

[63] J. B. Wachtman and D. G. Lam, “Young’s Modulus of Various Refractory Materials as a Function of Temperature,” *J. Am. Ceram. Soc.*, vol. 42, no. 5, pp. 254–260, 1959.

[64] “Granta’s CES EduPack and teaching resources: supporting Materials Education.” [Online]. Available: http://www.grantadesign.com/education/. [Accessed: 27-Sep-2013].

[65] R. G. Munro, “Material Properties of a Sintered α-SiC,” *J. Phys. Chem. Ref. Data*, vol. 26, no. 5, p. 1195, Sep. 1997.

[66] R. A. Alliegro, L. B. Coffin, and J. R. Tinklepaugh, “Pressure-Sintered Silicon Carbide,” *J. Am. Ceram. Soc.*, vol. 39, no. 11, pp. 386–389, 1956.

[67] S. Zhu, W. G. Fahrenholtz, and G. E. Hilmas, “Influence of silicon carbide particle size on the microstructure and mechanical properties of zirconium diboride–silicon carbide ceramics,” *J. Eur. Ceram. Soc.*, vol. 27, no. 4, pp. 2077–2083, 2007.

[68] M. Hotta and J. Hojo, “Inhibition of grain growth in liquid-phase sintered SiC ceramics by AlN additive and spark plasma sintering,” *J. Eur. Ceram. Soc.*, vol. 30, no. 10, pp. 2117–2122, Aug. 2010.

[69] J. Hu, H. Xiao, W. Guo, Q. Li, W. Xie, and B. Zhu, “Effect of AlN–Y2O3 addition on the properties and microstructure of in-situ strengthened SiC–TiB2 composites prepared by hot pressing,” *Ceram. Int.*, vol. 40, no. 1, Part A, pp. 1065–1071, Jan. 2014.

[70] V. A. Izhevskyi, L. A. Genova, A. H. A. Bressiani, and J. C. Bressiani, “Microstructure and properties tailoring of liquid-phase sintered SiC,” *Int. J. Refract. Met. Hard Mater.*, vol. 19, no. 4–6, pp. 409–417, Jul. 2001.

[71] L. S. Sigl, “Thermal conductivity of liquid phase sintered silicon carbide,” *J. Eur. Ceram. Soc.*, vol. 23, no. 7, pp. 1115–1122, Jun. 2003.

[72] W. M. Haynes, *CRC Handbook of Chemistry and Physics, 95th Edition*. CRC Press, 2014.

[73] P. U. T. P. R. Center, *Thermophysical Properties of Matter: Specific heat: metallic elements and alloys, by Y. S. Touloukian and E. H. Buyco*. IFI/Plenum, 1970.

[74] H. Nakano, K. Watari, Y. Kinemuchi, K. Ishizaki, and K. Urabe, “Microstructural characterization of high-thermal-conductivity SiC ceramics,” *J. Eur. Ceram. Soc.*, vol. 24, no. 14, pp. 3685–3690, Nov. 2004.

[75] K. Watari, H. Nakano, K. Sato, K. Urabe, K. Ishizaki, S. Cao, and K. Mori, “Effect of Grain Boundaries on Thermal Conductivity of Silicon Carbide Ceramic at 5 to 1300 K,” *J. Am. Ceram. Soc.*, vol. 86, no. 10, pp. 1812–1814, Oct. 2003.

[76] G.-D. Zhan, M. Mitomo, R.-J. Xie, and A. K. Mukherjee, “Thermal and Electrical Properties in Plasma-Activation-Sintered Silicon Carbide with Rare-Earth-Oxide Additives,” *J. Am. Ceram. Soc.*, vol. 84, no. 10, pp. 2448–2450, Oct. 2001.

[77] J. R. Groza and A. Zavaliangos, “Sintering activation by external electrical field,” *Mater. Sci. Eng. A*, vol. 287, no. 2, pp. 171–177, Aug. 2000.

[78] T. B. Jackson, A. V. Virkar, K. L. More, R. B. Dinwiddie, and R. A. Cutler, “High-Thermal-Conductivity Aluminum Nitride Ceramics: The Effect of

Thermodynamic, Kinetic, and Microstructural Factors," *J. Am. Ceram. Soc.*, vol. 80, no. 6, pp. 1421–1435, 1997.

[79] G. A. Slack, "Thermal Conductivity of Pure and Impure Silicon, Silicon Carbide, and Diamond," *J. Appl. Phys.*, vol. 35, no. 12, p. 3460, Dec. 1964.

[80] W. M. Yim and R. J. Paff, "Thermal expansion of AlN, sapphire, and silicon," *J. Appl. Phys.*, vol. 45, no. 3, p. 1456, Mar. 1974.

[81] K. Biswas, J. Schneider, G. Rixecker, and F. Aldinger, "Comparative bending creep behaviour of silicon carbide sintered with oxynitride additives," *Scr. Mater.*, vol. 53, no. 5, pp. 591–596, Sep. 2005.

[82] J. Gu, Q. Zhang, J. Dang, J. Zhang, and Z. Yang, "Thermal conductivity and mechanical properties of aluminum nitride filled linear low-density polyethylene composites," *Polym. Eng. Sci.*, vol. 49, no. 5, pp. 1030–1034, May 2009.

[83] W. Zhou, "Thermal and dielectric properties of the AlN particles reinforced linear low-density polyethylene composites," *Thermochim. Acta*, vol. 512, no. 1–2, pp. 183–188, Jan. 2011.

[84] R. Kochetov, T. Andritsch, U. Lafont, P. H. F. Morshuis, S. J. Picken, and J. J. Smit, "Preparation and dielectric properties of epoxy - BN and epoxy - AlN nanocomposites," in *IEEE Electrical Insulation Conference, 2009. EIC 2009*, 2009, pp. 397–400.

[85] B. L. Zhu, J. Ma, J. Wu, K. C. Yung, and C. S. Xie, "Study on the properties of the epoxy-matrix composites filled with thermally conductive AlN and BN ceramic particles," *J. Appl. Polym. Sci.*, vol. 118, no. 5, pp. 2754–2764, Dec. 2010.

[86] S. H. Risbud, J. R. Groza, and M. J. Kim, "Clean grain boundaries in aluminium nitride ceramics densified without additives by a plasma-activated sintering process," *Philos. Mag. Part B*, vol. 69, no. 3, pp. 525–533, 1994.

[87] K. A. Khor, K. H. Cheng, L. G. Yu, and F. Boey, "Thermal conductivity and dielectric constant of spark plasma sintered aluminum nitride," *Mater. Sci. Eng. A*, vol. 347, no. 1–2, pp. 300–305, Apr. 2003.

[88] M. Medraj, "Understanding AlN sintering through computational thermodynamics combined with experimental investigation," *J. Mater. Process. Tech*, vol. 161, no. 3, pp. 415–422.

[89] L. Qiao, H. Zhou, and R. Fu, "Thermal conductivity of AlN ceramics sintered with CaF2 and YF3," *Ceram. Int.*, vol. 29, no. 8, pp. 893–896, 2003.

[90] L. Qiao, H. Zhou, H. Xue, and S. Wang, “Effect of Y2O3 on low temperature sintering and thermal conductivity of AlN ceramics,” *J. Eur. Ceram. Soc.*, vol. 23, no. 1, pp. 61–67, Jan. 2003.

[91] L. Qiao, H. Zhou, K. Chen, and R. Fu, “Effects of Li2O on the low temperature sintering and thermal conductivity of AlN ceramics,” *J. Eur. Ceram. Soc.*, vol. 23, no. 9, pp. 1517–1524, Aug. 2003.

[92] J.-W. Bae, W. Kim, S.-H. Cho, and S.-H. Lee, “The properties of AlN-filled epoxy molding compounds by the effects of filler size distribution,” *J. Mater. Sci.*, vol. 35, no. 23, pp. 5907–5913, Dec. 2000.

[93] G. Ziegler, J. Heinrich, and G. Wötting, “Relationships between processing, microstructure and properties of dense and reaction-bonded silicon nitride,” *J. Mater. Sci.*, vol. 22, no. 9, pp. 3041–3086, Sep. 1987.

[94] M. Fukuhara, K. Fukazawa, and A. Fukawa, “Physical properties and cutting performance of silicon nitride ceramic,” *Wear*, vol. 102, no. 3, pp. 195–210, Apr. 1985.

[95] X. Zhu, “Effects of processing method and additive composition on microstructure and thermal conductivity of Si3N4 ceramics,” *J. Eur. Ceram. Soc.*, vol. 26, no. 4–5, pp. 711–718.

[96] X. Zhu, Y. Zhou, and K. Hirao, “Effect of Sintering Additive Composition on the Processing and Thermal Conductivity of Sintered Reaction-Bonded Si3N4,” *J. Am. Ceram. Soc.*, vol. 87, no. 7, pp. 1398–1400, Jul. 2004.

[97] B. R. Golla, “Effect of particle size and oxygen content of Si on processing, microstructure and thermal conductivity of sintered reaction bonded Si3N4,” vol. 595, no. Complete, pp. 60–66.

[98] K. G. Budinski and M. K. Budinski, *Engineering Materials: Properties and Selection*. Prentice Hall, 2010.

[99] M. A. Camerucci, G. Urretavizcaya, M. S. Castro, and A. L. Cavalieri, “Electrical properties and thermal expansion of cordierite and cordierite-mullite materials,” *J. Eur. Ceram. Soc.*, vol. 21, no. 16, pp. 2917–2923, Dec. 2001.

[100] K. S. Mazdiyasni and L. M. Brown, “Synthesis and Mechanical Properties of Stoichiometric Aluminum Silicate (Mullite),” *J. Am. Ceram. Soc.*, vol. 55, no. 11, pp. 548–552, 1972.

[101] M. I. Osendi and C. Baudín, “Mechanical properties of mullite materials,” *J. Eur. Ceram. Soc.*, vol. 16, no. 2, pp. 217–224, 1996.

[102] H. Schneider, J. Schreuer, and B. Hildmann, “Structure and properties of mullite—A review,” *J. Eur. Ceram. Soc.*, vol. 28, no. 2, pp. 329–344, 2008.

[103] T. M. Kyaw, Y. Okamoto, and K. Hayashi, “Thermal Conductivity of Mullite-Zirconia Composites,” *J. Ceram. Soc. Jpn.*, vol. 103, no. 1204, pp. 1289–1292, 1995.

[104] J.-M. Wu and C.-M. Lin, “Effect of CeO2 on reaction-sintered mullite-ZrO2 ceramics,” *J. Mater. Sci.*, vol. 26, no. 17, pp. 4631–4636, Sep. 1991.

[105] B. Hildmann and H. Schneider, “Heat Capacity of Mullite - New Data and Evidence for a High-Temperature Phase Transformation,” *J. Am. Ceram. Soc.*, vol. 87, no. 2, pp. 227–234, 2004.

[106] J. B. Wachtman, T. G. Scuderi, and G. W. Cleek, “Linear Thermal Expansion of Aluminum Oxide and Thorium Oxide from 100° to 1100°K,” *J. Am. Ceram. Soc.*, vol. 45, no. 7, pp. 319–323, 1962.

[107] S. A. Hassanzadeh-Tabrizi and E. Taheri-Nassaj, “Compressibility and sinterability of Al2O3–YAG nanocomposite powder synthesized by an aqueous sol–gel method,” *J. Alloys Compd.*, vol. 506, no. 2, pp. 640–644, Sep. 2010.

[108] J. G. Li and X. Sun, “Synthesis and sintering behavior of a nanocrystalline α-alumina powder,” *Acta Mater.*, vol. 48, no. 12, pp. 3103–3112, Jul. 2000.

[109] N. Shinohara, M. Okumiya, T. Hotta, K. Nakahira, M. Naito, and K. Uematsu, “Seasonal Variation of Microstructure and Sintered Strength of Dry-Pressed Alumina,” *J. Am. Ceram. Soc.*, vol. 82, no. 12, pp. 3441–3446, Dec. 1999.

[110] M. Munro, “Evaluated Material Properties for a Sintered alpha-Alumina,” *J. Am. Ceram. Soc.*, vol. 80, no. 8, pp. 1919–1928, Aug. 1997.

[111] R. Barea, M. Belmonte, M. I. Osendi, and P. Miranzo, “Thermal conductivity of Al2O3/SiC platelet composites,” *J. Eur. Ceram. Soc.*, vol. 23, no. 11, pp. 1773–1778, Oct. 2003.

[112] T. Nemoto, “Thermal conductivity of alumina and silicon carbide ceramics at low temperatures,” *Cryogenics*, vol. 25, no. 9, pp. 531–532.

[113] C. Y. Ho and R. E. Taylor, *Thermal Expansion of Solids*. ASM International, 1998.

[114] A. Polotai, K. Breece, E. Dickey, C. Randall, and A. Ragulya, “A Novel Approach to Sintering Nanocrystalline Barium Titanate Ceramics,” *J. Am. Ceram. Soc.*, vol. 88, no. 11, pp. 3008–3012, 2005.

[115] X. Wang, X. Deng, H. Wen, and L. Li, “Phase transition and high dielectric constant of bulk dense nanograin barium titanate ceramics,” *Appl. Phys. Lett.*, vol. 89, no. 16, p. 162902, 2006.

[116] Y. He, “Heat capacity, thermal conductivity, and thermal expansion of barium titanate-based ceramics,” *Thermochim. Acta*, vol. 419, no. 1–2, pp. 135–141, Sep. 2004.

[117] J.-F. Chen, Z.-G. Shen, F.-T. Liu, X.-L. Liu, and J. Yun, “Preparation and properties of barium titanate nanopowder by conventional and high-gravity reactive precipitation methods,” *Scr. Mater.*, vol. 49, no. 6, pp. 509–514, Sep. 2003.

[118] K. S. Mazdiyasni, R. T. Dolloff, and J. S. Smith, “Preparation of High-Purity Submicron Barium Titanate Powders,” *J. Am. Ceram. Soc.*, vol. 52, no. 10, pp. 523–526, Oct. 1969.

APPENDICES

Appendix A1: Density Measurements for Various Ceramic Feedstocks and the Wax Polymer Binder

Solid and melt density measurements was conducted for the silicon carbide, aluminum nitride, silicon nitride, mullite composite, ziroconia composite, alumina and barium titanate feedstocks and wax polymer binder system. The feedstock solid density measurement was done using Archimedes principle in accordance with ASTM D792. The feedstock melt density was measured using a capillary rheometer in accordance with ASTM D3835.

Table A2.1. Solid and melt densities for various ceramic feedstocks

feedstock	solid density, kg/m^3	melt density, kg/m^3
μ SiC	2020	1850
μ-n SiC	2180	1990
μ AlN	2150	1940
μ-n AlN	2310	2140
μ-n Si_3N_4	2300	2110
$Al_2O_3.2SiO_2$ composite	2520	2290
ZrO_2 composite	2830	2560
Al_2O_3	2580	2340
μ-n $BaTiO_3$	3690	3370
wax polymer binder	870	700

Appendix A2: Specific Heat Measurements for Various Ceramic Feedstocks and the Wax Polymer Binder

Specific heat measurements were conducted for the silicon carbide, aluminum nitride, silicon nitride, mullite composite, ziroconia composite, alumina and barium titanate feedstocks and wax polymer binder system. Specific heat measurements of all feedstocks were made using differential scanning calorimetry (DSC) for a range of temperatures and are presented in **Table A2.1-A2.10.**

Table A2.1. Specific heat as a function of temperature for the μ SiC feedstock

temperature, K	specific heat, J/kg.K
423	1200
374	1156
330	1108
319	2105
304	1402
303	1350
296	1098

Table A2.2. Specific heat as a function of temperature for the μ-n SiC feedstock

temperature, K	specific heat, J/kg.K
443	1252
384	1174
330	1105
320	2100
299	1149
291	1013
273	871

Table A2.3. Specific heat as a function of temperature for the μ AlN feedstock

temperature, K	specific heat, J/kg.K
423	1210
374	1125
331	1090
322	2811
304	1377
298	1114
283	918

Table A2.4. Specific heat as a function of temperature for the μ-n AlN feedstock

temperature, K	specific heat, J/kg.K
443	1413
384	1315
331	1274
322	2915
303	1472
293	1186
273	998

Table A2.5. Specific heat as a function of temperature for the μ-n Si_3N_4 feedstock

temperature, K	specific heat, J/kg.K
443	1163
384	1059
331	1009
322	1698
303	1004
293	913
273	791

Table A2.6. Specific heat as a function of temperature for the $Al_2O_3.2SiO_2$ composite feedstock

temperature, K	specific heat, J/kg.K
453	1044
403	968
359	936
349	1454
334	935
323	1748
303	1044

Table A2.7. Specific heat as a function of temperature for the ZrO_2 composite feedstock

temperature, K	specific heat, J/kg.K
443	902
384	844
331	835
322	1499
303	833
293	782
273	685

Table A2.8. Specific heat as a function of temperature for the Al_2O_3 feedstock

temperature, K	specific heat, J/kg.K
453	1298
389	1214
330	1137
320	1996
305	1392
303	1297
298	1146

Table A2.9. Specific heat as a function of temperature for the μ-n $BaTiO_3$ feedstock

temperature, K	specific heat, J/kg.K
443	712
399	698
360	687
350	1012
334	673
308	884
273	585

Table A2.10. Specific heat as a function of temperature for the wax polymer binder

temperature, K	specific heat, J/kg.K
443	2598
407	2473
377	2371
368	9286
352	3505
322	4894
283	2077

Appendix A3: Thermal Conductivity Measurements for Various Ceramic Feedstocks and Wax Polymer Binder

Thermal conductivity measurements were conducted for the silicon carbide, aluminum nitride, silicon nitride, mullite composite, ziroconia composite, alumina and barium titanate feedstocks and wax polymer binder system. Thermal conductivity measurements of all feedstocks were made using a transient line-source technique (ASTM D5930) for all feedstocks for a range of temperatures. Thermal conductivity measurements for all feedstocks are presented in **Table A3.1-A3.10.**

Table A3.1. Thermal conductivity measurements as a function of temperatures for the μ SiC feedstock

temperature, K	thermal conductivity, W/m.K
439	2.64
419	2.00
399	2.70
380	3.26
359	3.26
339	3.84
314	4.07

Table A3.2. Thermal conductivity measurements as a function of temperature for the μ-n SiC feedstock

temperature, K	thermal conductivity, W/m.K
460	1.58
440	2.07
420	3.33
400	3.57
380	2.25
360	3.18
339	2.93
319	3.21

Table A3.3. Thermal conductivity measurements as a function of temperature for the μ AlN feedstock

temperature, K	thermal conductivity, W/m.K
436	2.50
417	2.05
397	2.06
377	2.66
356	2.23
336	2.83
315	4.26

Table A3.4. Thermal conductivity measurements as a function of temperature for the μ-n AlN feedstock

temperature, K	thermal conductivity, W/m.K
459	3.27
439	2.09
419	3.38
399	2.47
379	2.20
359	3.25
339	3.06
318	3.09

Table A3.5. Thermal conductivity measurements as a function of temperature for the μ-n Si_3N_4 feedstock

temperature, K	thermal conductivity, W/m.K
457	1.13
427	1.53
396	1.28
366	1.50
335	1.43

Table A3.6. Thermal conductivity measurements as a function of temperature for the $Al_2O_3.2SiO_2$ composite feedstock

temperature, K	thermal conductivity, W/m.K
466	0.50
435	0.68
405	0.83
375	1.42
344	1.17
312	1.39

Table A3.7. Thermal conductivity measurements as a function of temperature for the ZrO_2 composite feedstock

temperature, K	thermal conductivity, W/m.K
458	0.71
438	0.71
418	0.82
398	0.84
378	0.87
357	0.93
337	0.83
316	0.67
303	0.75

Table A3.8. Thermal conductivity measurements of temperature for the Al_2O_3 feedstock

temperature, K	thermal conductivity, W/m.K
467	1.25
457	1.40
437	1.41
417	1.44
398	1.59
378	1.95
357	2.33
337	2.45
316	2.16

Table A3.9. Thermal conductivity measurements as a function of temperature for the μ-n $BaTiO_3$ feedstock

temperature, K	thermal conductivity, W/m.K
457	0.72
437	0.85
417	0.86
397	1.00
376	0.83
356	1.00
335	0.99
314	0.98
305	1.27

Table A3.10. Thermal conductivity measurements as a function of temperature for the wax polymer binder

temperature, K	thermal conductivity, W/m.K
459	0.16
440	0.16
420	0.16
401	0.17
381	0.17
360	0.19
340	0.19
320	0.19
314	0.19

Appendix A4: Viscosity Measurements for Various Ceramic Feedstocks and Wax Polymer Binder

Viscosity measurements were conducted for the silicon carbide, aluminum nitride, silicon nitride, mullite composite, ziroconia composite, alumina and barium titanate feedstocks, and wax polymer binder system for various shear rates and temperatures. A capillary rheometry was used to measure viscosity of all ceramic feedstocks. ASTM D3835 standard was used for conducting the measurements. Tests were run for temperatures between 415 K and 430 K at shear rates between $10s^{-1}$ and 10^4s^{-1}. The viscosity for different ceramic feedstocks and wax polymer binder at various shear rates and temperature are shown in **Table A4.1-A4.10**. Typical representations of viscosity shear rate dependence for all ceramic feedstock and wax polymer binder are shown in **Figure A4.1-A4.10**.

Table A4.1. Viscosity measurements as a function of temperatures and shear rate for the μ SiC feedstock

shear rate, s^{-1}	viscosity, Pa.s		
	415 K	425 K	430 K
10	7108	6599	6372
25	3287	3057	2955
50	1841	1713	1656
80	1250	1164	1126
100	1030	959	928
125	849	790	764
200	576	537	519
400	322	300	290
500	266	247	239
1000	149	138	134
2000	83	77	75
2500	68	64	62
3100	56	53	51
4000	46	43	42
5000	38	36	34
6300	32	29	28
8000	26	24	23
10000	21	20	19

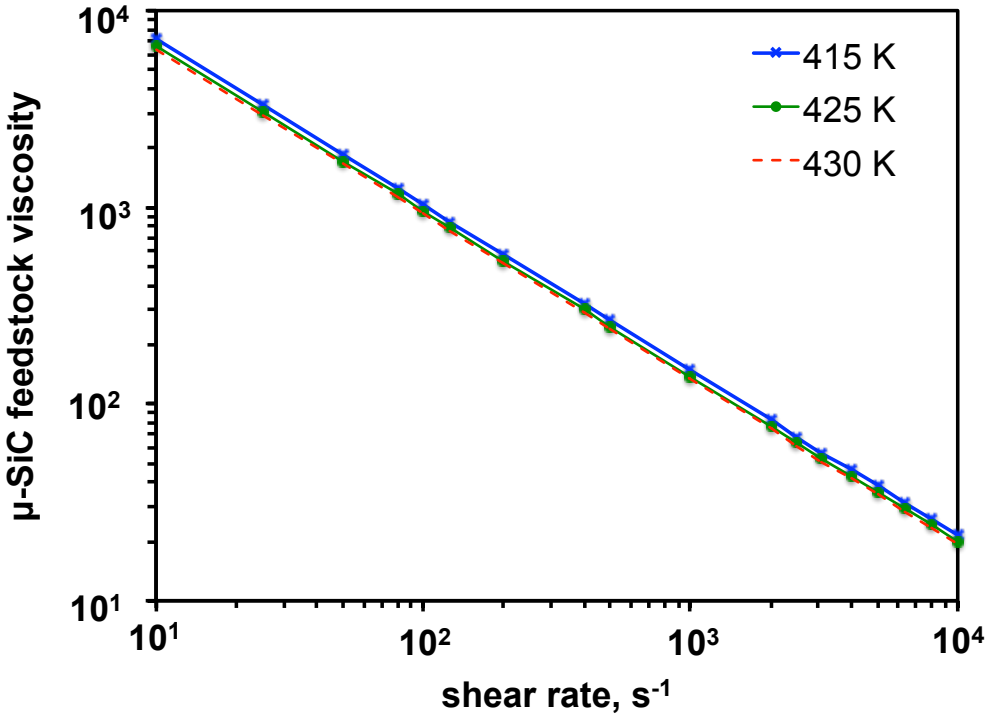

Figure A4.1. Viscosity measurements as a function of temperatures and shear rate for the μ SiC feedstock

Table A4.2. Viscosity measurements as a function of temperatures and shear rate for the μ-n SiC feedstock

shear rate, s^{-1}	viscosity, Pa.s		
	415 K	425 K	430 K
10	15555	14955	14666
25	6614	6382	6274
50	3474	3357	3303
80	2260	2185	2151
100	1823	1763	1735
125	1470	1422	1400
200	956	925	910
400	501	485	478
500	404	391	385
1000	212	205	202
2000	111	107	106
2500	90	87	85
3100	72	70	69
4000	58	56	55
5000	47	45	45
6300	38	37	36
8000	31	30	29
10000	25	24	23

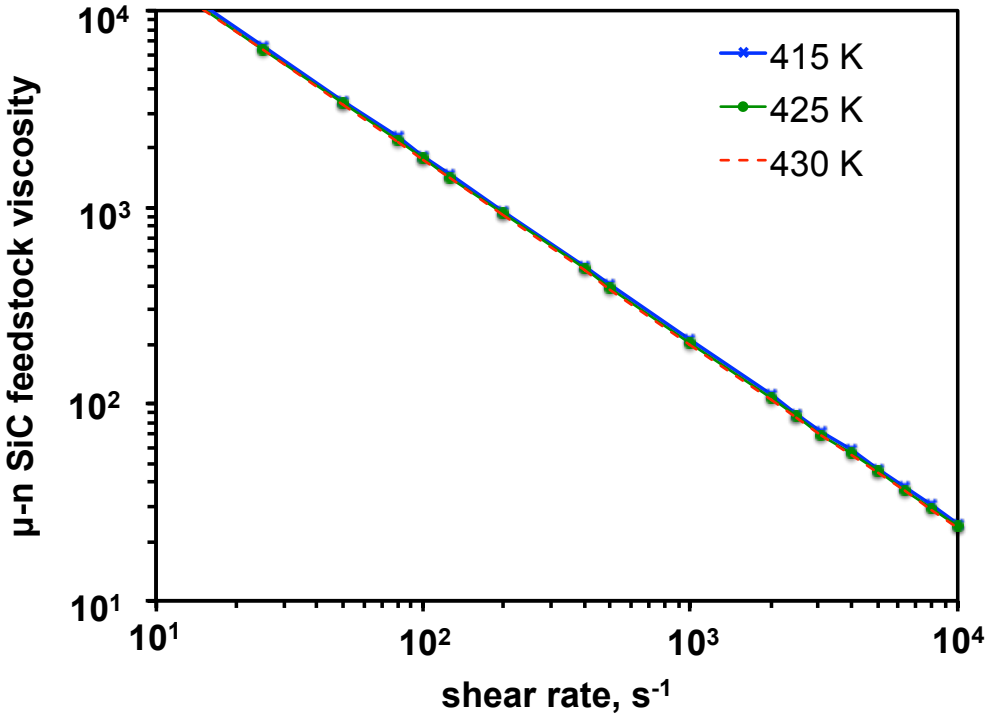

Figure A4.2. Viscosity measurements as a function of temperatures and shear rate for the μ-n SiC feedstock

Table A4.3. Viscosity measurements as a function of temperatures and shear rate for the μ-AlN feedstock

shear rate, s^{-1}	viscosity, Pa.s		
	415 K	425 K	430 K
10	1472	1381	1340
25	830	779	756
50	540	507	492
80	405	380	369
100	351	330	320
125	304	286	277
200	229	214	208
400	149	140	135
500	129	121	117
1000	84	79	76
2000	55	51	50
2500	47	44	43
3100	41	38	37
4000	35	33	32
5000	31	29	28
6300	27	25	24
8000	23	22	21
10000	20	19	18

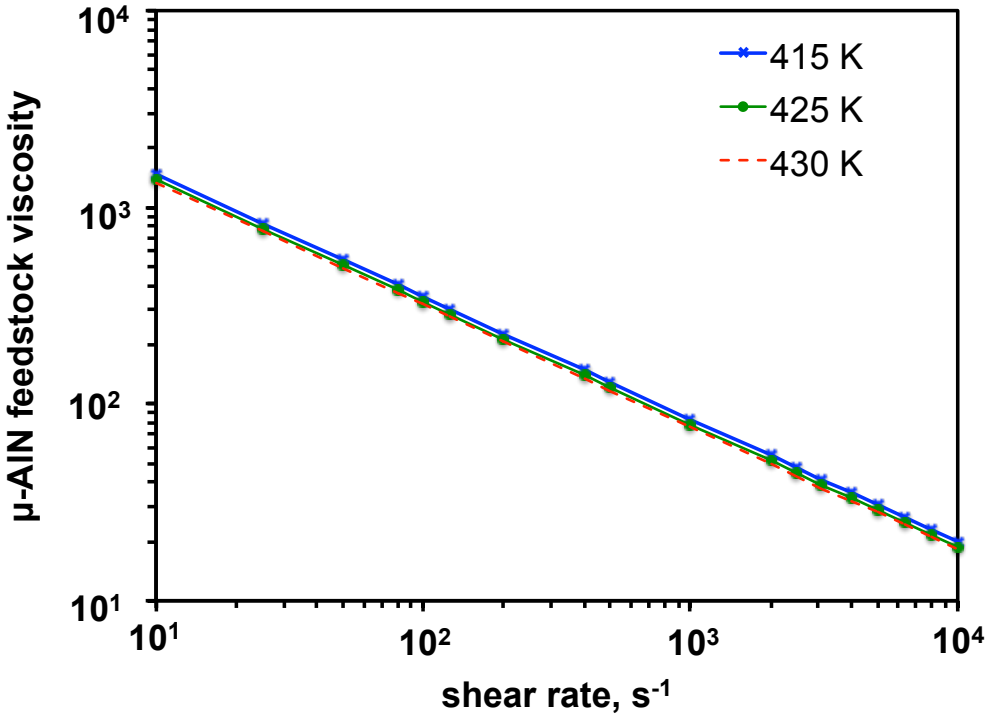

Figure A4.3. Viscosity measurements as a function of temperatures and shear rate for the μ-AlN feedstock

Table A4.4. Viscosity measurements as a function of temperatures and shear rate for the µ-n AlN feedstock

shear rate, s^{-1}	viscosity, Pa.s		
	415 K	425 K	430 K
10	34622	33979	33684
25	14478	14209	14085
50	7529	7389	7325
80	4869	4779	4737
100	3915	3843	3809
125	3149	3090	3063
200	2036	1998	1981
400	1059	1039	1030
500	851	836	828
1000	443	435	431
2000	230	226	224
2500	185	182	180
3100	149	146	145
4000	120	118	116
5000	96	95	94
6300	77	76	75
8000	62	61	61
10000	50	49	49

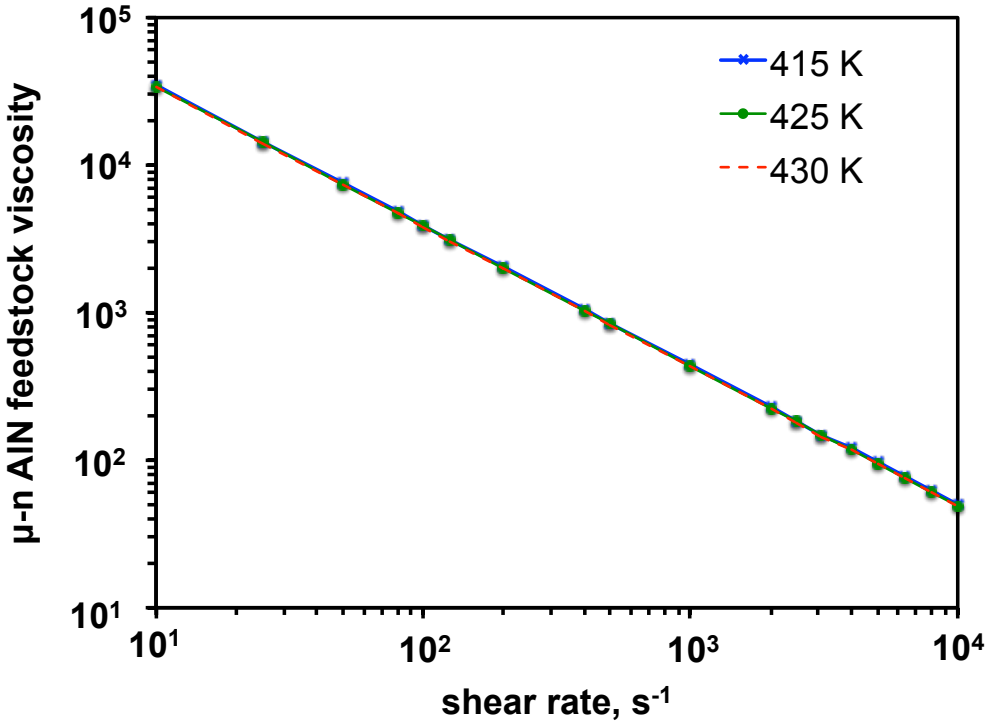

Figure A4.4. Viscosity measurements as a function of temperatures and shear rate for the μ-n AlN feedstock

Table A4.5. Viscosity measurements as a function of temperature and shear rate for the μ-n Si_3N_4 feedstock

shear rate, s^{-1}	viscosity, Pa.s		
	415 K	425 K	430 K
10	45216	40332	38393
25	18863	16825	16016
50	9792	8734	8314
80	6325	5641	5370
100	5083	4534	4316
125	4085	3644	3469
200	2638	2353	2240
400	1370	1222	1163
500	1101	982	935
1000	571	510	485
2000	297	265	252
2500	238	213	202
3100	192	171	163
4000	154	137	131
5000	124	110	105
6300	99	89	84
8000	80	71	68
10000	64	57	55

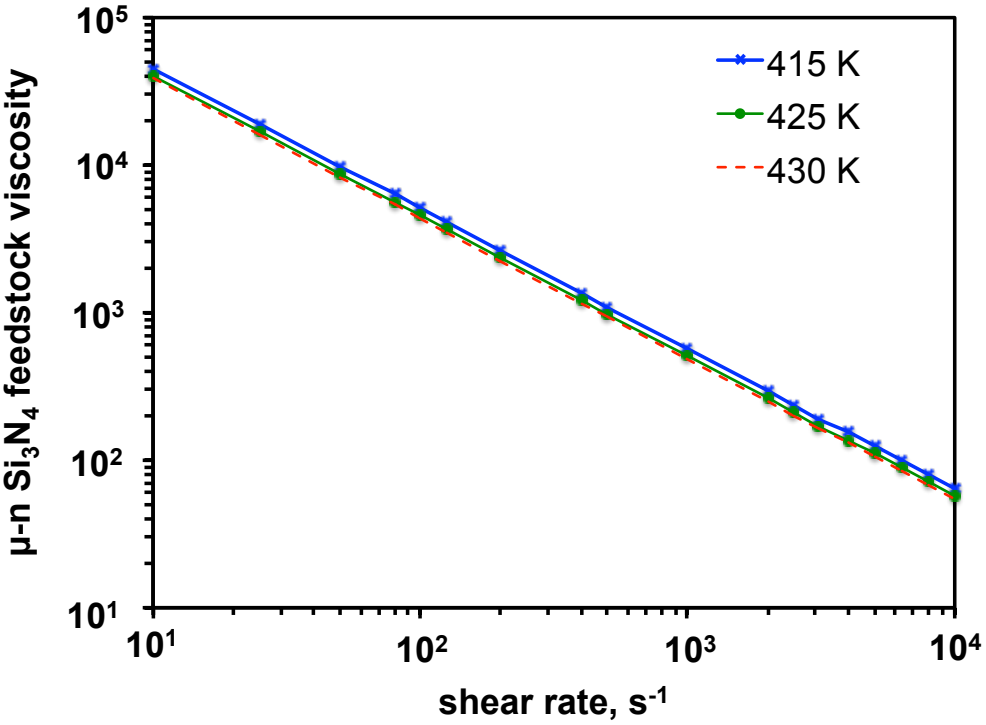

Figure A4.5. Viscosity measurements as a function of temperature and shear rate for the μ-n Si_3N_4 feedstock

Table A4.6. Viscosity measurements as a function of temperature and shear rate for the $3Al_2O_3.2SiO_2$ composite feedstock

shear rate, s^{-1}	viscosity, Pa.s		
	415 K	425 K	430 K
10	19946	19849	19804
25	8080	8041	8022
50	4103	4083	4074
80	2612	2599	2593
100	2083	2073	2069
125	1662	1654	1650
200	1058	1053	1050
400	537	535	533
500	429	426	425
1000	218	217	216
2000	110	110	110
2500	88	88	88
3100	70	70	70
4000	56	56	56
5000	45	45	44
6300	36	36	35
8000	28	28	28
10000	23	23	23

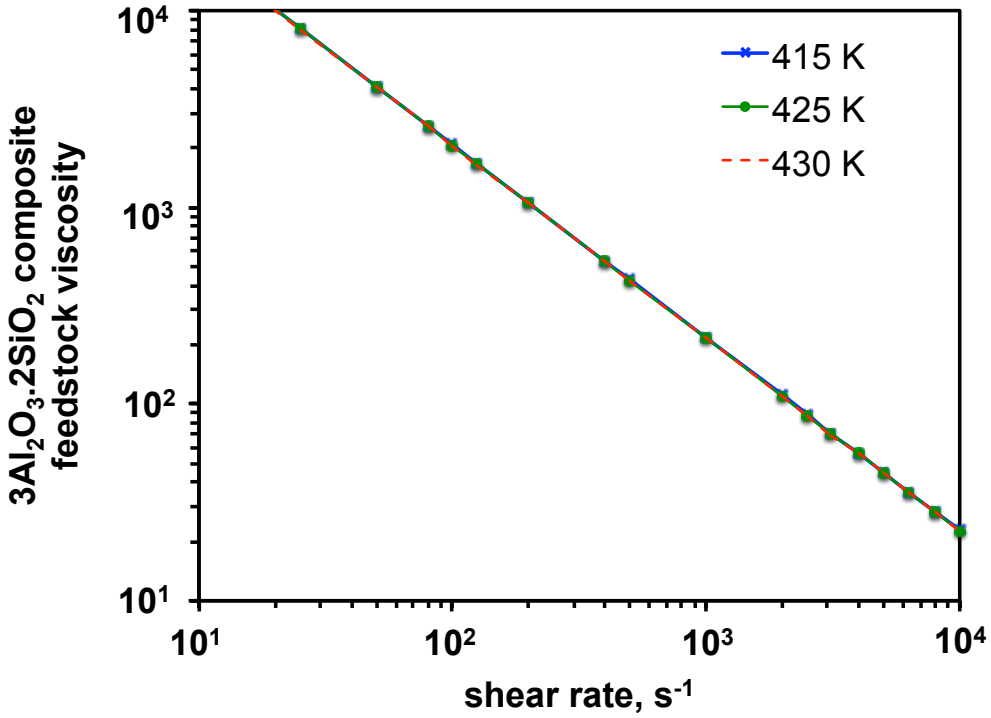

Figure A4.6. Viscosity measurements as a function of temperature and shear rate for the $3Al_2O_3.2SiO_2$ composite feedstock

Table A4.7. Viscosity measurements as a function of temperature and shear rate for the ZrO_2 composite feedstock

shear rate, s^{-1}	viscosity, Pa.s		
	415 K	425 K	430 K
10	11822	11626	11535
25	4921	4839	4801
50	2550	2508	2488
80	1645	1618	1605
100	1321	1299	1289
125	1061	1044	1036
200	685	673	668
400	355	349	346
500	285	280	278
1000	148	145	144
2000	76	75	75
2500	61	60	60
3100	49	49	48
4000	40	39	39
5000	32	31	31
6300	26	25	25
8000	21	20	20
10000	16	16	16

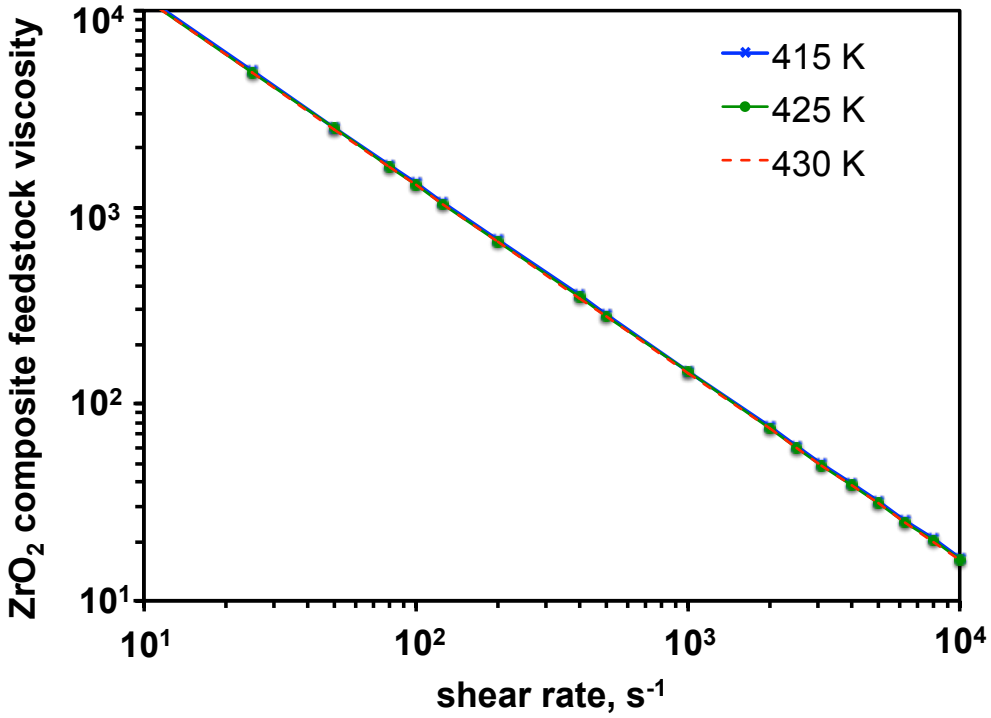

Figure A4.7. Viscosity measurements as a function of temperature and shear rate for the ZrO_2 composite feedstock

Table A4.8. Viscosity measurements as a function of temperature and shear rate for the Al_2O_3 feedstock

shear rate, s^{-1}	viscosity, Pa.s		
	415 K	425 K	430 K
10	4685	4330	4173
25	2310	2137	2060
50	1359	1257	1212
80	953	882	851
100	799	739	713
125	669	619	597
200	469	434	419
400	276	255	246
500	231	214	206
1000	136	126	121
2000	80	74	71
2500	67	62	60
3100	56	52	50
4000	47	43	42
5000	39	36	35
6300	33	30	29
8000	28	25	25
10000	23	21	21

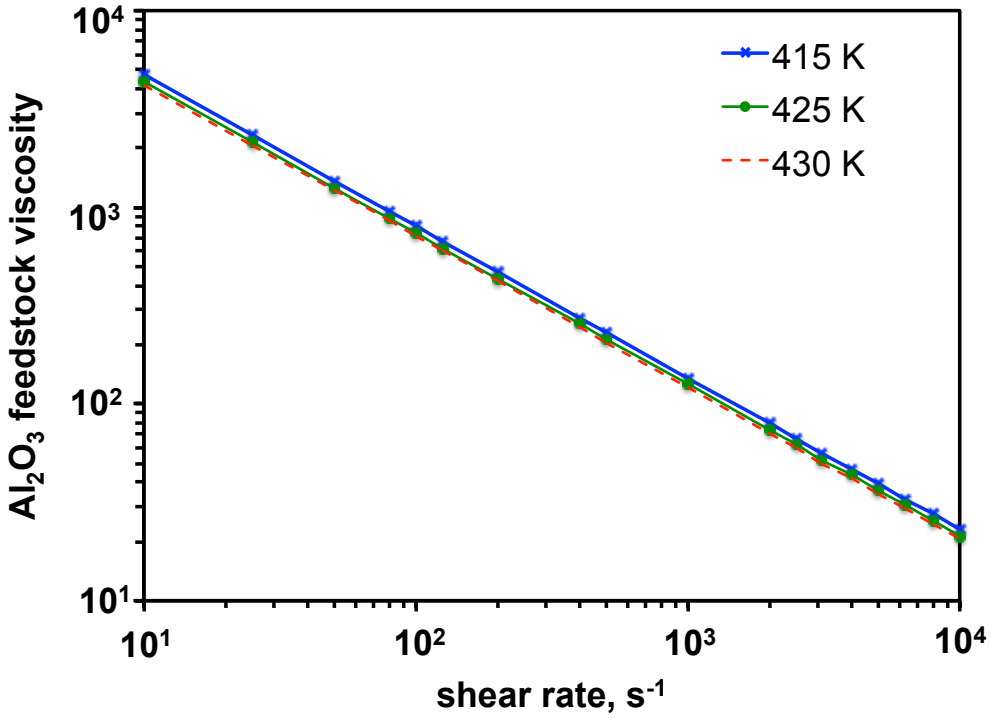

Figure A4.8. Viscosity measurements as a function of temperature and shear rate for the Al_2O_3 feedstock

Table A4.9. Viscosity measurements as a function of temperature and shear rate for the μ-n $BaTiO_3$ feedstock

shear rate, s^{-1}	viscosity, Pa.s		
	415 K	425 K	430 K
10	6325	5643	5281
25	2767	2527	2409
50	1477	1361	1306
80	970	897	863
100	786	728	701
125	637	590	569
200	418	387	374
400	222	206	199
500	179	167	161
1000	95	88	86
2000	50	47	45
2500	41	38	37
3100	33	31	30
4000	27	25	24
5000	22	20	19
6300	18	16	16
8000	14	13	13
10000	11	11	10

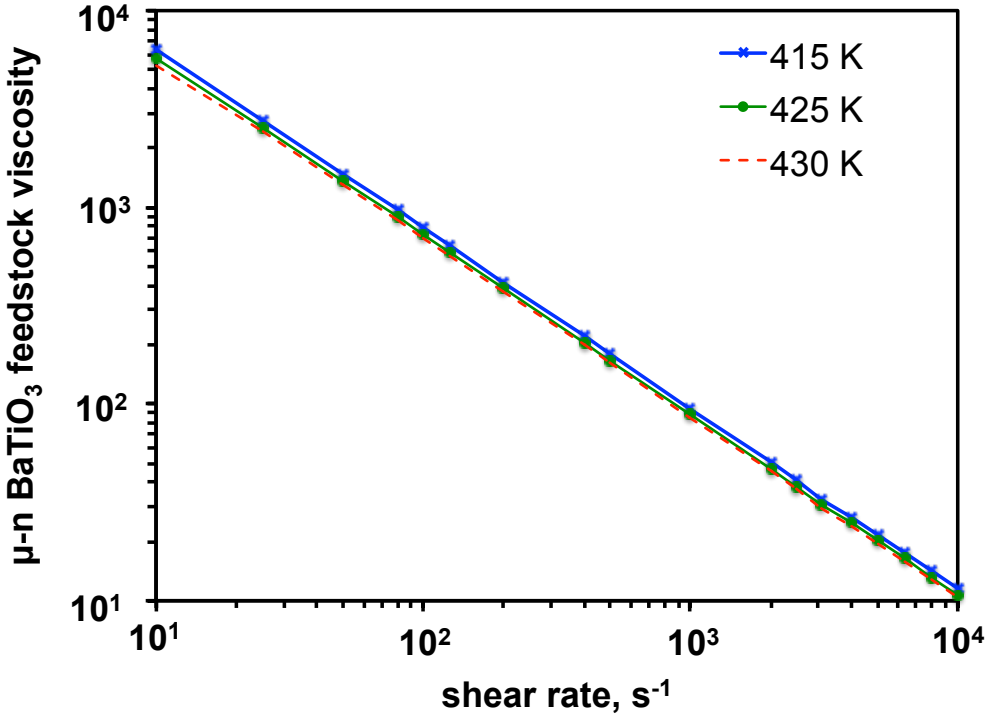

Figure A4.9. Viscosity measurements as a function of temperature and shear rate for the μ-n $BaTiO_3$ feedstock

Table A4.10. Viscosity measurements as a function of temperature and shear rate for the wax polymer binder

shear rate, s^{-1}	viscosity, Pa.s		
	415 K	425 K	430 K
10	142.5	39.3	19.5
25	90.7	28.8	15.4
50	63.0	21.7	12.3
80	49.0	17.7	10.3
100	43.1	15.9	9.4
125	37.9	14.2	8.5
200	29.2	11.3	6.9
400	19.6	7.8	5.0
500	17.1	6.9	4.4
1000	11.4	4.7	3.1
2000	7.6	3.2	2.1
2500	6.6	2.8	1.9
3100	5.8	2.4	1.6
4000	5.1	2.1	1.4
5000	4.4	1.9	1.3
6300	3.8	1.6	1.1
8000	3.4	1.4	1.0
10000	2.9	1.2	0.8

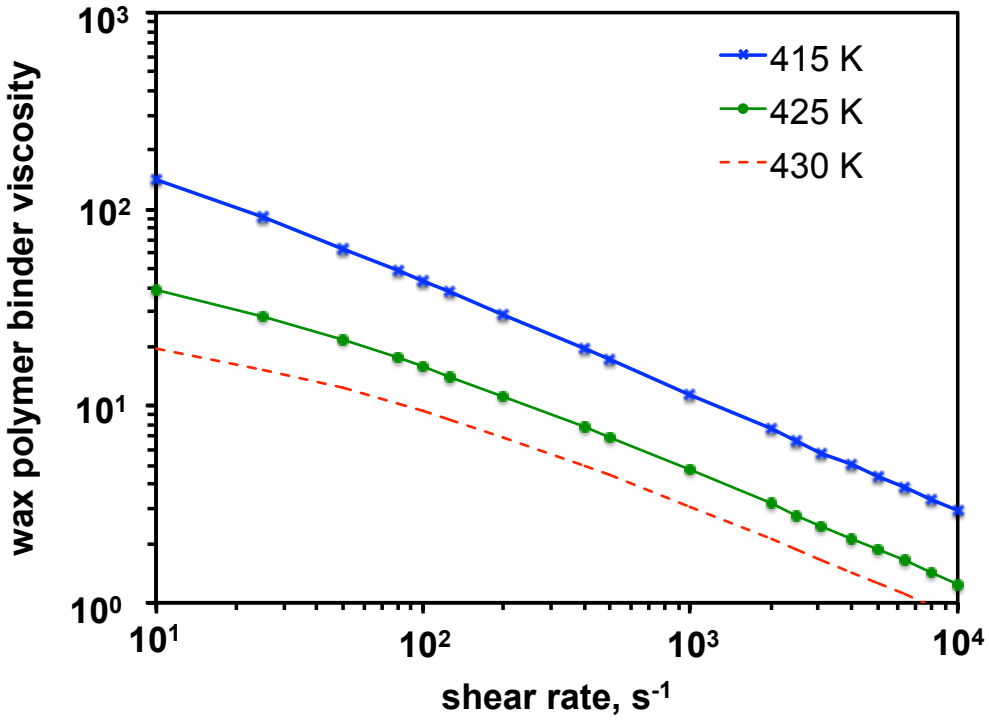

Figure A4.10. Viscosity measurements as a function of temperature and shear rate for the wax polymer binder

Appendix A5: PVT Measurements for Various Ceramic Feedstocks and the Wax Polymer Binder

PVT measurements were conducted for the silicon carbide, aluminum nitride, silicon nitride, mullite composite, ziroconia composite, alumina and barium titanate feedstocks and wax polymer binder system for various temperatures and pressure. A high pressure dilatometer was used to measure specific volume of all ceramic feedstocks. ASTM D792 standard was used for conducting the measurements. Tests were run for temperatures between 296 K and 435 K for pressure between 0 and 200 MPa. The specific volume for different ceramic feedstocks and the wax polymer binder at various pressure and temperature are shown in **Table A5.1-A5.10**. Typical representations of PVT behavior for all ceramic feedstock and the wax polymer binder are shown in **Figure A5.1-A5.10**.

Table A5.1. Specific volume measurements as a function of temperature and pressure for the μ SiC feedstock

temperature, K	specific volume, g/cm^3					
	0 MPa	40 MPa	80 MPa	120 MPa	160 MPa	200 MPa
295	0.4941	0.4906	0.4876	0.4847	0.4828	0.4809
305	0.4949	0.4913	0.4881	0.4856	0.4833	0.4814
314	0.4978	0.4933	0.4895	0.4865	0.4841	0.4819
324	0.5029	0.4988	0.4915	0.4880	0.4853	0.4829
330	0.5057	0.4991	0.4930	0.4889	0.4859	0.4832
344	0.5157	0.5089	0.5002	0.4940	0.4887	0.4854
359	0.5197	0.5122	0.5063	0.5016	0.4958	0.4903
374	0.5248	0.5157	0.5094	0.5046	0.5006	0.4972
389	0.5287	0.5194	0.5124	0.5070	0.5028	0.4991
404	0.5347	0.5236	0.5159	0.5102	0.5053	0.5013
419	0.5392	0.5283	0.5207	0.5146	0.5092	0.5045
435	0.5436	0.5310	0.5227	0.5164	0.5112	0.5072

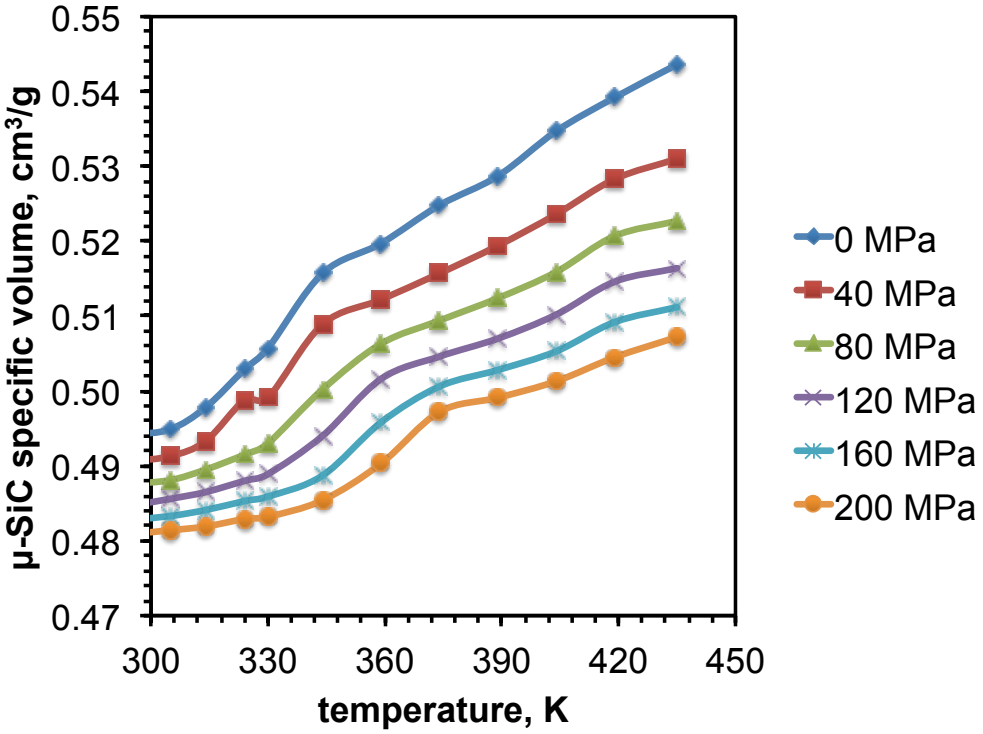

Figure A5.1. Specific volume measurements as a function of temperatures and pressure for the μ SiC feedstock

Table A5.2. Specific volume measurements as a function of temperatures and pressure for the μ-n SiC feedstock

temperature, K	specific volume, g/cm^3					
	0 MPa	40 MPa	80 MPa	120 MPa	160 MPa	200 MPa
300	0.4598	0.4561	0.4534	0.4512	0.4488	0.4478
311	0.4607	0.4568	0.4539	0.4517	0.4501	0.4482
321	0.4644	0.4590	0.4553	0.4526	0.4505	0.4494
332	0.4703	0.4633	0.4583	0.4549	0.4521	0.4501
348	0.4771	0.4723	0.4663	0.4600	0.4558	0.4525
365	0.4815	0.4745	0.4695	0.4653	0.4625	0.4572
380	0.4857	0.4773	0.4716	0.4674	0.4642	0.4612
396	0.4894	0.4802	0.4738	0.4695	0.4653	0.4626
412	0.4937	0.4844	0.4765	0.4714	0.4673	0.4640
426	0.4973	0.4866	0.4804	0.4749	0.4708	0.4675
441	0.5007	0.4888	0.4812	0.4767	0.4722	0.4684
456	0.5034	0.4911	0.4838	0.4780	0.4734	0.4699

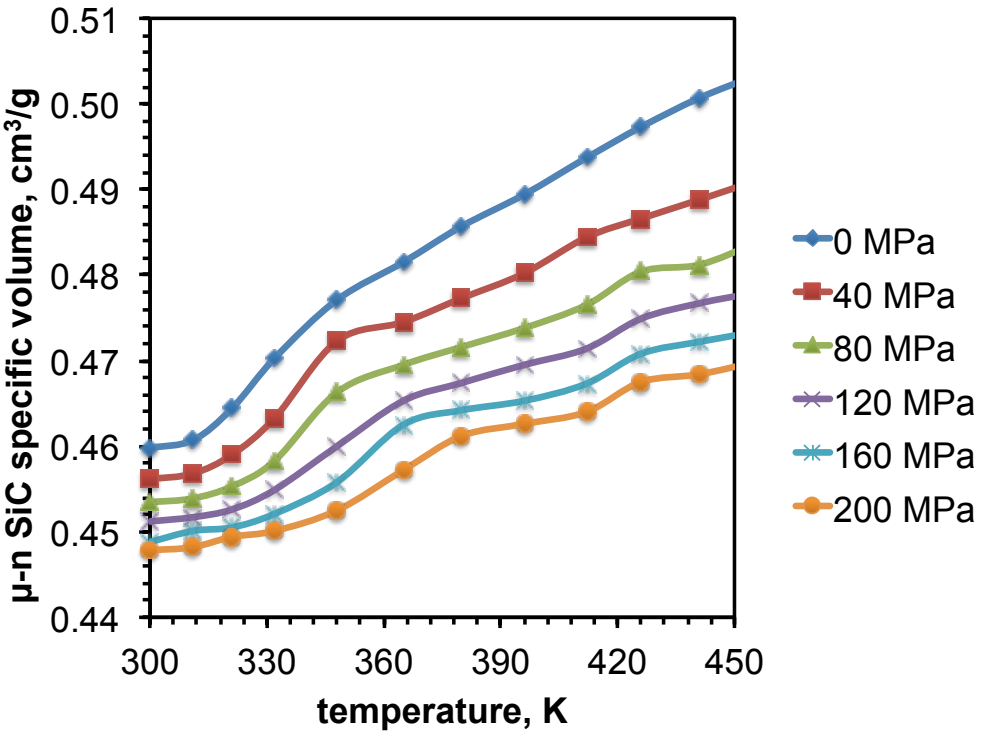

Figure A5.2. Specific volume measurements as a function of temperatures and pressure for the μ-n SiC feedstock

Table A5.3. Specific volume measurements as a function of temperatures and pressure for the μ-AlN feedstock

temperature, K	specific volume, g/cm^3					
	0 MPa	40 MPa	80 MPa	120 MPa	160 MPa	200 MPa
296	0.4658	0.4623	0.4600	0.4577	0.4557	0.4539
305	0.4674	0.4634	0.4607	0.4582	0.4561	0.4542
314	0.4700	0.4652	0.4615	0.4591	0.4568	0.4549
325	0.4747	0.4692	0.4638	0.4603	0.4580	0.4557
329	0.4782	0.4716	0.4654	0.4613	0.4586	0.4562
345	0.4892	0.4825	0.4735	0.4670	0.4621	0.4585
359	0.4930	0.4855	0.4799	0.4754	0.4689	0.4636
374	0.4971	0.4887	0.4825	0.4778	0.4738	0.4705
389	0.5014	0.4924	0.4855	0.4805	0.4761	0.4726
405	0.5069	0.4964	0.4891	0.4832	0.4786	0.4749
420	0.5120	0.5009	0.4933	0.4875	0.4827	0.4786
435	0.5154	0.5033	0.4952	0.4894	0.4846	0.4806

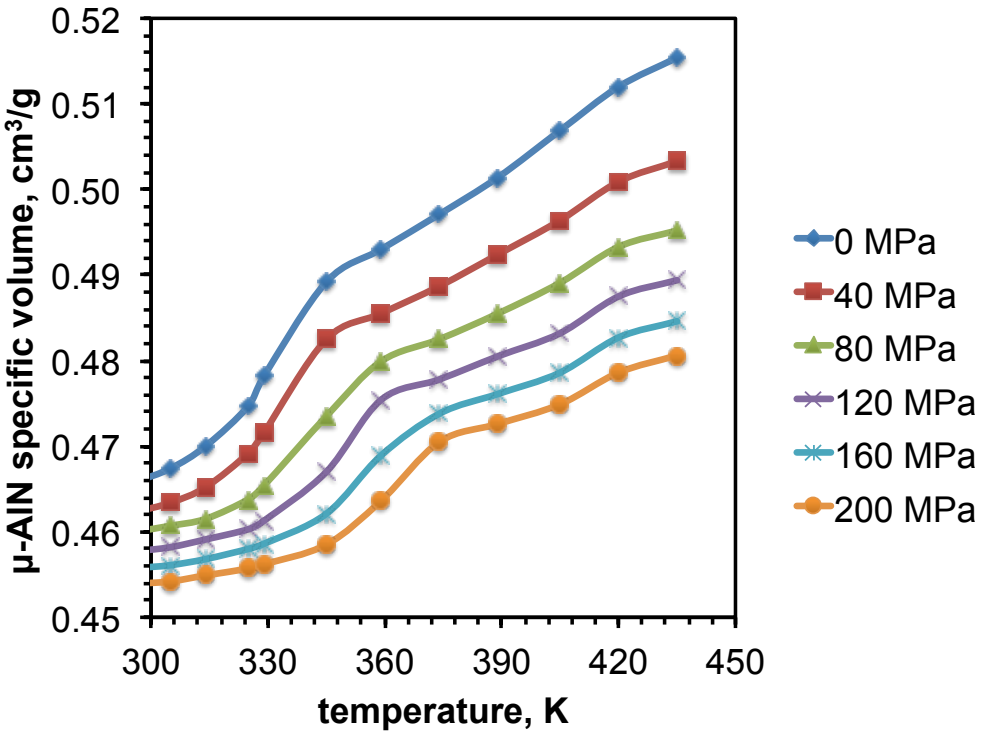

Figure A5.3. Specific volume measurements as a function of temperatures and pressure for the μ-AlN feedstock

Table A5.4. Specific volume measurements as a function of temperatures and pressure for the μ-n AlN feedstock

temperature, K	specific volume, g/cm^3					
	0 MPa	40 MPa	80 MPa	120 MPa	160 MPa	200 MPa
300	0.4326	0.4296	0.4274	0.4256	0.4237	0.4227
309	0.4329	0.4302	0.4279	0.4256	0.4241	0.4228
321	0.4360	0.4317	0.4287	0.4266	0.4246	0.4236
332	0.4411	0.4359	0.4310	0.4282	0.4256	0.4239
349	0.4484	0.4429	0.4377	0.4321	0.4287	0.4260
365	0.4503	0.4442	0.4402	0.4369	0.4344	0.4302
381	0.4536	0.4463	0.4417	0.4379	0.4354	0.4327
396	0.4565	0.4490	0.4439	0.4398	0.4369	0.4345
411	0.4609	0.4520	0.4463	0.4420	0.4385	0.4356
426	0.4638	0.4542	0.4486	0.4443	0.4411	0.4383
441	0.4654	0.4565	0.4502	0.4460	0.4423	0.4396
456	0.4687	0.4580	0.4519	0.4471	0.4437	0.4406

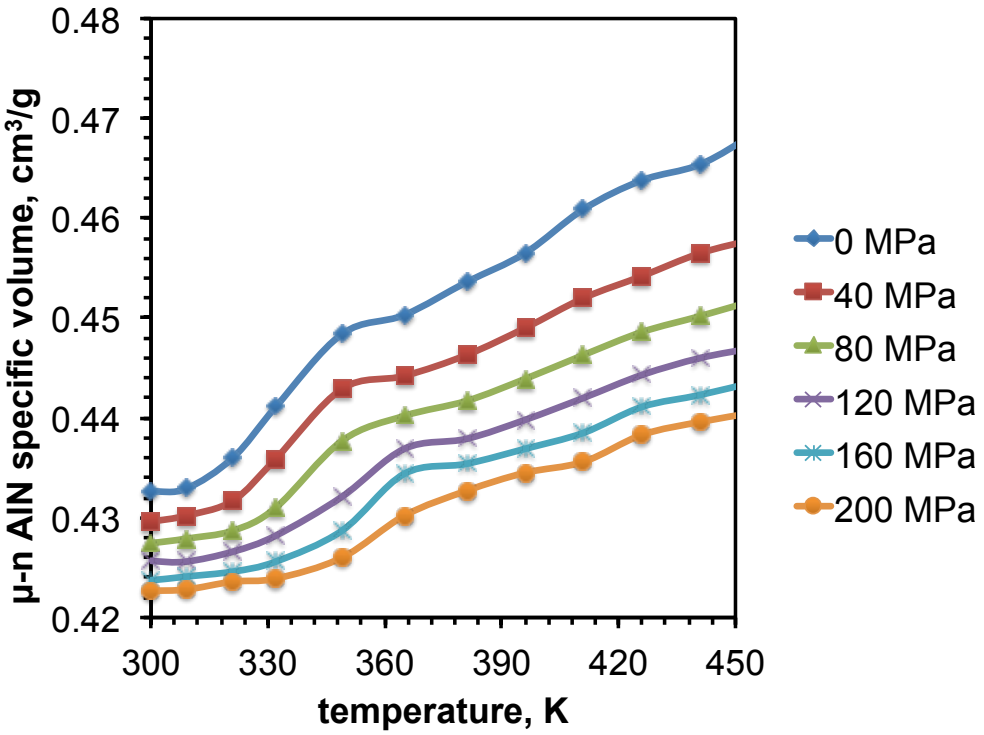

Figure A5.4. Specific volume measurements as a function of temperatures and pressure for the μ-n AlN feedstock

Table A5.5. Specific volume measurements as a function of temperatures and pressure for the μ-n Si_3N_4 feedstock

temperature, K	specific volume, g/cm^3					
	0 MPa	40 MPa	80 MPa	120 MPa	160 MPa	200 MPa
300	0.4326	0.4296	0.4274	0.4256	0.4237	0.4227
309	0.4329	0.4302	0.4279	0.4256	0.4241	0.4228
321	0.4360	0.4317	0.4287	0.4266	0.4246	0.4236
332	0.4411	0.4359	0.4310	0.4282	0.4256	0.4239
349	0.4484	0.4429	0.4377	0.4321	0.4287	0.4260
365	0.4503	0.4442	0.4402	0.4369	0.4344	0.4302
381	0.4536	0.4463	0.4417	0.4379	0.4354	0.4327
396	0.4565	0.4490	0.4439	0.4398	0.4369	0.4345
411	0.4609	0.4520	0.4463	0.4420	0.4385	0.4356
426	0.4638	0.4542	0.4486	0.4443	0.4411	0.4383
441	0.4654	0.4565	0.4502	0.4460	0.4423	0.4396
456	0.4687	0.4580	0.4519	0.4471	0.4437	0.4406

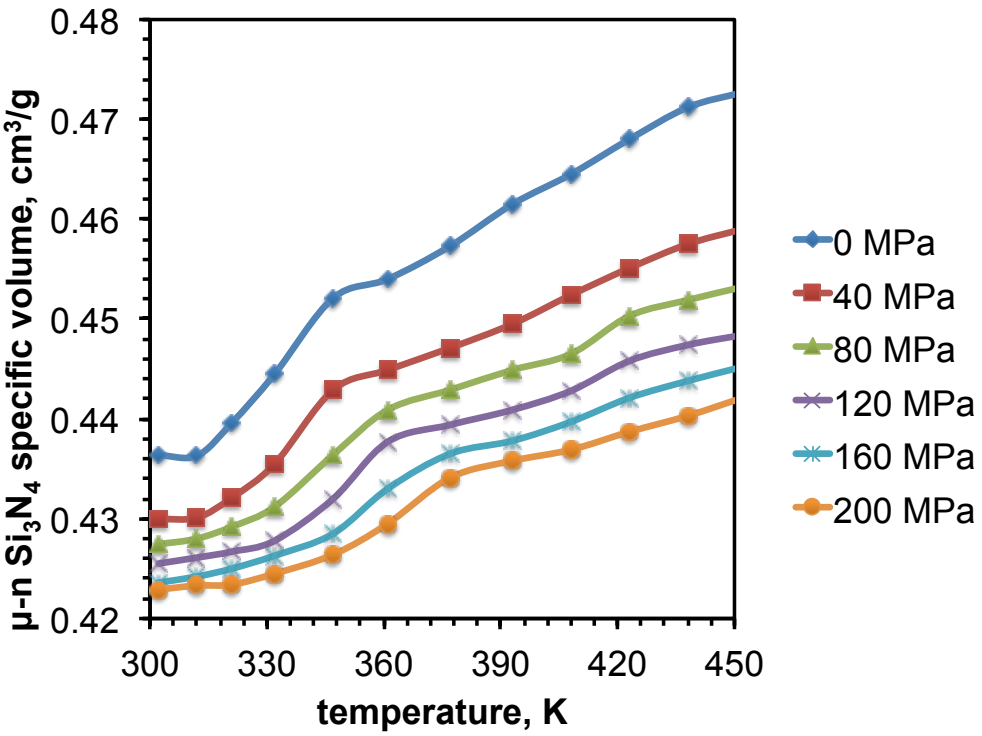

Figure A5.5. Specific volume measurements as a function of temperatures and pressure for the μ-n Si_3N_4 feedstock

Table A5.6. Specific volume measurements as a function of temperatures and pressure for the $3Al_2O_3.2SiO_2$ composite feedstock

temperature, K	specific volume, g/cm^3					
	0 MPa	40 MPa	80 MPa	120 MPa	160 MPa	200 MPa
303	0.3972	0.3930	0.3907	0.3888	0.3871	0.3858
309	0.3980	0.3936	0.3913	0.3893	0.3876	0.3862
319	0.4010	0.3951	0.3922	0.3902	0.3883	0.3868
339	0.4116	0.4024	0.3969	0.3935	0.3907	0.3888
354	0.4144	0.4068	0.4029	0.3982	0.3942	0.3913
369	0.4173	0.4089	0.4047	0.4014	0.3986	0.3953
384	0.4201	0.4110	0.4064	0.4029	0.4000	0.3975
399	0.4236	0.4134	0.4083	0.4045	0.4015	0.3988
414	0.4276	0.4169	0.4110	0.4069	0.4032	0.4003
430	0.4300	0.4189	0.4133	0.4093	0.4059	0.4029
445	0.4326	0.4206	0.4146	0.4107	0.4070	0.4039
460	0.4355	0.4225	0.4162	0.4119	0.4082	0.4050

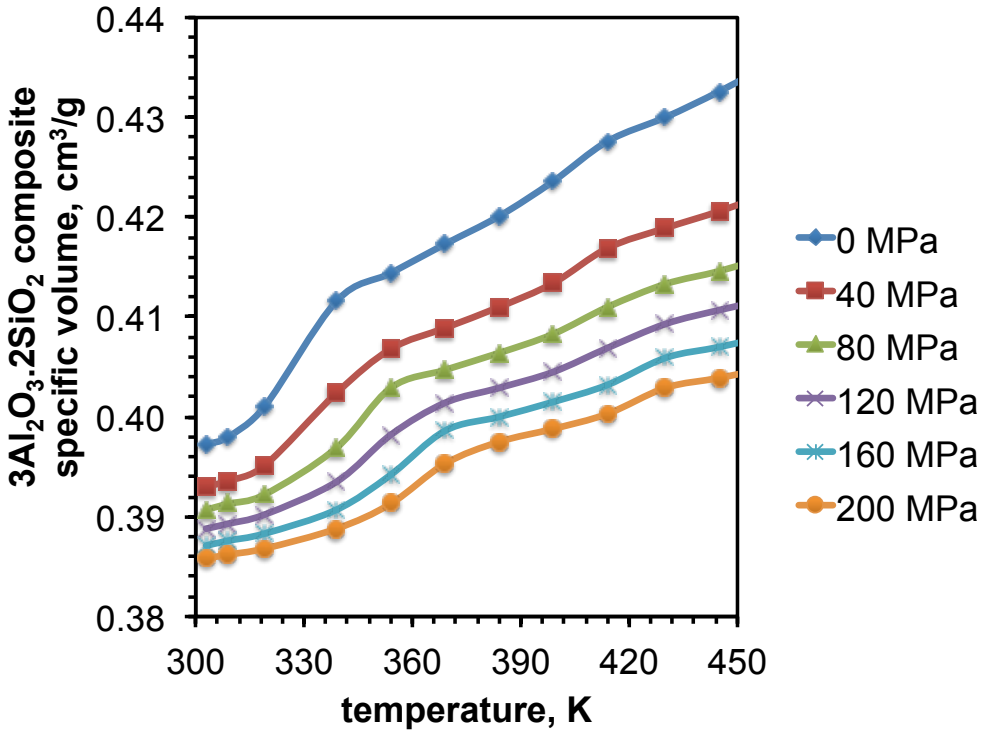

Figure A5.6. Specific volume measurements as a function of temperatures and pressure for the $3Al_2O_3.2SiO_2$ composite feedstock

Table A5.7. Specific volume measurements as a function of temperatures and pressure for the ZrO_2 composite feedstock

temperature, K	specific volume, g/cm^3					
	0 MPa	40 MPa	80 MPa	120 MPa	160 MPa	200 MPa
303	0.3972	0.3930	0.3907	0.3888	0.3871	0.3858
309	0.3980	0.3936	0.3913	0.3893	0.3876	0.3862
319	0.4010	0.3951	0.3922	0.3902	0.3883	0.3868
339	0.4116	0.4024	0.3969	0.3935	0.3907	0.3888
354	0.4144	0.4068	0.4029	0.3982	0.3942	0.3913
369	0.4173	0.4089	0.4047	0.4014	0.3986	0.3953
384	0.4201	0.4110	0.4064	0.4029	0.4000	0.3975
399	0.4236	0.4134	0.4083	0.4045	0.4015	0.3988
414	0.4276	0.4169	0.4110	0.4069	0.4032	0.4003
430	0.4300	0.4189	0.4133	0.4093	0.4059	0.4029
445	0.4326	0.4206	0.4146	0.4107	0.4070	0.4039
460	0.4355	0.4225	0.4162	0.4119	0.4082	0.4050

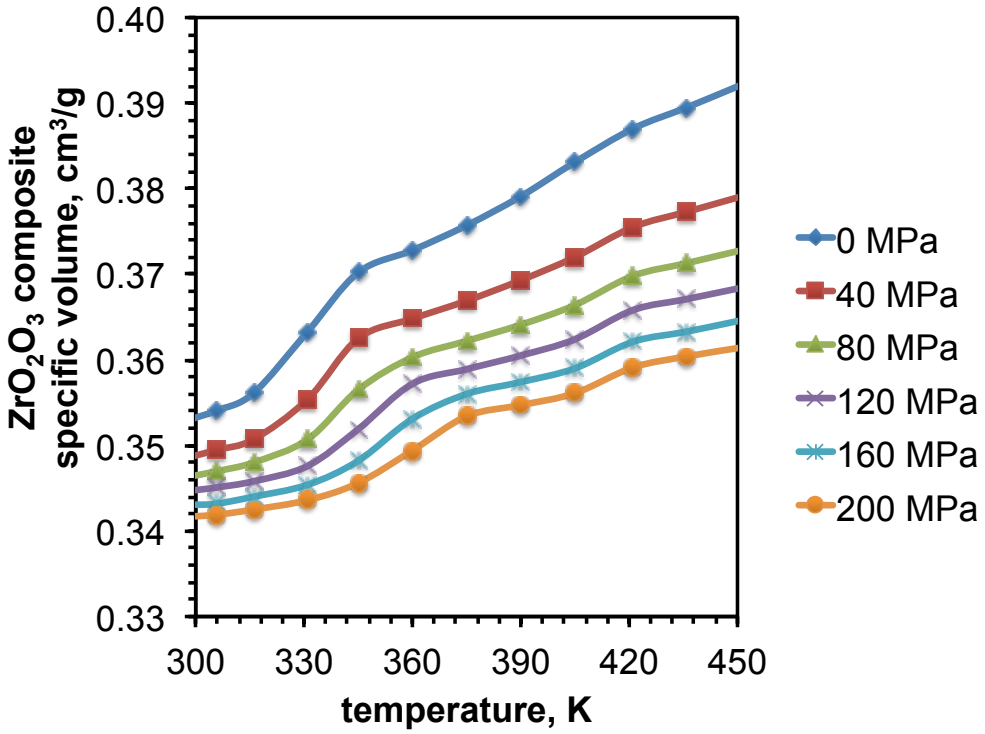

Figure A5.7. Specific volume measurements as a function of temperatures and pressure for the ZrO_2 composite feedstock

Table A5.8. Specific volume measurements as a function of temperatures and pressure for the Al_2O_3 feedstock

temperature, K	specific volume, g/cm^3					
	0 MPa	40 MPa	80 MPa	120 MPa	160 MPa	200 MPa
305	0.3891	0.3864	0.3839	0.3819	0.3805	0.3790
314	0.3911	0.3874	0.3846	0.3826	0.3807	0.3793
324	0.3946	0.3899	0.3859	0.3831	0.3814	0.3798
329	0.3970	0.3916	0.3869	0.3836	0.3817	0.3800
344	0.4043	0.3992	0.3922	0.3872	0.3836	0.3811
359	0.4070	0.4010	0.3968	0.3933	0.3882	0.3846
374	0.4102	0.4034	0.3987	0.3949	0.3920	0.3895
389	0.4136	0.4060	0.4006	0.3965	0.3933	0.3905
404	0.4174	0.4089	0.4028	0.3984	0.3948	0.3920
419	0.4213	0.4121	0.4060	0.4015	0.3978	0.3945
434	0.4239	0.4139	0.4077	0.4028	0.3990	0.3959
449	0.4268	0.4158	0.4092	0.4041	0.4002	0.3969

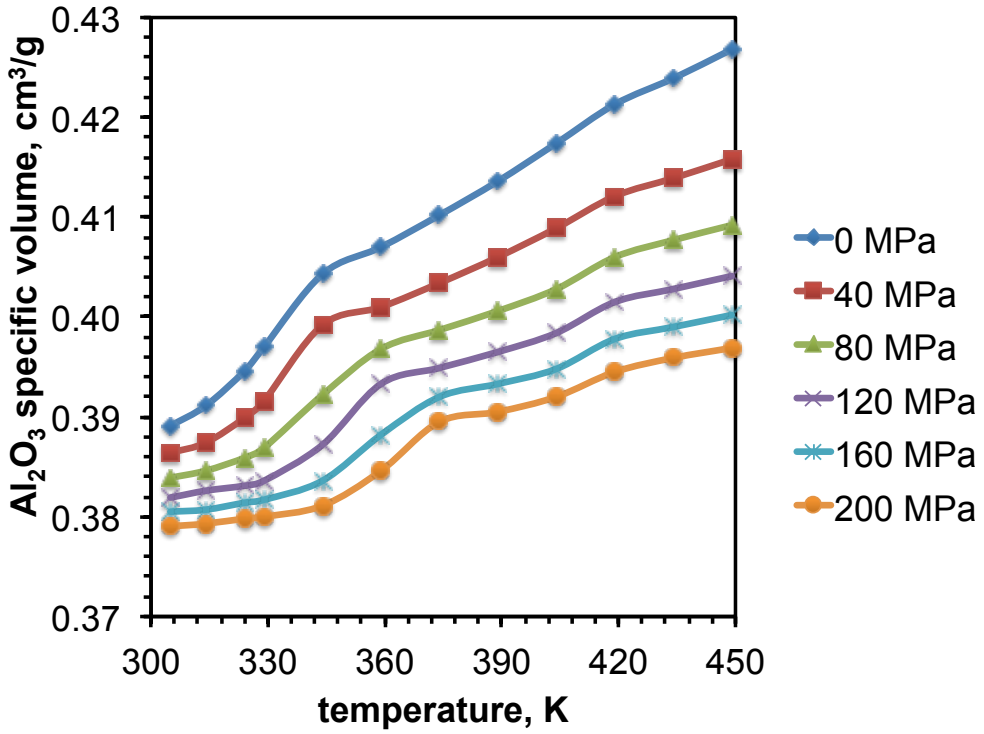

Figure A5.8. Specific volume measurements as a function of temperatures and pressure for the Al_2O_3 feedstock

Table A5.9. Specific volume measurements as a function of temperatures and pressure for the μ-n $BaTiO_3$ feedstock

temperature, K	specific volume, g/cm^3					
	0 MPa	40 MPa	80 MPa	120 MPa	160 MPa	200 MPa
300	0.2707	0.2684	0.2669	0.2655	0.2645	0.2637
311	0.2711	0.2687	0.2671	0.2656	0.2645	0.2640
322	0.2734	0.2700	0.2679	0.2666	0.2653	0.2641
333	0.2765	0.2725	0.2697	0.2673	0.2661	0.2647
349	0.2817	0.2783	0.2751	0.2710	0.2686	0.2664
366	0.2839	0.2798	0.2768	0.2747	0.2726	0.2695
380	0.2858	0.2815	0.2783	0.2758	0.2739	0.2721
396	0.2888	0.2835	0.2799	0.2771	0.2750	0.2732
411	0.2916	0.2853	0.2814	0.2787	0.2764	0.2743
427	0.2935	0.2874	0.2833	0.2807	0.2783	0.2759
441	0.2952	0.2884	0.2842	0.2815	0.2792	0.2769
458	0.2976	0.2897	0.2857	0.2842	0.2797	0.2778

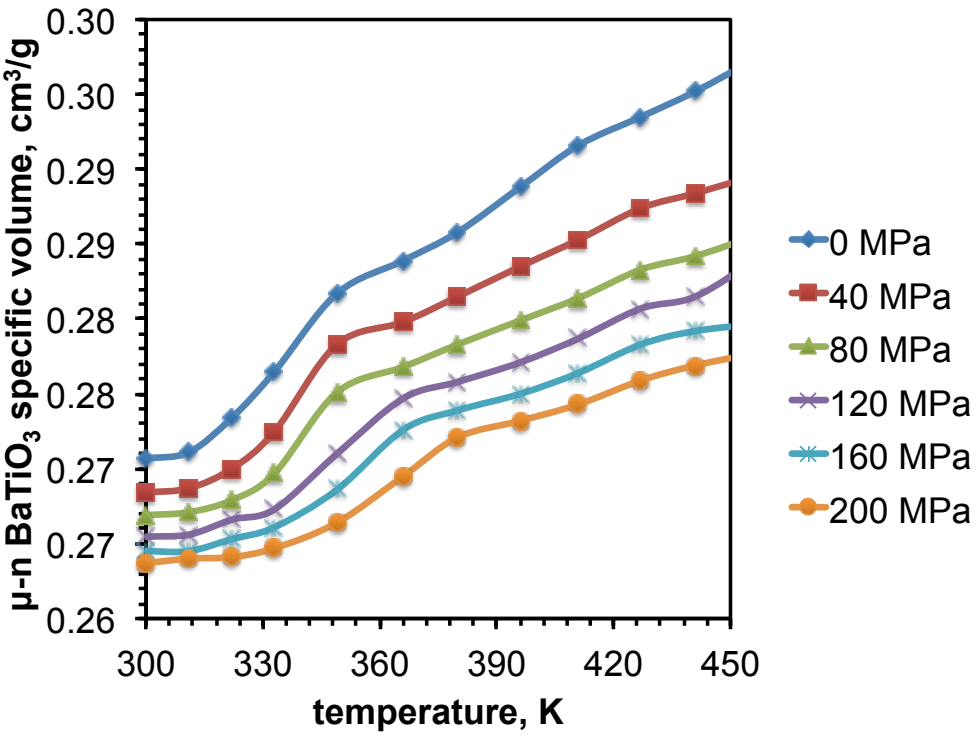

Figure A5.9. Specific volume measurements as a function of temperatures and pressure for the μ-n $BaTiO_3$ feedstock

Table A5.10. Specific volume measurements as a function of temperatures and pressure for the wax polymer binder

temperature, K	specific volume, g/cm^3					
	0 MPa	40 MPa	80 MPa	120 MPa	160 MPa	200 MPa
306	1.1521	1.1346	1.1207	1.1084	1.0980	1.0890
315	1.1640	1.1428	1.1261	1.1136	1.1024	1.0934
326	1.1929	1.1678	1.1394	1.1221	1.1090	1.0979
334	1.2467	1.2011	1.1678	1.1415	1.1194	1.1049
350	1.2733	1.2418	1.2174	1.1819	1.1527	1.1301
365	1.2897	1.2549	1.2277	1.2074	1.1898	1.1645
380	1.3088	1.2682	1.2393	1.2169	1.1981	1.1817
395	1.3324	1.2861	1.2534	1.2283	1.2079	1.1911
410	1.3615	1.3101	1.2745	1.2456	1.2229	1.2025
425	1.3805	1.3251	1.2882	1.2607	1.2385	1.2194
441	1.3975	1.3378	1.2983	1.2693	1.2464	1.2270
457	1.4138	1.3497	1.3085	1.2783	1.2542	1.2336

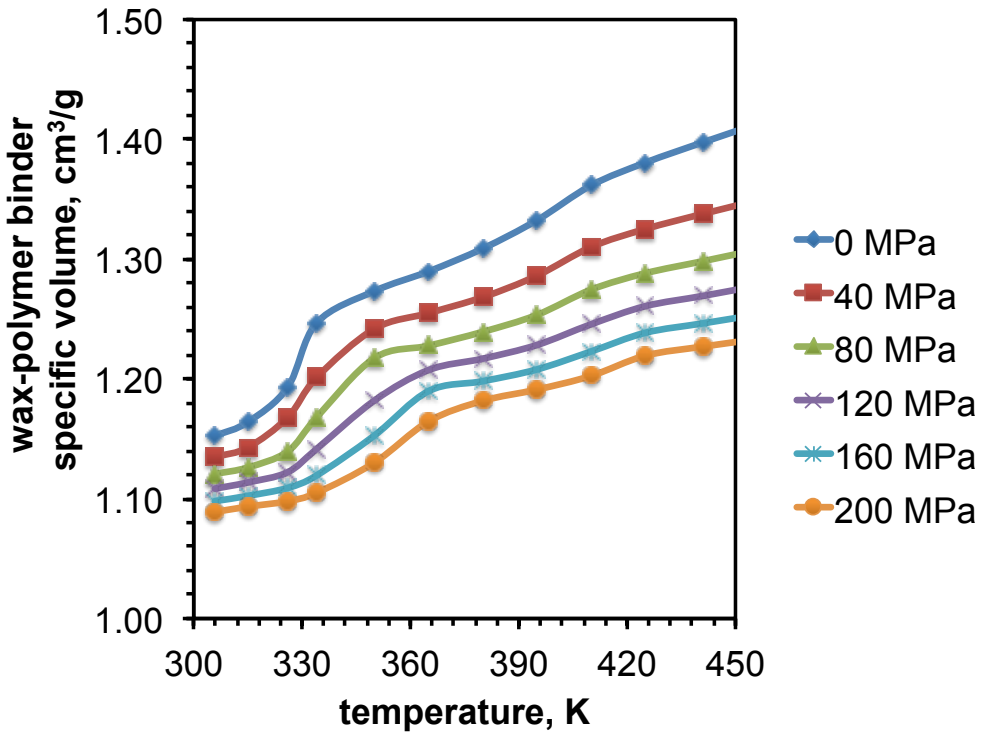

Figure A5.10. Specific volume measurements as a function of temperatures and pressure for the wax polymer binder

Appendix B1: Literature Data of Densities for Various Ceramic Fillers

Density of fillers were collected from literature for the silicon carbide, aluminum nitride, silicon nitride, mullite composite, ziroconia composite, alumina and barium titanate ceramics. Filler properties collected from the literature were reported for 300 K are presented in **Table B1.1-B1.7**

Table B1.1. Density for the SiC fillers

density, kg/m^3	reference
3080	[1]
3100	[2]
3160	[3]
3180	[4]
3220	[5]
3220	[5]
3200	[6]
3220	[5]
3220	[5]
3190	[7]
3360	[8]
3190	[9]
3200	[10]
3160	[3]
3200	[12]
3170	[12]
3200	[12]
2980	[12]
3000	[12]

Table B1.2. Density for the AlN fillers

density, kg/m^3	reference, #
3260	[2]
3330	[2]
3240	[12]
3260	[5]
3260	[13]
3260	[14]
3260	[15]
3260	[16]
3270	[17]
3270	[18]
3250	[19]
3120	[19]
3050	[19]
3250	[19]
3200	[19]
3260	[20]
3180	[21]
3260	[21]
3330	[22]
3280	[22]
3260	[22]
3260	[22]

Table B1.3. Density for the Si_3N_4 fillers

density, kg/m^3	reference, #
3100	[2]
3400	[23]
3200	[24]
3270	[25]
3240	[25]
3280	[26]
3120	[26]
3190	[26]
3210	[26]
3180	[26]
3270	[27]

Table B1.4. Density for the $Al_2O_3.2SiO_2$ fillers

density, kg/m^3	reference, #
2780	[28]
3160	[29]
3190	[30]
3070	[31]
3030	[32]

Table B1.6. Density for the Al_2O_3 fillers

density, kg/m^3	**reference #**
3710	[1]
3800	[2]
3980	[2]
3974	[28]
3840	[33]
3790	[33]
3590	[34]
3950	[34]
3940	[34]
3980	[35]

Table B1.7. Density for the $BaTiO_3$ fillers

density, kg/m^3	**reference #**
5830	[36]
5790	[37]
5970	[37]
5996	[38]
6000	[37]
5590	[39]
5480	[39]
5700	[40]
5900	[40]

Appendix B2: Literature Data of Specific Heats for Various Ceramic Fillers

Specific heats for fillers were collected from literature for the silicon carbide, aluminum nitride, silicon nitride, mullite composite, ziroconia composite, alumina and barium titanate ceramics. Filler properties collected from the literature were reported for 300 K are presented in **Table B1.1-B1.7**

Table B2.1. Specific heat for the SiC fillers

specific heat, J/kg.K	reference, #
663	[2]
650	[12]
671	[41]
690	[42]
656	[43]
672	[43]
676	[43]
682	[43]
661	[44]
661	[44]
660	[44]
662	[44]
715	[3]
660	[11]
660	[11]
670	[11]
700	[11]
670	[11]

Table B2.2. Specific heat for the AlN fillers

specific heat , J/kg.K	reference
780	[2]
820	[2]
734	[41]
820	[42]
740	[43]
710	[43]

Table B2.3. Specific heat for the Si_3N_4 fillers

specific heat, J/kg.K	reference, #
670	[2]
713	[42]
700	[42]
660	[45]
710	[46]

Table B2.4. Specific heat for the $Al_2O_3.2SiO_2$ fillers

specific heat, J/kg.K	reference, #
740	[41]
770	[43]
750	[47]
770	[47]
760	[48]

Table B2.6. Specific heat for the Al_2O_3 fillers

specific heat, J/kg.K	**reference #**
790	[2]
820	[2]
775	[41]
838	[42]
777	[43]
780	[43]
779	[43]
779	[43]
782	[43]
795	[43]
779	[43]
755	[35]
772	[49]

Table B2.7. Specific heat for the $BaTiO_3$ fillers

specific heat, J/kg.K	**reference #**
398	[50]
438	[50]
586	[43]
440	[43]
439	[43]
440	[43]
434	[50]
406	[50]

Appendix B3: Literature Data of Thermal Conductivities for Various Ceramic Fillers

Thermal conductivity of fillers were collected from literature for the silicon carbide, aluminum nitride, silicon nitride, mullite composite, ziroconia composite, alumina and barium titanate ceramics. Filler properties collected from the literature were reported for 300 K are presented in **Table B3.1-B1.7**

Table B3.1. Thermal conductivity for the SiC fillers

thermal conductivity, W/m.K	reference
130	[2]
114	[3]
135	[42]
135	[51]
270	[52]
270	[52]
152	[44]
200	[44]
202	[44]
206	[44]
120	[10]
114	[35]
270	[53]
150	[11]
161	[11]
165	[11]
242	[11]
163	[11]

Table B3.2. Thermal conductivity for the AlN fillers

thermal conductivity, W/m.K	reference, #
200	[2]
140	[2]
200	[12]
195	[5]
180	[13]
170	[14]
170	[15]
155	[16]
140	[17]
148	[18]
148	[19]
148	[19]
167	[19]
148	[19]
180	[19]
152	[20]
160	[21]
180	[21]

Table B3.3. Thermal conductivity for the Si_3N_4 fillers

thermal conductivity, W/m.K	reference, #
22	[2]
30	[2]
28	[42]
17	[42]
19	[51]
22	[52]
24	[47]
25	[54]
29	[55]
26	[55]
22	[46]
30	[51]

Table B3.4. Thermal conductivity for the $Al_2O_3.2SiO_2$ fillers

thermal conductivity, W/m.K	**reference #**
6	[36]
7	[42]
3	[51]
6	[52]
4	[52]
5	[36]
5	[47]

Table B3.6. Thermal conductivity for the Al_2O_3 fillers

thermal conductivity, W/m.K	reference, #
26	[2]
39	[2]
23	[56]
37	[42]
24	[51]
33	[52]
26	[52]
33	[3]
20	[57]
29	[49]
36	[27]

Table B3.7. Thermal conductivity for the $BaTiO_3$ fillers

thermal conductivity, W/m.K	**reference #**
2.59	[50]
2.89	[50]
2.60	[51]
2.61	[50]
2.85	[50]

References

[1] J. B. Wachtman and D. G. Lam, “Young’s Modulus of Various Refractory Materials as a Function of Temperature,” *J. Am. Ceram. Soc.*, vol. 42, no. 5, pp. 254–260, 1959.

[2] “Granta’s CES EduPack and teaching resources: supporting Materials Education.” [Online]. Available: http://www.grantadesign.com/education/. [Accessed: 27-Sep-2013].

[3] R. G. Munro, “Material Properties of a Sintered α-SiC,” *J. Phys. Chem. Ref. Data*, vol. 26, no. 5, p. 1195, Sep. 1997.

[4] R. A. Alliegro, L. B. Coffin, and J. R. Tinklepaugh, “Pressure-Sintered Silicon Carbide,” *J. Am. Ceram. Soc.*, vol. 39, no. 11, pp. 386–389, 1956.

[5] K. Biswas, J. Schneider, G. Rixecker, and F. Aldinger, “Comparative bending creep behaviour of silicon carbide sintered with oxynitride additives,” *Scr. Mater.*, vol. 53, no. 5, pp. 591–596, Sep. 2005.

[6] S. Zhu, W. G. Fahrenholtz, and G. E. Hilmas, “Influence of silicon carbide particle size on the microstructure and mechanical properties of zirconium diboride–silicon carbide ceramics,” *J. Eur. Ceram. Soc.*, vol. 27, no. 4, pp. 2077–2083, 2007.

[7] M. Hotta and J. Hojo, “Inhibition of grain growth in liquid-phase sintered SiC ceramics by AlN additive and spark plasma sintering,” *J. Eur. Ceram. Soc.*, vol. 30, no. 10, pp. 2117–2122, Aug. 2010.

[8] J. Hu, H. Xiao, W. Guo, Q. Li, W. Xie, and B. Zhu, “Effect of AlN–Y2O3 addition on the properties and microstructure of in-situ strengthened SiC–TiB2 composites prepared by hot pressing,” *Ceram. Int.*, vol. 40, no. 1, Part A, pp. 1065–1071, Jan. 2014.

[9] V. A. Izhevskyi, L. A. Genova, A. H. A. Bressiani, and J. C. Bressiani, “Microstructure and properties tailoring of liquid-phase sintered SiC,” *Int. J. Refract. Met. Hard Mater.*, vol. 19, no. 4–6, pp. 409–417, Jul. 2001.

[10] L. S. Sigl, “Thermal conductivity of liquid phase sintered silicon carbide,” *J. Eur. Ceram. Soc.*, vol. 23, no. 7, pp. 1115–1122, Jun. 2003.

[11] G.-D. Zhan, M. Mitomo, R.-J. Xie, and A. K. Mukherjee, “Thermal and Electrical Properties in Plasma-Activation-Sintered Silicon Carbide with Rare-Earth-Oxide Additives,” *J. Am. Ceram. Soc.*, vol. 84, no. 10, pp. 2448–2450, Oct. 2001.

[12] J. R. Groza and A. Zavaliangos, “Sintering activation by external electrical field,” *Mater. Sci. Eng. A*, vol. 287, no. 2, pp. 171–177, Aug. 2000.

[13] J. Gu, Q. Zhang, J. Dang, J. Zhang, and Z. Yang, “Thermal conductivity and mechanical properties of aluminum nitride filled linear low-density polyethylene composites,” *Polym. Eng. Sci.*, vol. 49, no. 5, pp. 1030–1034, May 2009.

[14] R. Kochetov, T. Andritsch, U. Lafont, P. H. F. Morshuis, S. J. Picken, and J. J. Smit, “Preparation and dielectric properties of epoxy - BN and epoxy - AlN nanocomposites,” in *IEEE Electrical Insulation Conference, 2009. EIC 2009*, 2009, pp. 397–400.

[15] W. Zhou, “Thermal and dielectric properties of the AlN particles reinforced linear low-density polyethylene composites,” *Thermochim. Acta*, vol. 512, no. 1–2, pp. 183–188, Jan. 2011.

[16] B. L. Zhu, J. Ma, J. Wu, K. C. Yung, and C. S. Xie, “Study on the properties of the epoxy-matrix composites filled with thermally conductive AlN and BN ceramic particles,” *J. Appl. Polym. Sci.*, vol. 118, no. 5, pp. 2754–2764, Dec. 2010.

[17] S. H. Risbud, J. R. Groza, and M. J. Kim, “Clean grain boundaries in aluminium nitride ceramics densified without additives by a plasma-activated sintering process,” *Philos. Mag. Part B*, vol. 69, no. 3, pp. 525–533, 1994.

[18] K. A. Khor, K. H. Cheng, L. G. Yu, and F. Boey, “Thermal conductivity and dielectric constant of spark plasma sintered aluminum nitride,” *Mater. Sci. Eng. A*, vol. 347, no. 1–2, pp. 300–305, Apr. 2003.

[19] M. Medraj, “Understanding AlN sintering through computational thermodynamics combined with experimental investigation,” *J. Mater. Process. Tech*, vol. 161, no. 3, pp. 415–422.

[20] L. Qiao, H. Zhou, K. Chen, and R. Fu, “Effects of Li2O on the low temperature sintering and thermal conductivity of AlN ceramics,” *J. Eur. Ceram. Soc.*, vol. 23, no. 9, pp. 1517–1524, Aug. 2003.

[21] L. Qiao, H. Zhou, and R. Fu, “Thermal conductivity of AlN ceramics sintered with CaF2 and YF3,” *Ceram. Int.*, vol. 29, no. 8, pp. 893–896, 2003.

[22] F. Miyashiro, N. Iwase, A. Tsuge, F. Ueno, M. Nakahashi, and T. Takahashi, “High thermal conductivity aluminum nitride ceramic substrates and packages,” *IEEE Trans. Compon. Hybrids Manuf. Technol.*, vol. 13, no. 2, pp. 313–319, 1990.

[23] G. Ziegler, J. Heinrich, and G. Wötting, “Relationships between processing, microstructure and properties of dense and reaction-bonded silicon nitride,” *J. Mater. Sci.*, vol. 22, no. 9, pp. 3041–3086, Sep. 1987.

[24] M. Fukuhara, K. Fukazawa, and A. Fukawa, “Physical properties and cutting performance of silicon nitride ceramic,” *Wear*, vol. 102, no. 3, pp. 195–210, Apr. 1985.

[25] X. Zhu, Y. Zhou, and K. Hirao, “Effect of Sintering Additive Composition on the Processing and Thermal Conductivity of Sintered Reaction-Bonded Si3N4,” *J. Am. Ceram. Soc.*, vol. 87, no. 7, pp. 1398–1400, Jul. 2004.

[26] B. R. Golla, “Effect of particle size and oxygen content of Si on processing, microstructure and thermal conductivity of sintered reaction bonded Si3N4,” vol. 595, no. Complete, pp. 60–66.

[27] X. Zhu, “Effects of processing method and additive composition on microstructure and thermal conductivity of Si3N4 ceramics,” *J. Eur. Ceram. Soc.*, vol. 26, no. 4–5, pp. 711–718.

[28] J. B. Wachtman, T. G. Scuderi, and G. W. Cleek, “Linear Thermal Expansion of Aluminum Oxide and Thorium Oxide from 100° to 1100°K,” *J. Am. Ceram. Soc.*, vol. 45, no. 7, pp. 319–323, 1962.

[29] M. A. Camerucci, G. Urretavizcaya, M. S. Castro, and A. L. Cavalieri, “Electrical properties and thermal expansion of cordierite and cordierite-mullite materials,” *J. Eur. Ceram. Soc.*, vol. 21, no. 16, pp. 2917–2923, Dec. 2001.

[30] K. S. Mazdiyasni, C. T. Lynch, and J. S. S. Ii, “Cubic Phase Stabilization of Translucent Yttria-Zirconia at Very Low Temperatures,” *J. Am. Ceram. Soc.*, vol. 50, no. 10, pp. 532–537, 1967.

[31] M. I. Osendi and C. Baudín, “Mechanical properties of mullite materials,” *J. Eur. Ceram. Soc.*, vol. 16, no. 2, pp. 217–224, 1996.

[32] T. M. Kyaw, Y. Okamoto, and K. Hayashi, “Thermal Conductivity of Mullite-Zirconia Composites,” *J. Ceram. Soc. Jpn.*, vol. 103, no. 1204, pp. 1289–1292, 1995.

[33] S. A. Hassanzadeh-Tabrizi and E. Taheri-Nassaj, “Compressibility and sinterability of Al2O3–YAG nanocomposite powder synthesized by an aqueous sol–gel method,” *J. Alloys Compd.*, vol. 506, no. 2, pp. 640–644, Sep. 2010.

[34] N. Shinohara, M. Okumiya, T. Hotta, K. Nakahira, M. Naito, and K. Uematsu, “Seasonal Variation of Microstructure and Sintered Strength of Dry-Pressed Alumina,” *J. Am. Ceram. Soc.*, vol. 82, no. 12, pp. 3441–3446, Dec. 1999.

[35] M. Munro, “Evaluated Material Properties for a Sintered alpha-Alumina,” *J. Am. Ceram. Soc.*, vol. 80, no. 8, pp. 1919–1928, Aug. 1997.

[36] H. Schneider, J. Schreuer, and B. Hildmann, “Structure and properties of mullite—A review,” *J. Eur. Ceram. Soc.*, vol. 28, no. 2, pp. 329–344, 2008.

[37] A. Polotai, K. Breece, E. Dickey, C. Randall, and A. Ragulya, “A Novel Approach to Sintering Nanocrystalline Barium Titanate Ceramics,” *J. Am. Ceram. Soc.*, vol. 88, no. 11, pp. 3008–3012, 2005.

[38] X. Wang, X. Deng, H. Wen, and L. Li, “Phase transition and high dielectric constant of bulk dense nanograin barium titanate ceramics,” *Appl. Phys. Lett.*, vol. 89, no. 16, p. 162902, 2006.

[39] J.-F. Chen, Z.-G. Shen, F.-T. Liu, X.-L. Liu, and J. Yun, “Preparation and properties of barium titanate nanopowder by conventional and high-gravity reactive precipitation methods,” *Scr. Mater.*, vol. 49, no. 6, pp. 509–514, Sep. 2003.

[40] K. S. Mazdiyasni, R. T. Dolloff, and J. S. Smith, “Preparation of High-Purity Submicron Barium Titanate Powders,” *J. Am. Ceram. Soc.*, vol. 52, no. 10, pp. 523–526, Oct. 1969.

[41] W. M. Haynes, *CRC Handbook of Chemistry and Physics, 95th Edition*. CRC Press, 2014.

[42] F. Cardarelli, *Materials Handbook: A Concise Desktop Reference*. Springer Science & Business Media, 2008.

[43] P. U. T. P. R. Center, *Thermophysical Properties of Matter: Specific heat: metallic elements and alloys, by Y. S. Touloukian and E. H. Buyco*. IFI/Plenum, 1970.

[44] Y. Zhou, K. Hirao, K. Watari, Y. Yamauchi, and S. Kanzaki, “Thermal conductivity of silicon carbide densified with rare-earth oxide additives,” *J. Eur. Ceram. Soc.*, vol. 24, no. 2, pp. 265–270, 2004.

[45] Anonym, “Amedica signs agreement with Kyocera for silicon nitride medical devices,” *PIM Int.*, vol. 8, no. 1, p. 11, 2014.

[46] J. F. Shackelford and W. Alexander, *CRC Materials Science and Engineering Handbook, Third Edition*. CRC Press, 2000.

[47] “By Material | Fine Ceramics (Advanced Ceramics) | Kyocera,” Jan-2010. [Online]. Available: http://global.kyocera.com/prdct/fc/list/material/index.html. [Accessed: 02-Jun-2015].

[48] N. P. Bansal, *Handbook of Ceramic Composites*. Springer Science & Business Media, 2006.

[49] R. Barea, M. Belmonte, M. I. Osendi, and P. Miranzo, “Thermal conductivity of Al2O3/SiC platelet composites,” *J. Eur. Ceram. Soc.*, vol. 23, no. 11, pp. 1773–1778, Oct. 2003.

[50] Y. He, “Heat capacity, thermal conductivity, and thermal expansion of barium titanate-based ceramics,” *Thermochim. Acta*, vol. 419, no. 1–2, pp. 135–141, Sep. 2004.

[51] Y. S. Touloukian, *Thermophysical Properties of Matter: Thermal conductivity : nonmetallic solids*. IFI/Plenum, 1970.

[52] M. Bauccio, *ASM engineered materials reference book*. ASM International, 1994.

[53] H. Nakano, K. Watari, H. Hayashi, and K. Urabe, “Microstructural Characterization of High-Thermal-Conductivity Aluminum Nitride Ceramic,” *J. Am. Ceram. Soc.*, vol. 85, no. 12, pp. 3093–3095, Dec. 2002.

[54] K. G. Budinski and M. K. Budinski, *Engineering Materials: Properties and Selection*. Prentice Hall, 2010.

[55] “Si3N4 brochure,” Ceradyne, press release.

[56] J.-W. Bae, W. Kim, S.-H. Cho, and S.-H. Lee, “The properties of AlN-filled epoxy molding compounds by the effects of filler size distribution,” *J. Mater. Sci.*, vol. 35, no. 23, pp. 5907–5913, Dec. 2000.

[57] T. Nemoto, “Thermal conductivity of alumina and silicon carbide ceramics at low temperatures,” *Cryogenics*, vol. 25, no. 9, pp. 531–532.

Appendix C: Procedure to determine Cross-WLF Constants

The Cross-WLF model **Equation C.1** was used to calculate viscosity values at different shear rates and four different temperatures using the experimentally available data for Cross-WLF coefficients (**Table C.1**) for matrix and 0.52 volume fractions AlN.

$$\eta = \frac{\eta_0}{1 + \left(\frac{\eta_0 \gamma}{\tau^*}\right)^{1-n}} \qquad \text{(C.1)}$$

where, η is the melt viscosity (Pa-s), η_0 is the zero shear viscosity, γ is the shear rate (1/s), τ^* is the critical stress level at the transition to shear thinning, and n is the power law index in the high shear rate regime.

Table B.1: Experimental values of Cross-WLF coefficients

	binder [b]	0.52 volume fraction of AlN [c]
n	0.40	0.38
tau	793.46	117.77
D1	4.29E+23	8.78E+10
D2	333.00	263.15
A1	78.13	14.24
A2	51.60	51.60
T*=D2		

Using the data given in **Table C.1** zero shear viscosity η_0 was calculated for both binder and 0.52 volume fraction of AlN at temperatures of 413, 419.5, 426 and 433 K. This was calculated using **Equation C.2**.

$$\eta_0 = D_1 exp\left[-\frac{A_1(T - T^*)}{A_2 + (T - T^*)}\right] \qquad C.2$$

where, T is the temperature (K). T^*, D_1 and A_1, are WLF coefficients. Using **Equation C.2** η_o values were calculated at 413, 419.5, 426, and 433 K at different shear rates for matrix and 0.52 volume fractions AlN. An illustration for this calculation is shown in **Table C.2:**

Table C.2: Calculation of zero shear viscosity for matrix and 0.52 volume fraction of AlN at different shear rates.

viscosity, Pa·s	binder [b]	0.52 volume fraction of AlN [c]
temperature, K	η_o, Pa·s	η_o, Pa·s
413	1013	2209728
419.5	239	1971689
426	64	1771490
433	18	1589698

This information was used to calculate viscosity values for binder and 0.52 volume fraction AlN at different shear rate ranging 1 x 10^{-10} to 7.5 x 10^{4}. This was done using **Equations C.1 and C.2.** Viscosity was calculated for four different temperatures 413, 426, 433, nd 433 K. An illustration for calculating viscosity at 413 K for different shear rates is shown in **Table C.3.**

Table B.3: Calculation of viscosity for matrix and 0.52 volume fraction of AlN for different shear rates and at 413 K.

shear rate, s^{-1}	viscosity, Pa·s	
	matrix [m]	0.52 volume fraction of AlN [c]
0.01	943.36	81855.52
0.02	911.30	53871.75
0.50	574.01	7422.34
0.70	523.40	6023.75
0.80	503.17	5544.56
0.90	485.32	5153.55
100.00	52.63	275.29
125.89	46.16	238.54
158.49	40.45	206.69
199.53	35.43	179.10
501.19	20.72	100.96
630.96	18.09	87.48
794.33	15.80	75.80
1000.00	13.79	65.68
1258.93	12.04	56.91
1584.89	10.50	49.31
1995.26	9.16	42.73
2511.89	7.99	37.02
10000.00	3.51	15.67

Further the simplified Krieger Dougherty model as given in **Equation C.1** was used to calculate critical solids loading (ϕ_{max}) for each shear rate between 0.48 to 0.52 volume fractions AlN. A floating ϕ_{max} (maximum packing fraction of the powder) value corresponding to each shear rate given in **Table C.4** was calculated at 413, 419.5, 426, and 433 K.

Table C.4: Calculation of maximum volume fraction for each individual temperature at different shear rates.

shear rate, s^{-1}	ϕ_{max} at temperature, 413 K
0.01	0.58
0.02	0.60
0.03	0.61
0.04	0.62
0.05	0.62
0.06	0.63
0.07	0.63
0.08	0.64
0.09	0.64
0.10	0.65
0.20	0.68
0.30	0.70
0.40	0.71
0.50	0.72
1000.00	0.96
1258.93	0.96
1584.89	0.97
1995.26	0.97
2511.89	0.97
3162.28	0.97
3981.07	0.98
5011.87	0.98
6309.57	0.98
7943.28	0.98
10000.00	0.99

Using the floating ϕ_{max} values at different shear rates and temperatures, viscosity (η) values are calculated using **Equation C.3** for 0.48, 0.49, 0.5, 0.51 and 0.52 volume fractions at the above mentioned four different temperatures. An illustration of η calculation at 413 K for 0.48 volume fractions AlN is shown in **Table C.5.**

Table C.5: Calculation of viscosity at different shear rates for 413 K using floating ϕ_{max} and **Equation C.1**

volume fraction powder	0.48
shear rate, s^{-1}	viscosity, Pa·s
0.10	11664.85
0.20	8311.55
0.30	6754.84
0.40	5808.88
0.50	5157.09
0.60	4673.52
0.70	4296.72
0.80	3992.66
0.90	3740.77
100.00	227.92
125.89	197.88
158.49	171.77
251.19	129.38
316.23	112.28
398.11	97.42
501.19	84.52
630.96	73.33
794.33	63.62
1000.00	55.19
1258.93	47.87
1584.89	41.52
1995.26	36.02
2511.89	31.24
3162.28	27.10
3981.07	23.50
5011.87	20.38
6309.57	17.68
7943.28	15.33
10000.00	13.30

In order to calculate Cross-WLF coefficients from the interpolated data as represented in **Table C.5** a GRG nonlinear solver was used. In order to do so, viscosities at different shear rate were calculated from **Equation C.1** in an

Excel spreadsheet. The zero shear viscosity value was taken as the constant value obtained from the interpolated data while an initial informed guess was done on the Cross-WLF coefficients n and τ*. A square of difference was calculated for viscosity values at each shear rate between the interpolated viscosity and viscosity calculated from **Equation C.1**. Sum of the square of difference was calculated and the GRG nonlinear solver was used to minimize the sum of square of difference (SSD). It was observed that the data fitted best in the low shear rate region but deviated in the high shear rate region. In order to further get a best fit between the experimental and the calculated data, SSD was calculated for high shear rate region and solver was used to find the Cross-WLF coefficients n (power law index) and τ* (critical stress level). An illustration of the curve-fitted data is shown in **Figure C.1** and SSD calculation is shown in **Table C.6.**

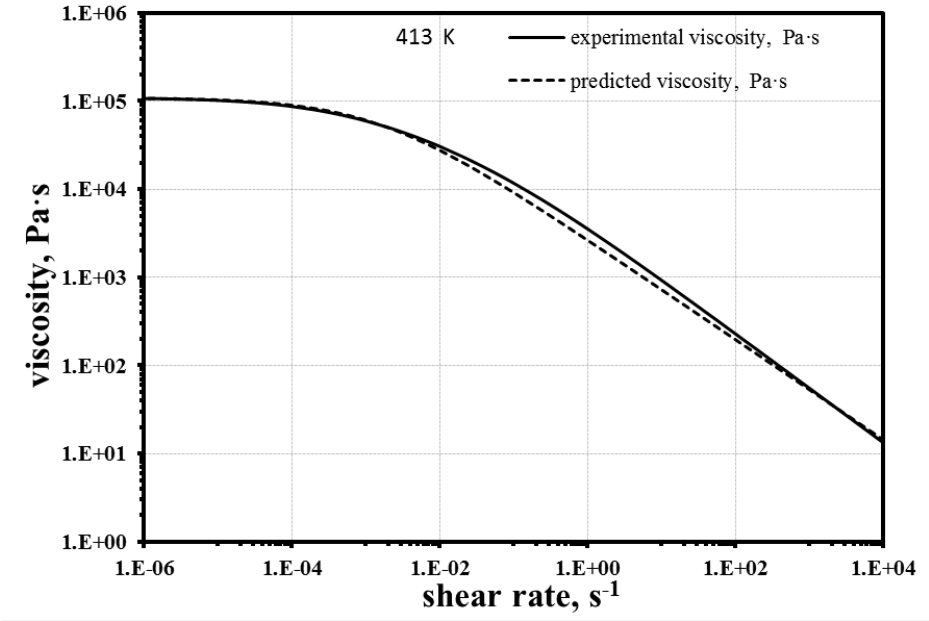

Figure C.1. Comparison of experimental and predicted values of viscosity as a function of shear rate.

Table C.6. Sum of square of difference method for 0.48 volume fractions AlN at 413 K to calculate η_0, n, and τ^*

shear rate, s^{-1}	experimental viscosity, Pa·s	predicted viscosity, Pa·s	difference^2
1E-10	108323.17	108696.78	1.40E+05
2E-10	108319.86	108692.37	1.39E+05
3E-10	108317.15	108688.85	1.38E+05
4E-10	108314.77	108685.82	1.38E+05
5E-10	108312.60	108683.10	1.37E+05
6E-10	108310.60	108680.61	1.37E+05
7E-10	108308.71	108678.29	1.37E+05
8E-10	108306.93	108676.11	1.36E+05
9E-10	108305.23	108674.05	1.36E+05
1E-09	108303.60	108672.08	1.36E+05
2E-09	108289.76	108655.75	1.34E+05
3E-09	108278.42	108642.76	1.33E+05
4E-09	108268.46	108631.55	1.32E+05
7E-09	108243.16	108603.73	1.30E+05
8E-09	108235.71	108595.68	1.30E+05
9E-09	108228.61	108588.06	1.29E+05
1000.00	55.19	53.09	4.40E+00
1258.93	47.87	46.58	1.66E+00
1584.89	41.52	40.87	4.24E-01
1995.26	36.02	35.86	2.39E-02
2511.89	31.24	31.47	5.13E-02
3162.28	27.10	27.61	2.64E-01
3981.07	23.50	24.22	5.24E-01
5011.87	20.38	21.25	7.62E-01
6309.57	17.68	18.65	9.45E-01
7943.28	15.33	16.36	1.06E+00
10000.00	13.30	14.36	1.13E+00
η_0	108705.94	**SSD**	**2.59E+08**
n	0.43	**High shear SSD**	**1.91E+01**
τ^*	161.54		

Use of solver to calculate Cross-WLF coefficients n and τ* are illustrated in the following steps. Step by step illustration shown was performed in Microsoft Excel 2010 using a Windows-based computer.

Step 1: Open Microsoft Excel 2010 and click on "*Data*" tab. In "Data" tab click "*Solver*" button that will pop-up a window called "*Solver Parameters*" as shown in **Figure C.2.**

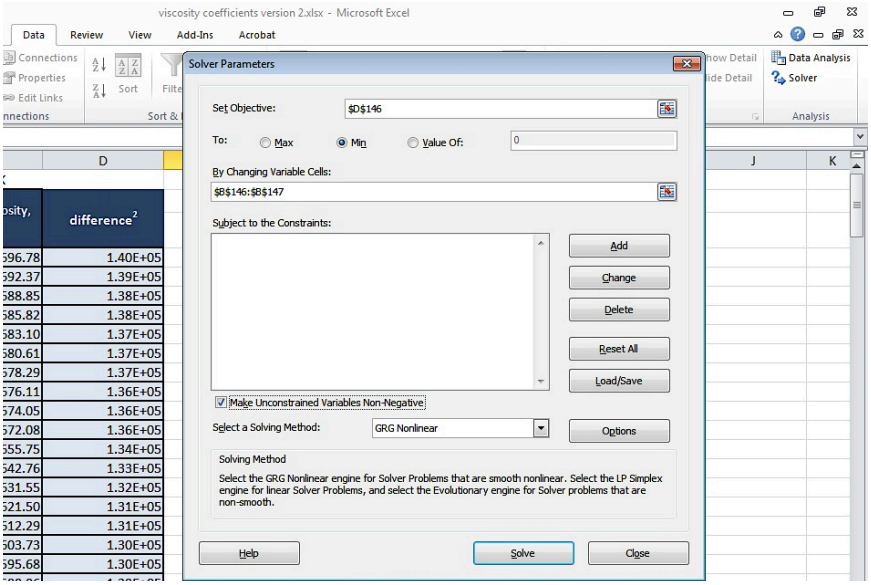

Figure C.2. Solver parameter window in Microsoft Excel 2010.

Step 2: Select "*high shear SSD*" cell similar to the one given in **Table C.6** in the "*set objective*" space. As the goal is to minimize SSD click on the circle besides "*Min*" as shown in **Figure C.3.** Select "*GRG Nonlinear*" as the solving method. Further select cells referring to Cross-WLF coefficients n and τ* in the "*changing variable cells*" space. n and τ* values are similar to the ones shown in **Table C.6**.

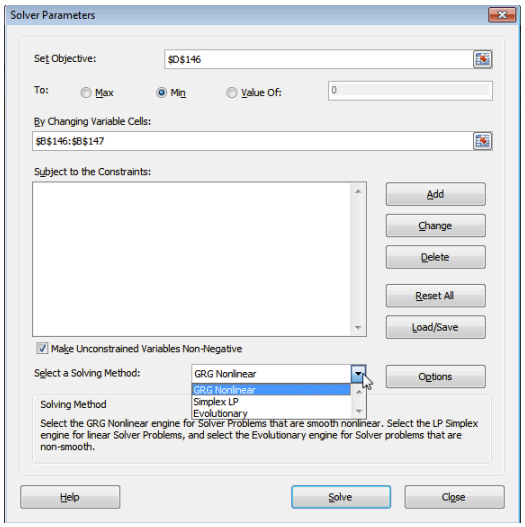

Figure C.3. Selection of solving method and input parameters for calculating n and τ*.

Step 3: In order to get good convergence click on "*option*" button in the solver parameter window. This will pop-up a small window as shown in **Figure B.4.** Click on "*GRG Nonlinear*" tab and set the convergence value $\geq 1 \times 10^{-12}$. Finally click the "*OK*" button.

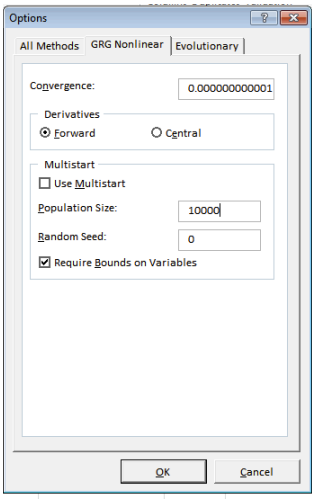

Figure C.4. Set convergence value for GRG Nonlinear method.

Step 4: Click on "*Solve*" button to get new values for n and τ*.

In order to calculate rest of the Cross-WLF coefficients again the same method of minimizing the SSD was used as illustrated in **Steps 1-4.** In this case the

objective cell was taken as SSD and the changing variable cells were taken as D_1 A_1 and T*. For this the zero shear viscosities were first predicted for four different temperatures 413 K, 419.5 K, 426 K and 433 K using **Equation C.1**. An illustration to calculate these coefficients is shown in **Table C.7.**

Table C.7. Sum of square of difference method for 0.48 volume fractions AlN at 413 K to calculate D1, A1 and T*

temperature, K	ηo, Pa.s	predicted ηo, Pa.s	difference^2
413	1.09E+05	1.09E+05	1.47E+04
419.5	3.17E+04	3.10E+04	4.37E+05
426	9.49E+03	1.04E+04	7.51E+05
433	2.78E+03	3.68E+03	8.09E+05
D_1	8.73E+10	SSD	2.01E+06
A_1	32.13		
T*	375.15		

Calculations represented in **Tables C.2** through **C.7** and **Figures C.1** through **C.4** were performed to calculate Cross-WLF coefficients for volume fractions 0.48, 0.49, 0.5, 0.51 and 0.52 of monomodal AlN-polymer mixtures and also for volume fractions 0.52, 0.54, 0.56, 0.58 and 0.6 of bimodal AlN-polymer mixtures.

Appendix D: Procedure to determine Dual-domain Tait Constants

Specific volume was calculated for a variety of ceramic feedstock for four different pressure values 0, 50, 100, 150 and 200 MPa between 298 to 433 K temperature ranges. **Equation D.1** was used to calculate specific volume.

$$v_c = X_f v_f + v_m(1 - X_f) \qquad \text{(D.1)}$$

An illustration for specific volume calculations is shown in **Table D.1** and a plot representing these values is as shown in **Figure D.1.**

Table D.1: Specific volume calculations for different solids loading at 50 MPa pressure.

volume fraction powder	0	0.48	0.49	0.5	0.51	0.52	1
temperature [K]	specific volume [m³/kg]	specific volume [m³/kg]	specific volume [m³/kg]	specific volume [m³/kg]	specific volume [m³/kg]	specific volume [m³/kg]	specific volume [m³/kg]
	AlN (binder)	AlN	AlN	AlN	AlN	AlN	AlN (filler)
298.00	1.12E-03	4.82E-04	4.77E-04	4.72E-04	4.67E-04	4.62E-04	3.20E-04
300.76	1.13E-03	4.82E-04	4.77E-04	4.72E-04	4.67E-04	4.62E-04	3.19E-04
303.51	1.13E-03	4.83E-04	4.78E-04	4.73E-04	4.68E-04	4.63E-04	3.19E-04
306.27	1.13E-03	4.83E-04	4.78E-04	4.73E-04	4.68E-04	4.63E-04	3.18E-04
309.02	1.14E-03	4.84E-04	4.78E-04	4.73E-04	4.68E-04	4.64E-04	3.18E-04
333.82	1.20E-03	4.94E-04	4.89E-04	4.83E-04	4.78E-04	4.72E-04	3.15E-04
336.57	1.22E-03	4.97E-04	4.92E-04	4.86E-04	4.80E-04	4.75E-04	3.15E-04
339.33	1.23E-03	5.01E-04	4.95E-04	4.90E-04	4.84E-04	4.79E-04	3.17E-04
342.08	1.23E-03	5.02E-04	4.96E-04	4.90E-04	4.85E-04	4.79E-04	3.17E-04
344.84	1.23E-03	5.03E-04	4.97E-04	4.91E-04	4.86E-04	4.80E-04	3.18E-04
421.98	1.33E-03	5.24E-04	5.18E-04	5.12E-04	5.06E-04	5.00E-04	3.22E-04
424.74	1.33E-03	5.25E-04	5.19E-04	5.12E-04	5.06E-04	5.00E-04	3.22E-04
427.49	1.33E-03	5.26E-04	5.19E-04	5.13E-04	5.07E-04	5.01E-04	3.22E-04
430.25	1.34E-03	5.27E-04	5.20E-04	5.14E-04	5.08E-04	5.02E-04	3.22E-04
433.00	1.34E-03	5.27E-04	5.21E-04	5.15E-04	5.08E-04	5.02E-04	3.22E-04

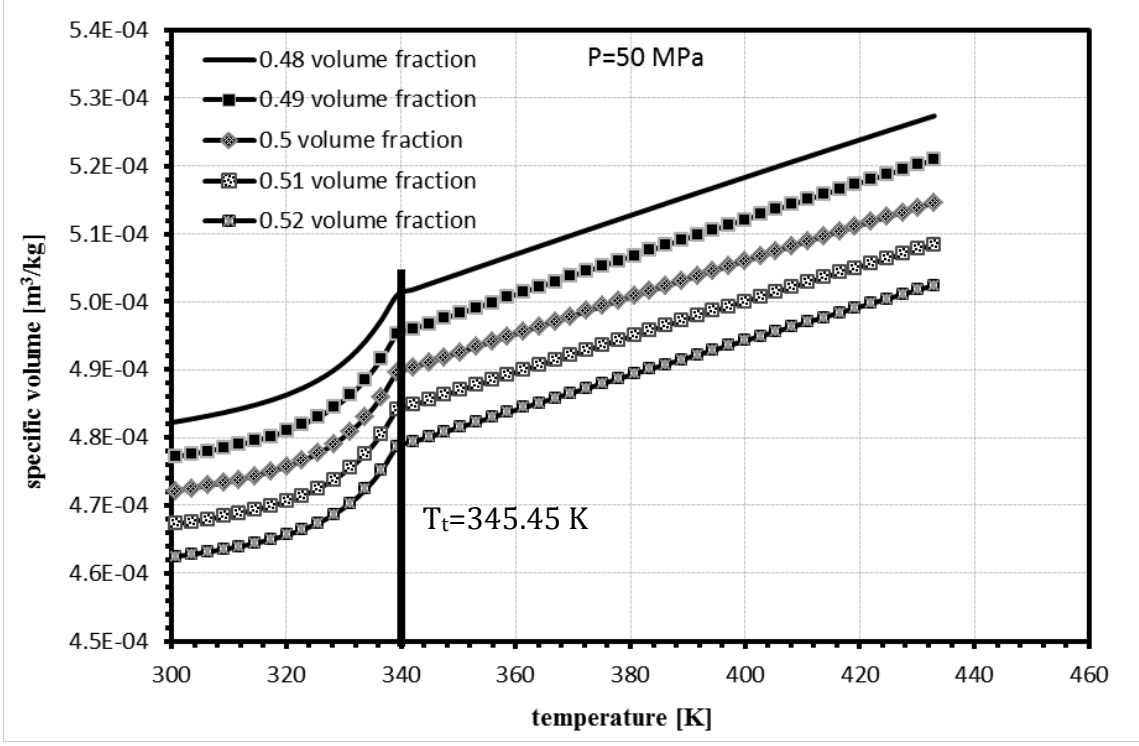

Figure D.1. Specific volume as a function of temperature at 50 MPa pressure.

In order to calculate the dual domain constants the specific volume calculated for 0.48 to 0.52 volume fractions AIN sum of square of difference (SSD) was calculated and a GRG nonlinear solver was used to minimize SSD value. Dual domain Tait model used for predicting specific volumes are shown in **Equations D.2 – D4**

$$\upsilon(T,p) = \upsilon_o(T)\left[1 - Cln\left(1 + \frac{p}{B(T)}\right) + \upsilon_t(T,p)\right] \qquad D2$$

where, υ (T,p) is the specific volume at a given temperature and pressure, u_o is the specific volume at zero gauge pressure, T is temperature in K, p is pressure in Pa, and C is a constant assumed as 0.0894. The parameter, B, accounts for the pressure sensitivity of the material and is separately defined for the solid and melt regions. For the upper bound [18] when $T > T_t$ (volumetric transition temperature), B is given by **Equation D.3**

$$v_o = b_{1m} + b_{2m}(T - b_5)B(T) = b_{3m}e^{[-b_{4m}(T-b_5)]}v_t(T,p) = 0 \qquad D3$$

where, b_{1m}, b_{2m}, b_{3m}, b_{4m}, and b_5 are curve-fitted coefficients. For the lower bound, when $T < T_t$, the parameter, B, is given by **Equation D.4:**

$$v_o = b_{1s} + b_{2s}(T - b_5)B(T) = b_{2s}e^{[-b_{4s}(T-b_5]}v_t(T,p) = b_7e^{[b_8(T-b_5)-(b_9p)]}$$

D4

where, b_{1s}, b_{2s}, b_{3s}, b_{4s}, b_5, b_7, b_8, and b_9 are curve-fitted coefficients. The dependence of the volumetric transition temperature, T_t on pressure can be given by $T_t(p) = b_5+b_6(p)$, where b_5 and b_6 are curve-fitted coefficients.

Calculation of Dual domain Tait constants was done in four stages. In the first stage constants b_5 and b_6 were calculated by plotting a graph of transition temperature (T_t) as a function of pressure. T_t value is read off the plot as shown in **Figure D.2.** A linear curve fitting step was done on intermediate T_t values and the values of b_5,and b_6 were determined.

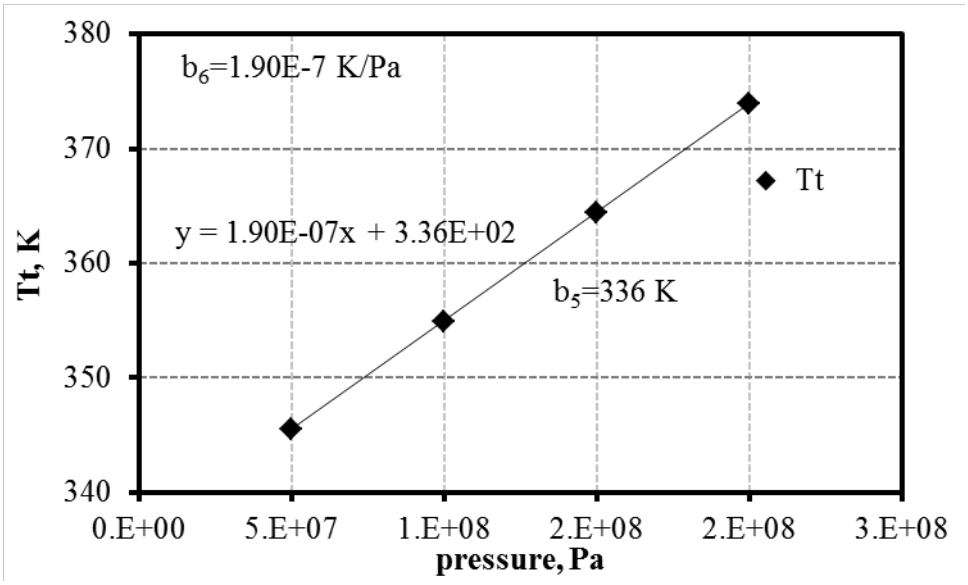

Figure D.2. Volumetric transition temperature as a function of pressure.

In stage two of the calculations constants b_{1s}, b_{2s}, and b_{1m}, b_{2m}, were calculated by reading the values of the plot as shown in **Figure D.3.** Using informed guess the remaining set of Tait constants were assumed. Using **Equations D.4-D.6** in an Excel spreadsheet, the specific volume was predicted for ranges of temperatures between 298 to 433 K.

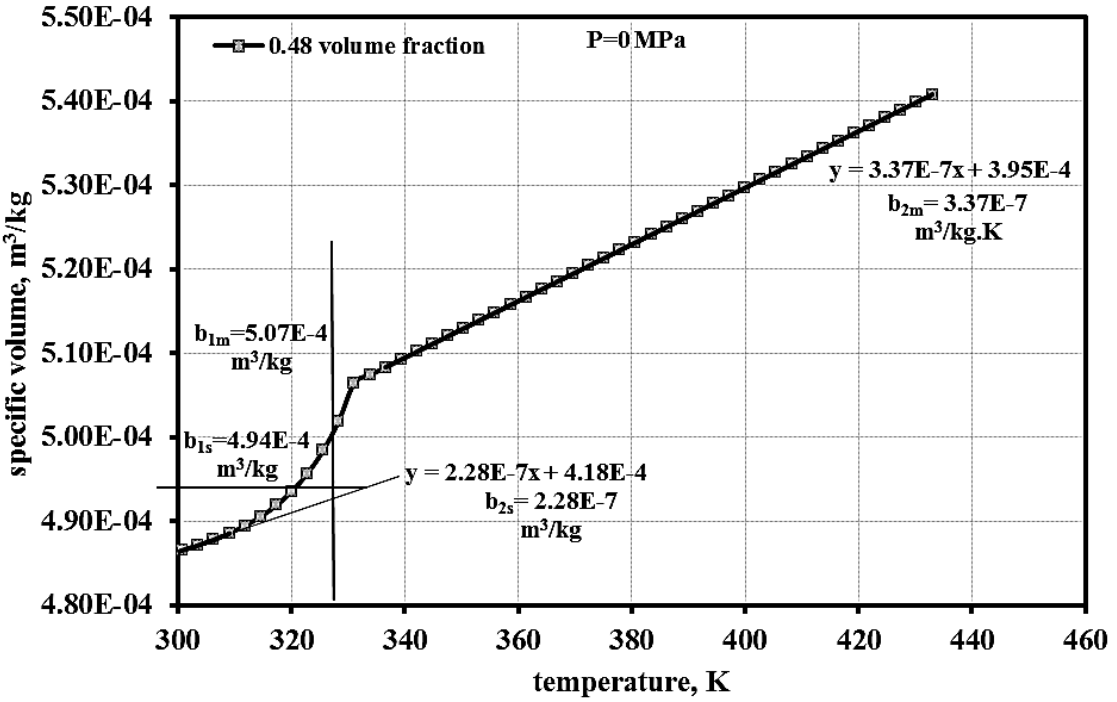

Figure D.3. Specific volume as a function of temperature for 0.48 volume fraction AlN at 0 MPa pressure.

In stage three of the calculations the SSD was calculated for the first domain which was used to calculate Tait constants b_{3s}, b_{4s}, b_7, b_8, and b_9. In order to do this the GRG nonlinear solver was used to minimize SSD and get a better fit. In the final stage of calculations the Tait constants b_{3m} and b_{4m} pertaining to second domain were calculated using GRG nonlinear solver which minimized SSD to obtain a better fit of experimental and predicted values. An illustration of SSD calculation is as shown in **Table C.2.**

The use of Solver to calculate dual-domain Tait constants, b_{3m}, b_{4m}, b_{3s}, b_{4s}, b_5, b_7, b_8, and b_9 are illustrated in the following steps. The step-by-step illustration

shown below was performed on Microsoft Excel 2010 using a Window-based computer.

Table C.2. Calculation of Tait constants with the use of SSD and a GRG nonlinear solver.

temperature, K	V(T,p), m^3/kg	V(T,p), m^3/kg predicted	$diff^2$	SSD	Tait constants	
298.00	4.86E-04	4.87E-04	5.09E-13	Zone 1	b_5	331
300.76	4.87E-04	4.87E-04	6.24E-13		b_6	1.65E-07
303.51	4.87E-04	4.88E-04	6.72E-13		b_{1m}	5.07E-04
306.27	4.88E-04	4.89E-04	6.18E-13		b_{2m}	3.37E-07
309.02	4.89E-04	4.89E-04	4.42E-13		b_{3m}	2.71E+08
311.78	4.89E-04	4.90E-04	1.77E-13		b_{4m}	4.88E-03
314.53	4.91E-04	4.91E-04	1.72E-16		b_{1s}	4.92E-04
317.29	4.92E-04	4.91E-04	3.87E-13		b_{2s}	1.82E-07
320.04	4.94E-04	4.92E-04	2.45E-12		b_{3s}	5.79E+08
				5.88E-12	b_{4s}	0.00126
336.57	5.08E-04	5.09E-04	3.16E-13	Zone 2	b_7	3.23E-06
339.33	5.09E-04	5.10E-04	3.17E-13		b_8	4.50E-02
342.08	5.10E-04	5.11E-04	3.17E-13		b_9	2.12E-08
344.84	5.11E-04	5.12E-04	3.17E-13			
347.59	5.12E-04	5.13E-04	3.18E-13			
350.35	5.13E-04	5.14E-04	3.19E-13			
413.71	5.34E-04	5.35E-04	3.27E-13			
416.47	5.35E-04	5.36E-04	3.27E-13			
419.22	5.36E-04	5.37E-04	3.28E-13			
421.98	5.37E-04	5.38E-04	3.28E-13			
424.74	5.38E-04	5.39E-04	3.28E-13			
427.49	5.39E-04	5.40E-04	3.29E-13			
430.25	5.40E-04	5.40E-04	3.29E-13			
433.00	5.41E-04	5.41E-04	3.29E-13			
				1.16E-11		

Step 1: Open Microsoft Excel 2010 and click on "*Data*" tab. In "Data" tab click "*Solver*" button that will pop-up a window called "*Solver Parameters*" as shown in **Figure D.4.**

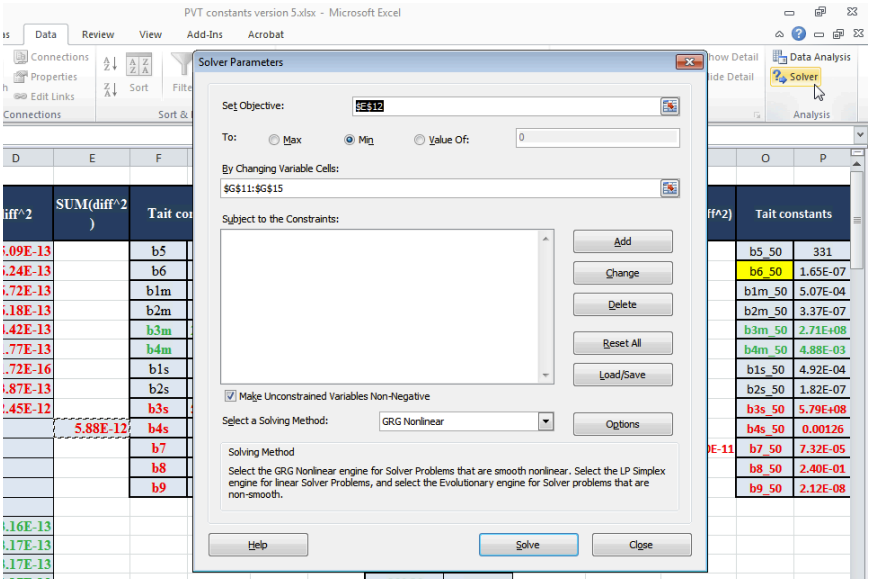

Figure D.4. Solver parameter window in Microsoft Excel 2010.

Step 2: Select "*SSD*" cell for "Zone 1" similar to the one given in **Table D.3** in the "*set objective*" space in order to solve for b_{3m}, b_{4m}. Since the goal is to minimize SSD click on the circle besides "*Min*" as shown in **Figure D.5.** Select "*GRG Nonlinear*" as the solving method. Further select cells referring to Tait constants b_{3m}, and b_{4m} in the "*changing variable cell*" space. b_{3m}, and b_{4m} values are similar to the ones shown in **Table D.2**.

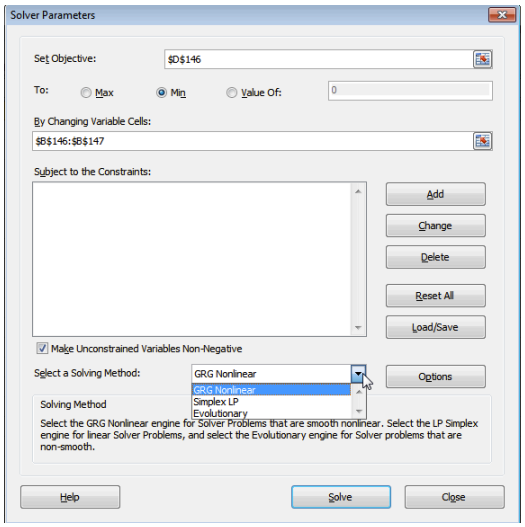

Figure D.5. Selection of solving method and input parameters for calculating b_{3m}, and b_{4m}.

Step 3: In order to get good convergence click on "*option*" button in the solver parameter window. This will pop-up a small window as shown in **Figure D.6.** Click on "*GRG Nonlinear*" tab and set the convergence value to be $\geq 1 \times 10^{-12}$. Finally click the "*OK*" button.

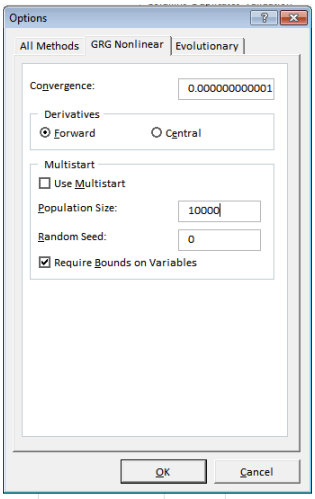

Figure D.6. Set convergence value for GRG Nonlinear method.

Step 4: Click on "*Solve*" button to get new values for b_{3m}, and b_{4m}.

Step 5: Repeat **Steps 2 to 4** to minimize SSD corresponding to Zone 2 b_{3s}, b_{4s}, b_5, b_7, b_8, and b_9 cells as shown in **Table D.2** are selected in the "*changing variable cell*" space and the "*objective cell*" space is set as zone 2 SSD.

Calculations presented in this section were performed to calculate the dual-domain Tait constants for volume fractions 0.48, 0.49, 0.5, 0.51 and 0.52 of monomodal AlN-polymer mixtures and also for volume fractions 0.52, 0.54, 0.56, 0.58 and 0.6 of bimodal AlN-polymer mixtures.

Appendix E: Sintered scanning electron micrographs of green micromachined aluminum nitride

Commercially available AlN (~1 μm and ~20 nm) and Y_2O_3 (~50 nm) were used as the starting materials in as received condition. The monomodal μ-AlN mixtures contained 80.5 wt.% micro scale AlN powder. The bimodal μ-n AlN mixtures contained 82 wt.% larger (μ) and 18 wt. % finer (n) AlN powder. The aluminum nitride monomodal and bimodal feedstock were injection molded into Charpy bars. The injection molded AlN parts were green micro-machined **(Figure 5.3)** by Dr. Ozdoganlar's research group at Carnegie Mellon University. The GMM parts were received and sintered at different times and temperatures to study the influence of micro-features and green micro machining on final part quality. Scanning electron microscope (SEM) image of green micromachined monomodal AlN sintered parts are presented in **Figure E1-6** and bimodal AlN sintered parts are presented in **Figure E7-10** at various processing conditions.

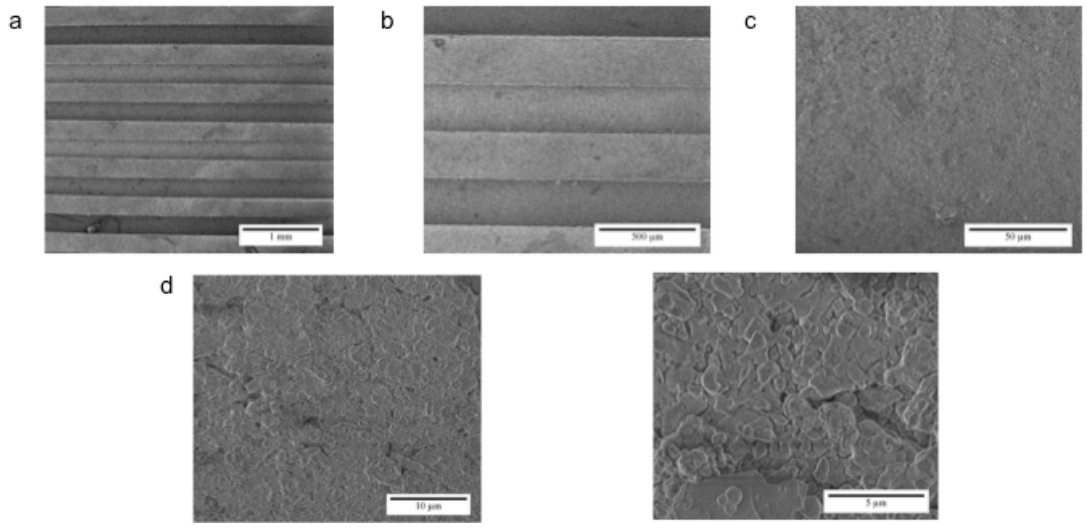

Figure E.1 SEM images of green micromachined monomodal AlN specimen #1 sintered at 1700°C for 1 hour in N_2

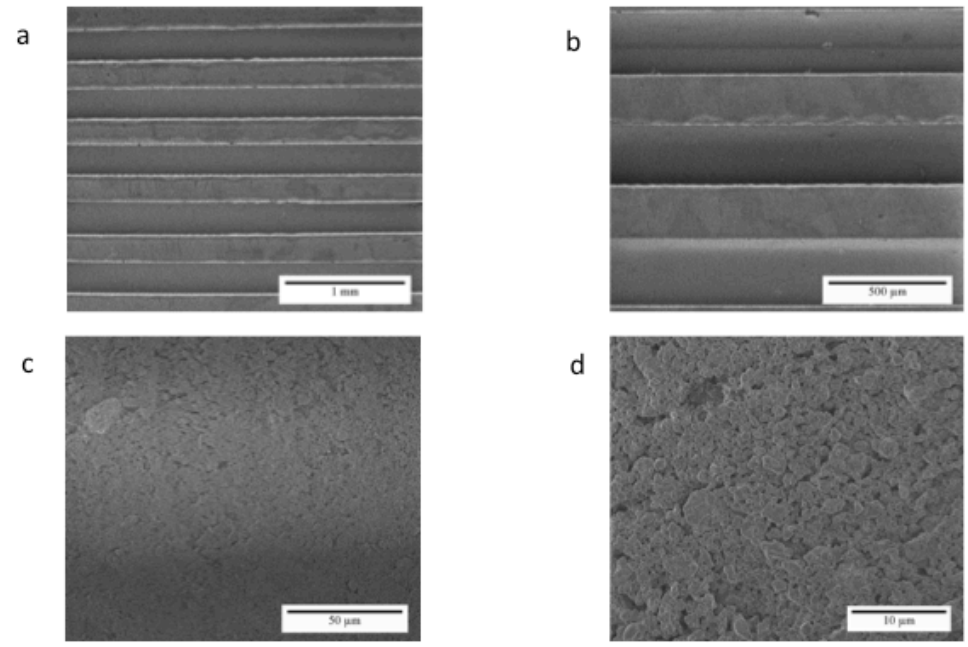

Figure E.2 SEM images of green micromachined monomodal AlN specimen #2 sintered at 1700^{o}C for 1 hour in N_2

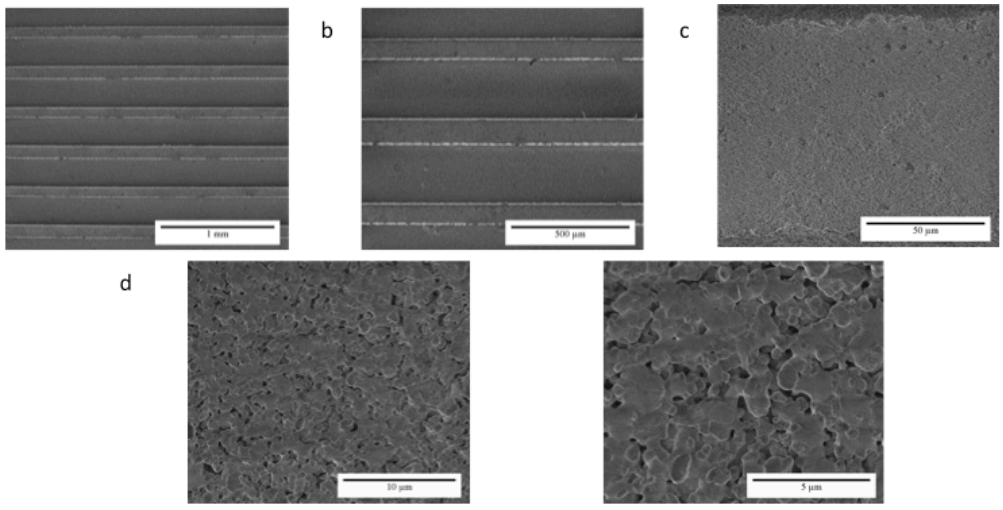

Figure E.3 SEM images of green micromachined monomodal AlN specimen #3 sintered at 1700oC for 1 hour in N_2

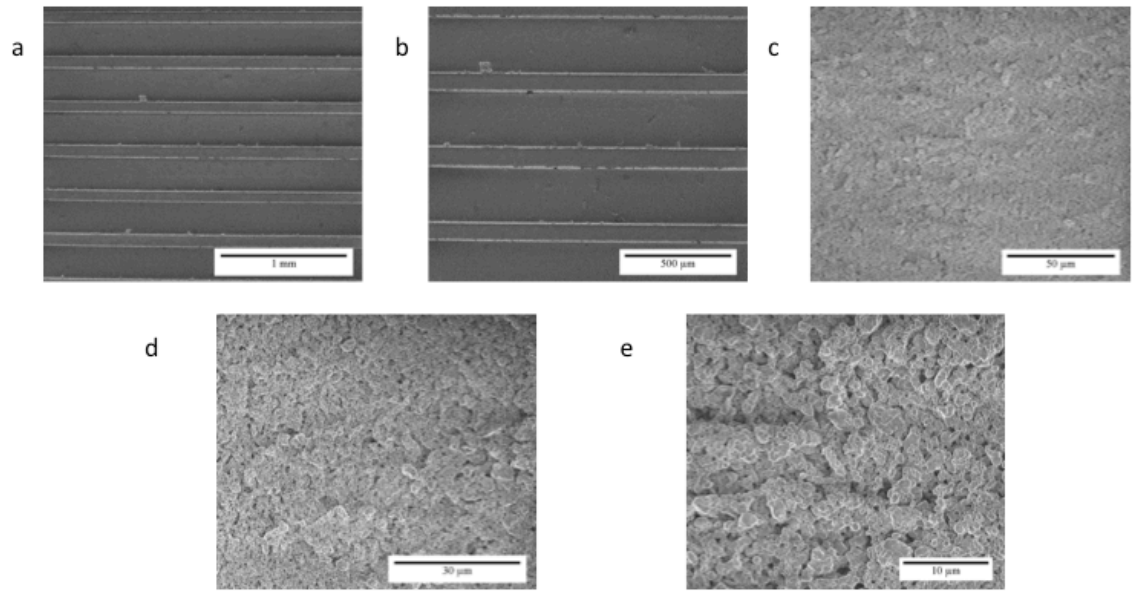

Figure E.4 SEM images of green micromachined monomodal AlN specimen #4 sintered at 1700°C for 1 hour in N_2

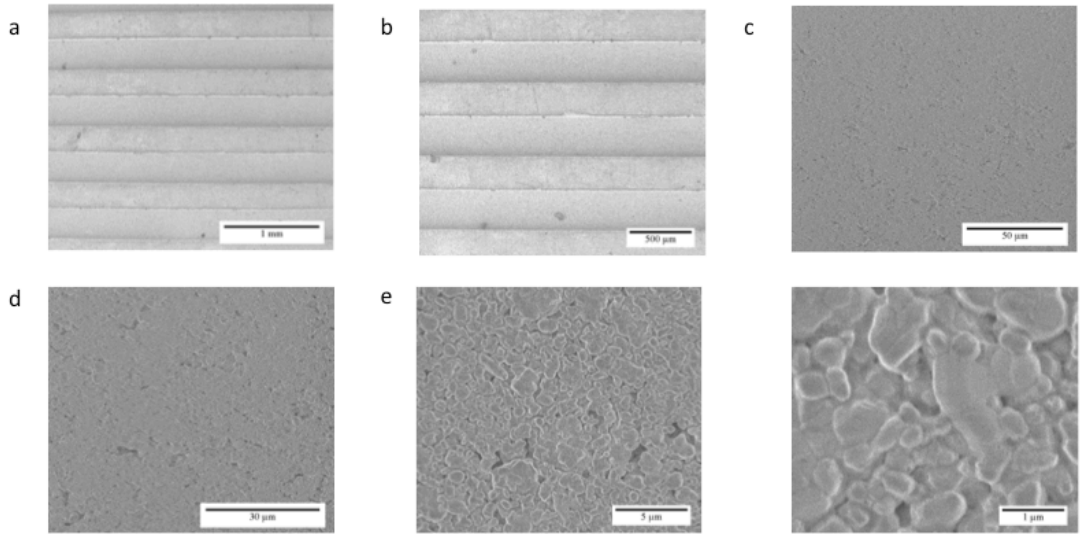

Figure E.5 SEM images of green micromachined monomodal AlN Specimen #9 sintered at 1700°C for 1 hour in N_2

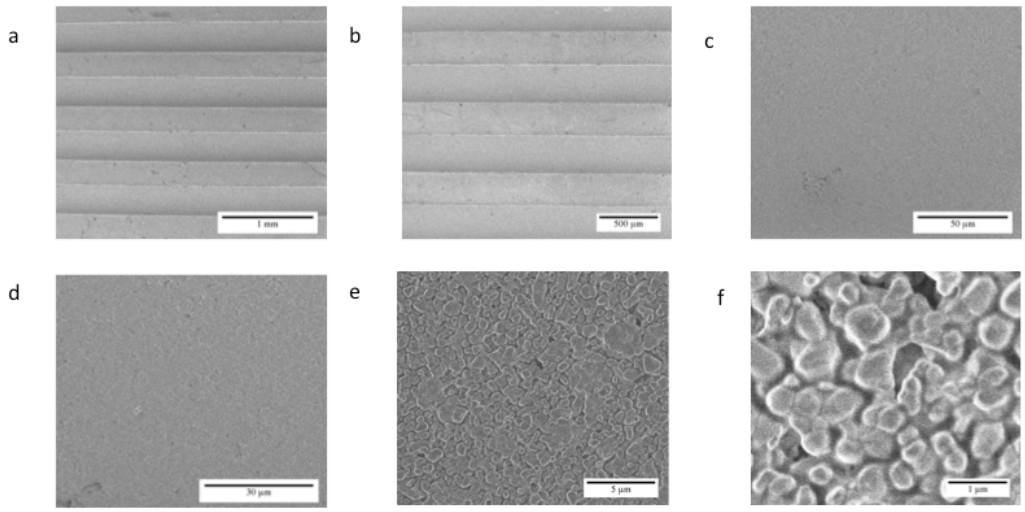

Figure E.6 SEM images of green micromachined monomodal AlN Specimen #10 sintered at 1650^{o}C for 1 hour in N_2

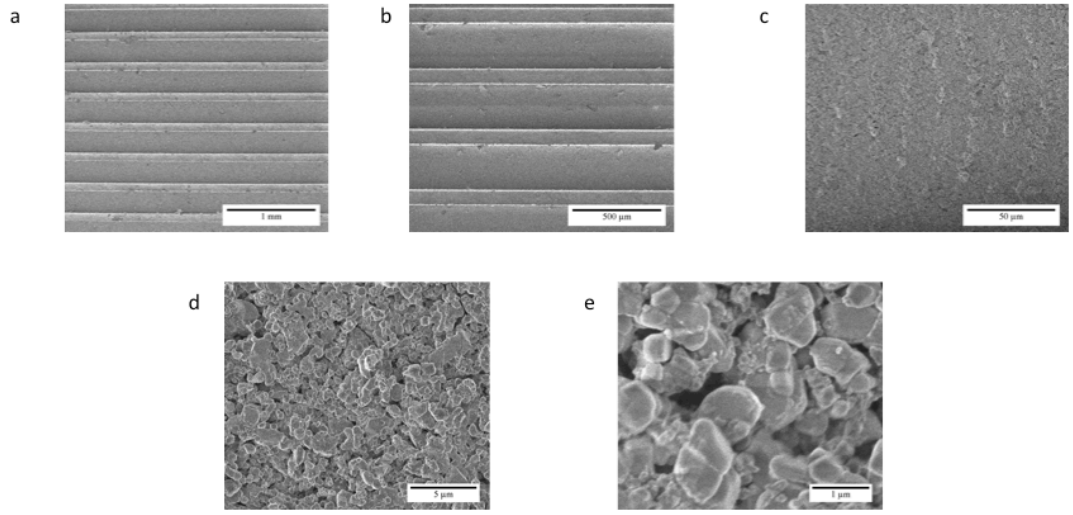

Figure E.7 SEM images of green micromachined bimodal AlN Specimen #5 sintered at 1700^{o}C for 1 hour in N_2

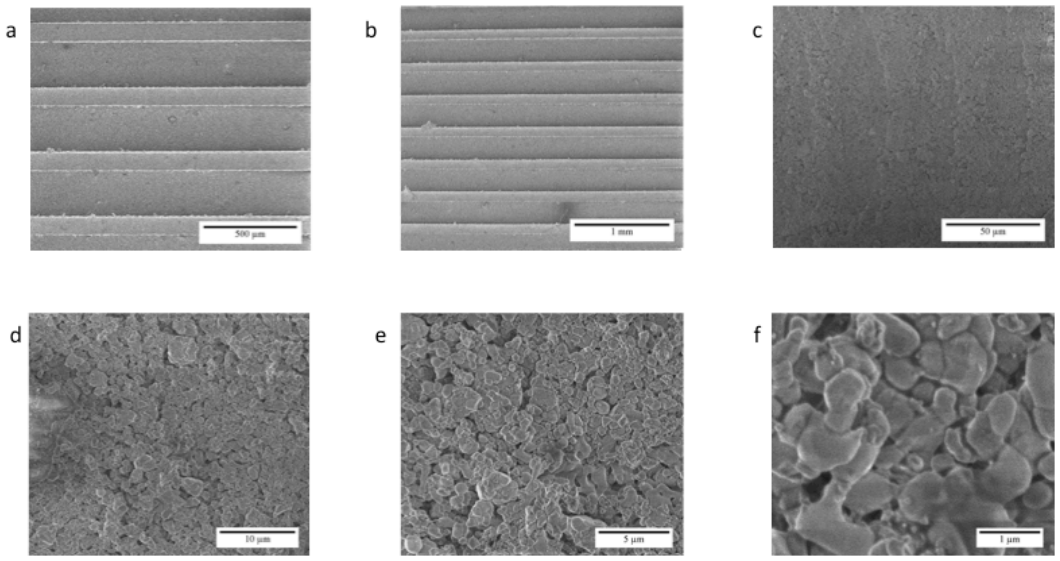

Figure E.8 SEM images of green micromachined bimodal AlN Specimen #6 sintered at 1700^{o}C for 1 hour in N_2

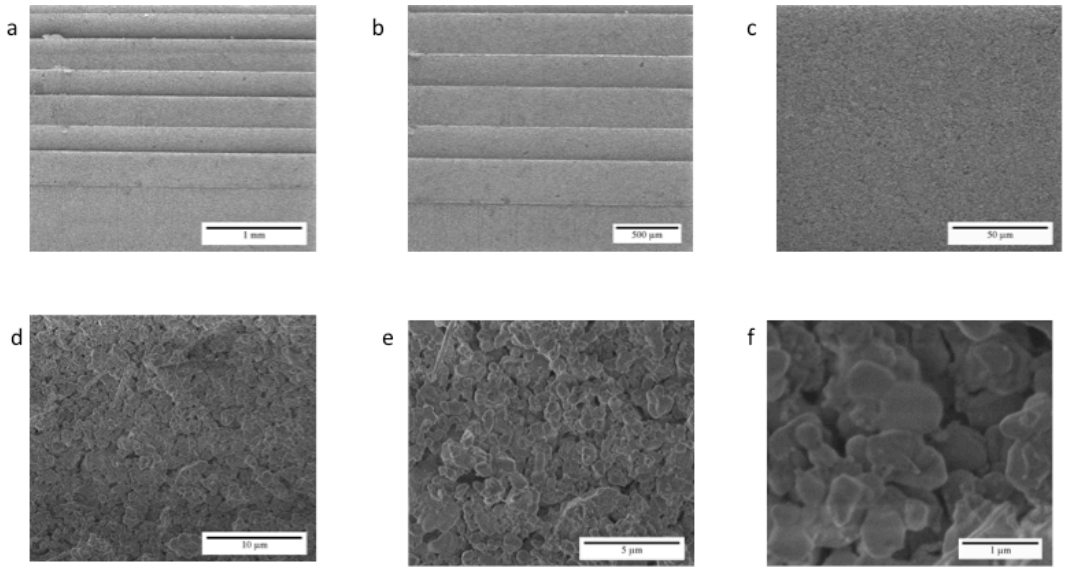

Figure E.9 SEM images of green micromachined bimodal AlN Specimen #7 sintered at 1700^{o}C for 1 hour in N_2

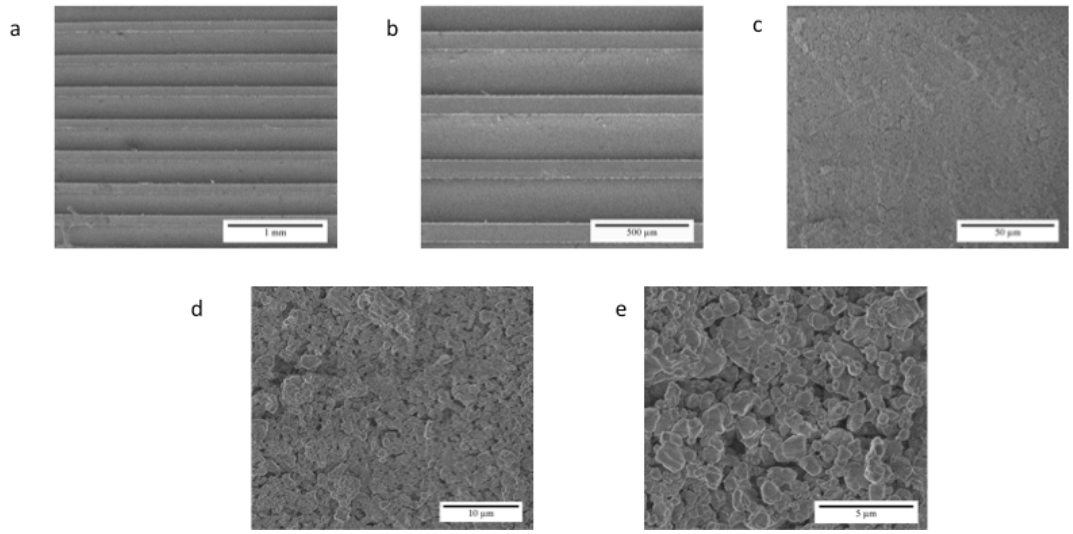

Figure E.10 SEM images of green micromachined bimodal AlN Specimen #8 sintered at 1700oC for 1 hour in N_2